Numerical Analysis of Laterally Loaded Piles in Clay

Peter John Houlston

St. Catherine's College

University of Oxford

A thesis submitted for the degree of

Doctor of Engineering

Trinity Term 2019

Acknowledgements

To my supervisors, Chris Martin and Harvey Burd, and their unwavering

support over the years made it possible for me to make it this far.

To my wife, Joan, and her patience as I locked myself

in my study for months on end to finish this thesis.

To my daughter, Evelyn, whose smile helped me through the final weeks.

Abstract

Numerical Analysis of Laterally Loaded Piles in Clay

A thesis submitted for the degree of Doctor of Engineering

Peter John Houlston

St. Catherine's College, Oxford

Trinity Term 2019

The rapid expansion of the offshore wind industry in recent decades has led to an increased scrutiny of methods traditionally used to design piles in the offshore environment. Investigations by the industry have been performed using a multitude of methods including finite element analysis (FEA), centrifuge testing, and large scale field testing. In this thesis, a novel numerical technique termed finite element limit analysis (FELA) is used to investigate the limiting capacity of laterally loaded piles in clay and the mechanisms that contribute to this resistance.

Finite element limit analysis is a modelling technique that permits rapid optimization-based analysis of plastic collapse mechanisms of boundary value problems with complex loading, structural geometry and soil parameter profiles. Unlike traditional FEA where the accuracy of a given solution is unknown, FELA provides lower and upper bound solutions between which the exact solution must lie within a known bracketing error. An additional benefit of FELA is that runtimes are significantly shorter than equivalent FEA models allowing large parametric studies to be performed in a fraction of the time.

Methods previously used for predicting ultimate resistance are revisited and compared to FELA; such as the moment equilibrium method used by Broms (1964) to calculate total capacity and the widely used Matlock (1970) methodology for determining p-y curves in clay. Relationships between key dimensionless groups of geometry and soil parameters are explored and recommendations about pile capacity are provided. Soil strength profiles including homogeneous conditions, strength gradients and abrupt changes in strength are considered, with recommendations provided on predicting the profile of limiting resistance in each case. An update to the traditional moment equilibrium approach for calculating pile capacity is proposed incorporating additional resistance mechanisms such as shear and moment resistance at the pile base, and a distributed moment resistance acting on the shaft of the pile. Finally, some case studies demonstrating use of the recommendations are presented with a comparison to some of the recently performed pile tests in the PISA joint industry project as a check on the validity of the proposed approach.

Nomenclature

α	Pile-soil adhesion ratio
γ	Soil unit weight
ε_{50}	Strain at half maximum deviator stress
ρ	Soil strength gradient
ψ	Angle about pile centreline
θ	Pile rotation
ξ	Component of lateral bearing resistance from Jeanjean (2009)
λ	Component of lateral bearing resistance from Jeanjean (2009)
κ	Normalised pile flexibility
σ_v'	Vertical effective stress
σ_n	Normal stress on interface elements in Plaxis 3D
σ_y	Yield stress
τ	Shear stress on pile shaft
τ_v	Shear stress acting vertically on pile shaft
τ_{max}	Maximum shear stress on the pile shaft
τ_1	Interface shear stress component in Plaxis 3D
τ_2	Interface shear stress component in Plaxis 3D
ν	Poisson's Ratio
d	Factor in calculation of lateral bearing capacity factor N_p (Jeanjean et al., 2017)
D	Pile diameter
E	Young's modulus
f_x, f_y, f_z	Forces acting on rigid bodies within Oxlim
F_{base}	Lateral shearing resistance at pile base
$F_{base,ult}$	Ultimate shearing resistance at pile base
h	Height of pile head above ground level (alternatively 'upstand height')
H	Lateral force applied at pile head

I	Second moment of area
L	Pile length
L_{crit}	Critical length for flexible pile behaviour
m	Distributed moment on pile shaft
$m_{y,oxlim}$	Distributed moment on pile shaft from Oxlim rigid bodies
m_{ult}	Ultimate distributed moment resistance on pile shaft
M	Moment at Pile Head
M_{base}	Moment resistance at pile base
$M_{base,ult}$	Ultimate moment resistance at pile base
M_p	Moment a plastic hinge forms
N_p	Lateral bearing capacity factor for pile shaft resistance
N_{p0}	Lateral bearing capacity factor for weightless soil
N_{pd}	Limiting lateral bearing factor (Jeanjean et al., 2017)
$N_{p,surface}$	Lateral bearing capacity factor at ground surface
$N_{p,flow}$	Lateral bearing capacity factor during flow around failure
$N_{p,ts}$	Modified lateral bearing capacity factor in stronger layer of two layer system
$N_{p,tw}$	Modified lateral bearing capacity factor in weaker layer of two layer system
N_m	Lateral moment capacity factor for pile shaft resistance
N_1, N_2	Components for calculating lateral bearing capacity factor (Jeanjean et al., 2017)
p_{ult}	Ultimate distributed lateral force on pile shaft
r	Pile radius
s_u	Undrained shear strength
s_{u0}	Undrained shear strength at ground surface
s_{u1}, s_{u2}	Undrained shear strengths in layered soil systems
$s_{u,base}$	Undrained shear strength at base of the pile
t	Wall thickness
T	Tension at pile-soil interface
y_c	Deflection at 50% maximum load for Matlock (1970) p-y curves

z	Depth from ground level
z_b	Vertical distance from pile toe
z_0	Depth of rotation point for rigid pile
z_{crit}	Depth plastic hinge forms on long slender piles
z_L	Depth to layer transition in two layer strength profile
z_e	Thickness of embedded layer
z_r	Transition depth for Matlock (1970) p-y curves
z_{ts}	Depth of influence of a layer boundary in stronger layer
z_{tw}	Depth of influence of a layer boundary in weaker layer
HXTWn	Homogeneous, fixed head, full interface tension, soil weight not included
HFTWn	Homogeneous, free head, full interface tension, soil weight not included
HXNWn	Homogeneous, fixed head, no interface tension, soil weight not included
HFNWn	Homogeneous, free head, no interface tension, soil weight not included
HXNWi	Homogeneous, fixed head, no interface tension, soil weight included
HFNWi	Homogeneous, free head, no interface tension, soil weight included
LXTWn	Strength gradient, fixed head, full interface tension, soil weight not included
LFTWn	Strength gradient, free head, full interface tension, soil weight not included
LXNWn	Strength gradient, fixed head, no interface tension, soil weight not included
LFNWn	Strength gradient, free head, no interface tension, soil weight not included
LXNWi	Strength gradient, fixed head, no interface tension, soil weight included
LFNWi	Strength gradient, free head, no interface tension, soil weight included

Contents

Chapter 1

Introduction

In this thesis, the ultimate response of piles in clay subjected to lateral loads is investigated. Analysis is performed using both conventional displacement finite element analysis (FEA) software and more recently developed finite element limit analysis (FELA) code that can obtain both lower and upper bound solutions to three-dimensional boundary value problems. Various studies are performed assessing the lateral and moment resistances that occur under commonly encountered design scenarios and insight into the mechanisms that control these responses is given. Detailed analyses of scenarios that are poorly documented in the literature are performed and recommendations for how to address these cases in design are made. Comparison between the approaches used, FEA and FELA, is made with the associated benefits and drawbacks highlighted. Finally, case studies of various design scenarios are provided showing how to incorporate the recommendations included within this thesis into the assessment of the lateral capacity of a pile.

1.1. Laterally loaded piles

Piles are widely used across the civil engineering industry and come in many forms and sizes. These can range from micro screw piles commonly used to support lightweight structures to the large diameter monopiles frequently used to support offshore wind turbines.

The loading applied to a pile is driven by both the structure it is supporting and the environment that structure is located in. Load regimes can vary from simple vertical loading to complex combinations of vertical, lateral and moment loads. The latter case is a scenario that has received a large amount of attention in recent years due to the rapid development of the offshore

wind industry. In Europe alone, 2016 saw 560 new offshore wind turbines with the majority of these, approximately 87%, supported on large diameter monopiles (Wind Europe, 2017). Each of these structures requires a significant investment to design, manufacture and install.

1.2. Research motivation

Despite the prevalence of laterally loaded piles in civil engineering there is surprisingly limited guidance regarding numerical estimation of a pile's lateral capacity. Eurocode 7 (British Standards Institute, 2004) provides no guidance on suitable calculation approaches and recommends performing pile tests or comparing to pile tests with similar geometry in similar material. The former is impractical for some design applications, especially large monopiles for offshore wind turbines, and the latter is hard to achieve due to the inherent variability of ground conditions, loading regimes and design geometry between specific designs. Offshore design guidance, such as the API RP 2GEO (American Petroleum Institute, 2011) and DNVGL-ST-0126 (DNVGL, 2016) standards, provides methods aimed at predicting pile deflection using the p-y approach (Matlock, 1970). However, it is widely recognised that the current guidance is overly conservative for monopiles, see Byrne et al. (2017), and can be unconservative for other design cases, such as fatigue calculations for conductors, see Jeanjean (2009). Simple methods for calculating pile ultimate capacity have been presented by Brinch Hansen (1961) and Broms (1964). These methods provide a quick way of estimating pile capacity, however their applicability as soil conditions become more complicated is debatable. The methods rely on simplifications of the assumed resistance profile that can result in underpredictions of the ultimate capacity: for example, Brinch Hansen (1961) reduces the assumed resistance to plane strain, resulting in lower resistances than even simple approximations of the 3D resistance mechanisms.

The p-y approaches proposed in the offshore standards provide guidance on predicting the ultimate lateral bearing resistance, termed p_{ult}, with depth. The methods presented for clays are

derived from tests performed on relatively small diameter, long slender piles. Many authors have identified that the p_{ult} profile predicted by Matlock (1970) underpredicts the likely profile of lateral resistance.

Finite element analysis (FEA) provides an alternative approach to predict the total and limiting resistance with depth. FEA permits complex ground conditions and pile geometry to be taken into account, offering a great deal of flexibility in the assessment. However, three dimensional (3D) FEA is a very computationally expensive approach that is typically only suitable at late stages of design where the cost of performing the analysis is greatly outweighed by the potential savings for the structure, e.g. for offshore monopiles. A drawback of FEA is that the potential inaccuracy of the approach is unknown and typically a mesh sensitivity study, a time intensive endeavour, is required to determine whether the results are reliable.

Upper bound plasticity based approaches have been shown to be a quick way of giving a more robust profile of p_{ult}. Murff and Hamilton (1993) presented a simple upper bound method using a composite conical wedge and cylinder flow-around mechanism (Randolph and Houlsby, 1984). Yu et al. (2016) proposed a rotated Newton interpolation polynomial as a means of creating the wedge mechanism alongside a toroidal surface at the wedge to flow transition. This method compared favourably to FEA of a limited number of cases. A drawback of both approaches is that only an upper bound solution is shown. This limits the application of the methods as an equivalent lower bound solution is preferable to ensure a conservative design. An equal lower bound solution implies the proposed mechanism is exact, while an unequal solution allows bracketing of the exact solution with a known maximum error.

Finite element limit analysis (FELA) is a technique that has the potential to overcome many of the shortcomings of both FEA and upper bound plasticity based approaches. FELA formulates a boundary value problem as a constrained optimisation over a finite element mesh. This allows rapid computation of rigorous upper and lower bound plasticity solutions with adaptive mesh refinement used to iteratively reduce the error between assessments. This approach is much

faster than traditional FEA techniques while also providing a bracketing error for the exact solution. It can also be considered more reliable than plasticity based approaches for complex problems as no assumptions need to be made regarding the shape of failure mechanisms. This means that FELA provides a means of performing a comprehensive numerical analysis of the failure mechanisms and resulting resistances of laterally loaded piles: a feat previously impractical due to either time constraints, i.e. FEA methods, or limits of the approach used, i.e. upper bound plasticity with an assumed mechanism.

This research aims at performing such a study and providing a rigorous review of the mechanisms of failure for a laterally loaded rigid pile and the associated resistances obtained in commonly encountered design scenarios in clay.

1.3. Research objectives

This research provides insight into the mechanisms that contribute to pile lateral resistance in clay using a novel numerical method: finite element limit analysis. The usefulness of 3D FELA has been demonstrated previously for shallow foundations (Martin et al., 2015) and suction caissons (Dunne, 2017). Similar analysis is performed here for laterally loaded short rigid piles to provide insight into total lateral capacity in simple ground conditions, with comparisons to widely used methods of predicting lateral resistance in clay. Upper and lower limits of resistance for full interface tension and no interface tension with weightless soil are established along with recommendations of how to predict the total resistance using moment equilibrium equations.

Previous work using FELA has focused on the global collapse loads, however recent updates to OxLim (the in-house FELA code developed at the University of Oxford) allow the assessment of local resistances acting on a foundation. For laterally loaded piles this allows detailed assessment of the distribution of lateral resistance with depth and this forms a key output of this thesis. The use of FELA to provide both upper and lower bound plasticity

solutions gives greater certainty of the results as opposed to just using upper bound solutions; as was used in previous work by Murff and Hamilton (1993) and Zhang et al. (2016). OxLim has been used to provide insight into the following aspects of the problem, and methods for predicting the resistance in each case are provided:

- Profiles of lateral bearing factor with depth for general strength profiles in clay consisting of a surface shear strength, s_{u0}, and a strength gradient, ρ
- The increase in lateral bearing factor that occurs near the toe of a pile
- The influence of abrupt changes in soil shear strength on the lateral bearing factor above and below the layer boundary
- The lateral bearing factor at the ground surface

The methods of predicting each mechanism can be used for both short stocky and long slender piles and it is envisaged that these methods will provide valuable insight into lateral pile response during early stage design for large offshore wind projects. While the detailed design stage is predominantly performed using detailed displacement FEA, it is essential to have reliable methods of predicting resistance at early stages of design so that informed choices can be made regarding expected foundation sizes for the various pile options available to a developer. This research aims to provide tools to aid in these early assessments and the decision-making process that is performed.

Investigations have been performed into other resistance mechanisms that affect a pile's lateral capacity. These consist of the additional mechanisms outlined by the PISA project (Byrne et al., 2017) consisting of:

- Distributed moments acting on the pile shaft
- Lateral shear at the pile base
- Moment resistance at the pile base

Methods for predicting the resistance contribution for each of these mechanisms are provided along with an approach for including them into a moment equilibrium calculation for obtaining the total capacity of a short pile.

A final output of this thesis is a comparison of FELA (with a rigid pile) to FEA (with an elastic pile) to assess the significance of the rigid pile assumption used in FELA. This investigation explores the effect of pile flexibility on the total lateral resistance of a pile with reference to typical properties of piles installed for offshore wind farms. This direct comparison between FELA and FEA provides useful insight into the applicability of the new method along with the benefits it can bring.

1.4. Outline of thesis

This thesis is split into seven chapters:

- A detailed literature review of historical methods used to predict pile lateral resistance and more recent attempts at addressing this problem
- An outline of the methodology used within this thesis including verification of OxLim against analytical plasticity solutions
- Assessment of resistance in homogeneous strength profiles
- Investigation of non-homogeneous strength profiles including the effect of abrupt strength changes on the distributed lateral resistance
- Investigations into the resistance at the pile base and distributed moments along the length of the pile
- Comparison between FELA and FEA to show the effect of pile flexibility on total lateral resistance and the variation of mobilised resistance with depth.
- Case studies showing how the techniques presented within this thesis could be used in a design context

Chapter 2

Background

This chapter provides background information on typical design approaches for laterally loaded piles and the numerical methods that are used within this thesis. Where relevant, literature for similar foundation types, such as suction caissons, is included and discussed.

Piles are a versatile foundation type that can range in size from small I-sections supporting lightweight structures to the large diameter steel tubular piles that can be over 100m long supporting offshore oil and gas platforms. Monopiles supporting offshore wind turbine generators (WTG) typically consist of large open-ended steel tubes with a length to diameter ratio, L/D, in the range of 3 to 6 and diameters from 2.5m to greater than 7m. The design of monopiles is principally driven by the response to lateral loading in both the short term and over the life of the structure. Design of these foundations focuses on three key aspects; serviceability limit state (SLS), the fatigue limit state (FLS) and the ultimate limit state (ULS) (DNVGL, 2016). The SLS design criterion focuses on limiting the deformations of the structure to acceptable levels. For WTG foundations this is done by designing the foundation such that under SLS loading the deflection at the pile head does not exceed some percentage of the pile diameter; typically 1% of the pile diameter is used. The FLS design criterion seeks to limit damage to the foundation that arises from cyclic stresses in the pile wall from both installation and cyclic environmental loading over the lifetime of a foundation. Monopiles are typically installed by percussive driving using a hydraulic hammer, a process which can cause substantial levels of fatigue in a pile. The ULS design criterion ensures that the total capacity of the foundation is sufficient to resist loading from an extreme design state; typically determined

from a 1 in 100 year sea state for offshore loading. The main focus of this thesis is on mechanisms that relate to the ULS design state, however the findings can also aid assessment of the SLS state when combined with appropriate modelling techniques that incorporate soil stiffness and deformation.

2.1. Failure mechanisms

Historically, piles installed offshore have typically consisted of long slender piles with a *L/D* ratio more than 20 with typical pile diameters around 1m to 2m for oil and gas platforms. This high *L/D* ratio means that the ultimate lateral resistance of the pile would be driven by the formation of a plastic hinge in the pile itself and not by the resistance of the soil (Randolph and Gourvenec, 2011). This contrasts with a low *L/D* monopile which will essentially undergo a rigid body rotation under loading with the toe of the pile "kicking" out in the opposite direction to that of the loading. In this instance the ultimate resistance of the foundation will be determined by the response of the soil as opposed to the structural capacity of the pile.

Accounting for pile head fixity, whereby a pile is restrained against rotation at the pile head, there are five modes that a laterally loaded pile can fail in, shown schematically in Figure 2.1 (Randolph & Gourvenec, 2011). Free head piles with a low *L/D* typically fail as shown in Figure 2.1(a). In this case the pile rotates as a rigid body about a rotation point located at some depth down the pile; usually in the lower half of the pile. As the *L/D* ratio of the pile increases, the likelihood of the mechanism in Figure 2.1(b) occurring increases; i.e. a plastic hinge forms in the pile at some depth. In this case the ultimate lateral resistance of the pile can be found by integrating the lateral resistance from the soil over the length of pile above the plastic hinge. This mechanism represents a limiting case for the lateral resistance of a pile, i.e. increased pile length will provide no further increase in lateral resistance.

In many cases the pile head is constrained by some means, such as for offshore jacket structures where the pile head is constrained through its connection to the jacket structure. This constraint results in the mechanisms shown in Figure 2.1(c), (d), and (e). Rigid lateral translation, Figure 2.1 (c), will occur when there is both sufficient pile head restraint and high pile stiffness relative to the soil strength occurs. The remaining mechanisms represent failure at the connection of the pile to the structure, Figure 2.1(d), or the minimum of the resistance required to cause a plastic hinge in the pile and the resistance of the structural connection, Figure 2.1(e).

At failure, a pile loaded laterally in cohesive soil will generate soil resistance from two principal mechanisms shown schematically in Figure 2.2. Near the surface, a wedge of soil will be displaced by the pile while below some depth, typically referred to as the transition depth, a

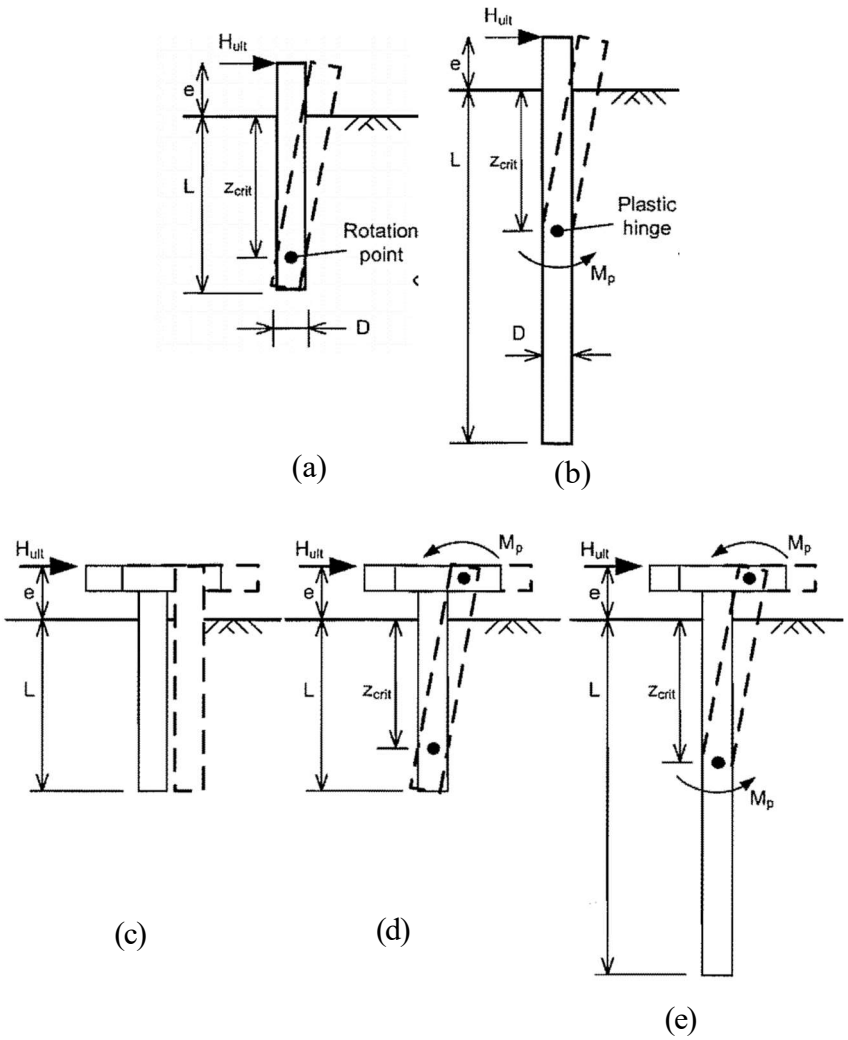

Figure 2.1 - Failure mechanisms of free and fixed head piles, (a) free head rigid rotation, (b) free head with plastic hinge, (c) fixed head rigid translation, (d) fixed head with plastic hinge at pile head, and (e) fixed head with two plastic hinges (Randolph and Gourvenec, 2011)

flow around mechanism will occur which represents the maximum resistance that can be obtained when the pile translates through the soil under plane strain conditions. The resistance over the top part of the pile will be determined by a combination of the soil strength, soil weight and interface tension behaviour. These factors also determine whether a gap forms behind the pile under loading; the assumed impact of gapping is shown schematically in Figure 2.3.

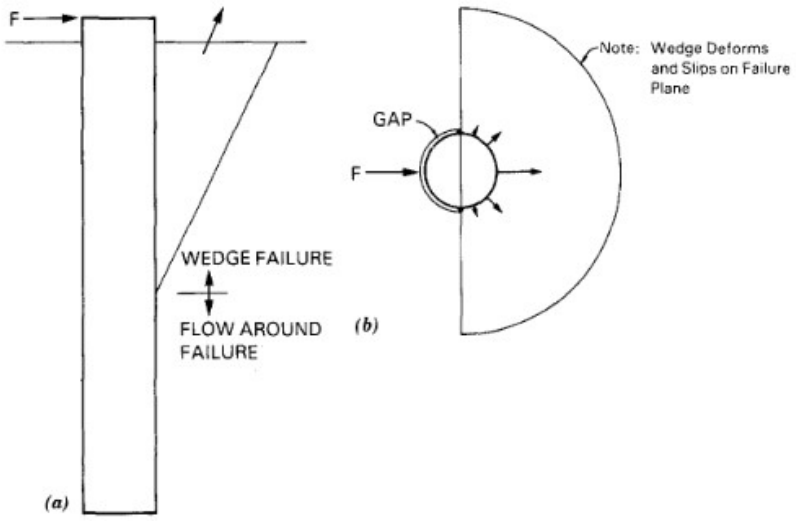

Figure 2.2 - Schematic of wedge failure mechanism (Murff and Hamilton, 1993)

The first two cases, Figure 2.3(a) and (b), are the typical limiting cases considered when performing a numerical assessment, see e.g. Murff and Hamilton (1993). Full interface tension, Figure 2.3(a), is considered to provide the highest possible resistance by having mobilised soil wedges both in front of and behind the pile: behind the pile the soil is pulled down and towards the pile by the interface tension and the weight of the soil. At the other extreme, the assumption of weightless soil and no interface tension results in resistance only from the soil shear strength along the boundary of the wedge of soil in front of the pile. Figure 2.3(c) and (d) show two potential intermediate cases where the gap extends either below the wedge or to some depth within the wedge. This is expected to lead to a total resistance between the limiting cases shown in Figure 2.3(a) and (b).

The ultimate lateral resistance per unit length is typically given as

$$p_{ult} = N_p s_u D \tag{2.1}$$

where p_{ult} is the ultimate resistance, s_u is the undrained shear strength, D is the pile diameter and N_p is a depth-dependent lateral bearing capacity factor. The value of N_p will vary with depth where the wedge failure mechanism is occurring and will remain constant at a maximum value where the flow around failure occurs.

The flow around mechanism, an example of which is shown in Figure 2.4, occurs below the wedge mechanism. In this failure mechanism there is no vertical movement of the soil and as such the mechanism can be represented by plane strain conditions. In this failure mechanism two fans of soil rotate around the exterior of the pile as the pile displaces. Detailed assessment of the flow around mechanism using plasticity theory has been performed by Randolph and Houlsby (1984). In plasticity theory upper and lower bound solutions are proposed with an exact solution obtained if the upper and lower bounds are equal. Lower bound solutions consist of an assumed stress distribution in the soil which is in equilibrium with the applied load. In upper bound solutions the plastic collapse load is estimated by comparing the work done by an external load to the rate of dissipation of energy within the soil. An example of the characteristic mesh used by Randolph and Houlsby (1984) to obtain the lower and upper bound solutions is shown in Figure 2.4. This analysis shows a clear variation in flow around resistance (henceforth expressed in terms of the lateral bearing factor $N_{p,flow}$) with the pile-soil adhesion ratio, α. Randolph and Houlsby (1984) proposed the equation

$$N_{p,flow} = \pi + 2\Delta + 4\cos(\psi)\left(\sqrt{2} + \sin(\psi)\right) \tag{2.2}$$

where $\psi = \pi/4 - \Delta/2$ and $\sin\Delta = \alpha$. Randolph and Houlsby (1984) suggest that for most design scenarios this can be simplified to

$$N_{p,flow} = 9 + 3\alpha \tag{2.3}$$

It was later found that the upper bound solution involved a region of negative plastic work (Murff et al., 1989). Work by Martin and Randolph (2006) provided an upper bound solution close to the lower bound from Randolph and Houlsby (1984), as shown in Figure 2.5. The upper bound solution presented by Martin and Randolph (2006) only matches the lower bound, thus providing an exact solution, at $\alpha = 1$. However, the difference at $\alpha = 0$ is only 0.65% suggesting that either bound is suitably representative of the exact solution if used for design. Yu et al. (2018) used the extended mobilised strength design (EMSD) method to obtain upper bound solutions for the flow around mechanism obtaining resistances slightly higher than those derived by Martin and Randolph (2006).

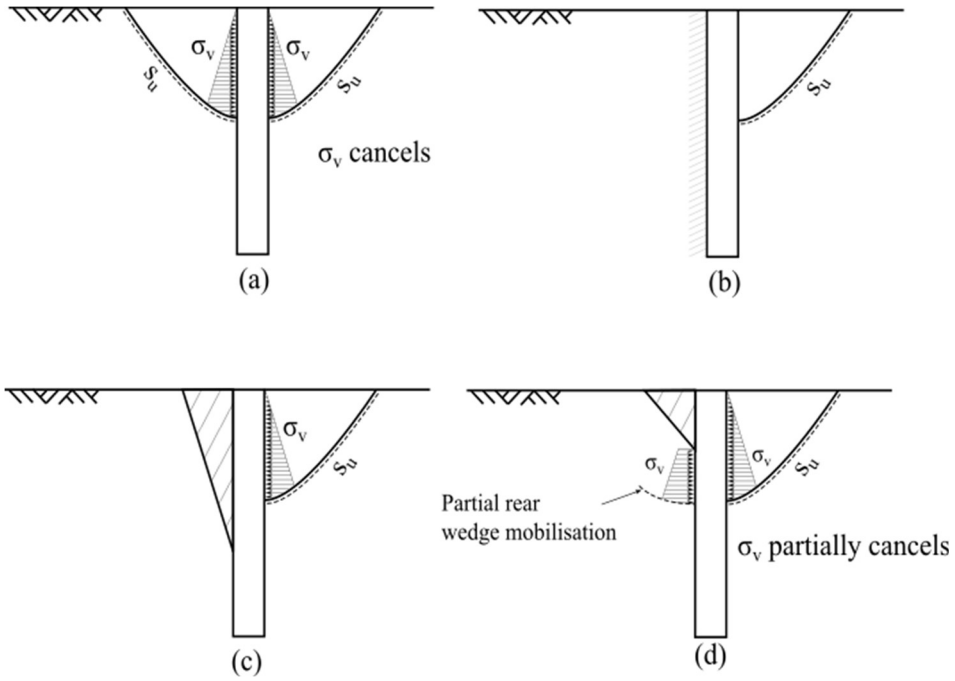

Figure 2.3 - Different possible mobilisations of resistance from wedge mehanism. Resistance from soil weight shown as σ_h and soil shear strength as s_u, (a) full interface tension resulting in a wedge being pulled behind the pile (b) no interface tension in weightless soil resulting in a gap the full length of the pile, (c) no interface tension with gap closing below the soil wedge and (d) no interface tension with the gap closing within the soil wedge

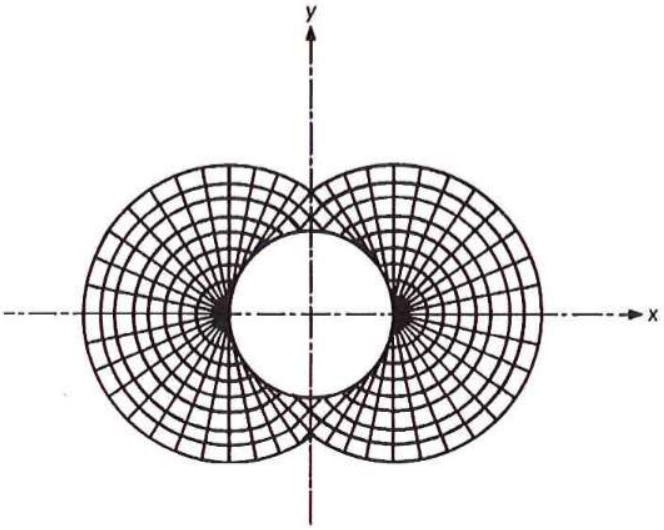

Figure 2.4 - Characteristic mesh for plasticity calculation of flow around mechanism from Randolph and Houlsby (1984). Pile displacement is along the y-axis

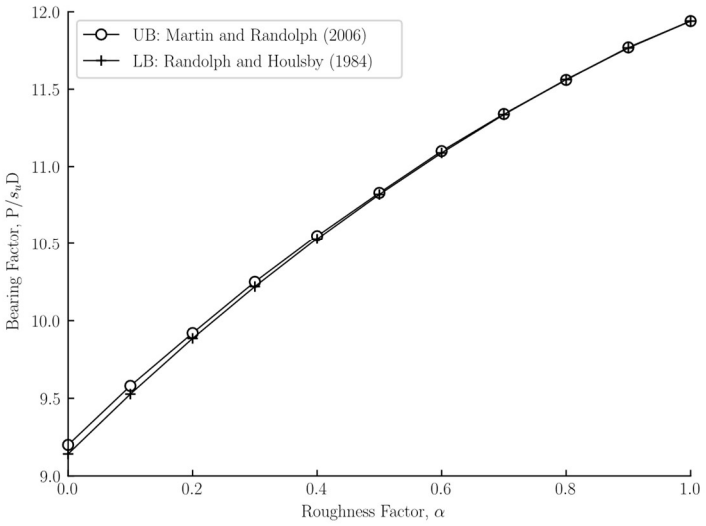

Figure 2.5 - Variation of lateral bearing factor with pile-soil adhesion. Both lower bound (LB) and upper bound (UB) solutions are shown

The mechanisms presented thus far consider only lateral reactions acting on the pile. In work by Lam and Martin (1986) it was proposed that for short foundations with very low *L/D* ratios, in the range of 1 to 2 in the work performed, there would be a significant component of lateral resistance derived from the rotation of the pile. This predominantly consisted of the resistance from the pile shaft however Lam and Martin (1986) also included considerations for the resistance generated at the base of the pile. These mechanisms proposed by Lam and Martin (1986) are shown in Figure 2.6. Previous design methods, such as the Reese (1975) and Matlock

(1970) p-y curve methods, only considered the resistance arising from lateral translation of the pile with resistance solely acting on the pile shaft, i.e. no consideration of base resistances. The laboratory and field test piles used to develop the p-y curve methods can be considered long and slender, i.e. $L/D > 20$. The implication of this is that at some depth the pile will not displace laterally as the total resistance of the soil will exceed the moment capacity of the pile, as shown in Figures 2.1(b) and (e). As such, there will likely be no movement at the toe of pile, removing the need to model base effects for these types of piles.

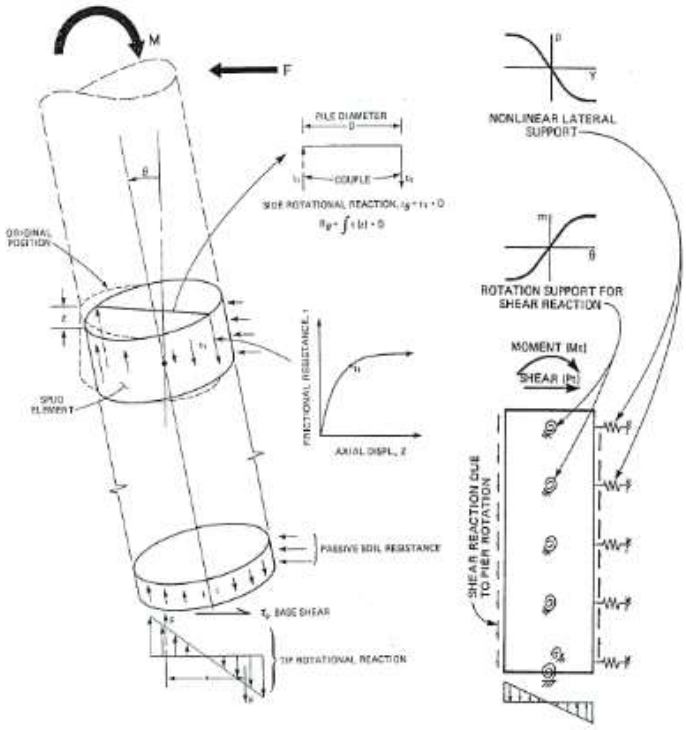

Figure 2.6 - Rotational components of resistance (Lam and Martin, 1986)

2.2. Ultimate pile capacity

The ultimate lateral capacity of a pile can be calculated using a moment equilibrium approach as outlined by Brinch Hansen (1961). Assessment is performed by assuming a load, H, is applied at some upstand, e, and then solving for moment equilibrium of the pile (idealised as a rigid body) about a rotation point at some depth within the piles length, termed z_0. A schematic

of this from Broms (1964) is shown in Figure 2.7. In general terms the moment equilibrium for a laterally loaded pile can be expressed as:

$$H(e + z_0) = \int_{z=0}^{z_0} p_{ult}(z_0 - z)dz + \int_{z=z_0}^{L} p_{ult}(z - z_0)dz \quad (2.4)$$

where p_{ult} is the lateral resistance at a given depth. Brinch Hansen expressed p_{ult} as a resultant of the passive and active earth pressures acting on the front and back of the pile respectively. This method was developed assuming a plane strain wedge acting on a square pile and resulted in a lateral bearing factor at the surface, $N_{p0} = 2.6$, and a limiting value $8.3 \leq N_{p,flow} \leq 11.4$ at depth. This is a conservative assumption when applied to piles with a circular cross section as it results in a limiting resistance at depth less than the smooth case of $\alpha = 0$ from the lower bound resistance shown in Figure 2.5. Other researchers at the time proposed different values for N_{p0} and $N_{p,flow}$ such as Reese and Welch(1958) who proposed $N_{p0} = 2$ and $N_{p,flow} = 12$.

These recommendations are summarised in Broms (1964) who investigates the capacity of rigid piles in undrained clays. Broms (1964) adopts a simplified profile of N_p using a constant value of $N_p = 9$ with depth, i.e. the same as later proposed by Randolph and Houlsby (1984) for a smooth pile in Equation 2.3, with the top $1.5D$ of the pile having no resistance. This assumption along with the deflection and moment profiles assumed by Broms (1964) are shown in Figure 2.7. In Broms (1964) the author compares the expected distribution of reactions on a laterally loaded rigid pile to the bearing pressures that occur on a rigid footing: shown schematically in Figure 2.8. This suggests that at the pile toe there would be an increase in resistance above the plane strain flow around resistance. This differs from other work where $N_{p,flow}$ is considered to be a limiting resistance that cannot be exceeded: see Jeanjean (2017), Murff and Hamilton (1993) and Matlock (1970). However, it should be noted that the prominent literature looking at the distribution of lateral resistance with depth has predominantly focused on long slender piles when performing either model calculations or tests. As such, an increase in resistance near

the toe of the pile would not influence the results of such analyses as the toe of the pile would be unlikely to move a significant amount.

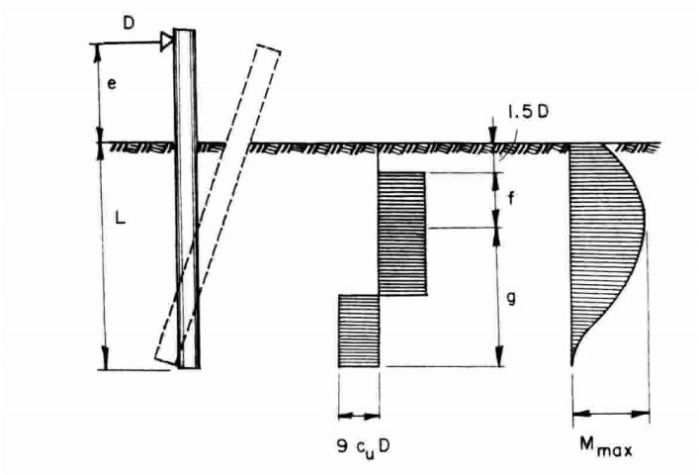

Figure 2.7 - Assumed deflection, soil reaction and bending moment profile for a short rigid pile from Broms (1964)

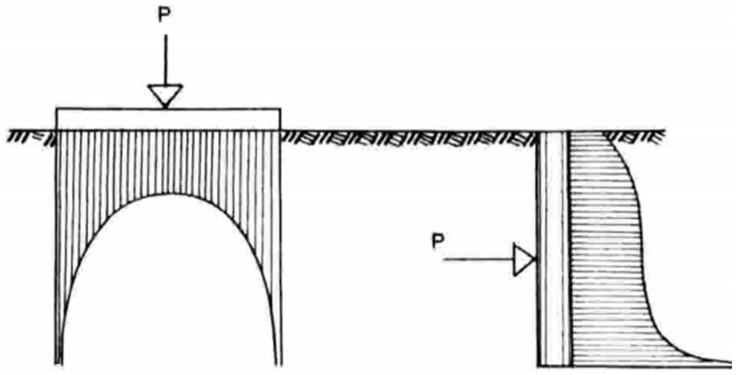

Figure 2.8 - Expected distribution of bearing pressure of a rigid footing on elastic soil and lateral resistances for a translating pile from Broms (1964)

Extensive work has also been performed relating to the lateral capacity of suction caissons and suction piles; offshore foundation types with similar geometry to piles that are frequently used in mooring systems (Bang et al., 2000). For examples see Aubeny et al. (2001), Randolph and House (2002), Aubeny et al. (2003), Doyle et al. (2004), Aubeny and Murff (2005), Clukey et al. (2004), Ahn et al. (2014), Dunne (2017), Li et al. (2018).

2.3. Subgrade reaction approaches

The subgrade reaction approach uses the Winkler approximation for a foundation bearing on soil. In this method the soil response is represented by a series of discrete non-linear springs that are attached to a beam element model of the pile. This can be characterised in its one-dimensional form as shown in Figure 2.9. This representation can be combined with either finite element or finite difference techniques in order to find the deflection, and hence soil mobilisation, in each spring. The soil reactions are typically presented as non-linear curves that relate local displacement, y, to soil reaction, p. In the literature these are known as p-y curves and the term "p-y curve methodology" is frequently used to refer to the subgrade reaction method.

Current design guidance for WTG monopiles, for example DNVGL-ST-0126 (2016), has been derived from the standards used in the offshore oil and gas industry. These standards, such as the API 2nd series of standards in particular API RP 2GEO (2011), recommend use of the subgrade reaction method. The recommendations for p-y curves are based on pile tests performed by Matlock (1970) and Reese (1975). In both cases the response of the soil is modelled by a non-linear curve.

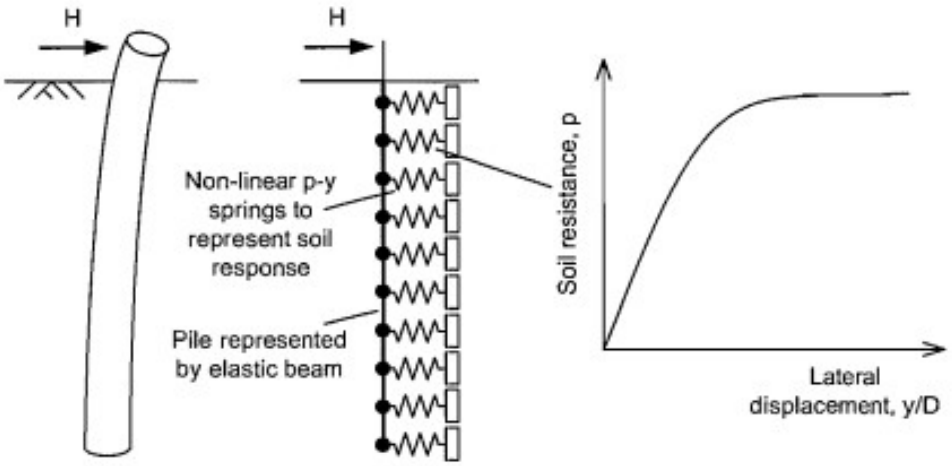

Figure 2.9 - Winkler approximation of foundation response using non-linear p-y curves (From Randolph, 2011)

Matlock (1970) presented p-y curves for soft clay based on both pile load testing and laboratory scale model tests. The tests were performed in normally consolidated clays representative of the conditions typically encountered in the Gulf of Mexico. The field piles used were 610mm in diameter and instrumented with strain gauges to allow assessment of the deflections with depth and subsequent estimation of the bending moment, shear and soil resistance profiles. The results from the field pile tests were compared to the laboratory testing to formulate a backbone response curve that could be combined with Masing's rule to allow cyclic assessments. The general form of the Matlock soft clay p-y curve is shown in Figure 2.10.

The value of the ultimate lateral resistance per unit length, p_{ult}, is calculated as

$$p_{ult} = N_p s_u D$$

$$N_p = \begin{cases} 3 + \dfrac{\sigma_v{}'}{s_u} + J\dfrac{z}{D} \text{ for } z \leq z_r \\ 9 \text{ for } z > z_r \end{cases} \tag{2.5}$$

Where $\sigma_v{}'$ is the vertical effective stress at the depth assessed, J is an empirical constant dependent on undrained shear strength, z is the depth being assessed, and z_r is the depth where maximum resistance is reached. The value of J is typically taken as 0.5 for soft clays, considered to be those with undrained shear strength less than 96kPa, and 0.25 for stiff clays. However, there is some debate over appropriate values, as Matlock (1970) notes the analysis method used by Reese (1975) for the Lake Sabine pile tests would result in $J = 2.83$. The variation of N_p with depth occurs until a limiting value of $N_p = 9$ is reached. This value of $N_p = 9$ roughly corresponds to the limiting resistance of a smooth circular pile translating through soil undergoing full plastic flow-around (Randolph and Houlsby, 1984; Martin and Randolph, 2006). The load-displacement response of the Matlock p-y curves is calculated using a power law

$$\frac{p}{p_{ult}} = 0.5\left(\frac{y}{y_c}\right)^{\frac{1}{3}} \tag{2.6}$$

where y is the local deflection and y_c is reference deflection at $p/p_{ult} = 0.5$.

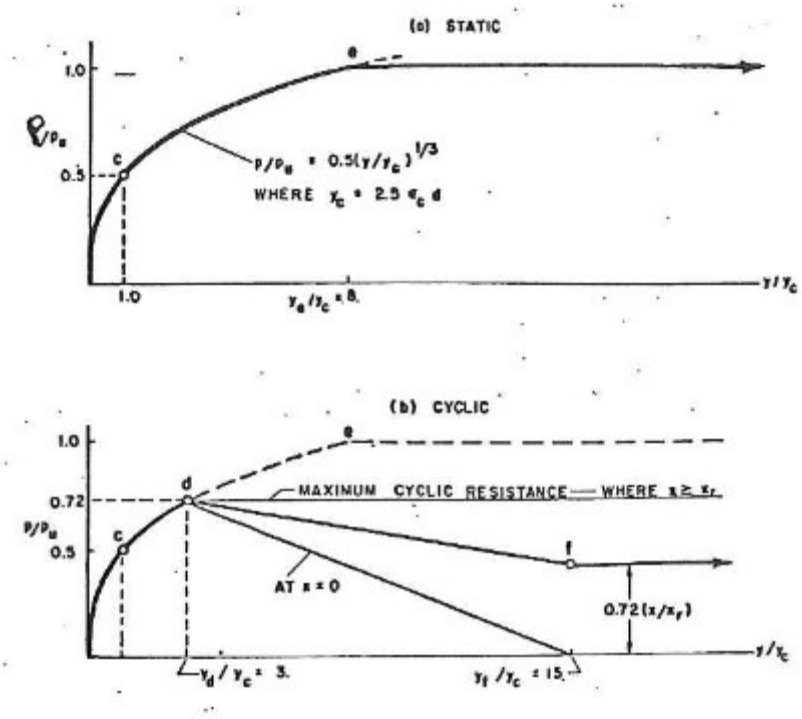

Figure 2.10 - General form of Matlock (1970) p-y curve with key parameters

Assuming a soil profile of constant strength with depth, equating the two equations for N_p in Equation 2.5 gives a transition depth, z_r, as

$$z_r = \frac{6D}{\frac{\gamma D}{s_u} + J} \tag{2.7}$$

For real soil profiles, it is very rare to find a constant shear strength with depth profile over sufficient length to determine z_r. As such, different approaches are needed to estimate z_r. Matlock (1970) suggests calculation of separate values of z_r at each depth, whereas API RP 2GEO (API, 2011) recommends that the depth where the first N_p expression first exceeds the limiting value of 9 is taken as z_r.

The deflection to peak resistance for the Matlock family of p-y curves is based on the work of Skempton (1951). In this work, the deflection required to mobilise peak resistance for strip footings was characterised by a combination of elasticity theory, ultimate strength methods and laboratory soil properties. This gave a value of deflection at 50% maximum load, y_c, of

$$y_c = 2.5\varepsilon_{50}D \tag{2.8}$$

where ε_{50} is the strain at half maximum deviator stress in unconsolidated undrained triaxial tests. Peak static resistance is reached at $8y_c$ as shown in Figure 2.10.

Reese (1975) presented a methodology for constructing p-y curves for stiff clay based on pile load testing performed at Sabine Lake in Texas. The clay at the site was noted as having a significant secondary structure of fissures which is likely to have occurred from repeated desiccation of the soil as the clay was repeatedly saturated and dried. As such, the p-y curves presented are suggested for use for unstructured clays in API RP WSD. The pile load testing performed demonstrated that under cyclic loading the resistance of the clay would rapidly deteriorate and this is accounted for in the curves by a rapid reduction from peak resistance as deflection increases. The general form of the Reese stiff clay p-y curve is shown in Figure 2.11. The limiting resistance with depth is taken as the lesser of Equations 2.9 and 2.10,

$$p_{c1} = 2s_u D + \gamma' Dz + 2.83 s_u z \tag{2.9}$$

$$p_{c2} = 11 s_u b \tag{2.10}$$

where γ' is the effective unit weight of the soil. Normalising by the undrained shear strength and diameter to obtain N_p, akin to the Matlock formulation, gives the variation given in Equation 2.11. Here the $\gamma' z$ term has been replaced by the vertical effective stress, σ_v', to facilitate comparison to the Matlock formulations.

$$N_p = \begin{cases} 2 + \dfrac{\sigma_v'}{s_u} + \dfrac{2.83z}{D} \text{ for } z \leq z_r \\ 11 \text{ for } z > z_r \end{cases} \tag{2.11}$$

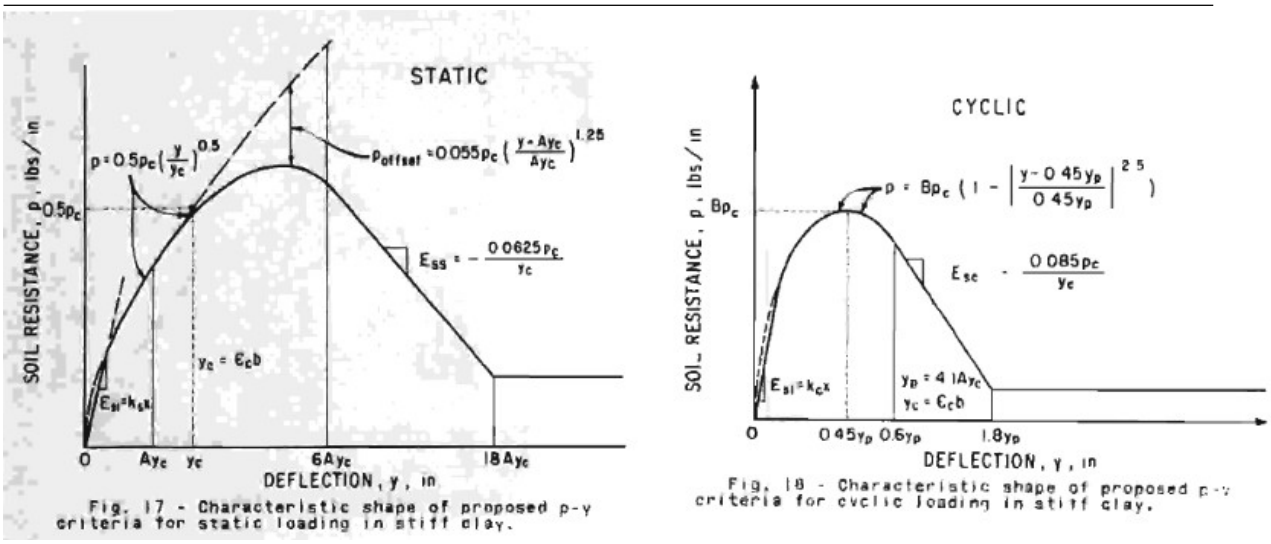

Fig. 17 - Characteristic shape of proposed p-y criteria for static loading in stiff clay.

Fig. 18 - Characteristic shape of proposed p-y criteria for cyclic loading in stiff clay.

Figure 2.11 - General form of Reese (1975) p-y curve for stiff clays

For a constant shear strength with depth this gives a transition depth, z_r, of

$$z_r = \frac{9D}{\frac{\gamma' D}{s_u} + 2.83} \tag{2.12}$$

Since the original publication of the Matlock (1970) and Reese (1975) p-y curves and their subsequent adoption in the API standards there have been multiple modifications proposed. Based on a review of available case histories, Stevens and Audibert (1979) argued that the existing p-y methodologies underpredicted the pile head deflection. The authors propose modifications to the bearing factor, N_p, and critical deflection, y_c, to obtain more representative pile head deflections. A more rapid increase of N_p with depth, and relating y_c to the square root of the pile diameter, are suggested as two means of obtaining more accurate results. Sullivan et al. (1980) present a unified method for clays based on the results of both Matlock (1970) and Reese (1975). However, the authors note that in this case two empirical parameters are used with little guidance available, introducing uncertainty into the applicability of the unified method in design. For structured stiff clays, the use of a modified form of the Matlock (1970) soft clay p-y curves was suggested by Bhattacharya et al. (2006). This form of the Matlock (1970) p-y curve was intended to account for the rapid degradation that can occur in stiff clays at higher deflections.

Murff and Hamilton (1993) were the first to approach this problem using upper bound plasticity theory. They present an empirical equation relating the change in lateral bearing factor with depth to the pile diameter and the soil shear strength profile. The general form of this is shown below.

$$N_p = f\left(\frac{z}{D}, \frac{s_{u0}}{\rho D}\right) \tag{2.13}$$

where z is the depth, D is the pile diameter, s_{u0} is the undrained shear strength at the surface and ρ is the rate of increase of shear strength with depth.

The lateral bearing factor is then calculated as follows:

$$N_p = N_1 - N_2 e^{\left(-\frac{\xi z}{D}\right)} \tag{2.14}$$

where N_1 is the maximum bearing factor, N_2 is the difference between the maximum bearing factor and the bearing factor at soil surface and ξ is defined as

$$\xi = 0.25 + 0.05\lambda \text{ for } \lambda = \frac{s_{u0}}{\rho} \leq 6 \tag{2.15}$$

Jeanjean (2009) proposed the use of N_p =12 for the limiting pressure based on both FEA, (Templeton, 2009) and centrifuge modelling. However, this recommendation was aimed at design of offshore oil and gas conductors where design is driven by fatigue. For fatigue design a higher resistance and hence higher stiffness of the pile head response is conservative; whereas previous lateral resistance methods such as Broms (1964) and Matlock (1970) work on the assumption that a lower resistance is conservative for estimating the ULS and SLS states.

A drawback of the approach proposed by Murff and Hamilton(1993), and a possible factor in why it was never adopted into industry standards, is that only an upper bound analysis was performed with no corresponding lower bound analysis. Such a solution can only be considered exact, and potentially reliable, if an equivalent lower bound analysis is performed and provides an equal solution to the upper bound analysis. Without a corresponding lower bound solution,

the potential accuracy of the approach is uncertain. Another drawback of the approach is the restrictive assumption for the shape of the failure surfaces. In 3D problems it is difficult to form a rational set of mechanisms that give a reliable approximation of the actual failure mechanism. Klar and Randolph (2008), Yu et al. (2015) and Zhang et al. (2016), later adopted by Jeanjean (2017) in a proposed improvement to the p-y framework, took steps to improve upon the Murff and Hamilton (1993) failure mechanisms, however again they did not present a corresponding lower bound solution.

The method proposed for incorporating soil weight into the response is also questionable. The value of N_p calculated by Equation 2.14 has no term incorporating soil weight, with the authors instead opting to add the vertical stress, either total or effective depending on ground water conditions, to the predicted resistance and then take the minimum of either this resistance with unit weight or the resistance from the flow-around mechanism, i.e. Randolph and Houlsby (1984). For the gapping case and a soil with a high unit weight to strength ratio this implies that the limiting case of the flow around mechanism would be reached very near the surface. In reality, the soil at the back of the pile would likely collapse under these conditions thus closing the gap and lowering the lateral bearing factor by virtue of the lateral force the soil exerts on the back of the pile.

In the work preferred by Jeanjean (2017) an empirical equation is fitted to the results obtained by upper bound analysis of the mechanisms shown in Figure 2.2. The empirical equation is shown in Equations 2.16 to 2.20.

$$N_p = \begin{cases} N_{p0} + \dfrac{\gamma z}{s_{u0} + s_{u1} z} \leq N_{pd} & \text{(Gapping)} \\ 2N_{p0} \leq N_{pd} & \text{(No Gapping)} \end{cases} \tag{2.16}$$

$$N_{p0} = N_1 - (1 - \alpha) - (N_1 - N_2)\left[1 - \left(\frac{z}{dD}\right)^{0.6}\right]^{1.35} \leq N_{pd} \tag{2.17}$$

$$d = 16.8 - 2.3 \log_{10}(\lambda) \geq 14.5 \tag{2.18}$$

$$\lambda = \frac{s_{u0}}{s_{u1}D} \tag{2.19}$$

$$N_{pd} = 9 + 3\alpha \tag{2.20}$$

In these equations N_1 = 12, N_2 = 3.22, s_{u0} and s_{u1} are as defined in Equation 2.13, and α is the pile-soil adhesion ratio.

Recent pile testing (Byrne et al, 2017) and numerical modelling as part of the PISA project has shown that for short rigid piles the use of Matlock style p-y curves results in underprediction of the pile resistance and overprediction of lateral deflection when loaded. In the PISA work, pile tests were performed on piles up to 2m in diameter with L/D ratios that approximated those typically used for monopiles in offshore WTG installations. The tests were performed at Cowden and Dunkirk: sites which provide representative clay and sand profiles for a significant part of the North Sea. The pile tests were compared with results from numerical modelling performed using state of the art constitutive models (Zdravkovic et al., 2015) with a good match found for all pile tests. The PISA research proposed inclusion of several resistance components that had previously not been actively considered in pile design in the offshore industry. These consist of the base shear, and shaft and base moment resistances outlined in Figure 2.12. These additional resistance components are potentially significant for foundations with low *L/D* ratios, such as the large diameter monopiles used in offshore wind farms. For more information on the PISA project see Zdravkovic et al. (2019), Burd et al. (2019), Byrne et al. (2019), McAdam et al. (2019), Zdravkovic et al. (2019), and Taborda et al. (2019).

A 1D FEA model has been proposed as part of the PISA project, shown schematically in Figure 2.12(b). This 1D model provides a means of rapidly calculating the load-displacement response of a pile while incorporating the additional resistance mechanisms proposed in PISA. Use of this approach is discussed in detail for clays in Byrne et al. (2020) and sands in Burd et al. (2020).

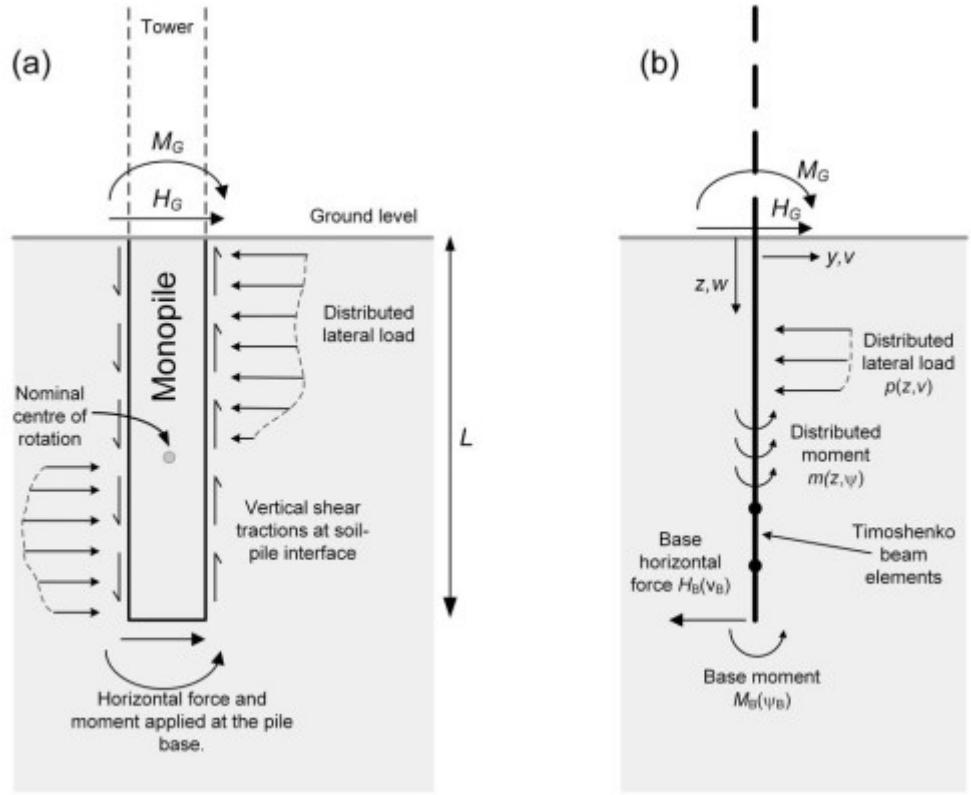

Figure 2.12 - (a) Summary of soil resistance components considered as part of PISA and (b) outline discretisation used for 1D modelling approach (from Byrne et al, 2017)

2.4. Finite element analysis

With the increase in computing power over the last few decades it is becoming more common to perform complex numerical analysis of engineering problems. Numerical methods used for geotechnical problems typically consist of either the finite element method, for example PLAXIS and Abaqus software, or finite difference method, for example FLAC software. The main advantage of these methods is that they allow a more comprehensive assessment of the soil response compared with simpler methods, such as the subgrade reaction approach. However, numerical methods can be computationally expensive and require careful consideration of inputs to be reliable.

There have been several studies using numerical methods to examine the response of piles to static, cyclic and dynamic loading conditions. Ahmadi and Ahmari (2009) present comparisons of finite element models to the Matlock (1970) and Wu et al. (1998) families of p-y curves. The authors used a strain hardening von Mises model to represent the soil with the pile represented

by a solid cylinder. Soil profiles for comparison are back calculated based on the results of the Matlock (1970) and Reese (1975) field tests. The authors comment that there is a satisfactory correspondence between the FEA predictions and the assessed p-y curves for the soft clay assessment, however this is mostly due to the same case study being used for the back analysed soil parameters and the original p-y curve formulations. Page et al. (2019) demonstrate that macro element models can be used to represent monopile behaviour under multidirectional loading based on finite element modelling.

Jeanjean (2009) and Templeton (2009) present results from numerical and centrifuge modelling of laterally loaded conductors under static and cyclic loading. Soil behaviour in this study was modelled using an elastic-plastic work hardening model with a von Mises yield condition. The numerical and centrifuge modelling gave closely matching results that showed a higher ultimate lateral resistance and stiffness than p-y curves formulated following the API standards. Jeanjean (2009) goes on to recommend a general set of equations for forming p-y curves based on modifications to the methodology proposed by Murff and Hamlilton (1993) for calculating the ultimate lateral resistance of a pile in undrained clay.

Hamre et al. (2011) compare results from finite difference modelling in FLAC3D to lateral deflections from API p-y curves for cohesive materials. Three p-y curve cases are assessed with modifications to account for cyclic loading, Achmus et al. (2005) and Achmus et al. (2007), and the impact of a large pile diameter, Stevens and Audibert (1979). The authors conclude that the API formulations give the largest deformations of any of the assessments even with values of ε_{50}, the strain at half the maximum deviator stress, taken from consolidated anisotropic undrained compression (CAUc) triaxial tests.

Zdravkovic et al. (2019b) present the finite element models used as part of the PISA project alongside the field testing and one-dimensional modelling methodology presented by Byrne et al. (2015). The work presented advances on the rotational mechanisms introduced by Lam and

Martin (1986) and presents a rational approach to incorporate these into simpler one-dimensional models that incorporate the additional shaft rotational resistances and base resistances for monopiles.

2.5. Finite element limit analysis

Finite element limit analysis (FELA) is a method that has gained increasing traction in recent years (Sloan, 2013). In traditional limit analysis, lower and upper bound solutions for the plastic collapse load are found by determining both a statically admissible stress field and a kinematically admissible velocity field. When combined, these lower and upper bound solutions provide a rigorous bracket for the exact solution; with the exact solution being known if the lower and upper bound are equal. The requirement of having to specify the failure surface limits traditional mechanism based upper bound analysis to simple problems. This typically limits the approach to plane strain problems in 2D or simple 3D mechanisms. The work by Murff and Hamilton (1993) and Yu et al. (2015) presented earlier in this chapter discussed application of limit analysis to a 3D problem however this work only involved an upper bound solution based on an assumed velocity field. Using only the upper bound without an associated lower bound means that the potential error of the solution is not known.

FELA offers an alternative approach to obtaining lower and upper bound plasticity solutions. By applying the bound theorems of plasticity across a finite element mesh, lower and upper bound solutions can be found without specifying the form of the stress and velocity fields in advance (as is performed for more traditional limit analysis). The immediate advantage of this is that more complex systems involving non-homogeneous soil conditions and complex geometry can be readily analysed as no prior assumption needs to be made regarding the shape of the failure surface. Early attempts at FELA were performed by linearising the failure criterion, for example the Drucker-Prager and Mohr-Coulomb yield functions, and using simplex optimisation methods to resolve the lower and upper bound solutions (Bottero et al., 1980). The drawback of this is that the approach is computationally expensive and as such the number of

elements that could be included in the mesh was limited (Sloan, 1988). More recently, non-linear (Lyamin and Sloan, 2002(a); 2002(b)) and second order cone programming (SOCP) techniques have been demonstrated as effective numerical optimisation methods for performing FELA on large meshes in a reasonable time frame. In SOCP the yield criterion is expressed in a conic quadratic form; an approach that has been demonstrated for both lower bound (Makrodimopoulos and Martin, 2006) and upper bound (Makrodimopoulos and Martin, 2007) problems. FELA using SOCP has been used to analyse the capacity of shallow footings (Martin et al., 2015; Dunne et al., 2015; Dunne and Martin, 2017), pipelines (Martin and White, 2012) and slopes (Makrodimipoulos and Martin, 2008). Research on 3D FELA has typically focused on the use of the von Mises and Drucker-Prager yield criteria however it has been demonstrated that semi-definite programming can allow 3D problems to be analysed using the Tresca and Mohr-Coulomb criterion (Martin and Makrodimopoulos, 2008; Krabbenhoft et al., 2008).

A key part of modern FELA techniques is use of adaptive meshing to reduce the bracketing error of a given boundary value problem as efficiently as possible (Martin, 2011; Dunne, 2017). A benefit of adaptive meshing is the potential to visualise slip-line fields for a given problem, allowing comparison to collapse mechanisms that have been posited for use in limit analysis. See Martin (2011) for an example of this for shallow foundations and tunnel collapse problems.

For detailed review of the application of FELA to geotechnical problems see Makrodimopoulos and Martin (2006, 2007), Sloan (2013) and Dunne (2017).

Chapter 3

Methodology

This chapter outlines the methods and software used in this thesis to assess the problem of laterally loaded pile resistance in undrained clay. The first section outlines the general modelling considerations and provides an outline of what is being assessed. The next section describes the FELA software OxLim alongside a description of how it is used here. Analysis of benchmark problems are presented alongside descriptions of features of the modelling process and outputs that are relevant throughout this thesis. The final section describes the application of the FEA software PLAXIS 3D along with a calibration exercise to demonstrate the similarities and differences between the FEA and FELA approaches.

3.1. Outline of problem

The work in this thesis investigates the laterally loaded pile system shown in Figure 3.1(a). This system can be broken down into five key areas:

1. Geometry
2. Soil parameters
3. Interface conditions
4. Structural properties
5. Loading

Geometry of tubular piles consists of three parameters: length, L, diameter, D, and wall thickness, t. An additional geometric parameter of the upstand height, h, is also typically used however this is more relevant to the applied loading conditions and as such will be discussed later. These parameters are typically expressed in terms of the dimensionless groups of length

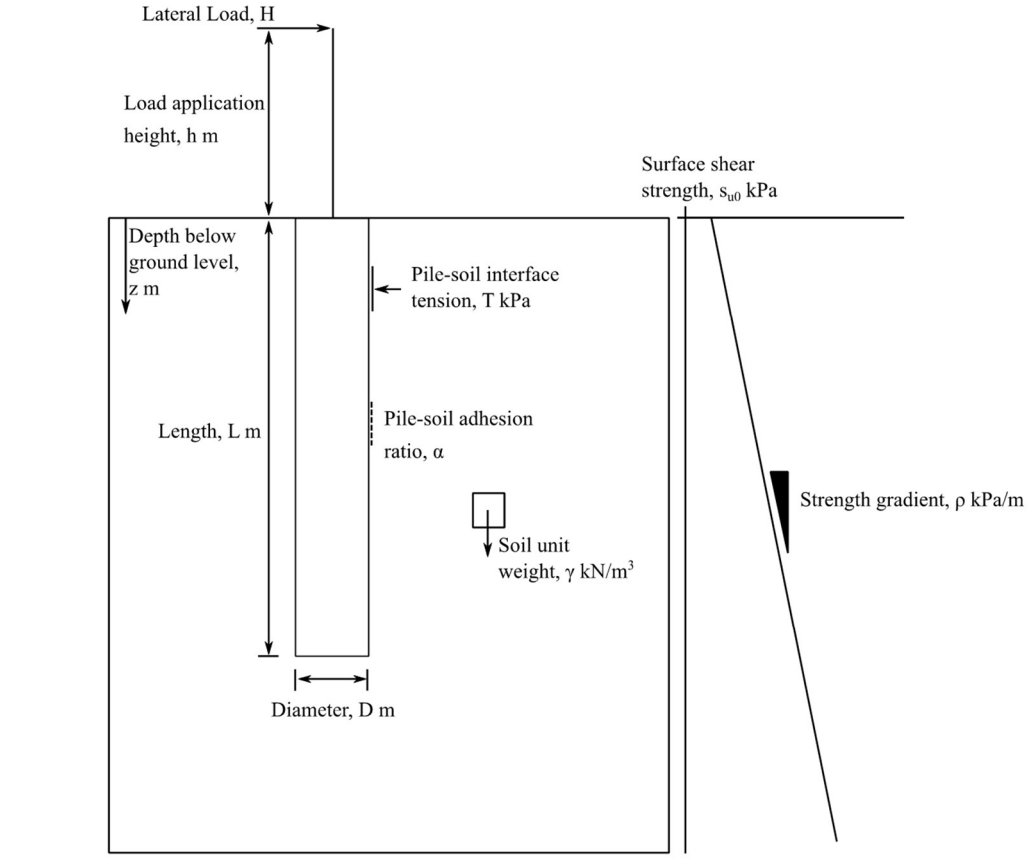

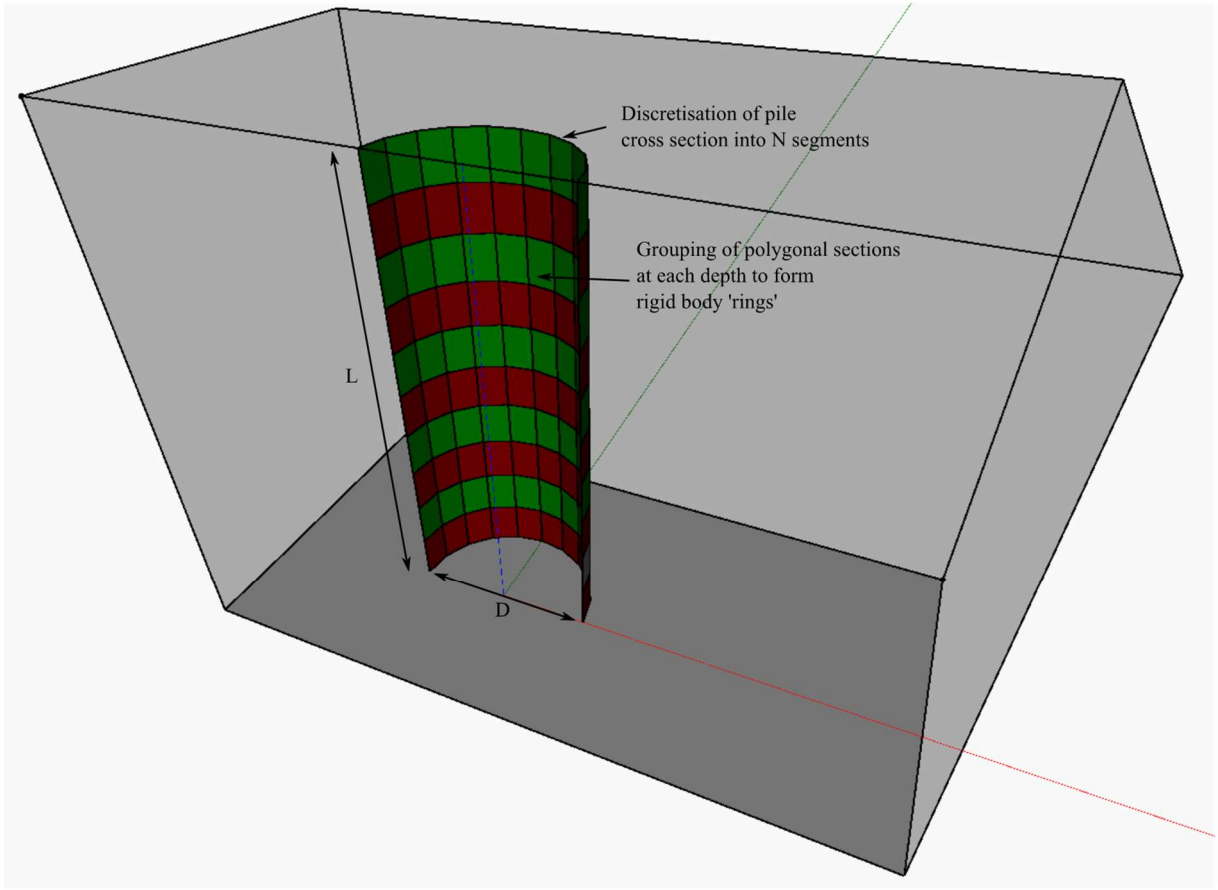

Figure 3.1 - (a) Schematic of pile soil system with key parameters, (b) 3D representation of pile discretisation used in OxLim

to diameter ratio, *L/D*, and wall thickness to diameter ratio, *t/D*. The group *L/D* is used to define the slenderness of a pile and, when coupled with other parameters, can be used as an indicator of when a pile will switch between short rigid and long flexible behaviours, i.e. the failure mechanisms shown in Figure 2.1(a) and (b) respectively. This group is used throughout this thesis with a range of *L/D* = [1, 10] used in each investigation. This range is considered to represent potential lower and upper limits for this group when considering short rigid pile behaviour. The group is relevant to a pile's flexural rigidity, *EI*. However, the majority of analyses in this thesis assume a rigid pile; a necessary assumption when using FELA. As such, variation of *t/D* will not have any impact on the results obtained using FELA.

The soil parameters relevant to this thesis are shown in Figure 3.1(a). These are the undrained shear strength at ground surface, s_{u0}, the strength gradient, ρ, and soil unit weight, γ. In Offshore (or fully submerged) conditions the effective unit weight, γ', should be used in place of the total unit weight, γ. Analysis presented in Chapter 5 introduces more complex strength profiles, however the parameters shown here are representative of all other cases presented within this thesis. For very simple profiles that consider either a constant shear strength or a linearly increasing strength profile starting from zero shear strength at the surface, the following dimensionless groups are frequently used:

$$\text{Homogeneous: } \frac{\gamma D}{s_u} \tag{3.1}$$

$$\text{Strength gradient: } \frac{\gamma}{\rho} \tag{3.2}$$

In both cases these groups represent the normalised ratio of the weight of the soil to the strength of the soil. When the soil has both a strength at the surface and a strength gradient, the dimensionless group

$$\frac{\rho D}{s_{u0}} \tag{3.3}$$

is used to characterise the relative non-homogeneity of the strength profile and the expression

$$\frac{\gamma D}{s_{u0} + \rho D} \tag{3.4}$$

can be used to quantify the weight to strength ratio. Note that Equation 3.4 will reduce to either Equation 3.1 or Equation 3.2 for $\rho = 0$ or $s_{u0} = 0$ respectively. Ranges of $\gamma D/s_u$ = [0.2, 5] and γ/ρ = [0.2, 5] are commonly used when exploring these dimensionless groups and this range is adopted for the majority of investigations performed in this thesis. However, in a few cases there will be a benefit to exploring a wider range than this to aid explanation of observed phenomena.

In parts of this thesis a special case of $\gamma D/s_u = \gamma/\rho = 0$ has been used. This case represents an idealised scenario of weightless soil and it is expected that this will provide a lower limit for the lateral resistance in cases where interface gapping is permitted to occur. Note that in FELA no soil stiffness is modelled, hence the exclusion of any stiffness related terms in this section. Soil stiffness however is required for the FEA and will be discussed in the relevant section of this chapter.

Interface properties are characterised by two parameters: the pile-soil adhesion ratio, α, and interface tension capacity, T. The pile-soil adhesion ratio is defined as the fraction of the shear strength of the neighbouring soil that can be mobilised on the interface, i.e.

$$\alpha = \frac{\tau_{max}}{s_u} \tag{3.5}$$

in the full range of α = [0, 1] have been investigated. These limits correspond to the assumptions of fully smooth and fully rough interfaces respectively (see Randolph and Houlsby, 1984). Interface tension capacity is harder to quantify than other parameters owing to a degree of uncertainty over the amount of tension that could be reasonably expected to develop under loading. It is generally accepted that the extreme cases of zero allowable interface tension (T = 0) and no allowable separation between soil and structure ($T = \infty$) are suitable for

modelling purposes (Murff and Hamilton, 1993). As such these two cases have been used throughout this thesis when investigating potential limits of resistance.

The FELA assumes a rigid structure and as such the structural properties of the pile have no bearing on the results of these analyses. However, for the FEA the structural properties of the pile are required. Unless otherwise stated, elastic properties of steel have been assumed with Young's modulus, E, of 205GPa and Poisson's ratio, v, of 0.3.

Loading conditions on a laterally loaded pile are typically expressed as a combination of horizontal, H, and moment, M, loads applied at the level of the ground level. For convenience in modelling these loads, a method commonly adopted is a horizontal load applied at an upstand, h, resulting in a moment at pile head level of $M = Hh$.

In this thesis, a wide parameter space is explored for multiple different parameters that will influence the pile response. In the interest of brevity, a code is used to identify the key components of the modelling that is being performed. This code consists of four parts:

- The type of strength profile being investigated: Homogeneous (H) or Linear increase with depth (L)
- Whether the pile head is fixed (X) or free (F)
- Whether interface tension is used in the modelling (T) or interface separation is allowed (N)
- Whether the soil is weightless (Wn) or soil unit weight is included in the modelling (Wi)

For example, a free head pile model performed in homogeneous soil with no interface tension in weightless soil will have the code HFNWn in text and figures. A full list of model codes that have been used is included in the nomenclature at the start of this thesis.

3.2. Finite element limit analysis

The FELA software OxLim has been developed at the University of Oxford since 2009. The software has previously been applied to analysis of slopes (Makrodimopoulos and Martin, 2008), pipelines (Martin and White, 2012), shallow footings (Martin et al., 2015) and suction caissons (Dunne, 2017). Two versions of the software exist: a 2D version for plane strain or axisymmetric problems and a 3D version. The work in this thesis focuses entirely on the use of the 3D version however reference is made to the 2D version in this chapter as part of a verification exercise.

3.2.1. Description of modelling process

Limit analysis using both versions of OxLim follows these general steps:

1. A control file is created specifying boundary conditions, model parameters and solver settings
2. An unstructured initial mesh of triangular (2D) or tetrahedral (3D) elements is created
3. The OxLim formulates the specified boundary value problem as a constrained optimisation problem
4. The Mosek (2010) library of solvers is used to maximise (lower bound) or minimise (upper bound) the objective function subject to the constraints set out by OxLim
5. Dissipation rates across the upper bound velocity field are used to define a refined mesh
6. Repeat steps 3 to 5 with further mesh refinement until a set criterion is met for the bracketing of the exact solution between the lower or upper bounds

Operation of the above steps depends on the version of OxLim used; the 2D version automatically handles steps 2 to 6 whereas the 3D version will only perform steps 3 and 4 with

user intervention required for the remaining steps. In this thesis, the open source programming language Python (van Rossum, 2011) has been used to encapsulate the above steps into a single process for the 3D version. A flow diagram of this process is outlined in Figure 3.2. More detail on each of these steps is provided below.

Geometry in OxLim 3D is defined in terms of nodes, facets and regions. Nodes are the simplest geometry primitive and are used to define sets of X, Y, Z coordinates. A facet is a polygon or collection of polygons that are used to represent 2D geometry assets within the model; e.g. the boundaries of the model and the exterior surfaces of the rigid body elements are represented by facets. Each polygon is represented by a list of nodes. A region is a 3D object that is bounded by a collection of facets. The facet and region geometry primitives are specified with an integer tag which is then used by OxLim to apply the appropriate parameters. Geometry is defined as a piecewise linear complex, stored in a 'poly' file, which is then used to create the tetrahedral mesh in step 2. The control file for OxLim defines the input parameters for the analysis by specifying region tags, facet tags and rigid bodies. Region tags specify soil parameters and facet tags are used to define boundary conditions and properties for rigid bodies in the model. Properties applied to facet tags for rigid bodies represent the interface conditions for that rigid body; e.g. a cohesion specified in a facet tag will represent a pile-soil interface adhesion. Rigid bodies in OxLim are used to specify the structural elements within the model.

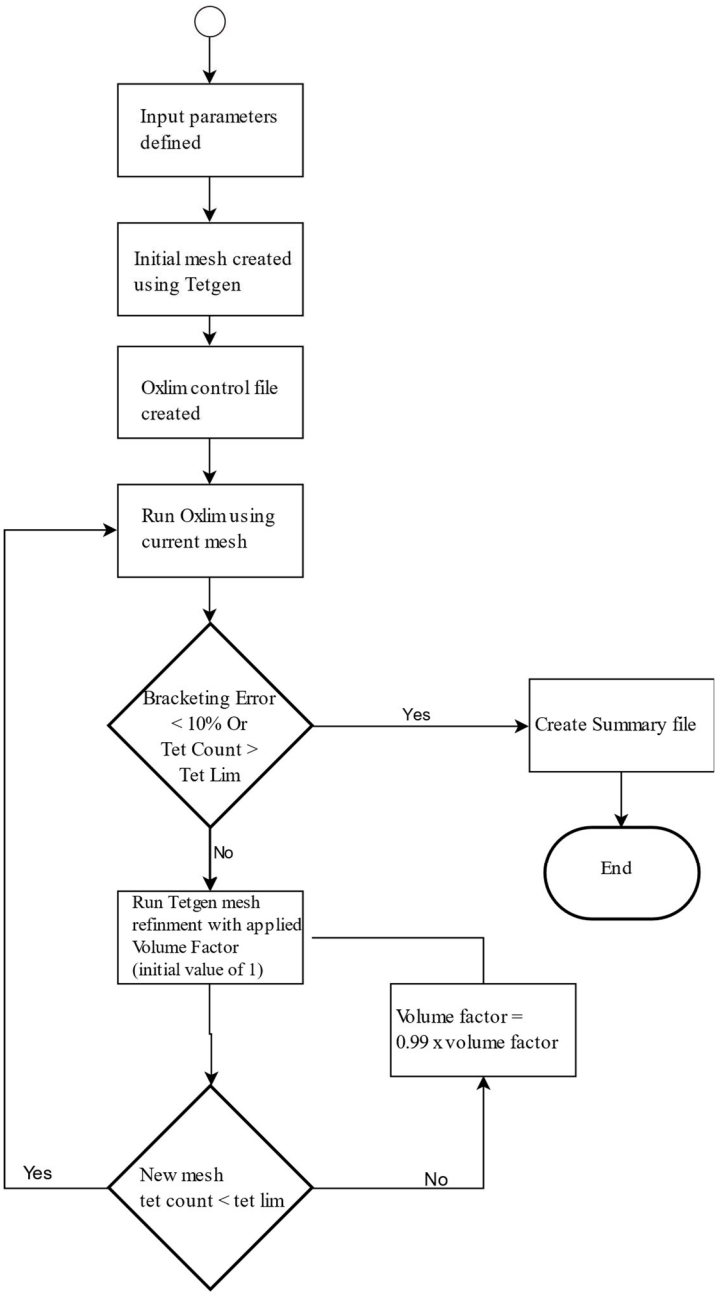

Figure 3.2 - Summary flow diagram of OxLim modelling process with mesh refinement strsategy

The initial and adaptive tetrahedral meshes in this thesis have been created using TetGen (Si, 2015). TetGen allows generation of tetrahedral meshes for any 3D polyhedral domain; for FELA the software is useful for creating high-quality boundary-conforming Delaunay tetrahedral meshes. High-quality meshes are important when performing finite element analysis to reduce potential ill-conditioning of the calculation from badly shaped elements.

Note that a high-quality mesh does not guarantee an accurate solution. Solution accuracy is improved by having a refined mesh in appropriate areas of the model; in the case of FELA this

can be achieved by adaptively refining the mesh in areas of high dissipation. A process of adaptive remeshing is possible using TetGen by specifying a volume file to use when creating a new mesh. This volume file provides a maximum volume constraint for each tetrahedron in the background mesh. The process of mesh refinement is based on Dunne (2017) and outlined briefly below.

3.2.2. Plane strain verification

This section presents a comparison between OxLim and the lower and upper bound plasticity solutions for the flow-around mechanisms presented by Randolph and Houlsby (1984) and Martin and Randolph (2006) respectively. Both OxLim 2D and OxLim 3D have been used to obtain the lateral resistance of a section of a pile translating through a rigid-plastic soil medium. In OxLim 2D the problem has been analysed in plane strain whereas in the 3D analysis plane strain conditions have been imposed by using symmetry boundary conditions at the top and bottom of the model. In both cases, a half model has been used with an axis of symmetry along the centreline in the direction of loading; the edge of the model along this centreline uses a symmetry boundary. In both models, the rigid elements representing the pile are fixed against all displacement except in the X direction, with a unit load applied in this direction. A constant undrained shear strength, s_u, is used in both models. The pile-soil adhesion ratio is varied between fully smooth, $\alpha = 0$, and fully rough, $\alpha = 1$. The final parameter is the pile-soil interface tension which is set such that no separation can occur at the interface between the pile and the soil.

An important factor in the calculation of the lateral resistance of a translating section of pile is the number of straight segments, henceforth referred to as pile facets, used to discretise the circular cross section of the pile. Dunne (2017) showed that the number of pile facets used could have a significant impact on the predicted resistance for the flow-around mechanism, with a relatively high number of facets required to obtain a close match with the corresponding

theoretical solutions. This becomes especially important in 3D models as a balance needs to be found between having a sufficiently high number of pile facets to achieve adequate resolution close to the pile while also maintaining a reasonably low number of tetrahedra in the model to prevent excessive runtimes.

Comparisons between the OxLim-obtained bearing factors and the values in the literature are shown in Figure 3.3. Figure 3.3(a) shows the result of setting the facet count in OxLim 2D to $N = 200$, i.e. 100 facets in the half model. This results in a very close match over the full range of pile-soil adhesion ratio; at $\alpha = 0$ the difference is 0.5% while at $\alpha = 1$ the difference reduces to less than 0.1%. This gives confidence that FELA can give a very good to match to analytical limit analysis solutions. Figure 3.3(b) shows the OxLim results when $N = 40$, i.e. 20 facets in the half model, which is representative of the number of facets that might be used in a full 3D model of a pile. From these results we can see that there is a much more significant deviation in the predicted bearing factor at $\alpha = 0$. The 2D analysis results in $N_p = 9.52$ and the 3D analysis results in $N_p = 9.55$; differences of 3.5% and 3.8% from the upper bound solution for a smooth circular pile (Martin and Randolph, 2006). At $\alpha = 1$ the differences from the known exact solution of $N_p = 11.94$ are 0.1% and 0.9% for the 2D and 3D analyses respectively.

Figure 3.4 shows the change in the predicted bearing factors for $\alpha = 0$, 0.5 and 1.0 with the number of pile facets, N. The results show that the effect the number of pile facets has on the resistance is greatest at low values of α. For a smooth pile, $\alpha = 0$, the discretisation of the pile into straight facets almost always leads to an overprediction unless very high values of N are used. The exception being at $N < 10$ where the resistance is less than the theoretical flow-around value and closer to $N_p = 8.28$ which is theoretical resistance for a smooth, square rigid section moving edge-on into the soil (Broms, 1964). Figure 3.5 show the refined mesh and velocity contours for three different facet counts using smooth and rough interfaces.

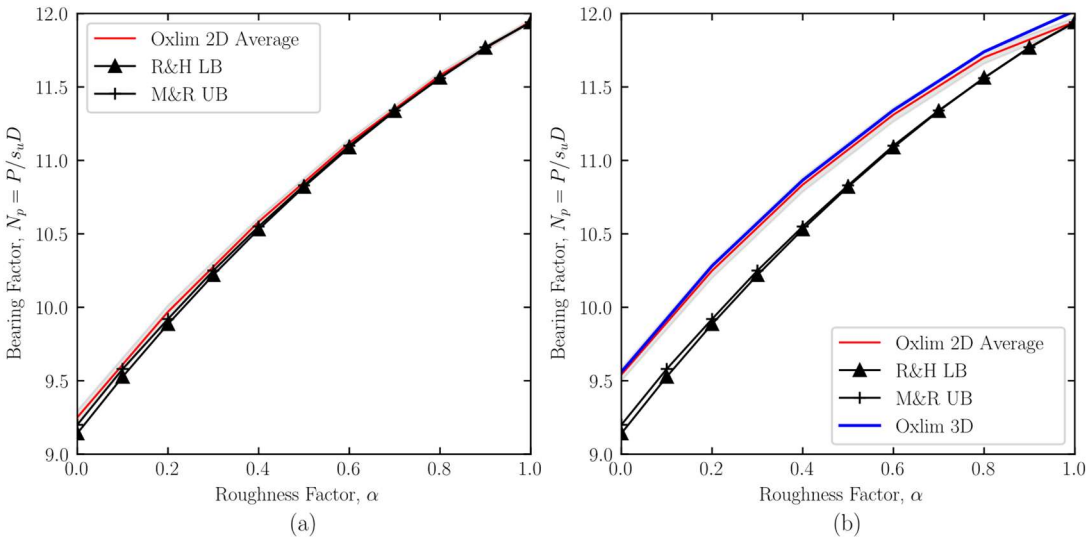

Figure 3.3 - Comparison of lateral bearing factor N_p for (a) OxLim 2D with 200 pile facets, (b) OxLim 2D and OxLim 3D with 40 pile facets. Analytical solutions are shown for Randolph and Houlsby (1984), R & H, and Martin and Randolph (2006), M & R

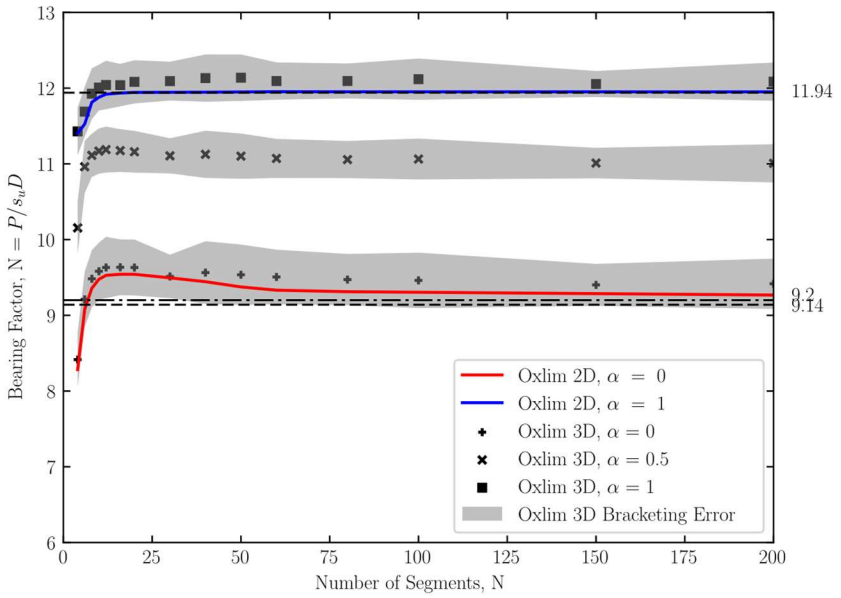

Figure 3.4 - Lateral bearing factor with number of facets used in pile discretisation with theoretical values from Randoph and Houlsby (1984) and Martin and Randolph (2006) shown

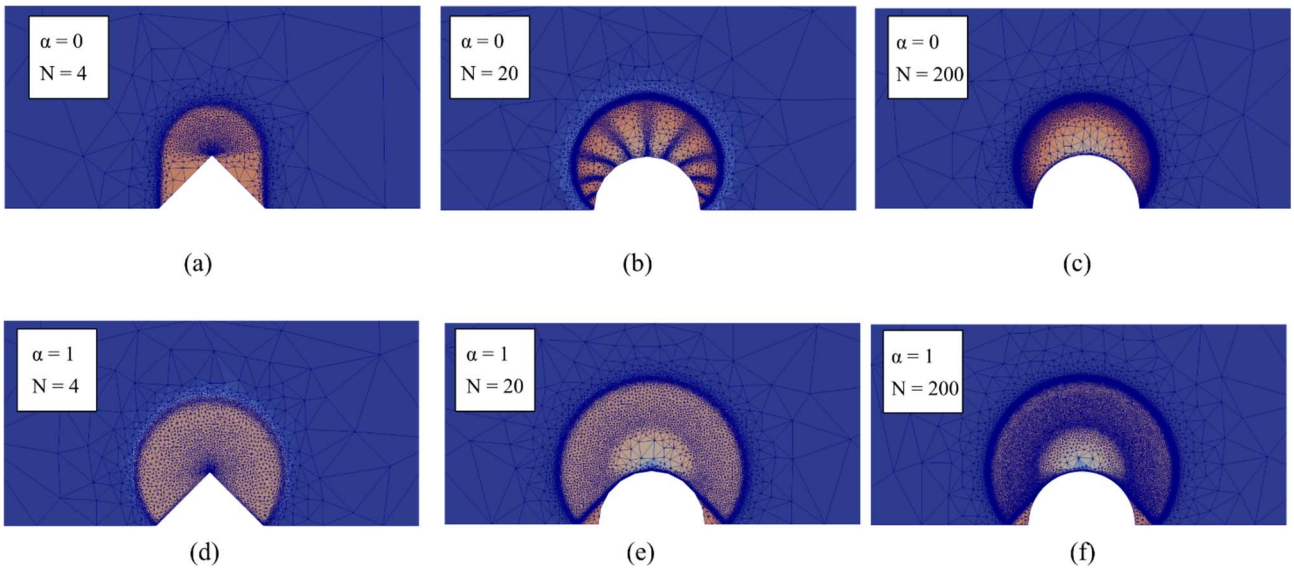

Figure 3.5 - Failure mechanisms for two values of pile-soil adhesion ratio (α = 0, 1) and three numbers of pile facets (N=4, 20, 200)

3.2.3. 3D example

This section provides an outline of the full pile model. Due to variations in the modelling process performed in order to investigate specific features of resistance in each chapter, this section will only focus on the general modelling approach with discussion on how the models are created and how results are extracted.

Two main model geometries are; a quarter model and a half model as shown in Figure 3.7. The quarter model utilises two planes of symmetry that can be exploited for a pile with full interface tension. A symmetry boundary condition is used on the X-Z plane while an anti-symmetry condition is used on the Y-Z plane. For the half model, symmetry only occurs on the X-Z plane. This is to account for possible differing behaviour in front of and behind the pile when interface separation is allowed to occur.

The model geometry consists of a soil volume formed from 6 large rectangular polygons and then a collection of smaller rectangular polygons to represent the pile. The polygons used to represent the pile form the faceted cross section outlined in Section 3.2.2. The geometry of the

pile is also split vertically into a number of discrete 'rings' with each ring being treated as a seperate rigid body in OxLim; this is shown schematically in Figure 3.1(b). This process allows extraction of the pile-soil contact forces that occur over the depth of the pile by obtaining the reaction forces on each rigid body. The pile rings are specified with both internal and external facing interfaces; thus allowing the internal and external soil resistances on the pile to be obtained. All geometry is created relative to the model origin at X = Y = Z = 0 and the pile head is centred on this point.

Model boundaries are set to be fixed (fully rough) for the base of the model and positive X and Y faces. Fixity of the pile is set to allow only displacement in the X-axis, rotation about the Y-axis, or a combination of both of these. Limiting the pile to only displacement along the X-axis results in a rigid pile translation; Figure 2.1(c) in Chapter 2. Limiting the pile to only rotation about the Y-axis forces the pile to rotate about the model origin. Allowing both X displacement and rotation about the Y-axis results in a free head pile, see Figure 2.1(a).

To demonstrate the modelling process, both a quarter and a half model have been run for homogeneous soil conditions; i.e. a constant strength with depth is used, for a pile with L/D = 5. Both models simulate full interface tension, i.e. no gapping is permitted between the soil and the pile, and assume weightless soil (i.e. γ = 0kN/m^3 resulting in $\gamma D/s_u = 0$). It should be noted that for the quarter model, weightless conditions should always be used. Applying a downwards body force, i.e. in the negative Z direction in this modelling, when using an anti-symmetry boundary is equivalent to modelling an upwards body force on the opposite side of the anti-symmetry boundary. This is not an appropriate modelling scenario and as such body forces should only be included within the half model. Free head conditions are adopted and a unit lateral load is applied at the pile head, i.e. with upstand h = 0m. In both models the lateral extents of the model are set to 5D with vertical extent set to 1.5L.

Figure 3.6 shows the variation of lateral soil resistance with depth and change of total lateral resistance and bracketing error with the number of tetrahedral elements. The half and quarter

models give similar values of resistance; the main benefit of using the quarter model is the increased element density and subsequent reduction in bracketing error; as can be seen in Figure 3.6(b). It is interesting to note that the average resistance for both models does not change significantly with element count, suggesting that even quite coarse meshes can give good estimates of the collapse load. Figure 3.7 shows the mesh refinement steps for both models, in each case the number of tetrahedra is shown below the mesh. For the purpose of this assessment the usual criterion of halting the mesh refinement process if the bracketing error falls below 10% has not been used, to demonstrate the reductions in error that can be achieved when using a larger number of tetrahedral elements. The meshes for the quarter model are shown in Figure 3.7(a) to (d). The initial mesh, Figure 3.7(a), has 3,762 tetrahedra that are predominantly located at the pile-soil interface due to the use of 40 pile facets in the full circle; using fewer facets in the cross section results in a lower initial element count at the cost of increasing the lateral resistance as outlined in Section 3.2.2. This results in a bracketing error of 16.6%. Successive refinements shown in (b) and (c) increase the element count to 11,763 and 30,888; the next refinement stage resulted in a mesh of 72,500 which is above the limit of 60,000 used for this assessment. As such, the iterative loop (shown in Figure 3.2) to reduce the element count is called resulting in a final mesh element count of 57,169. These meshes result in reductions of the bracketing error to 8.8%, 5.9% and 4.7%. For the half model, an initial mesh of 7,253 elements is created resulting in a bracketing error of 17.9%. Refining from this initial mesh leads to a mesh of 24,880 elements and a bracketing error of 8.7%, and further refinement results in a mesh of 59,692 tetrahedral elements and a bracketing error of 5.9%.

The lateral resistance profile, shown in Figure 3.6(a), is obtained from the OxLim results that provide the reaction forces acting on the exterior facing rigid bodies. As a unit lateral force is applied to the models, the resistance obtained needs to be multiplied so that it is equivalent to

$$N_p = \frac{p_u}{s_u D} \tag{3.1}$$

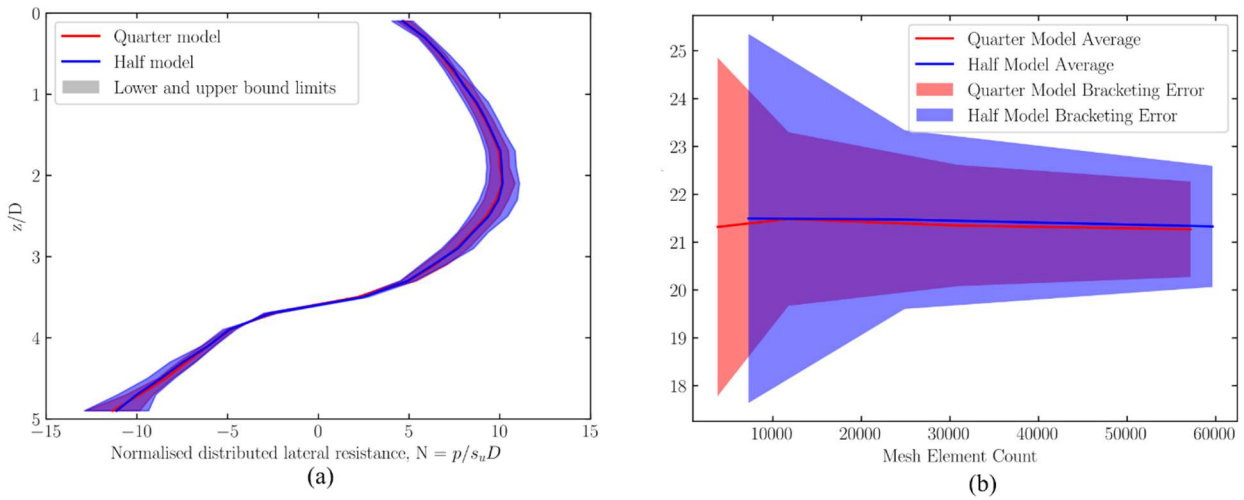

Figure 3.6 - Resistance of laterally loaded pile with L/D = 5 and full interface tension using quarter and half model geometry in OxLim (a) distribution of lateral bearing resistance with depth, and (b) total resistance and bracketing error with mesh element count.

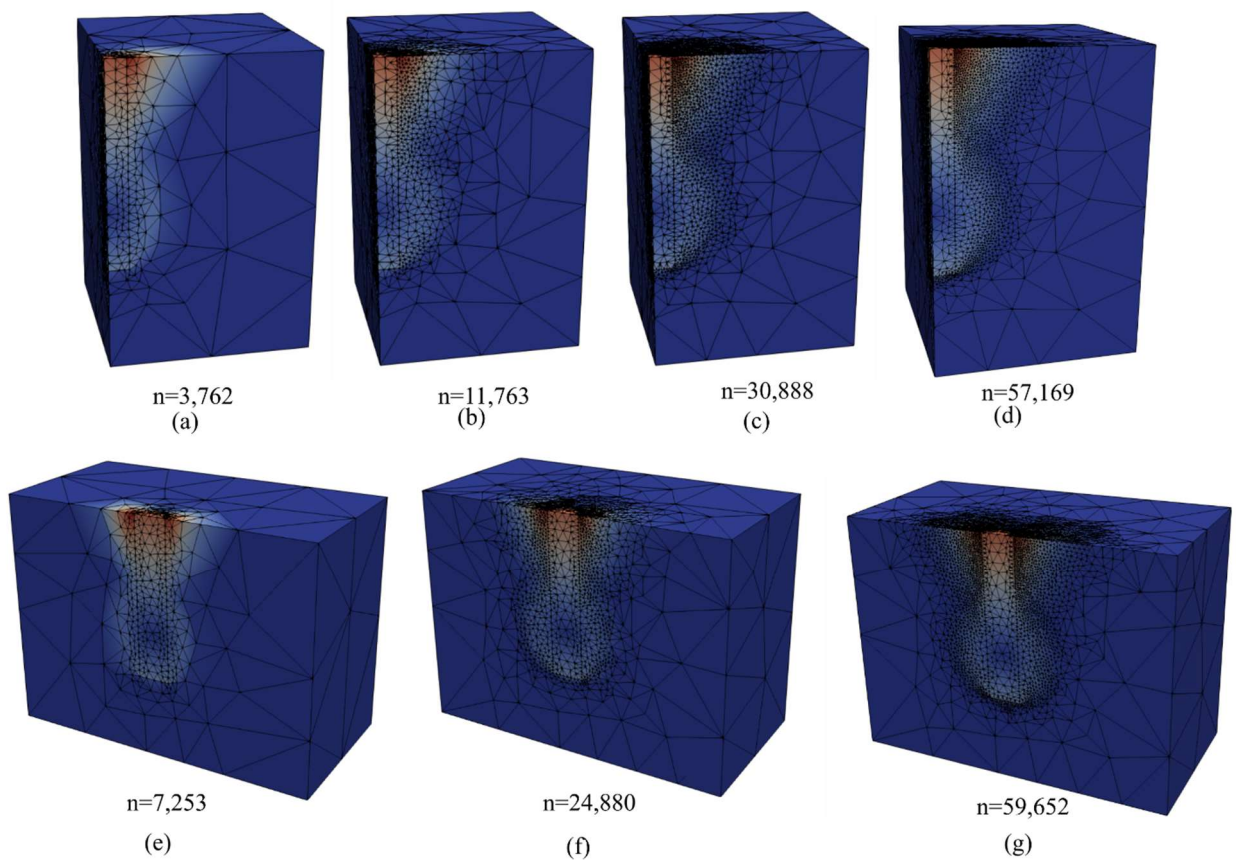

Figure 3.7 - Mesh refinement stages for (a) to (c) quarter pile and (d) to (e) half pile OxLim models

a full model; i.e. the results from the half model need to be multiplied by 2 while the results from the quarter model need to be multiplied by 4. The lateral reaction on each rigid body then needs to be divided by the height of the ring (see Figure 3.1(b)) to obtain the distributed force per unit length of the pile, $p_{u,}$ which is expressed in terms of kN/m. This can then be converted to the lateral bearing factor by dividing by the undrained shear strength times by the diameter, i.e.

$$N_p = \frac{p_{ult}}{s_u D} \tag{3.1}$$

3.3. Finite element analysis

Later parts of this thesis compare the results of the FELA simulations performed using OxLim to displacement based (FEA) using PLAXIS 3D. This section provides a brief overview of the modelling process used in PLAXIS and compares some FEA obtained results to the outputs of the example FELA calculations performed in Section 3.2 as a calibration exercise. One key difference between the FEA and FELA modelling is the constitutive model used to represent the soil behaviour. In FELA a rigid-plastic model is used, whereby no account of elastic soil deformations and hence pre-failure displacements is made. In the FEA modelling, a linear elastic-perfectly plastic model is used; i.e. pre failure soil deformations can occur. Two commonly used constitutive models to perform elastic-perfectly plastic modelling in terms of effective stress are the Drucker-Prager and Mohr-Coulomb models (Potts and Zdravkovic, 1999). For total stress modelling with materials where the strength is not dependent on the mean total stress (such as undrained clays) these models reduce to the von Mises and Tresca yield conditions respectively. The PLAXIS 3D software contains the Mohr-Coulomb model by default and can be extended to include the Drucker-Prager model by use of a user defined soil model. However the Drucker-Prager user defined soil model available from PLAXIS only allows consideration of homogeneous soil conditions and as such will not be used herein.

The modelling performed in PLAXIS 3D uses the same outline geometry for the half pile model used in OxLim shown in Figure 2.1(b). A symmetry boundary is specified on the X-Z plane with full fixity at the base of the model and a free surface on the X-Y plane; i.e. the same boundary conditions as used in the OxLim modelling. The exterior faces of the soil geometry at the positive X, negative X and positive Y faces all use a symmetry boundary condition; i.e. different to the OxLim modelling where a fully fixed boundary condition is used. This difference in boundary conditions is needed to account for the fact that pre-failure deformation of the soil can occur in the FEA models due to an elastic-perfectly plastic constitutive model being used.

An important part of FEA modelling is understanding the degree of mesh refinement required to give a reliable result. As with upper bound analysis in FELA, using a coarse mesh in FEA will typically result in a higher resistance than the true resistance. As such it is important to perform a mesh sensitivity study when performing FEA to understand the potential effect that the mesh will have on the result. Such a study has been performed using PLAXIS with the results shown in Figure 3.8. The model has been set up with the same input parameters as the half model in OxLim in Section 3.2 of this chapter; i.e. full interface tension, homogeneous soil conditions and no upstand (h = 0m). Meshes have been produced with 950, 3028, 15930 and 40462 elements, and the model has been set up to have larger elements towards the extents of the model with a higher degree of refinement closer to the pile. The mesh with 40462 elements is shown in Figure 3.9. The results in Figure 3.8 show a reduction in resistance with increasing element count that is similar to the reduction shown in Figure 3.6(b) for the upper bound results obtained from OxLim. Using 40462 mesh elements in PLAXIS 3D results in 6.7% difference from the average OxLim results obtained with 60000 mesh elements. For the purpose of comparing FEA and FELA this is considered satisfactory as it is within the desired bracketing error for the FELA.

Further information on the FEA modelling is presented in the chapters of this thesis where FEA is used.

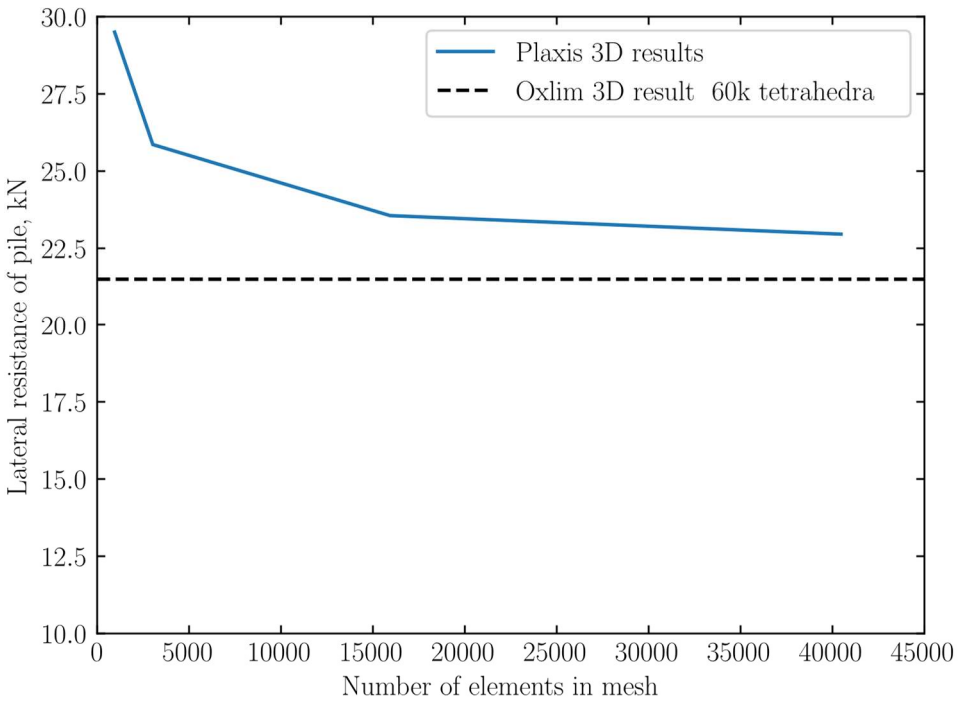

Figure 3.8 - Lateral load at pile head with increasing element count from PLAXIS 3D modelling of laterally loaded pile with L/D = 5 and full interface tension

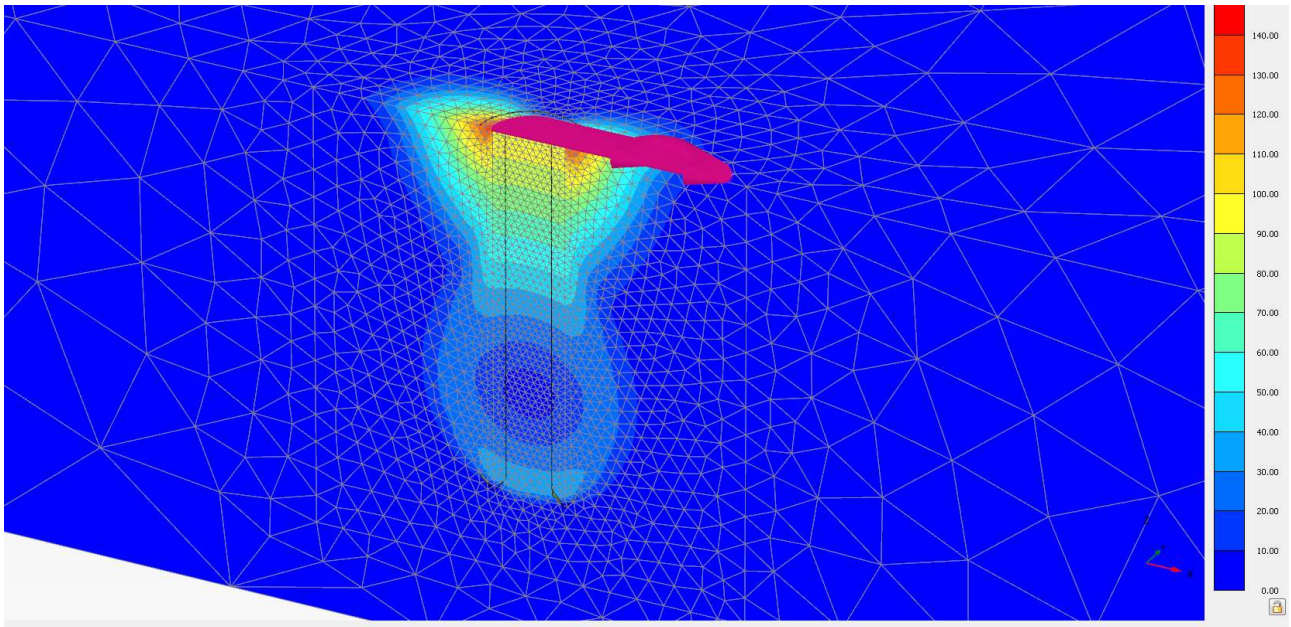

Figure 3.9 - Mesh in PLAXIS with 40462 elements showing total displacement contours and arrows indicating the prescribed displacement at pile head

Chapter 4

Homogeneous strength profiles

This chapter considers the ultimate response of a laterally loaded pile in homogeneous clays. A comprehensive and rigorous numerical assessment of the lateral capacity of piles in homogeneous clays has been performed. The investigation has been performed using the Oxlim Finite Element Limit Analysis software developed at the University of Oxford. The focus of the investigation has been on the response of short rigid piles to loading, i.e. the mechanisms in Figure 2.1(a) and (c), however some of the results are applicable to the other mechanisms. The investigation is split into six parts with variations on pile head fixity, capability for tension to develop at the pile-soil interface and the unit weight of the soil. Non-dimensional groups relevant to homogeneous conditions are outlined in Table 4.1.

The first stage of the investigation starts with the simplest case of a translating pile where full interface tension can develop. Each subsequent stage then adds an additional layer of complexity. The different stages of the investigation are:

1. HXTWn - Translating pile with full interface tension
2. HFTWN - Free head pile with full interface tension
3. HXNWn - Translating pile in weightless soil with no interface tension
4. HFNWn - Free head pile in weightless soil with no interface tension
5. HXNWi - Translating pile in soil with varying unit weight with no interface tension
6. HFNWn - Free head pile in soil with varying unit weight with no interface tension

The first two stages focus on allowing full tension to develop: potentially representative of suctions developing on the back of a pile under rapid loading. This allows soil unit weight to

be omitted from this stage of the investigation as it will have no impact on the response. The two scenarios of a fixed and free head pile are examined and the results of capacity for the two cases are compared. The mechanisms that contribute to the response are investigated and assessment is made of total pile lateral and moment resistance, change of resistance with depth, and impact of the key non-dimensional groups on the pile response.

In the third and fourth stage of the investigation, interface tension is not allowed to develop in the model: resulting in a gap forming between the pile and soil. Analysis is performed on fixed and free head piles in weightless soil and results are compared to those of the full tension model.

The final stages of the investigation review the impact of varying $\gamma D/s_u$ on the response of the pile and the mechanisms that form said response. It is established that the results from the first four stages of the investigation form upper and lower limits to the total pile capacity and the variation of capacity with depth. Comparison of results across all stages and discussion on the implications on pile design are made.

The final part of this chapter compares the results from the investigation to approaches in the literature. Comparison is made to the widely used Matlock (1970) p-y approach, the upper bound plasticity approach of Murff and Hamilton (1993), and the proposed modification to the p-y framework by Jeanjean (2017) which utilises the improved upper bound plasticity approached of Yu et al. (2015).

Table 4.1 - Summary of dimensionless groups for homogeneous soil modelling

Group	Description
$\gamma D/s_u$	Ratio of soil weight to strength
L/D	Length to diameter ratio
α	Pile-soil adhesion ratio
h/D	Normalised load application height
F_x/s_uD	Normalised lateral load at pile head
M_y/s_uD	Normalised moment at pile head

4.1. Analysis

4.1.1. Translating pile with full interface tension

In the first stage of the study the pile is fixed against rotation and translated laterally; i.e. HXTWn conditions. Interface separation is disabled simulating development of full tension on the back of the pile. These assumptions permit a quarter model to be used: achieved by specifying the Y-Z plane as a plane of anti-symmetry. The assumption of full interface tension also negates the impact of soil unit weight on the results; as such the soil has been assumed weightless in this first stage. The upper and lower bound resistance for each of the rigid bodies specified in the model are output, allowing calculation of the average resistance and local bracketing error. In all figures a plotted line represents the average of the lower and upper bound solutions unless otherwise stated. The total resistance of a translating pile of varying Length to Diameter, L/D, ratio is shown in Figure 4.1(a). The line on the figure represents the average of the lower and upper bound solutions with the limits of the lower and upper bound shown with the shaded region. The resistance varies from 8.65 at an L/D of 1 up to 113.1 at L/D = 10. The error varies from 4.1% to 8.1% for L/D = 1 and 10 respectively: owing to an increasing coarseness of the finite element mesh relative to the pile geometry as L/D increases. A simplified estimate of capacity is presented on the figure as a sense check of the results. This simplified capacity assumes the flow around mechanism occurring at all depths, in this case taking the value of $N_p = 10.8339$ for $\alpha = 0.5$ from Martin and Randolph (2006), and multiplying it by the L/D of the pile. This results in an estimated capacity slightly lower than the average of the Oxlim analysis. This can be predominantly attributed to the increased resistance that occurs from the segmentation of the pile cross section with a small component coming from the shearing at the base of the pile.

Figure 4.1(b) shows the resistance with depth of a translating pile with the lower and upper bounds shown; expressed in terms of the lateral bearing factor N_p. Three distinct components

of the overall response are evident. At shallow depths the response varies from a value of $N_p \approx 5$ at ground surface and $N_p \approx 12$ at a normalized depth of $z/D = 2$. Below this normalized depth a constant value of N_p is obtained: corresponding to the resistance of the plane-strain mechanism (Randolph and Houlsby, 1984, Martin and Randolph, 2006). As the toe of the pile is reached the resistance increase to approximately 17% more than the equivalent resistance at that depth for a pile with a larger L/D ratio. This increase of resistance near the toe fits the predicted mechanism from Broms (1964). A comparison of the N_p profiles obtained when using different values of pile-soil adhesion, α, is shown in Figure 4.1(c). In Figure 4.1(c), $N_{p,flow}$ is the resistance of the flow around mechanism for the relevant pile-soil adhesion.

Appropriate values of $N_{p,flow}$ for this investigation are taken from the results of the plane strain analysis presented in Chapter 3. The profiles for each case are near identical with variation only occurring near the soil surface. The results of $\alpha = 0$ plot slightly lower to the other two cases, however it is likely that this is due to the higher error that occurred in this model arising from the zero-interface tension assumption.

The lateral base resistance has been calculated by summing the forces acting on the interior rigid bodies in the model. Figure 4.1(d) shows the lower bound, upper bound and average base resistance. The results show a normalised resistance of $\frac{F_{base}}{s_u D^2} \approx 0.785 = \frac{\pi}{4}$: as would be expected for planar sliding of a circular section. The results come in below $\pi/4$ due to the segmenting of the circular pile cross section into a regular polygon. For the quarter model there are 10 segments per quarter resulting in a 40-sided polygon: a tetracontagon. This shape has an area given by Equation 4.1, where t is the edge length, resulting in an area of 0.7822 which matches the upper bound solution obtained from Oxlim. The upper bound solution shows no variation across models due to the explicit inclusion of a facet along the base of the pile. This provides the preferred failure path for this case. Analysis of this system without the base facet results in an upper bound solution that is greater than shown here owing to the more convoluted

route the failure surface would take through the resulting mesh. However, it is expected that the average of the lower and upper bound solution would give the same result as the upper bound in this case.

$$A = 10t^2 \cot\frac{\pi}{40} \tag{4.1}$$

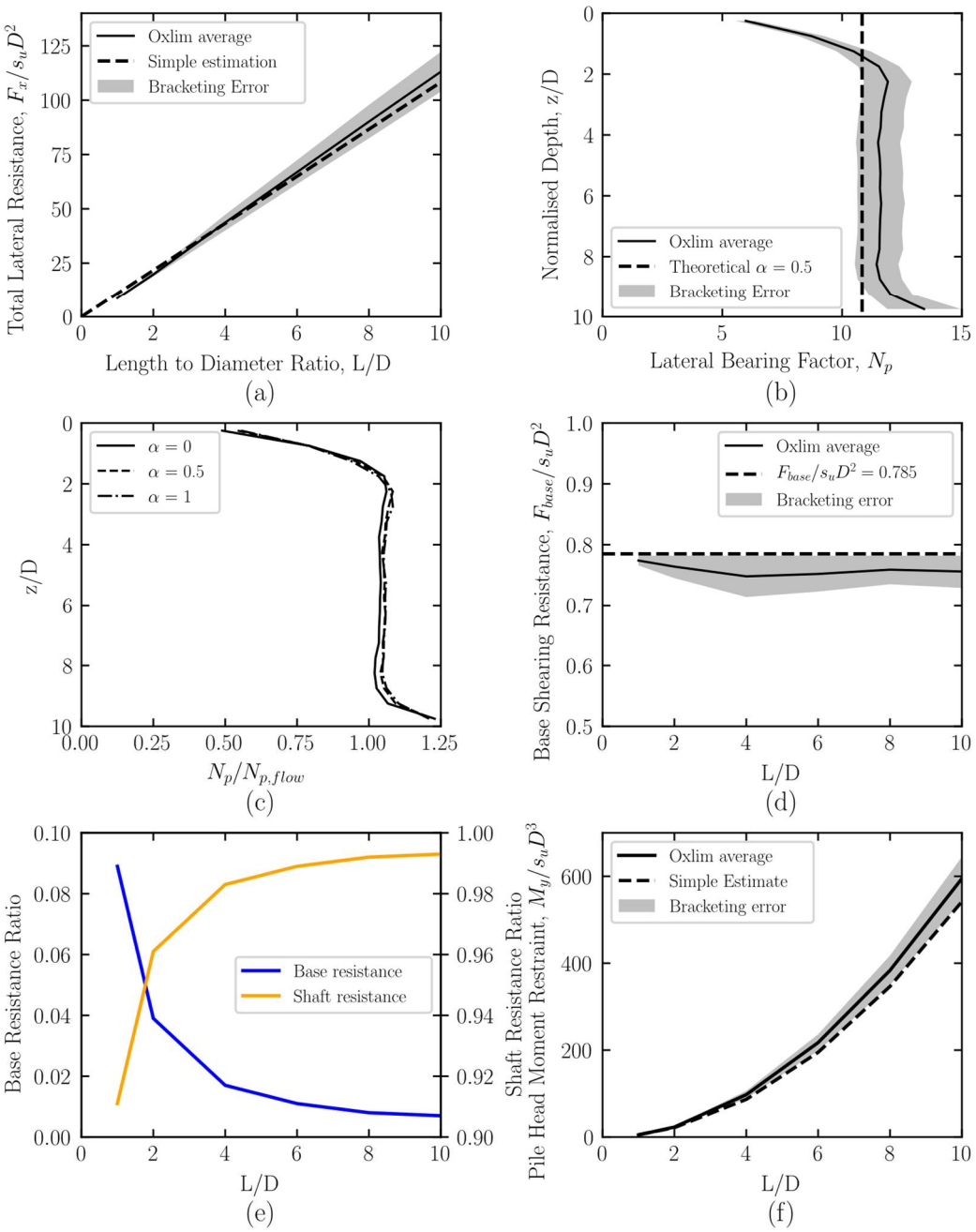

Figure 4.1 - Results from analysis of case HXTWn using α = 0.5, (a) total resistance with L/D, (b) distribution of lateral resistance, (c) effect of pile-soil adhesion, α, on distribution of resistance, (d) base shearing resistance with L/D, (e) contribution of base and shaft resistance to total resistance with L/D, and (f) pile head restraining moment with L/D

Figure 4.1(e) shows the proportion of the total resistance that both the base shearing and the lateral force acting on shaft form. At low *L/D* ratios the base resistance provides approximately 9% of the total resistance. This rapidly decreases as the *L/D* ratio increases: at *L/D* = 4 the proportion of resistance arising from the base is approximately 2% while at *L/D* = 8 the proportion has dropped to below 1%.

As stated, fixity against rotation is used to cause lateral translation under loading in these models. In practice, this condition would arise when sufficient restraint is present at the pile head to prevent rotation occurring, e.g. due to presence of a pile cap, and the pile is stiff enough to not deform significantly as it displaces through the soil. Figure 4.1(f) shows the moment restraint required to cause translation of a rigid pile, i.e. the value of M_p in Figure 2.1(d) required to switch the mechanism to Figure 2.1(c). As with total capacity, a simplified calculation of the resistance is presented on the figure. The simplified resistance is obtained using Eqn. 4.2. As with the total resistance case, the simplified resistance is slightly lower than the Oxlim predicted due to the higher resistance from segmenting the pile cross section.

$$\frac{M_{simplified}}{s_u D^3} = 0.5\left(\frac{L}{D}\right)^2 N_p \tag{4.2}$$

As with the lateral resistance calculation, N_p = 10.8339 is used in calculating the simplified moment response. The adaptive mesh refinement process used as part of the OxLim modelling process permits visualisation of the failure mechanisms. Figure 4.2 shows the deformed meshes from *L/D* = 1, 2, 4, 6, and 8 with contours of velocity magnitude and arrows showing velocity direction. The vectors in the figure are scaled by velocity magnitude. A mechanism similar to the wedge mechanism referred to in the literature is clear at the top of the mesh where velocity in the soil is predominantly in a positive z direction. It is evident however that the wedge does not have a conical shape as assumed in Murff & Hamilton (1993). The velocity direction vectors appear similar to the curved wedge suggested by Yu et al. (2015). The flow around mechanism

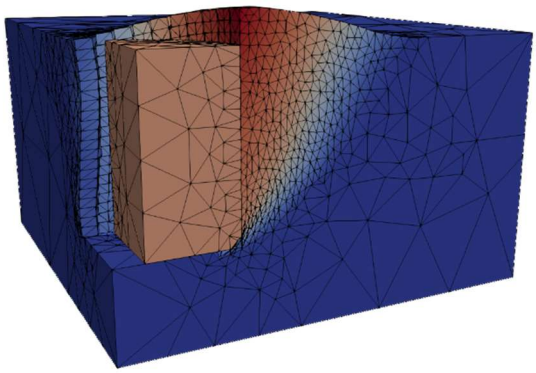

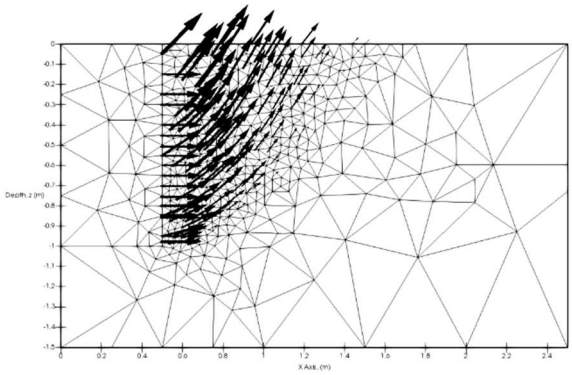
Depth, z (m)
X Axis (m)

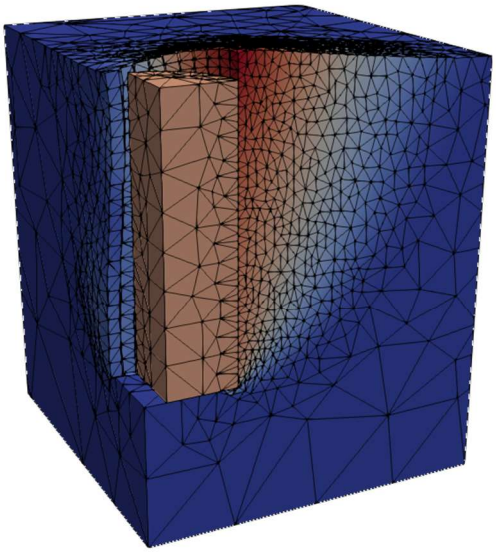

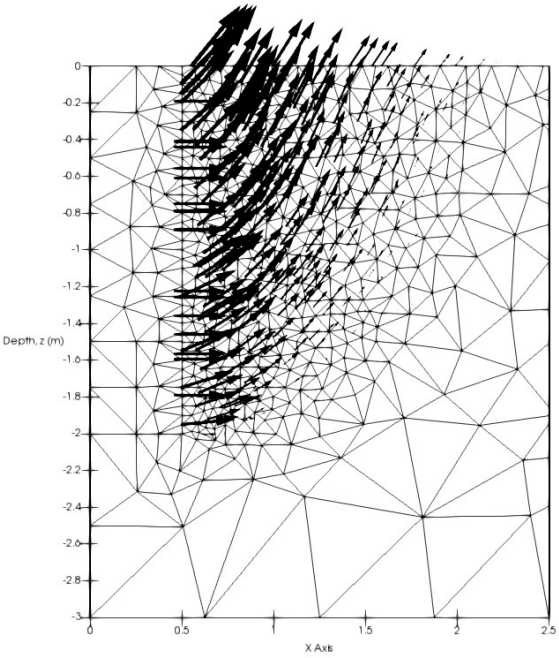
Depth, z (m)
X Axis

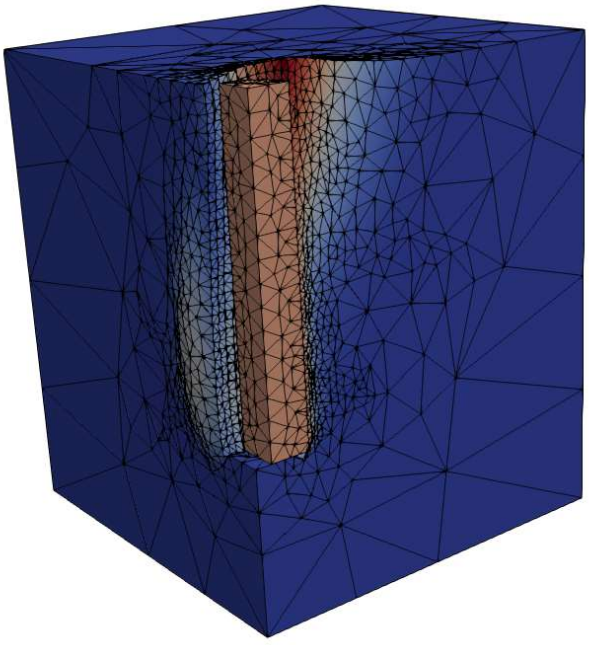

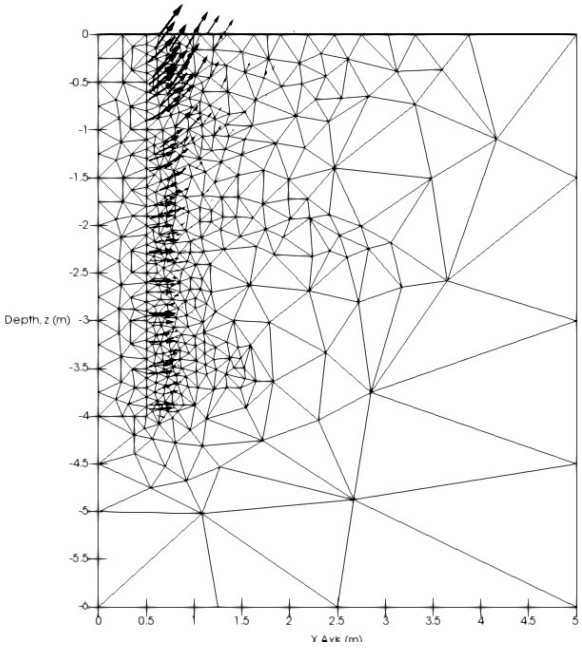
Depth, z (m)
X Axis (m)

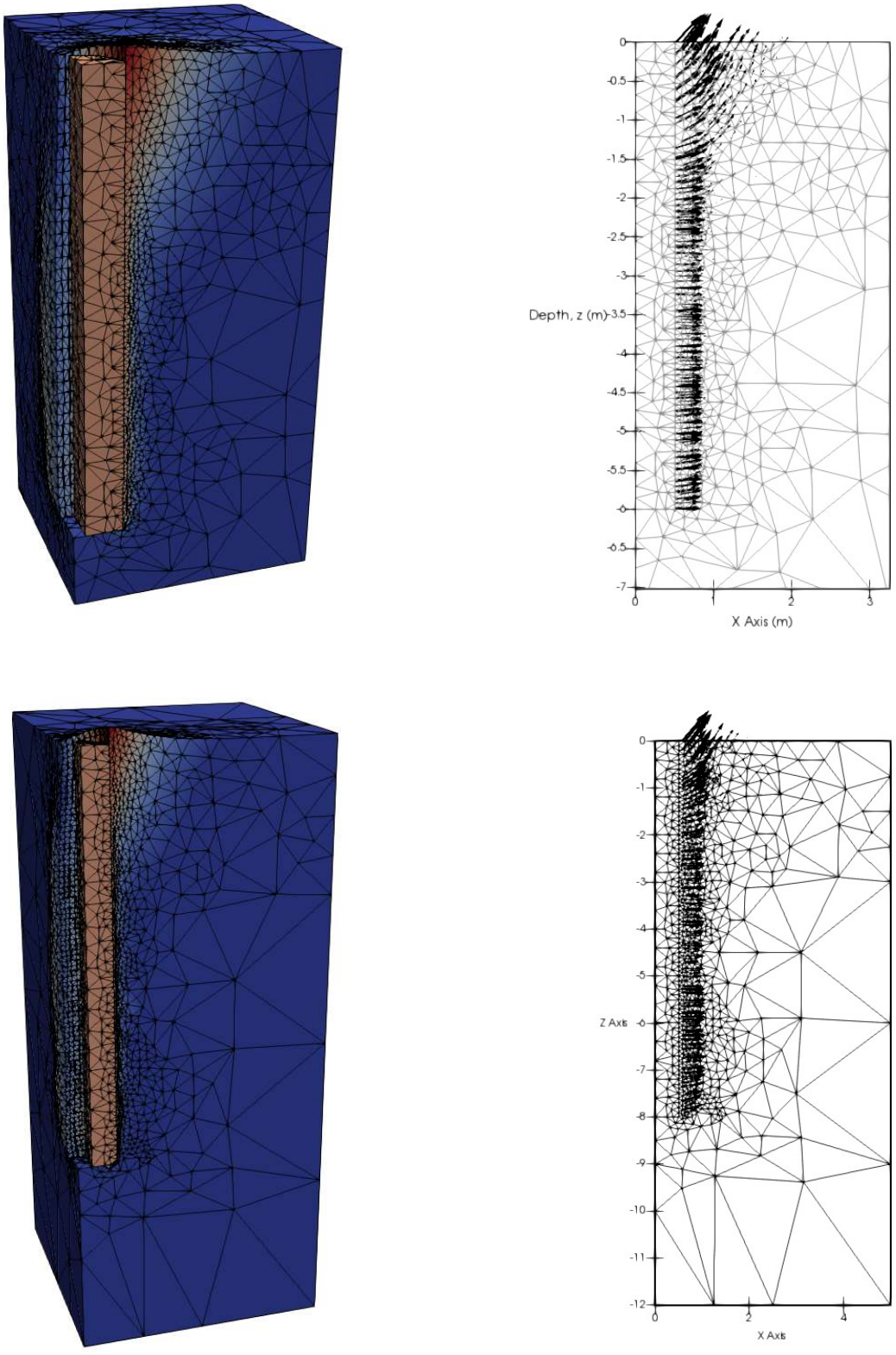

Figure 4.2 - Images of deformed mesh and displacement vectors for HXTWn modelling with α = 0.5 for (a) L/D = 1, (b) L/D = 2, (c) L/D = 4, (d) L/D = 6, and (e) L/D = 8

is also evident: in the deeper parts of the *L/D* = 4, 6, and 8 meshes there is minimal soil velocity in front of the pile and on the Y-Z plane there is a distinct bulge in the deformed mesh indicating a velocity in the opposite direction to the pile movement. This can be best seen in Figure 14(c), *L/D* = 6.

4.1.2. Free head pile with full interface tension

For the second stage of the investigation, the fixity against rotation was removed; i.e. HFTWn conditions. The same modelling conditions as the HXTWn modelling are used with the focus of the results widened to incorporate the impact of the rotation on the response.

Figure 4.3(a) shows the evolution of normalised lateral resistance with increasing *h/D* for *L/D* = 4. At *h/D* = 0, i.e. a lateral load applied at the ground surface, $\frac{F_x}{s_u D^2} \approx 30$. As *h/D* increases the normalised resistance rapidly decreases to $\frac{F_x}{s_u D^2} \approx 10$ at *h/D* = 5 then tends towards zero as *h/D* tends to infinity. Increasing the value of *L/D* results in a similar trend across the range of *L/D* values reviewed: as shown in Figure 4.3(b) which shows the results for the range of *L/D* values analysed. Figure 4.3(c) shows the same results normalised by the lateral resistance obtained for *h/D* = 0. From this it is evident that for higher *L/D* values the decrease in resistance from increasing *h/D* is more pronounced.

An alternative way of showing the results is to plot $\frac{F_x}{s_u D^2}$ against L/D, as shown in Figure 4.3(b). Plotting this way allows comparison to the HXTWn results. When the pile head is fixed against rotation and lateral translation occurs, a pile has significantly more capacity than when a free head is allowed. When the pile head is not fixed the lateral resistance will decrease with increasing upstand: to zero lateral resistance as *h/D* approaches infinity, i.e. pure moment loading. In practical terms, it is often more convenient to express the lateral resistance as an envelope that varies with applied moment: as has been done in Figure 4.3(d). The results in this plot represents the limiting combinations of moment and horizontal load that can be applied

to a pile. Additional models where a pure moment load has been applied have been included here to show the complete envelope for $F_x > 0$ and $M_y > 0$. The envelopes can be extended into the $F_x < 0$, $M_y > 0$ and $F_x > 0$, $M_y < 0$ quadrants for cases when the load and moment act in opposite directions and when load application is below ground level respectively.

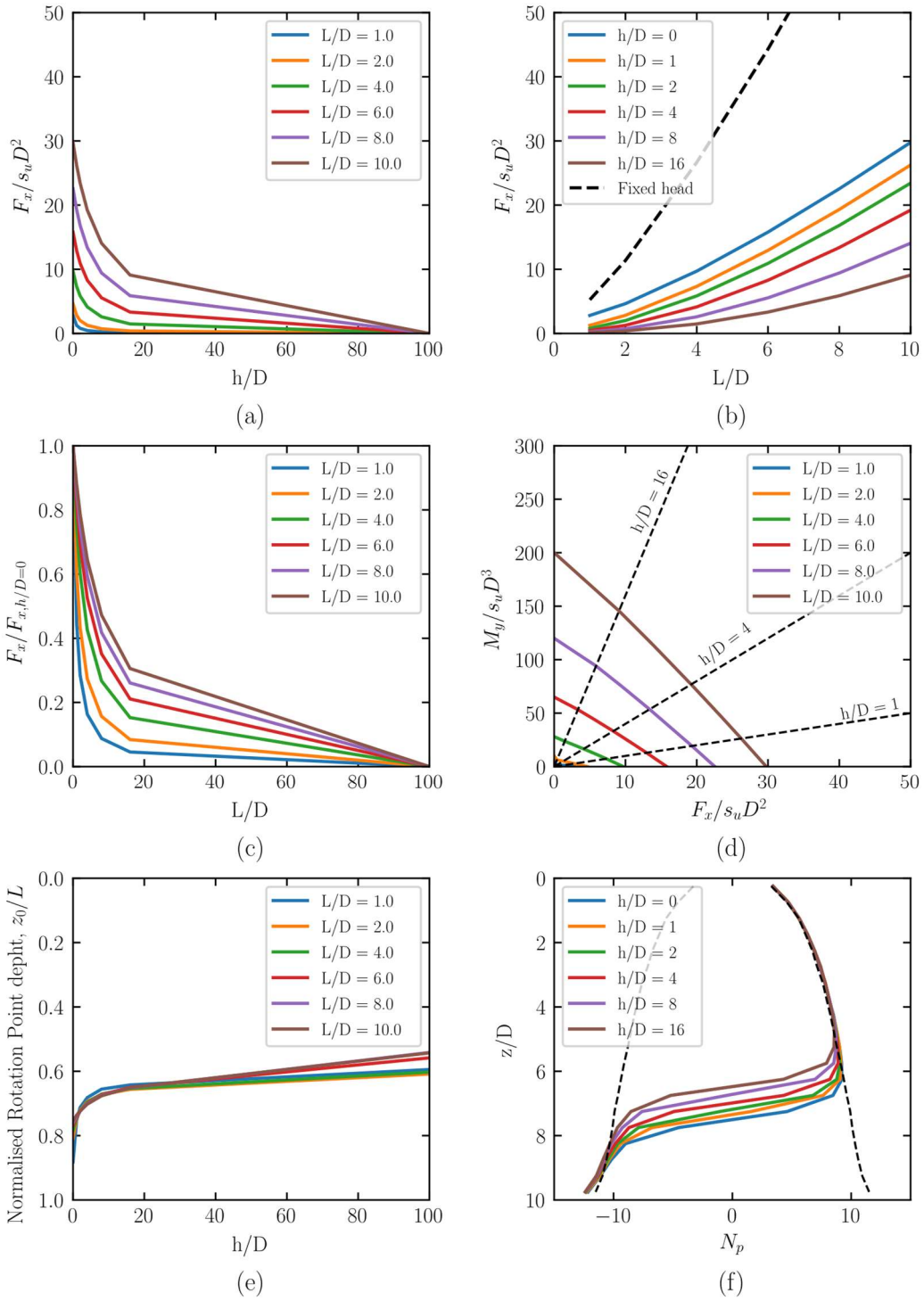

Figure 4.3 – HFTWn modelling with α = 0.5 (a) total resistance with h/D, (b) total resistance with L/D (c) lateral resistance normalised by resistance at h/D = 0, (d) lateral load moment envelopes, (e) rotation point depth, and (f) distribution of lateral resistance

However these scenarios are typically quite rare and as such have been omitted.

Figure 4.3(e) shows the depth of the rotation point in the pile with increasing *h/D*. As *h/D* increase the rotation point tends to a depth of approximately $z_0/L = 0.6$ at $h/D = 20$. At even higher *h/D* the value of z_0/L approaches a value near 0.5: this is consistent across all *L/D* ratios with only minor variations. In these models a value of $z_0/L = 0.5$ would never be achieved due the variation in lateral resistance that occurs near the ground surface and the resistance arising at the base of the pile.

The mobilised resistance for $L/D = 10$ for varying *h/D* is shown in Figure 4.3(f). The results from HXTWn for the same *L/D* are shown as black lines. The mobilised response can be separated into five distinct sections:

- From the ground surface to $z/D \approx 2$ the resistance increase from its initial value up to the limiting value of the flow around mechanism: in this instance the flow around mechanism results in $N_p \approx 11.5$.
- From $z/D = 2$ to $z/D = 4$ the resistance stays at this limiting value.
- The resistance then transitions from the soil acting on the front of the pile to corresponding negative values for the soil acting on the rear of the pile. This transition is symmetrical around the rotational point for homogeneous soils and occurs over a depth of approximately $z/D = 3$. As shown on Figure 4.3(e) the rotation point depth decreases with increases *h/D* and this is reflected in the results shown on Figure 4.3(f). However, the depth that the transition occurs over appears independent of h/D.
- At the base of the transition the resistance is at the flow around value.
- Finally, as the toe of the pile is approached the resistance starts increasing to a value approximately 15% above that of the flow around mechanism.

At all stages except the transition the N_p profiles of the free head pile conform to the profile obtained from HXTWn conditions suggesting this is a reliable method for obtaining a limiting resistance profile.

Figure 4.4 shows the final mesh and a plot of the upper bound velocity vectors on the X-Z plane for each of models except for *L/D* = 10. There are several mechanisms that are observable in each case. In all cases a body of soil is pushed up ahead of the pile with a corresponding body of soil that would be pulled down at the back of the pile: not shown due to the use of a plane of anti-symmetry on the Y-Z plane. This soil corresponds to the wedge failure mechanism assumed in the literature. As with the translation case, this wedge appears to be slightly curved in align with the assumptions of Yu et al. (2015) as to the shape of the wedge.

In all cases a body of soil rotates with the pile about the rotation depth. This rotating body of soil corresponds with the transition zone outlined previously whereby the lateral resistance acting on the pile switches between the front and back faces of the pile. At *L/D* = 1 and 2 the body of rotating soil starts immediately at the base of the wedge mechanism and extends to some depth below pile toe. This contrasts to *L/D*=4, 6, and 8 where there is a noticeable gap between wedge and rotation. This gap will correspond to an area where the flow around mechanism occurs. The base of the rotating mechanism also appears to be coincident with the pile toe suggesting that only shearing is occurring at the base in these cases: i.e. there is minimal rotation at the base compared to *L/D* = 1 and 2.

4.1.3. Translating pile with no interface tension in weightless soil

In the third stage of the investigation, a translating pile was used again however now with no interface tension included in the model; i.e. HXNWn conditions. This necessitates use of a half model with a plane of symmetry on the X-Z plane: as opposed to the quarter model used previously with symmetry on X-Z and anti-symmetry on Y-Z. This change was required to

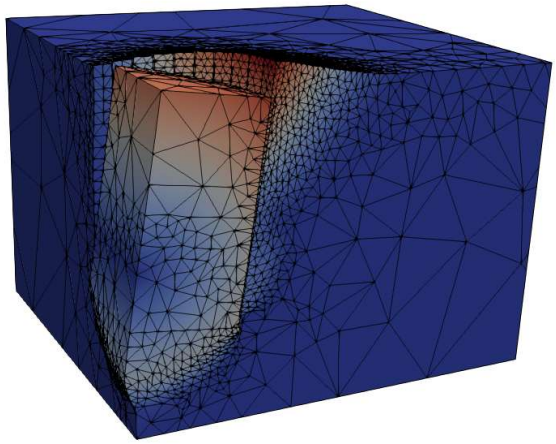

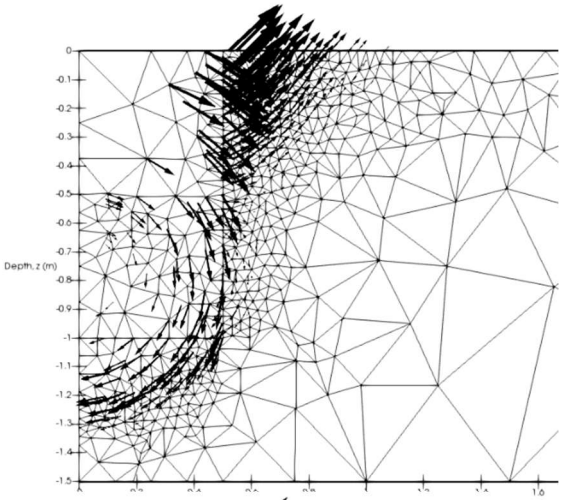
Depth, z (m)

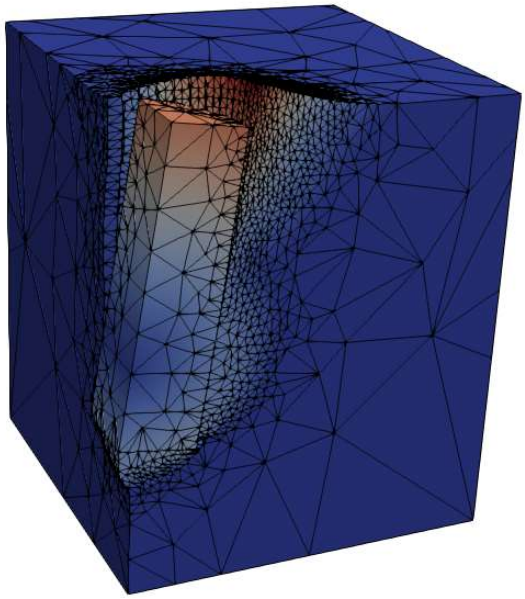

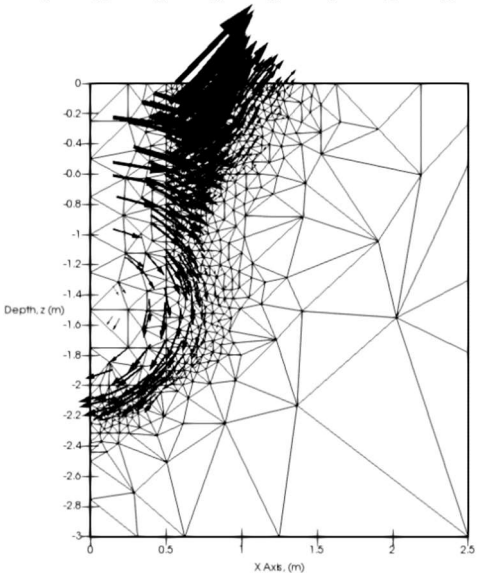
Depth, z (m)
X Axis, (m)

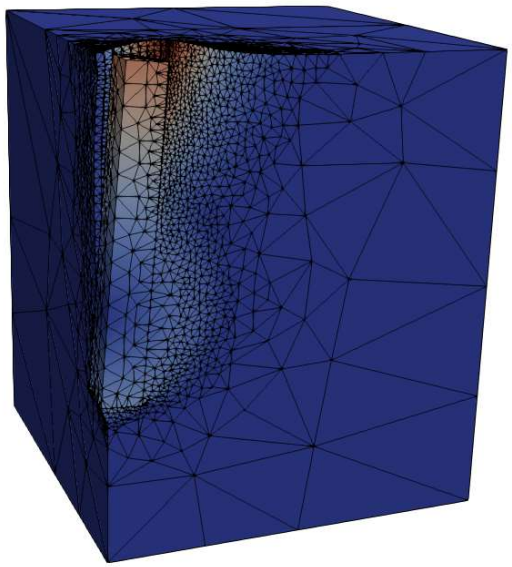

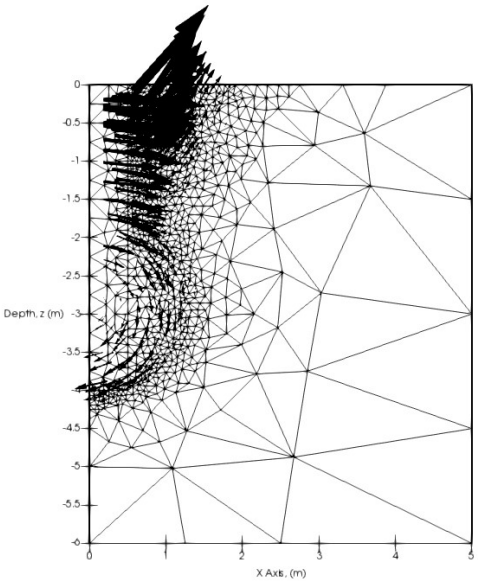
Depth, z (m)
X Axis, (m)

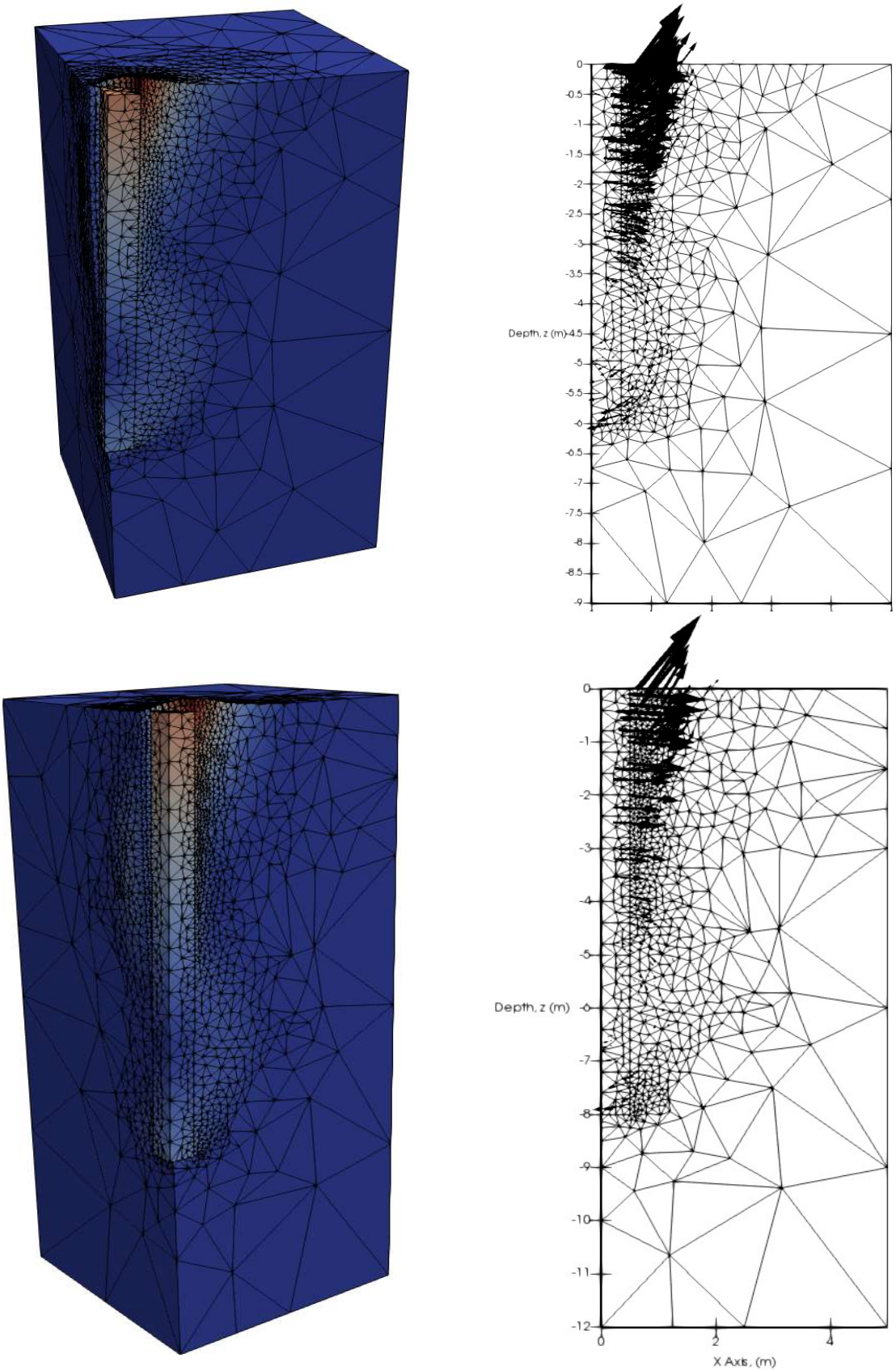

Figure 4.4 - Deformed mesh and velocity vectors for HFTWn modelling with α = 0.5 for (a) L/D = 1, (b) L/D = 2, (c) L/D = 4, (d) L/D = 6, and (e) L/D = 8

accommodate the different behaviours that occur in front and behind of a pile as a gap can form between the rear face of the pile and the soil. To prevent an overly large number of tetrahedra being specified by the mesh generator the pile was segmented into ten parts per half circle, i.e. 20 segments for the full circular section. This will result in a marginally higher resistance that the equivalent quarter section model, however the variation is expected to be less than 1% for most scenarios. This stage of the investigation, and the subsequent free head pile analysis, were performed in weightless soil: the aim being to provide a minimum resistance that should occur for fixed or free piles in undrained clay.

The total resistance is shown on Figure 4.5(a). The results obtained follow a similar pattern to those from the HXTWn modelling, however the capacity is now approximately 60% to 70% of the HXTWn models. The error between upper and lower bound is also marginally higher however this is to be expected owing to the increased size of each model, twice that of the HXTWn models, while keeping the same limit on the number of tetrahedral elements. The cause of this reduction of total capacity compared to the HXTWn modelling is evident from Figure 4.5(b) which shows the profile of Np with depth. The value of Np corresponding to the flow around mechanism is only reached at $z/D = 10$: a significant change from the $z/D = 2$ required in the HXTWn case. The flow around mechanism, marked as a dashed line for a circular section, is not achieved in this case. At $z/D = 10$, the resistance has reached the equivalent value of the flow around mechanism however a plane strain state has not been reached owing to the proximity to the pile toe. There is some evidence of the increase of resistance at the toe of the pile for this case. Though it should be noted that the bracketing error at this depth is greater than the rest of the profile and therefore it is difficult to draw conclusions about the magnitude of this increase in this instance.

Base resistance for this case is shown in Figure 4.5(c) and Figure 4.5(d). The results are largely the same as for the HXTWn modelling, shown in Figure 4.1(d) and Figure 4.1(e). This is expected as the body of soil inside the pile will be largely unaffected by interface separation

due to the assumption of zero volumetric change occurring. As with the full tension model the Oxlim results are below the ideal semi-circular section, marked by the dashed line on the figure. For a diameter, the area of a 20 sided polygon is approximately 0.7725: i.e. the same as the upper bound result from the Oxlim analysis. Where this case differs from the HXTWn case is the proportion of total resistance that the base forms. At L/D = 1 the base resistance forms 14.6% compared to the 9% proportion observed in the full tension case.

The pile head restraining moment is shown in Figure 4.5(e) with the results from the HXTWn models. The average value increases from 3.13 at L/D = 1 up to 481.73 at L/D = 10. The removal of tension and use of weightless soil leads to a 20% reduction in restraining moment required at L/D = 10.

The deformed mesh and velocity vectors for this stage of the investigation are shown in Figure 4.6 for L/D = 2, 4, and 6. In each case the gap behind the pile is open to the base of the pile owing to the use of weightless soil in the modelling. As noted in Figure 4.5(b) the limiting resistance of the flow around mechanism is not achieved at L/D = 10 and as such is not observable in any of the results shown in Figure 4.6. However, the shape of the wedge mechanism is much more apparent in these case with the mesh refinement showing a distinct curvature in refined elements at the extents of the wedge body of soil.

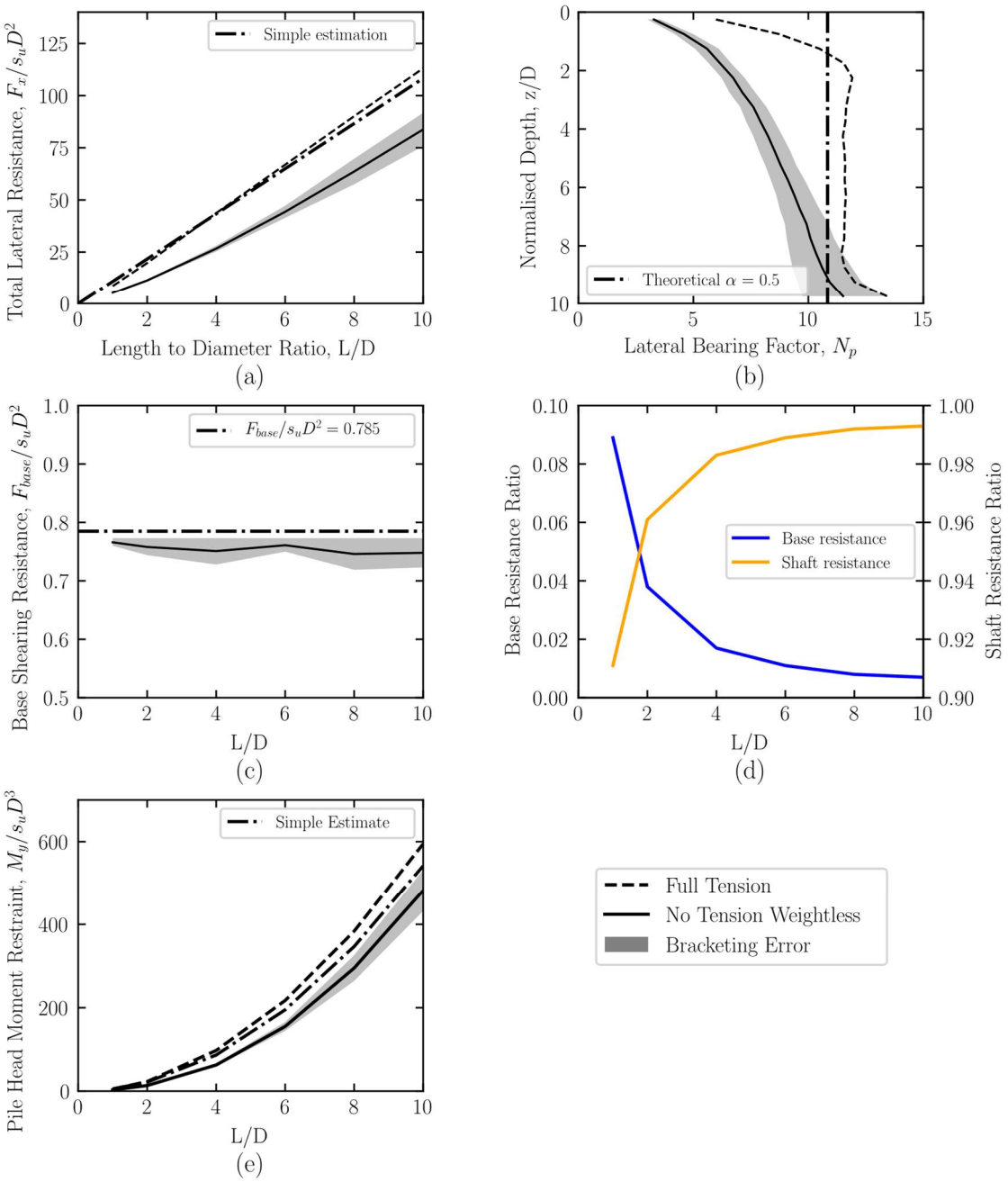

Figure 4.5 - Results from analysis of a HXNWn with α = 0.5, (a) total resistance with L/D, (b) distribution of lateral resistance, (c) base shearing resistance with L/D , (d) contribution of base and shaft resistance to total resistance with L/D, and (e) pile head restraining moment with L/D

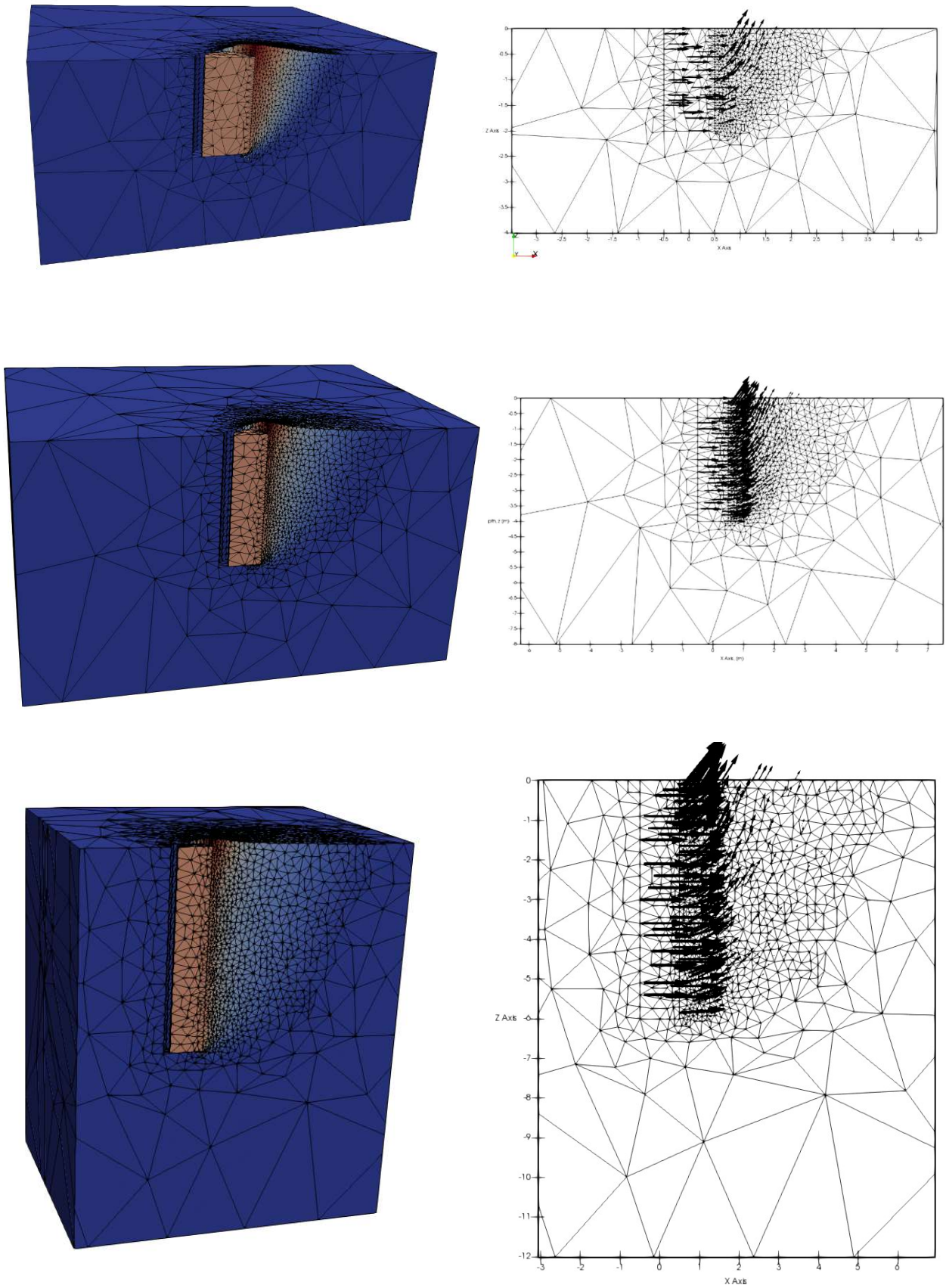

Figure 4.6 - Deformed mesh and velocity vectors of HXNWn modelling with α = 0.5 for (a) L/D = 2, (b) L/D = 4, and (c) L/D = 6

4.1.4. Free head pile with no interface tension in weightless soil

For the fourth stage of the investigation, a free head pile was modelled with no interface tension; i.e. HFNWn conditions. As with the HXNWn modelling, a half model was required. Figure 4.7(a) shows the normalised resistance with h/D for L/D = 4 α = 0.5 and weightless soil is specified giving a ratio of $\gamma D/s_u = 0$. As with the HFTWn model, the lateral resistance decreases rapidly as load application height increases for this case. The results for the remaining L/D ratios are shown in Figure 4.7(b). The results are significantly lower than for the full tension models with reductions in lateral resistance ranging from 30% to 40% at $h/D = 0$. Figure 4.7(b) shows the lateral resistance when plotted against L/D.

Figure 4.7(d) shows the load – moment envelopes for this case. A similar overall shape of the data is seen when compared with HFTWn modelling however, as with the horizontal load, the values of moment resistance are lower than for the HFTWn case. Figure 4.7(e) shows the rotation point depth for this case. The same general trend of a lower rotation point depth at low h/D is observed however the results now show a more pronounced scatter at $h/D = 0$ with all results giving much closer change in rotation depth with h/D. The rotation point for all cases is lower than the HFTWn case, shown in Figure 4.3(e). This occurs due to differences in how the limiting resistance is distributed along the pile. For HFTWn the limiting resistance is relatively uniformly distributed, this is contrary to HFNWn where the resistance is increasing with depth all the way to the pile toe. In the latter case, more of the mobilised resistance is located towards to the toe of the pile.

The mobilised resistance profiles for the HFNWn are shown in Figure 4.7(f). The profiles follow much the same pattern observed for the HFTWn models, shown in Figure 4.3(f), albeit with the reduced N_p profile. The transition of the resistance about the rotation point starts between $z/D = 5$ and $z/D = 6$ depending on h/D, and occurs over a depth of approximately 3D,

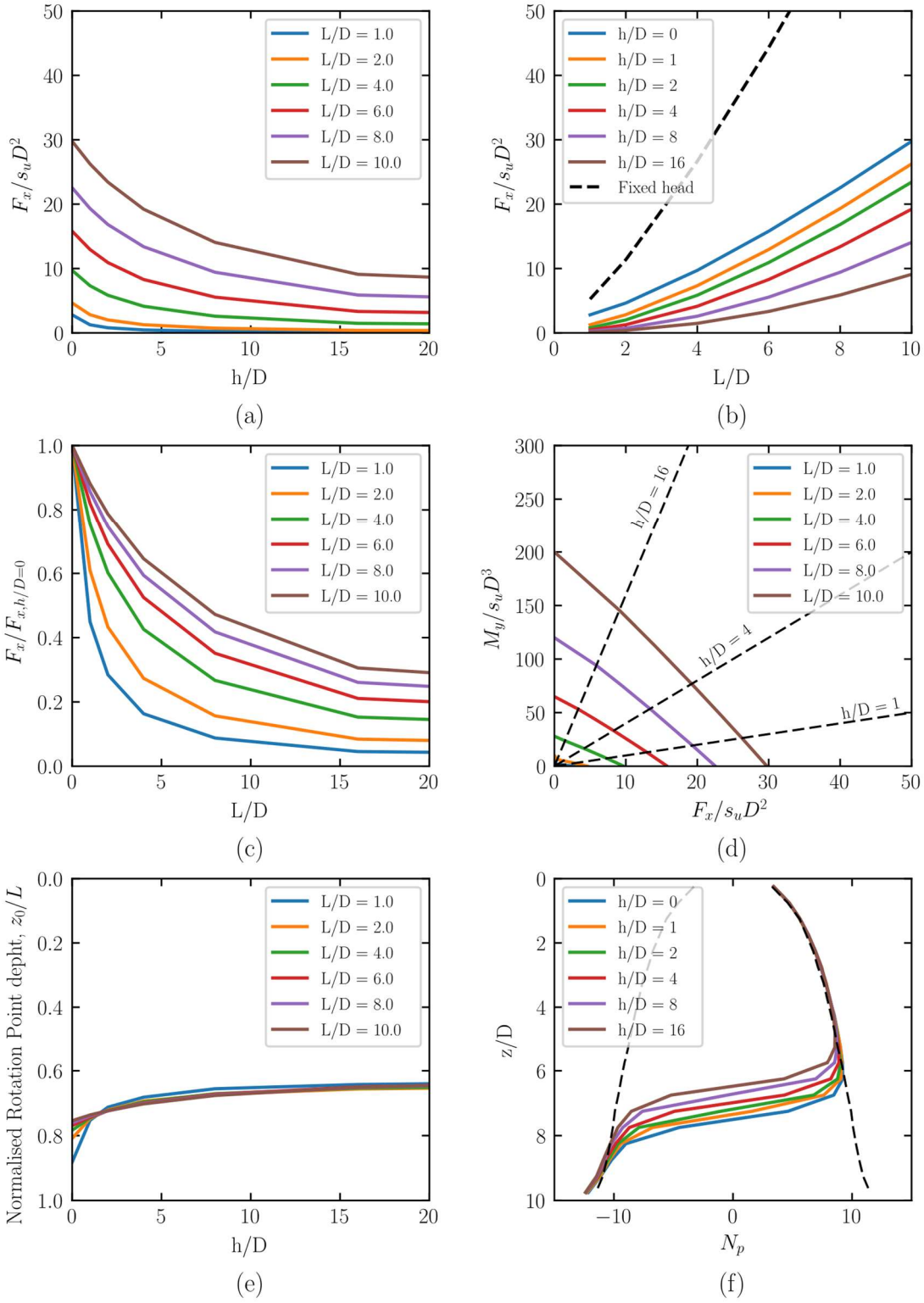

Figure 4.7 – HXNWn modelling with α = 0.5 (a) total resistance with h/D, (b) total resistance with L/D (c) lateral resistance normalised by resistance at h/D = 0, (d) lateral load moment envelopes, (e) rotation point depth, and (f) distribution of lateral resistance

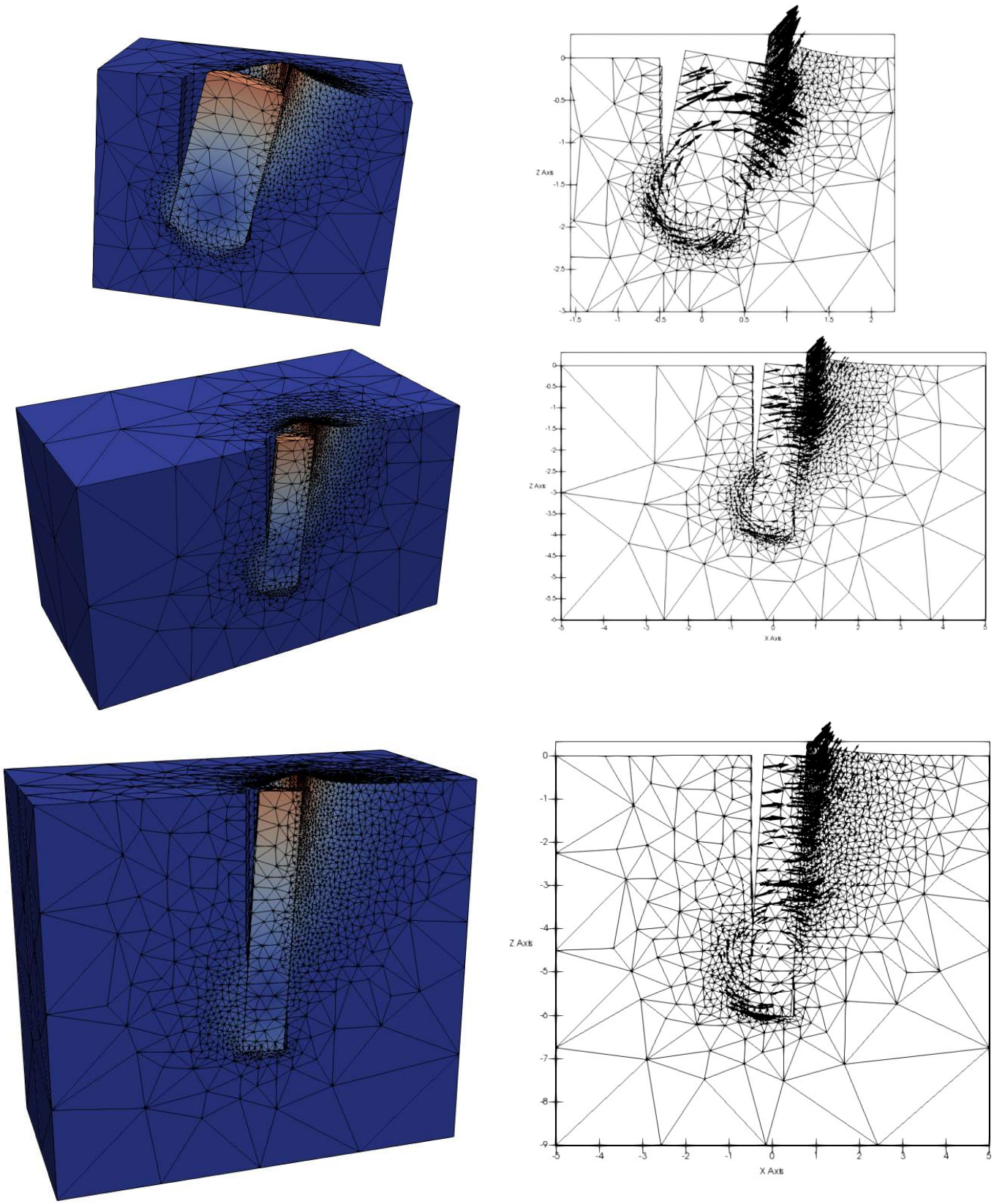

Figure 4.8 - Mesh and velocity vector figures of a HFNWn modelling with α = 0.5 for (a) L/D = 2, (b) L/D = 4, and (c) L/D = 6

i.e. the same as for the HFTWn case. This is suggestive of the depth of the transition zone being proportional to the diameter irrespective of which resistance mechanism, i.e. wedge or flow, that it occurs in. However this would need to be verified through review of the transition behaviour in non-homogeneous profiles.

The final deformed mesh and velocity vectors for HFNWn are shown in Figure 4.8. In this figure, the velocity vectors are plotted over the deformed mesh to make the gap behind the pile apparent. As with the HXNWn models, a gap has formed behind the pile in each of the models. However in this case the gap has formed down to the rotation point. While not immediately apparent, a gap has also opened on the front face of the pile between the rotation point and the toe of the pile. In most scenarios, it is not envisaged that a gap could form here as the weight of the soil above the pile would likely force the gap to close. However, there are a few scenarios where this could feasibly occur such as low *L/D* piles in very high strength clay.

The resulting mechanisms are somewhat similar to the full tension case however with some distinct differences. Firstly, the soil wedge only occurs in front of the pile now with the soil behind not moving with the pile. Secondly, the rotational mechanism now only occurs on one side of the pile with the aforementioned gap near the toe of the pile seemingly preventing the rest of the mechanisms forming. As with the HXNWn cases, the scale of the wedges formed is much larger than the HXTWn and HFTWn cases.

4.1.5. Translating pile with no interface tension with soil weight included

For the second to last stage of this investigation, a translating pile was modelled with no interface tension and soil unit weight included; i.e. HXNWi. Soil unit weight has been varied to fit dimensionless ratios of $\frac{\gamma D}{s_u} = 1$, 2, and 4. Higher values of $\frac{\gamma D}{s_u}$ were considered however at and above $\frac{\gamma D}{s_u}$ = 4 all the results became increasingly similar to those of the HXTWn models.

This is readily apparent when comparing Figure 4.9(a), which shows the total capacity for $\frac{\gamma D}{s_u} =$ 1, 2, and 4, against the results in Figure 4.1(a) and Figure 4.5(a). As expected, increasing the ratio of $\frac{\gamma D}{s_u}$ above zero, i.e. introducing vertical stress into the model, causes the resistance to increase above the HXNWn case. At $\frac{\gamma D}{s_u}$ = 4 the total resistance at *L/D* = 10 is less than 1% different than the HXTWn modelling. However it should be noted that the error in this model $\frac{\gamma D}{s_u}$ = 4 is 12%, compared to the HXTWn models bracketing error of 8%, which means the true difference between these results could be larger.

Profiles of N_p with *z/D* for $\frac{\gamma D}{s_u} =$ 1, 2, and 4 are shown in Figure 4.9(b) alongside the profiles for the HXNWn and HXTWn cases. The introduction of unit weight leads to the flow around failure occurring at increasingly shallow depths as $\frac{\gamma D}{s_u}$ increases. This occurs as the flow around mechanism requires a certain amount of vertical constraint to occur: something which happens as the vertical stress in the model relative to the soil strength increases. For $\frac{\gamma D}{s_u} = 4$ the transition from wedge to flow around occurs around *z/D* = 2: as with the results from the total resistance this is similar to the full tension case and increasing $\frac{\gamma D}{s_u}$ above 4 led to minimal changes from this value. It should be noted though that the resistance at surface is different for the high $\frac{\gamma D}{s_u}$ and full tension cases. The HXTWn case has approximately double the resistance at surface level of the no interface tension models, including the HXNWn case. Due to the coarseness of the mesh near the surface, the results are not sufficient to make a reasonable approximation of the at surface resistance. This will be reviewed in a separate set of analyses in Chapter 6 with models designed to provide an accurate assessment of this.

The ratios of base and shaft resistance to total resistance are shown in Figure 4.9(c). For $\frac{\gamma D}{s_u}$ = 1 the base forms 13.3% of the total resistance at *L/D* = 1 decreasing to below 1% at *L/D* = 8. For

$\frac{\gamma D}{s_u}$ = 4 the base resistance forms 10.6% of the total resistance decreasing to below 1% at *L/D* = 6. The magnitude of the base resistance is similar to that of the previous assessments with no variation caused by the introduction of vertical effective stress into the modelling.

The pile head restraining moment, in Figure 4.9(d), shows little variation with $\frac{\gamma D}{s_u}$. The results are very similar to the HXTWn case with each having a moment restraint of 600 M_y/s_uD^3 ± 2%.

The final deformed mesh and velocity vectors are shown in Figure 4.10. As with the HXNWn case, the gap behind the pile is evident: the depth of the gap varies with $\frac{\gamma D}{s_u}$ with the largest and smallest gap depths at $\frac{\gamma D}{s_u}$ = 1 and 4 respectively. For $\frac{\gamma D}{s_u}$ = 1 the gap does not close fully at the toe of the pile. The soil starts to slump at approximately *z/D* = 1 above the toe of the pile however at the toe of the pile there is still a gap that remains open. For $\frac{\gamma D}{s_u}$ = 2 and 4 the gap closes at approximately *z/D* = 4 and 2 respectively. At higher $\frac{\gamma D}{s_u}$ the gap decreases in depth until a point where the final deformed mesh resembles that of the HXTWn modelling, i.e. no gap forming and the response being anti-symmetric between the front and back of the pile across the Y-Z plane.

The size of the wedge mechanism at the front of the pile is clearly dependent on $\frac{\gamma D}{s_u}$: with the wedge decreasing in size as $\frac{\gamma D}{s_u}$ increases. However, from the assessment it is apparent that the wedge has a minimum size which corresponds to the size in the HXTWn modelling.

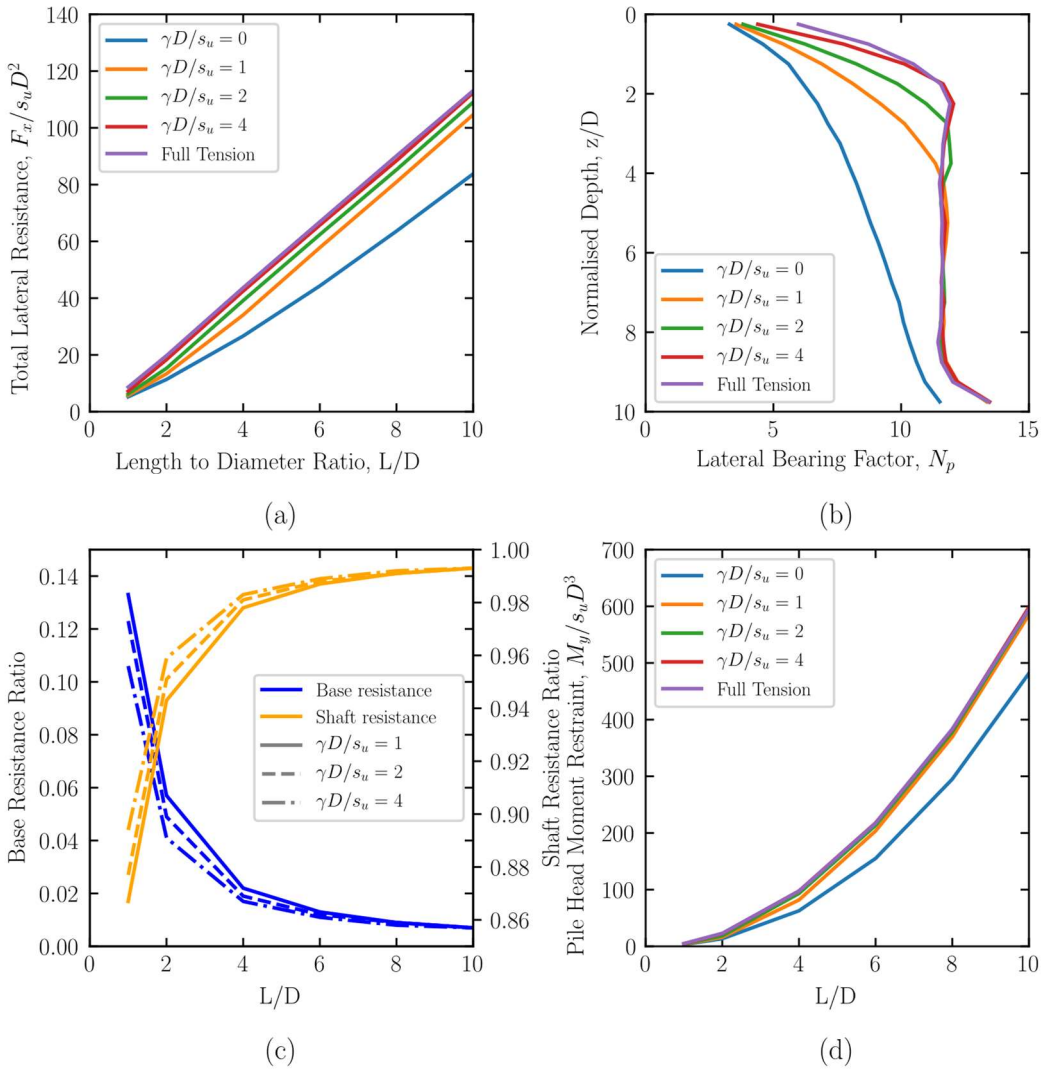

Figure 4.9 - Results from analysis of HXNWi conditions with varying γD/s_u and α = 0.5, (a) total resistance with L/D, (b) distribution of lateral resistance, (c) contribution of base and shaft resistance to total resistance with L/D, and (d) pile head restraining moment with L/D

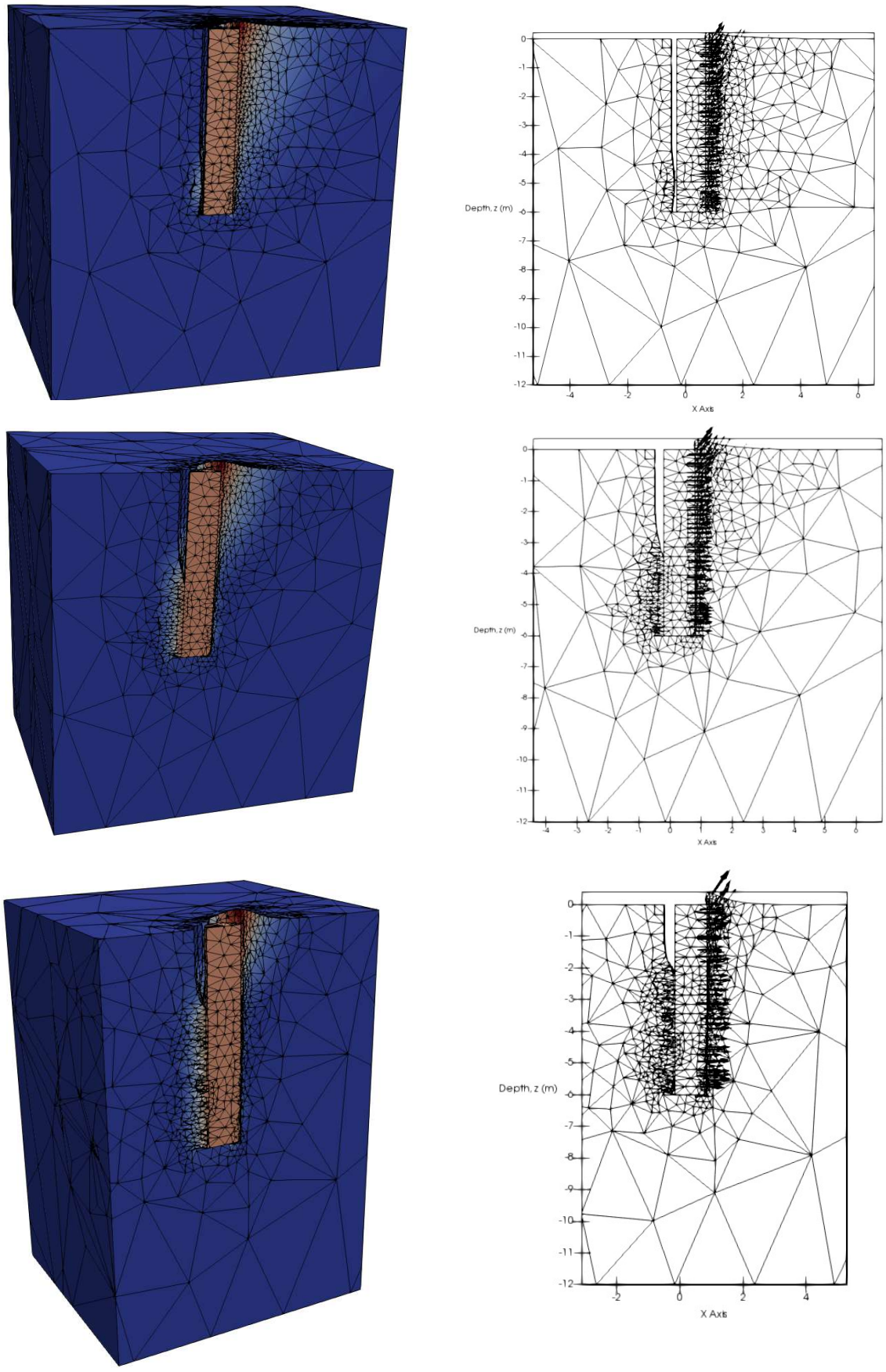

Figure 4.10 - Mesh and veclocity vectors for HXNWi, L/D = 6, and α = 0.5 for (a) γD/su = 1, (b) γD/su = 2, and (c) γD/su = 4

4.1.6. Free head pile with no interface tension with soil weight included

The final stage of this investigation used a free head pile with no interface tension and varying $\frac{\gamma D}{s_u}$; i.e. HFNWi conditions. Total resistance with h/D is shown in Figure 4.11 for L/D ratios between 1 and 10. At $\frac{\gamma D}{s_u}$ = 4 the results closely match those of the HFTWn model, shown in Figure 4.3. The total resistance decreases with decreasing $\frac{\gamma D}{s_u}$ with the HFNWn case giving an apparent lower limit to the resistance. This is similarly shown when plotting total resistance against L/D, as in Figure 4.11(f) to (j), and when plotting the load moment envelopes, in Figure 4.12. For all values of $\frac{\gamma D}{s_u}$ the translation case has about twice the resistance as the *h/D* = 0 case.

The rotation point depth is shown on Figure 4.13, the results are similar to those of the HFNWn and HFTWn cases with higher *h/D* resulting in a rotation point closer to the mid depth of the pile.

The final deformed mesh and velocity vectors are shown in Figure 4.14. The same general mechanisms as the previous free head pile analyses are present: i.e. a wedge at the front of the pile near the soil surface, a brief section where the flow around mechanism occurs, and a block of soil rotating with the pile. As with the HFNWn case, a gap forms behind the pile as it is loaded. For these models, the gap depth no longer extends to the rotation point but now varies with $\frac{\gamma D}{s_u}$. The depth of the gap is similar to the HXNWi cases: i.e. approximately *z/D* = 2 and 4 for $\frac{\gamma D}{s_u}$ = 4 and 2 respectively. However, for $\frac{\gamma D}{s_u}$ = 1 the gap extends to the rotation point. There is no gap forming below the rotation point: the vertical stdress at this depth is sufficient to collapse the soil onto the front face of the pile.

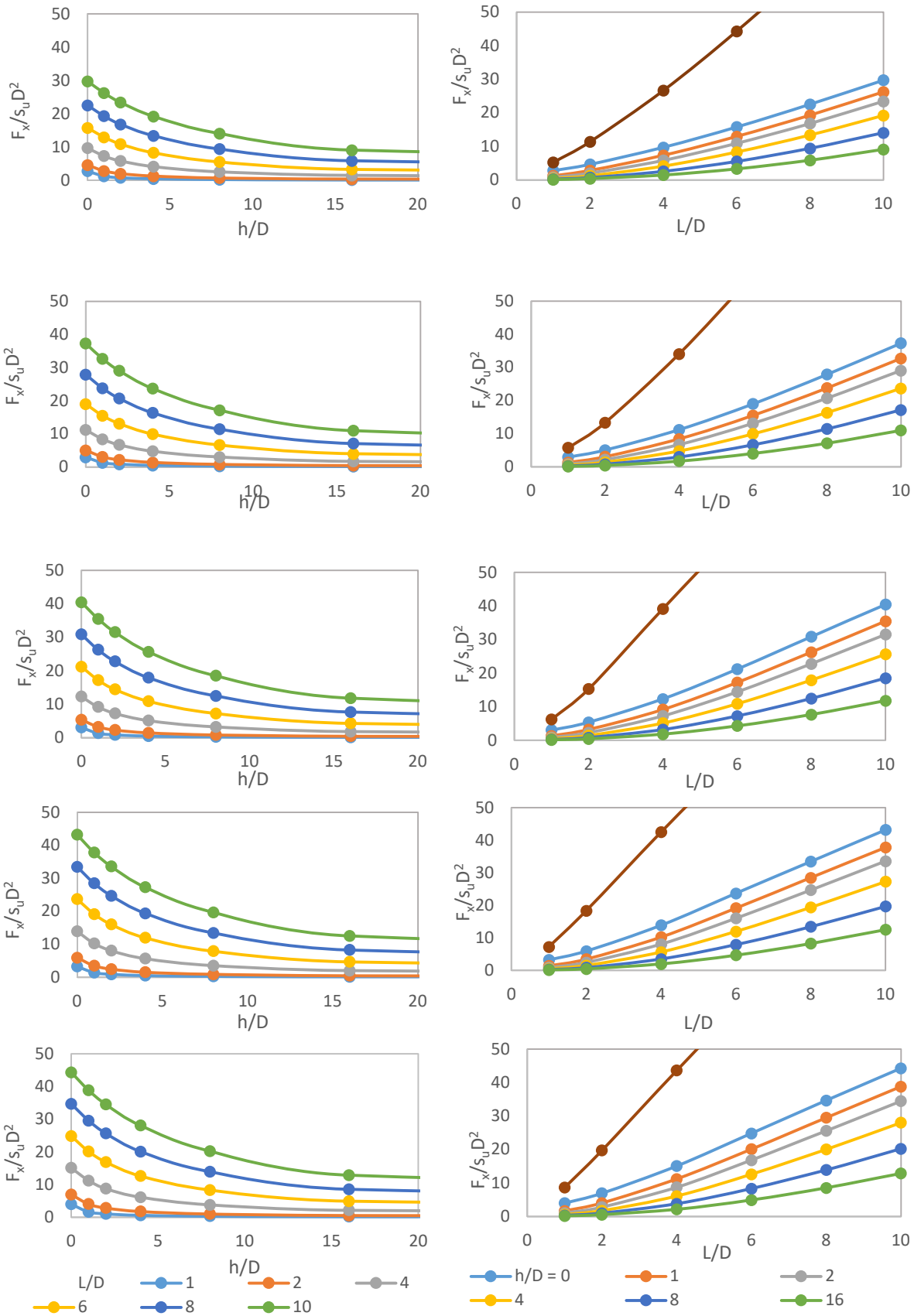

Figure 4.11- Lateral resistance with load with increasing load application height for multiple L/D and lateral resistance with increasing L/D for varying load application height. HFNWi, α = 0.5, for (a) γD/su = 0, (b) γD/su = 1, (c) γD/su = 2, (d) γD/s_u = 4, and (e) full tension (i.e. γD/s_u = ∞)

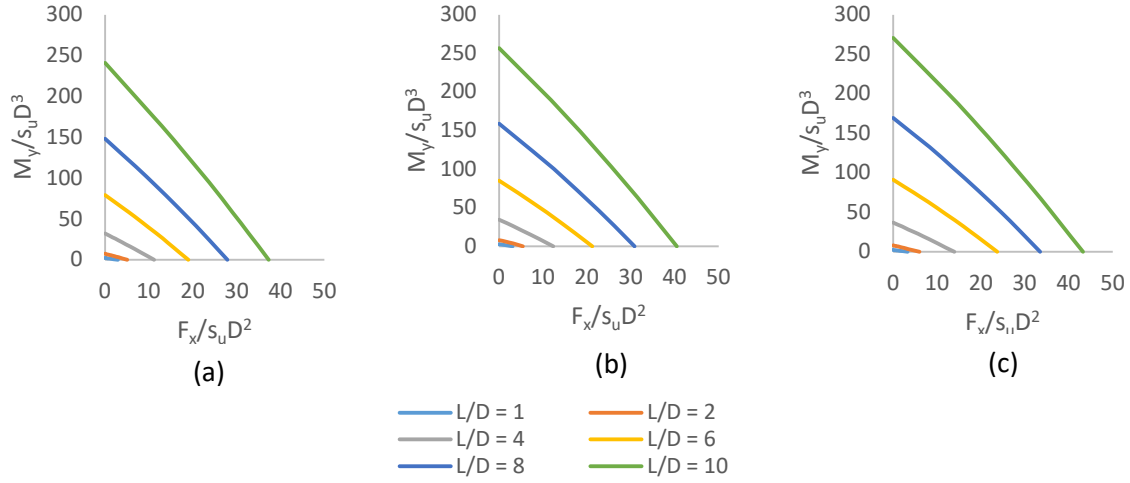

Figure 4.12- Load Moment Envelopes. HFNWi, α = 0.5, for (a) $\gamma D/s_u = 1$, (b) $\gamma D/s_u = 2$, and (c) $\gamma D/s_u = 4$

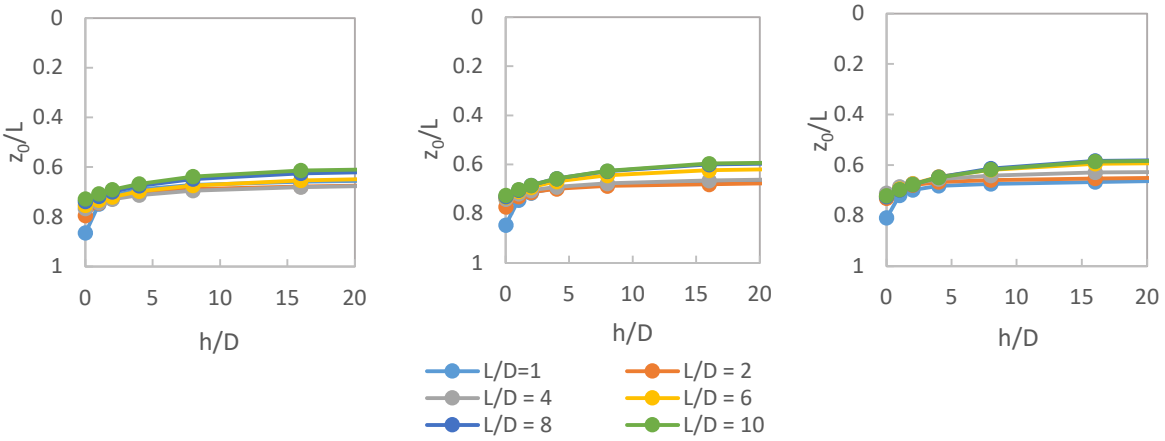

Figure 4.13 - Rotation point depth with h/D for HFNWi with α = 0.5for (a) $\gamma D/s_u = 1$, (b) $\gamma D/s_u = 2$, and (c) $\gamma D/s_u = 4$

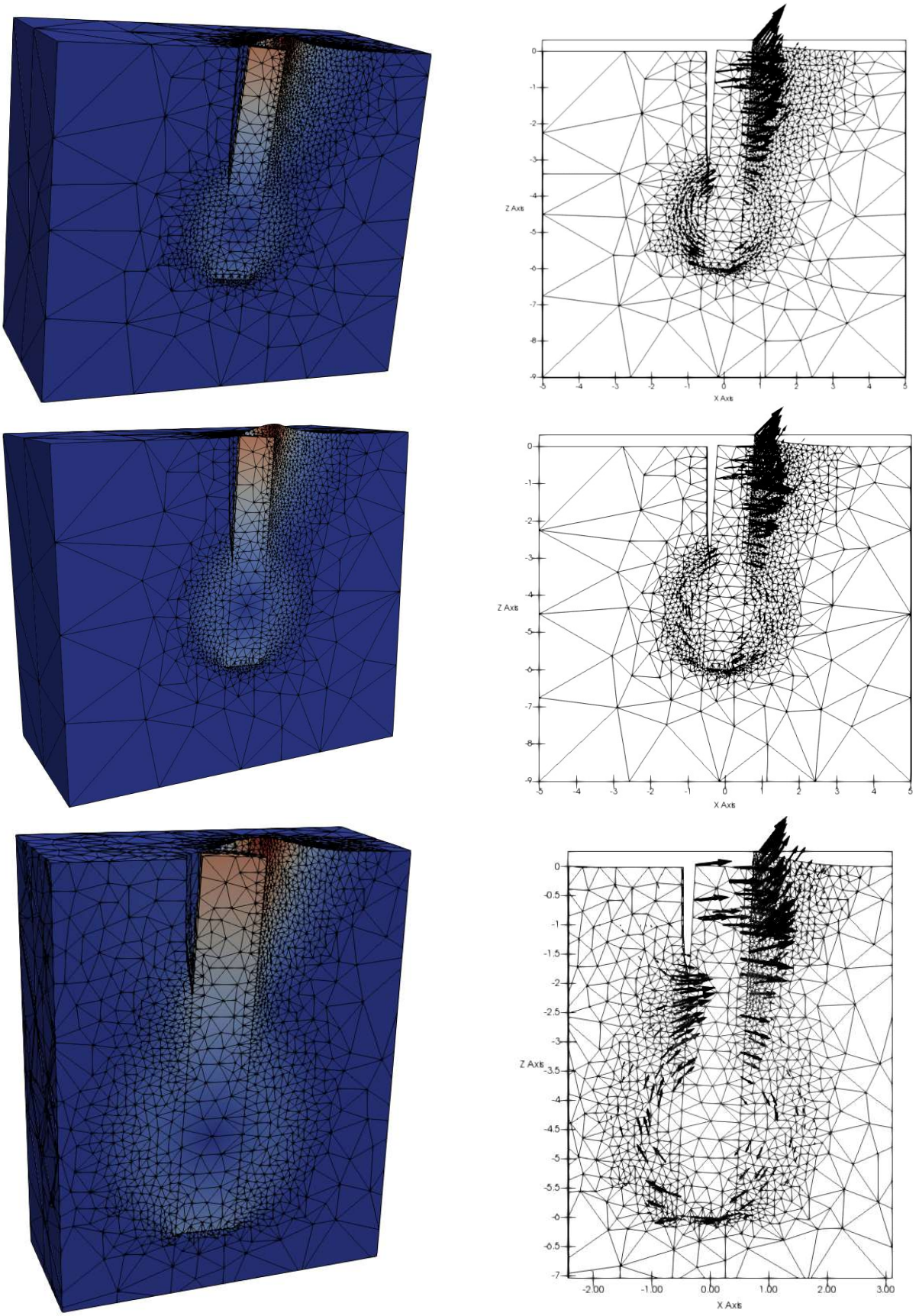

Figure 4.14 Mesh and velocity vector images, HFNWi, L/D = 0, and α = 0.5 for (a) γD/su = 1, (b) γD/su = 2, and (c) γD/su = 4

4.2. Comparison of Oxlim to Literature

Comparison of the N_p profiles from the fixed head models has been made to several published methods, namely: Matlock (1970), Murff and Hamilton (1993), and Jeanjean (2017). The results from this comparison are shown in Figure 4.15. The following notes are made with respect to the methods used:

- The Matlock approach has been adopted as specified in the literature using Equation 2.5.
- The Murff and Hamilton approach has been performed with N_1 = 11.5 and N_2 = 8.5 to match the surface and flow around conditions in the literature. The profile of N_p generated from Equation 2.14 takes no account of soil unit weight and is equivalent to the N_{p0} term from Jeanjean (2017). To facilitate comparison the Oxlim results the equivalent N_p accounting for soil unit weight has been calculated using Equation 14.

$$N_{p,eq} = \frac{P_u}{s_u D} = \frac{\left(N_p s_u + \gamma z\right)}{s_u} \tag{4.3}$$

- The Jeanjean approach has been performed taking N_{pd}=11.5 to match the flow around conditions from the Oxlim analysis. All other parameters for the method are kept as presented in the literature.

It is immediately apparent that the prediction using the Matlock method is significantly below the other methods. This is predominantly due to the explicit assumption of a smooth pile in the method. Taking the limiting value of N_p as a value that matches the higher values observed when pile-soil adhesion is taken into account would improve the match in the deeper sections of the pile. However the profile near surface would be unaffected by such a change and still give an underprediction. This underprediction of N_p matches the observations in the literature as to the appropriateness of the Matlock approach.

Conversely to the Matlock approach, the Murff and Hamilton approach overpredicts the resistance profile in all cases. The error of the method increases with decreasing $\gamma D/s_u$ with the maximum deviation from the Oxlim results occurring for the weightless case, shown in Figure 4.15(a).

The Jeanjean approach gives a very good match across all variations of $\gamma D/s_u$. The only exception to this is at the toe of the pile where the resistance increases however this is expected as the Jeanjean method was derived for long slender piles where the increase in resistance at the toe of the pile would be inconsequential to the design of the pile.

A shortcoming of the Jeanjean approach though is the inclusion of α into the empirical formulation. This results in the transition depth between wedge and flow mechanisms varying with this parameter. This is contrary to the results from Oxlim which indicate that, in homogeneous materials at least, there is no variation in the transition depth with pile-soil adhesion. This is shown in Figure 4.1(c) for the HFTWn case. A comparison of Oxlim results and Jeanjean approach for weightless soil and no interface tensions is shown in Figure 4.16. As previously seen the Jeanjean approach gives a very good match for $\alpha = 0.5$ however the $\alpha = 0$ and 1.0 case under predict and over predict the transition depth respectively.

4.3. Summary

The problem of a Laterally loaded pile in homogeneous clay has been analysed using Finite Element Limit Analysis with the Oxlim software. Charts of ultimate capacity have been presented showing the variation of total resistance with varying L/D, h/D and $\gamma D/s_u$. The impact of modelling both full interface tension and no interface modelling is shown and it has been demonstrated that these conditions form upper and lower limits for a piles lateral capacity: both in terms of the total capacity and the variation of capacity with depth.

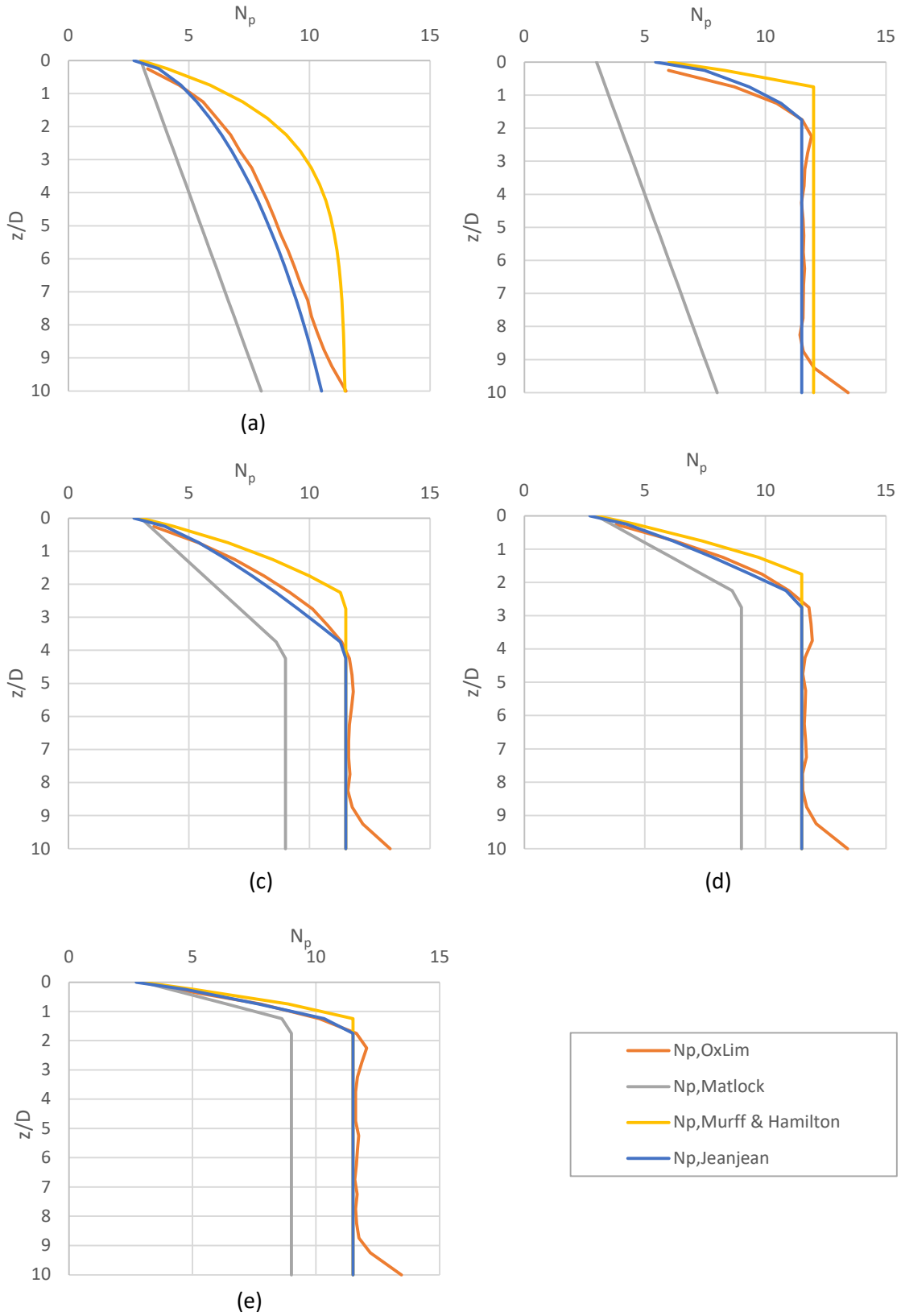

Figure 4.15 - Comparison of Oxlim results to empirical methods, \alpha = 0.5, L/D = 10, (a) $\gamma D/s_u = 0$, (b) Full Tension, (c) $\gamma D/s_u = 1$, (d) $\gamma D/s_u = 2$, and (e) $\gamma D/s_u = 4$

A review of the variation of lateral bearing factor with depth shows a significant variation of the profile of N_p with $\gamma D/s_u$: in weightless soil the wedge mechanism extends to beyond z/D = 10 whereas as $\gamma D/s_u$ approaches 4 the wedge extends to z/D = 2 and the profile approaches the full interface tension case. The value of pile-soil adhesion, α, was seen to have no impact on the overall shape of the N_p profile however further work is required to confirm whether α causes a variation of N_p at the ground surface.

Comparison was made to several empirical methods available in the literature: namely the Matlock, Murff and Hamilton and Jeanjean approaches. The Matlock approach under-predicted the profile of N_p in all scenarios whereas the Murff and Hamilton approach led to an overprediction in all cases. The Jeanjean approach was seen to give a good match in all cases for α = 0.5 however it was seen that the approach gives incorrect results when α varies from this value.

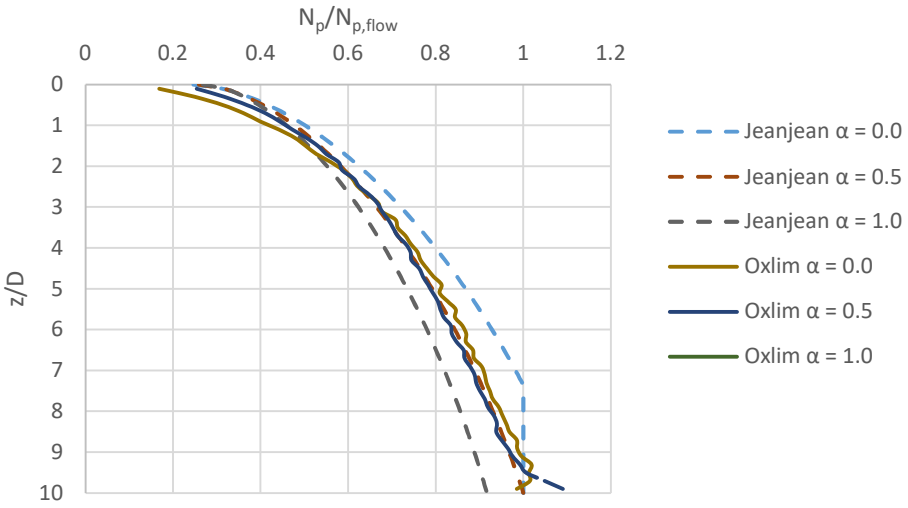

Figure 4.16 - Comparison of Jeanjean (2017) to Oxlim results, weightless soil, no interface tension, α = (0,0.5, 1.0)

Chapter 5

Lateral resistance in non-homogeneous profiles

This chapter considers the ultimate response of a laterally loaded pile in various non-homogeneous clay profiles. The calculations have been performed using the OxLim FELA software. As with the study on homogeneous profiles, the focus of this study is predominantly on the mechanisms in Figure 2.1(a) and 2.1(c). Three cases are presented:

- single layer with strength proportional to depth (Figure 5.1(a))
- Two-layer profile with an abrupt strength change (Figure 5.1(b))
- Embedded layer with a significant strength variation from the surrounding material (Figure 5.1(c)).

To present the results obtained from these cases, additional dimensionless groups to those presented in Table 4.1 are needed. These are given in Table 5.1. The additional parameters in Table 5.1 to those presented previously are s_{u1} and s_{u2} which are shear strengths of a given soil layer (either top and bottom layers or surrounding soil and embedded layer) and z_L and z_e which are the depth to the layer boundary from mudline and thickness of the embedded layer respectively. The definitions of these parameters in context of the studies in this chapter are shown on Figure 5.1.

The first part of this chapter shows the assessment of strength proportional with depth profiles. These profiles are frequently encountered in the offshore environment, such as the soft clays encountered in the Gulf of Mexico and the firm to stiff clays of the London Clay group encountered in the south east of England. The format of this study is similar to that for homogeneous clays; starting with a translating pile with full interface tension and progressing

to a free head pile with no interface tension and a varying ratio of unit weight to strength gradient, γ/ρ. The stages of this assessment are:

1. LXTWn - Translating pile with full interface tension
2. LFTWn - Free head pile with full interface tension
3. LXNWn - Translating pile with no interface tension in weightless soil ($\gamma/\rho = 0$)
4. LFNWn - Free head pile with no interface tension in weightless soil ($\gamma/\rho = 0$)
5. LXNWi - Translating pile with no interface tension and varying soil γ/ρ ratio
6. LFNWi - Free head pile with no interface tension and varying γ/ρ ratio

The analyses performed for each stage are similar to those performed for homogeneous strength profiles in Chapter 4. The key difference being the use of the dimensionless group γ/ρ instead of $\gamma D/s_u$. Where appropriate comparison is made to the equivalent normalised response for a homogeneous profile however this is not possible in all cases. As a final part of this section, comparison is made to published approaches for obtaining profiles of the lateral bearing factor, N_p, and recommendations on the appropriateness of these methods are made.

The second part of this chapter focuses on the resistance that occurs when there is an abrupt change in the soil strength: e.g. when a soft clay lies on top of a stiff clay as can occur in paleochannels in near coastal areas. This is shown schematically in Figure 5.1 (b). The focus of this study is on how the lateral bearing factor profile varies near the layer boundary and the subsequent influence on the resistance. Three cases are assessed representing common design scenarios, these are:

- The layer boundary occurs in the flow-around zone
- The layer boundary occurs in the wedge when no gap forms
- The layer boundary occurs in the wedge when a gap forms

The resulting variations of the bearing factor N_p with depth are presented, alongside recommendations on incorporating these results into an estimation of an N_p profile.

The final part of this chapter presents the assessment of the variation of the lateral bearing factor across an embedded layer of finite thickness and with strength that differs significantly from the surrounding soil. This is shown schematically in Figure 5.1(c). Assessment is made on the thickness of embedded layer required to allow treatment as two separate layer boundaries and the influence that embedded layers of small thickness have on the overall response: whether through increasing the resistance in the low strength layers or conversely decreasing the resistance in the high strength material.

5.1. Strength proportional to depth

This section investigates the lateral and moment resistance that occurs for linearly increasing strength with depth: shown schematically in Figure 5.1(a). The modelling process used for this study is the same as used for the study on the response in homogeneous soil conditions presented in Chapter 4.

All models in this section use $\alpha = 0.5$ unless otherwise specified.

5.1.1. Translating pile with full interface tension

In the first stage of the study the rigid pile is fixed against rotation and translated laterally; i.e. LXTWn conditions. Interface separation is disabled, allowing the development of full tension on the back of the pile. These assumptions permit a quarter model to be used: achieved by specifying the Y-Z plane as a plane of anti-symmetry. The assumption of full interface tension also negates the influence of soil unit weight on the results. The upper and lower bound resistance at discrete points down the pile are output, allowing calculation of the average resistance and local bracketing error. In all figures a plotted line represents the average of the lower and upper bound solutions unless otherwise stated. Where a shaded region is present on a graph, this represents the regions between the upper and lower bound solutions unless otherwise stated.

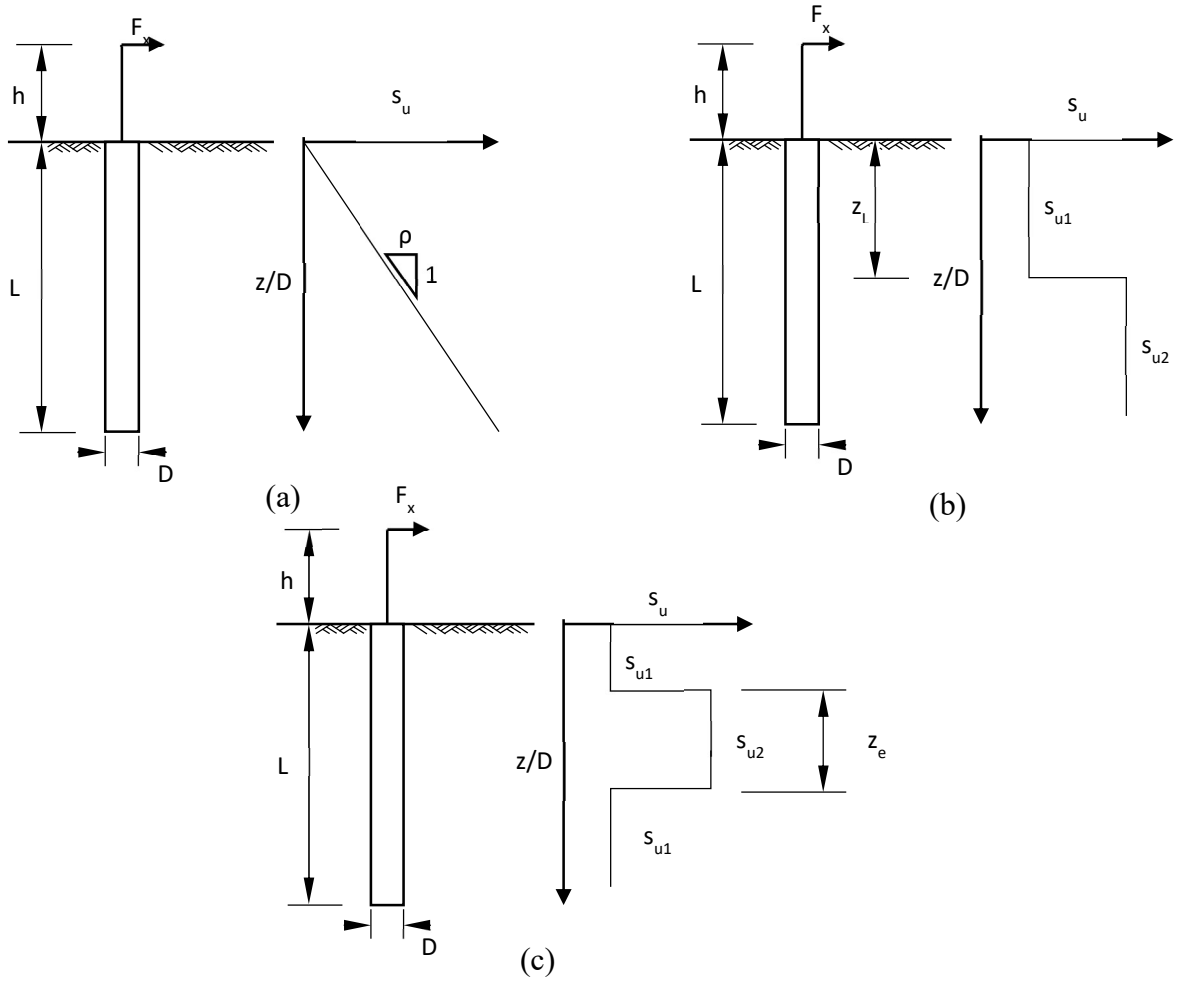

Figure 5.1 - Schematics of assessment cases (a) Linearly increasing strength, (b) abrupt change in strength and (c) embedded layers

Table 5.1 - Dimensionless groups for non-homogeneous study

Dimensionless group	Description	Range
$\frac{\gamma}{\rho}$	Soil strength to weight ratio	[0.1, 10]
$\frac{s_{u2}}{s_{u1}}$	Ratio of soil layer strengths	[0.1, 10]
$\frac{z_L}{D}$	Normalised depth to top of layer boundary	[0.5, 8][1]
$\frac{z_e}{D}$	Normalised thickness of embedded layer	[0.25, 8]

Notes
1. Where required, this ratio is limited to the L/D value for a given case, i.e. $z_L/D < L/D$

The total resistance of a fixed head pile for varying *L/D* is shown on Figure 5.2. Two case of normalisation are shown:

1. Normalisation by the average soil shear strength over the length of the pile, i.e. $s_{u,ave} = 0.5\rho L$ (Figure 5.2(a))
2. Normalisation by the strength gradient (Figure 5.2(b))

Normalising by the average shear strength gives results comparable to those obtained for homogeneous profiles, see the HXTWn modelling in Chapter 4.1, however a drawback of this is that both axes now contain both the length and diameter, making it difficult to use the plot as a design chart. Normalising by the strength gradient removes the length as a component of the y-axis, thus allowing the results to be easily used to assess design pile lengths directly from the plot: i.e. for a known D and ρ the required L to achieve a given F_x can be determined directly from the graph. A drawback of this normalisation approach is that the results for total resistance are not directly comparable to the HXTWn profile results, however for this assessment it is considered that the increased usefulness of the second normalisation approach outweighs the capability to be compared to the homogeneous profile results. Comparison between the two normalisation approaches is performed for the initial case of lateral translation with full tension. However for the subsequent analyses, only results using the strength gradient normalisation will be presented. It should be noted that this only applies to the total resistance results, i.e. F_x and M_y, and comparisons are still made to the homogeneous results for other aspects of the resistance such as the depth of the rotation point and the variation of the lateral bearing factor with depth. As for the HXTWn profiles a simplified total capacity is also shown in Figure 5.2,

i.e. taking a constant $N_p = 10.83$ for $\alpha = 0.5$ (Martin & Randolph, 2006) over the length of the pile. For Figure 5.2(a) this capacity is calculated as

$$\frac{F_x}{s_{u,ave}D^2} = N_p \frac{L}{D} \tag{5.1}$$

Whereas for Figure 5.2(b)

$$\frac{F_x}{\rho D^3} = 0.5\left(\frac{L}{D}\right)^2 N_p \tag{5.2}$$

The results for the first normalisation approach are very similar to those of the homogeneous profiles; this normalisation is effectively the average lateral bearing factor over the length of the pile multiplied by the length to diameter ratio with some variation due to the base resistance. As shown later in Figure 5.3 the lateral bearing factor near surface is less for linearly increasing strength profiles, which would suggest a reduced normalised total capacity for this case however this normalisation approach results in a normalised base resistance twice that of the HXTWn case: i.e. the average shear strength will be half the shear strength at the toe of the pile. This results in an overall response which differs little from the homogeneous case when using this normalisation. The second normalisation approach results in a non-linear relationship between the length to diameter ratio and normalised lateral resistance. This varies from $F_x/\rho D^3 = 10$ at $L/D = 1$ to $F_x/\rho D^3 = 580$ at $L/D = 10$. For both cases presented in Figure 5.2 the simplified estimate of the capacity plots near the lower bound results.

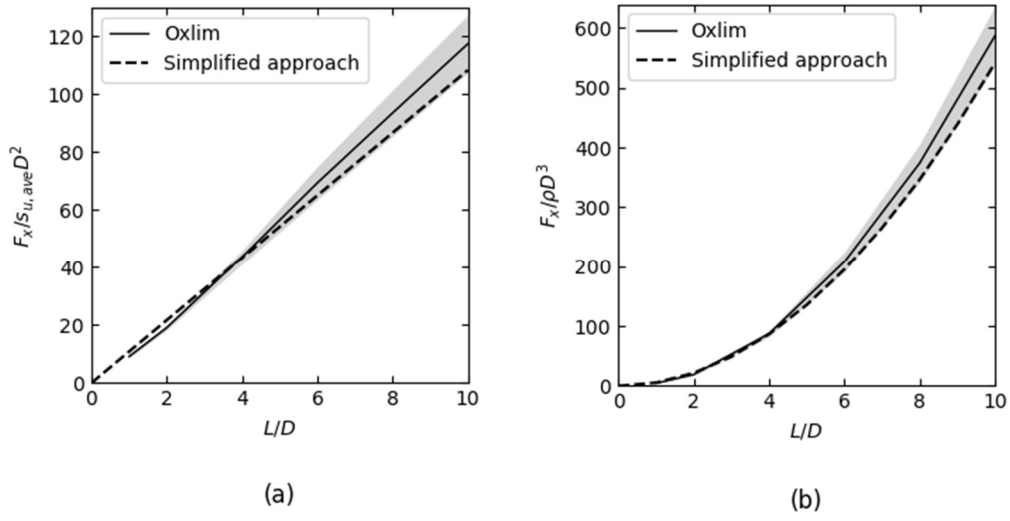

Figure 5.2 - Lateral capacity of a pile in a linearly increasing strength profile with full interface tension, LXTWn, normalising by (a) average shear strength over length of pile and (b) the change of strength with depth

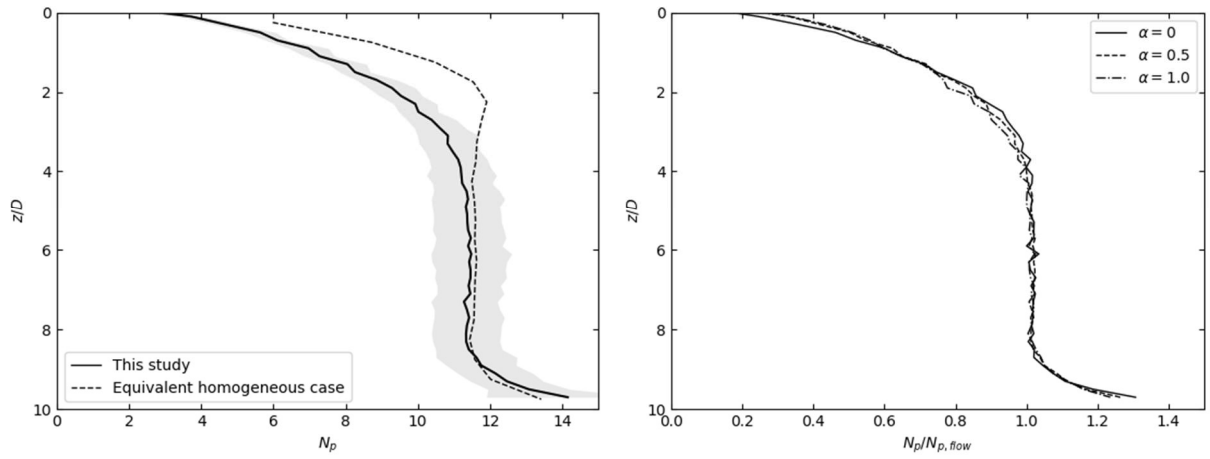

(a) (b)

Figure 5.3 - Lateral bearing factor distribution for pile in LXTWn conditions (a) comparison to equivalent homogeneous case, and (b) effect of varying pile-soil adhesion

This difference between simplified and OxLim arises from the additional resistances that act on the pile; such as the base shearing and distributed moment acting on the pile wall.

Figure 5.3(a) shows the variation of the lateral bearing factor with depth for the L/D = 10. The N_p profile follows the same general form as seen for the HXTWn profiles, shown in Figure 4.1(b): a rapid increase in resistance near the surface in the wedge zone from a surface value of N_p = 3, a constant value with depth in the flow-around zone and then an increase above the flow-around resistance as the toe is approached. The corresponding profile from HXTWn is shown as the black dashed lines. The depth of the wedge is greater for the linearly increasing strength profile with flow-around conditions being reached at $z/D \approx 5$. Figure 5.3 (b) shows the lateral bearing factor profiles obtained for different values of the roughness factor, α. As for the homogeneous profile, varying the pile-soil adhesion has minimal effect on the $N_p/N_{p,flow}$ profile, except at the ground surface where there is a small variation between the three cases assessed: for α = 0.5 and 1.0 the N_p at surface is approximately $0.3N_{p,flow}$ whereas for $\alpha = 0$, $N_p \approx 0.2N_{p,flow}$. Figure 5.3 shows that the increase in lateral bearing factor at the toe of the pile is of the same magnitude as the HXTWn case (see Figure 4.1(d)), suggesting that the increase at the toe is unaffected by use of a linearly increasing strength for this scenario. Figure 5.4 (a) and (b) show

the meshes with contours of velocity from the upper bound analysis for HXTWn and LXTWn respectively. Both meshes have been clipped at the base to show the top z/D = 6 of the models. It can readily be seen that the mobilised mass of soil for linearly increasing strength profiles is larger than the homogeneous case. The soil wedge in Figure 5.4 (b) extends approximately 4 diameters both down and away from the pile.

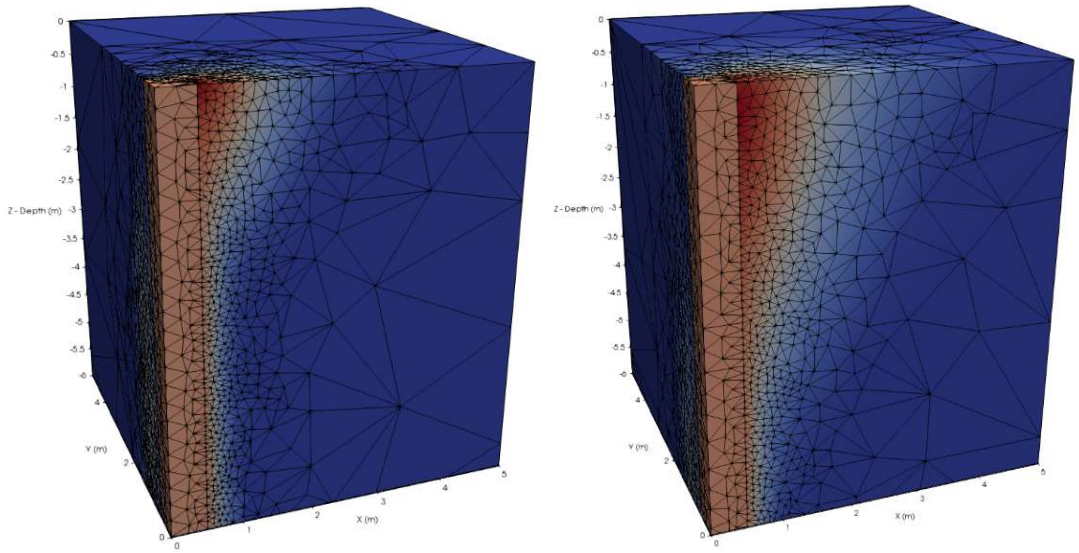

Figure 5.4 - Final meshes for full tension translation modelling of L/D = 10 with contours of velocity for (a) HXTWn and (b) LXTWn

The pile head moment reaction during lateral translation is shown in Figure 5.6. As with the lateral resistance plots, two normalisations are used: the first being normalisation by the average shear strength and the second the strength gradient. Simplified predictions of moment resistance using a constant N_p =10.83 with depth are calculated using

$$M_y = \int_{z=0}^{L} (\rho z N_p D) z dz = \frac{1}{3} \rho L^3 N_p D \tag{5.3}$$

Normalisation of this expression by the average shear strength gives

$$\frac{M_y}{s_{u,ave} D^3} = \frac{1}{3} \frac{\rho L^3 N_p D}{s_{u,ave} D^3} \tag{5.4}$$

Remembering that $s_{u,ave} = 0.5\rho L$, Equation. 5.4 can be simplified to

$$\frac{M_y}{s_{u,ave}D^3} = \frac{1}{3}\frac{\rho L^3 N_p D}{(0.5\rho L)D^3} = \frac{2}{3}\left(\frac{L}{D}\right)^2 N_p \tag{5.5}$$

Normalisation by the strength gradient gives

$$\frac{M_y}{\rho D^4} = \frac{1}{3}\frac{\rho L^3 N_p D}{\rho D^4} = \frac{1}{3}\left(\frac{L}{D}\right)^3 N_p \tag{5.6}$$

5.1.2. Free head pile with full interface tension

For the second stage of the study, fixity against rotation of the rigid pile was removed; i.e. LFTWn conditions. The same modelling conditions as the LXTWn modelling were used with the focus of the results widened to incorporate the effect of the rotation on the response.

Figure 5.5(a) shows the normalised lateral load capacity for various load application heights, h (see Figure 5.1): in this case normalised by ρ. The results show a similar pattern to the HFTWn case: the capacity of a free head pile is significantly lower than that of a fixed head pile, with the capacity decreasing as the load application height increases. The resistances for $h/D = 0$ are approximately 25% of the corresponding fixed head pile results with $F_x/\rho D^3$ decreasing further as h/D increases. Normalised F_x-M_y failure envelopes for L/D = 2, 4, 6, and 8 are shown in Figure 5.5(b).

Figure 5.5(d) shows the depth of the rotation point, z_0. The results indicate that the rotation point occurs deeper than the HFTWn case (see Figure 4.3(e)): most results are around z_0/L = 0.8 compared to $z_0/L \approx 0.6$ for HFTWn. As for HFTWn, the depth of the rotation point converges to a constant value as h/D increase: corresponding to the z_0/L for pure moment loading. The depth of z_0/L for pure moment loading can be approximated using the pile capacity equation,

$$F_x(h + z_0) = \int_{z=0}^{z_0} p_{ult}(z)(z_0 - z)dz - \int_{z=z_0}^{L} p_{ult}(z)(z - z_0)dz \tag{5.7}$$

and finding z_0 such that the two integrals on the RHS of Equation 5.7 are equal: i.e. resulting in

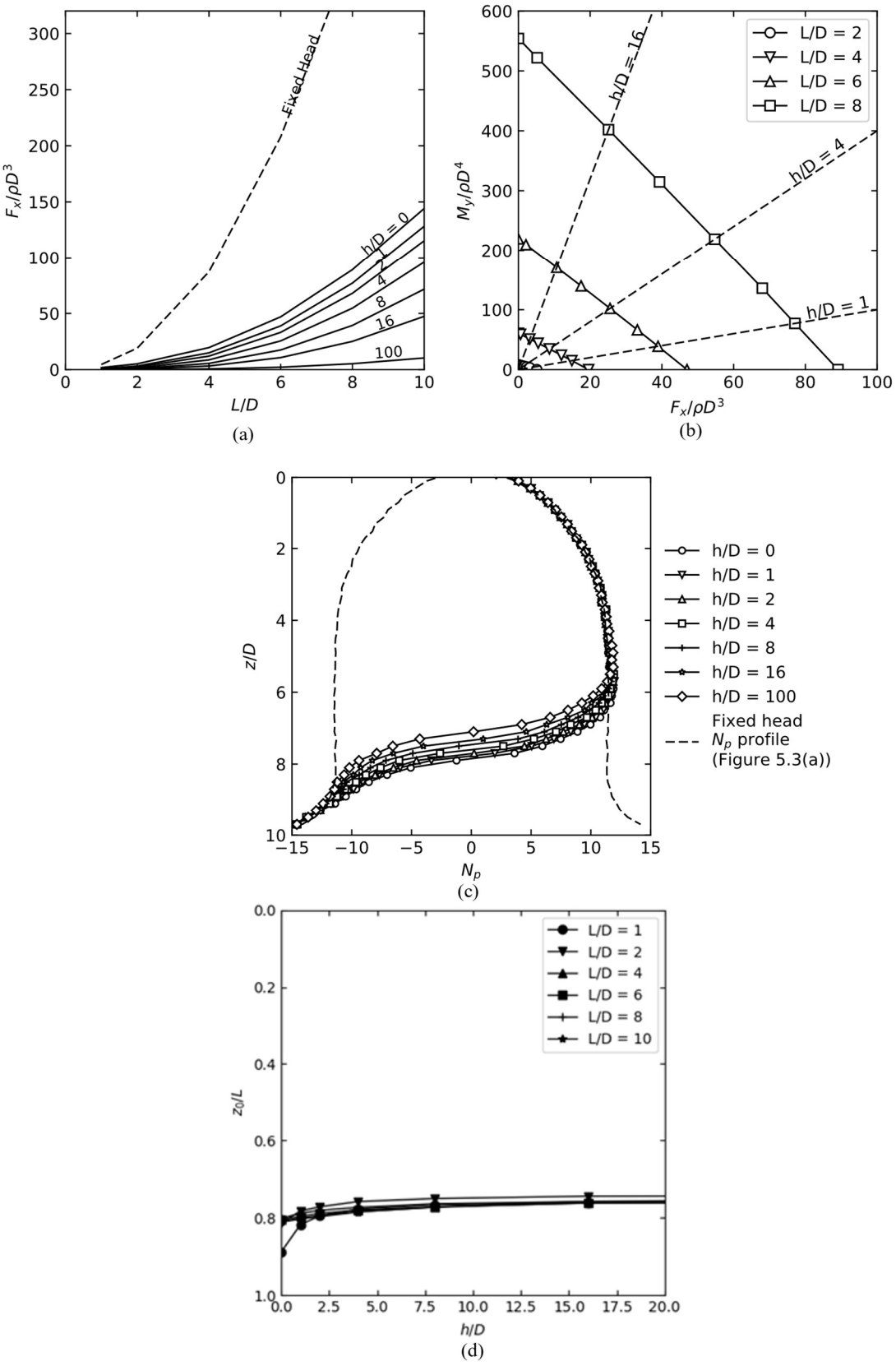

Figure 5.5 – (a) Pile head lateral capacity with varying load application height for LFTWn, (b) Lateral load moment envelope for LFTWn, (c) Distribution of mobilised lateral bearing factor for LFTWn (d) Rotation point depth with load application height for LFTWn

$F_x(h + z_0) = 0$. Assuming a constant N_p over the length of the pile results in the following for homogeneous soils

$$\int_{z=0}^{z_0} N_p s_u D(z_0 - z)dz = \int_{z=z_0}^{L} N_p s_u D(z - z_0)dz \tag{5.8}$$

Solving the integrals on both sides and then rearranging results in

$$\frac{z_0}{L} = \frac{2}{3} \tag{5.9}$$

As stated the values of z_0/L shown in Equation 5.9 correspond to the simplified case of a constant N_p with depth. Considering the lower N_p near surface and other factors that affect pile resistance, such as the shearing along the base of the pile, will result in z_0/L varying from these simple estimates. However, they still provide a useful indication of the potential shallowest depth that the rotation point will occur at.

The variation of N_p with depth for L/D = 10 and various h/D is shown in Figure 5.5(c). The results show a similar trend to HFTWn, Figure 4.3(f), with the N_p variations at the top and bottom of the pile matching the bearing factor profile of the translation case, and the transition around the rotation point occurring over approximately 3D. The increased depth of the rotation point in all cases means that the flow-around mechanism is not achieved again below the rotation point, with instead the mobilised resistance going straight from the transition zone to the toe kick zone.

5.1.3. Translating pile with no interface tension in weightless soil

For the third stage of the study the limiting interface tension between the pile and the soil is set to zero, i.e. LXNWn conditions. This permits gapping to occur between the pile and soil if this leads to a lower collapse load. As gapping can now occur, the unit weight of the soil will now affect the capacity calculation. As was done for HXNWn, the soil unit weight in this stage is taken as zero to establish the limiting lower resistances that can occur. To include account for

gapping, and hence the different soil behaviour in front of and behind the pile, a half model is now used.

Figure 5.7 shows the lateral capacity of a translating pile under these conditions when normalised by $s_{u,ave}$ and ρ respectively. The results from the corresponding analysis with full interface tension (Section 5.2.1) are also shown on the plots as dashed lines. As expected, the use of no tension and weightless soil causes a reduction in the available capacity with a 10% reduction at L/D = 1 and up to a 33% reduction at L/D = 10. This reduction is similar in magnitude to that observed for HXNWn (Section 4.3.2, Figure 4.5(a)).

As seen in the HXNWn analyses, Figure 4.5(b), the increase of N_p with depth is significantly lower for no interface tension, weightless soil than for full interface tension; this is shown in Figure 5.8. A distinitive feature of the weightless profile is that even at L/D = 10 the resistance has not yet approached the limiting case of the flow-around mechanism, i.e. N_p = 10.83 for the α = 0.5 used in the analysis. Rough extrapolation from the graph suggests that the wedge mechanism could extend to L/D = 14: i.e. far below the depth of interest for rigid piles. It should be noted however that modelling weightless soil is not a practical design case but provides a useful indication of minimum values of N_p that should occur over the length of a pile. As with the HXNWn profile, Figure 4.5(b), the surface resistance with no interface tension is approximately 50% that with full interface tension. However, the values of N_p at the surface appear lower for the linearly increasing strength scenario, with the no-tension, Figure 5.8, and full tension, Figure 5.3(a), cases having surface lateral bearing factors of approximately 2 and 3 respectively.

Finally for this stage of the study, The pile head moment reaction during lateral translation is shown in Figure 5.9 for both the average shear strength and strength gradient normalisations. The corresponding results from the full tension analysis, from Figure 5.2, are also shown. As with the lateral capacity, Figure 5.7, the restraining moment reaction is reduced by a similar magnitude to that observed in the homogeneous cases, i.e. approximately 30%.

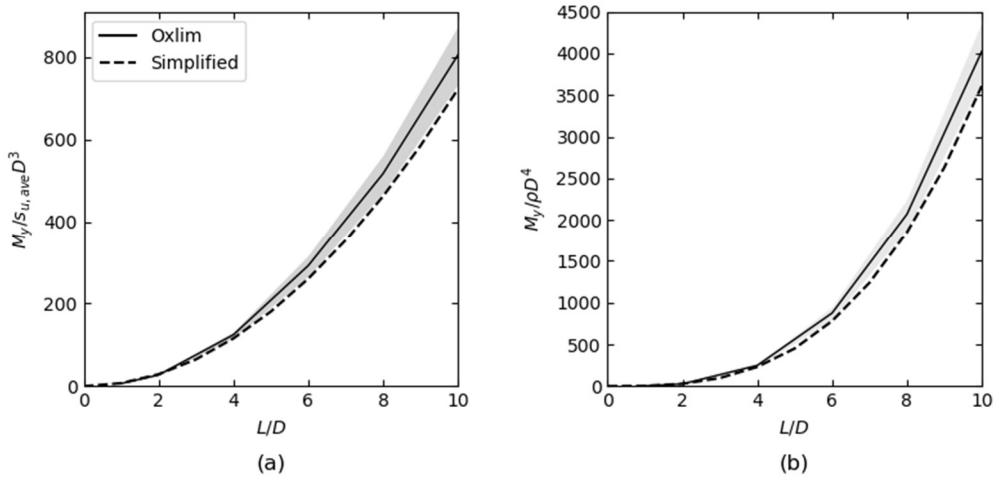

Figure 5.6 - Moment restraint required for LXTWn conditions. Normalised by (a) average shear strength over length of pile and (b) change of strength with depth

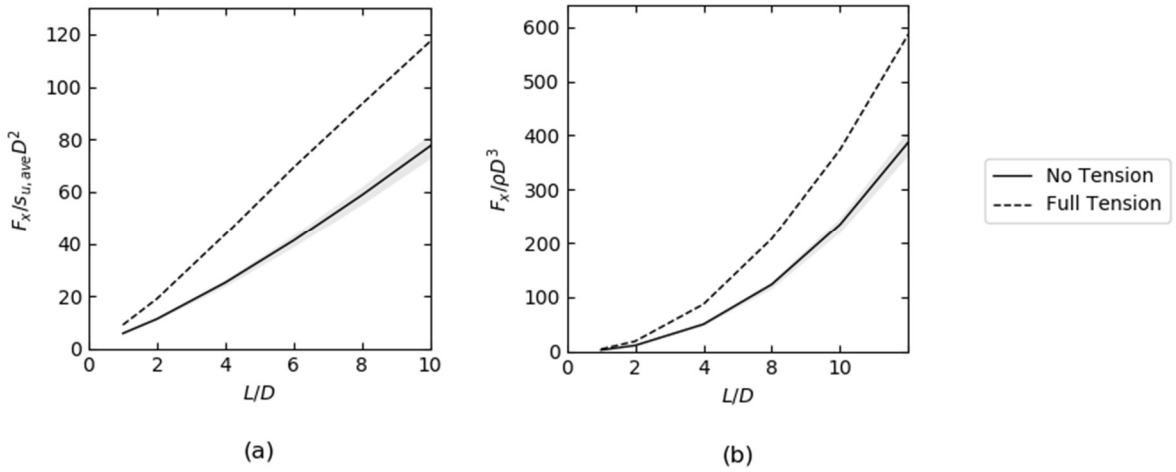

Figure 5.7 - Lateral capacity for LXNWn normalising by (a) average shear strength over length of pile and (b) the change of strength with depth

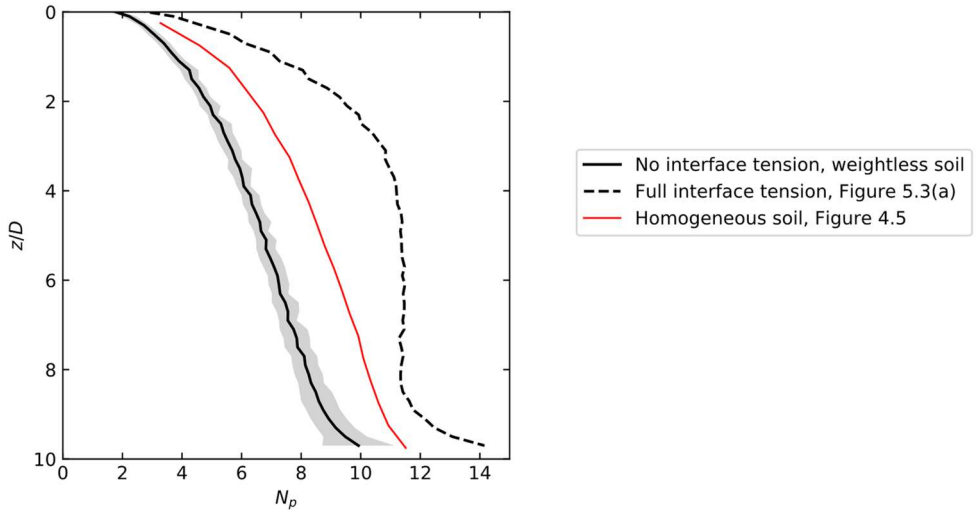

Figure 5.8 - Lateral bearing factor profile for LXNWn

5.1.4. Free head pile with no interface tension in weightless soil

The fourth stage of the study uses the same parameters as the previous stage but with the constraint against rotation removed; i.e. LFNWn conditions. As before, a half model is used with no tension to permit separation to occur at the pile-soil interface. Figure 5.10(a) shows the lateral capacity obtained with these conditions for varying load application heights. The capacity from the fixed head case, from Figure 5.7, is shown for comparison. As with the LFTWn scenario, Figure 5.5 (b), the fixed head capacity is significantly higher than the free head capacity. The capacity of LFNWn is lower than that obtained when full interface tension is used. Normalized F_x-M_y failure envelopes for different L/D values in weightless soil with no interface tension are shown in Figure 5.10(b).

The rotation point depths for these conditions are shown in Figure 5.10(d). The rotation point typically occurs at z_0/L = 0.8; slightly lower than observed in the full tension modelling, Figure 5.5(d). This is due to the significant reduction in the lateral bearing factor over the length of the pile, as shown in Figure 5.8. This causes more of the lateral resistance to be mobilised near the toe of the pile thus increasing the depth that the rotation point occurs across all values of h/D.

The distribution of the lateral bearing factor is shown in Figure 5.10(c), follows the same pattern as previous cases. The resistance in the upper part of the pile follows the profile of N_p obtained

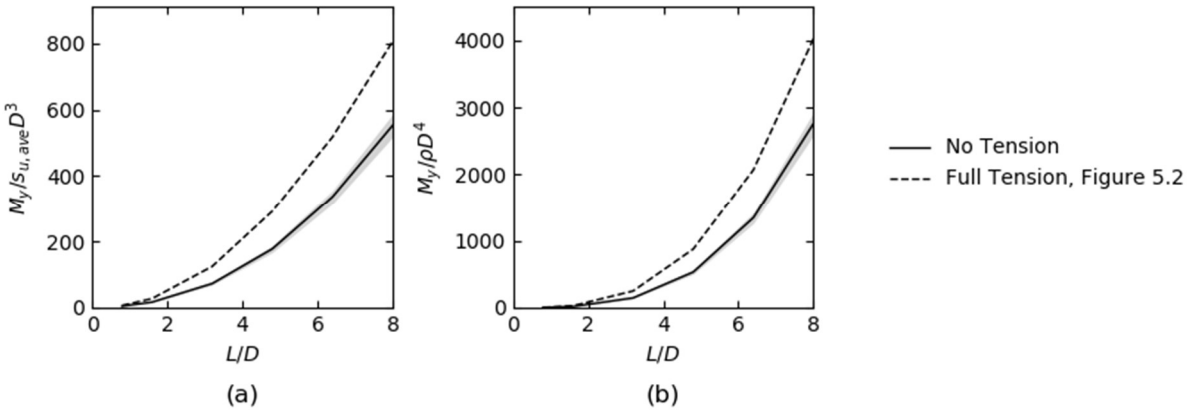

Figure 5.9 - Moment restraint required for LXNWn conditions. Normalised by (a) average shear strength over length of pile and (b) change of strength with depth

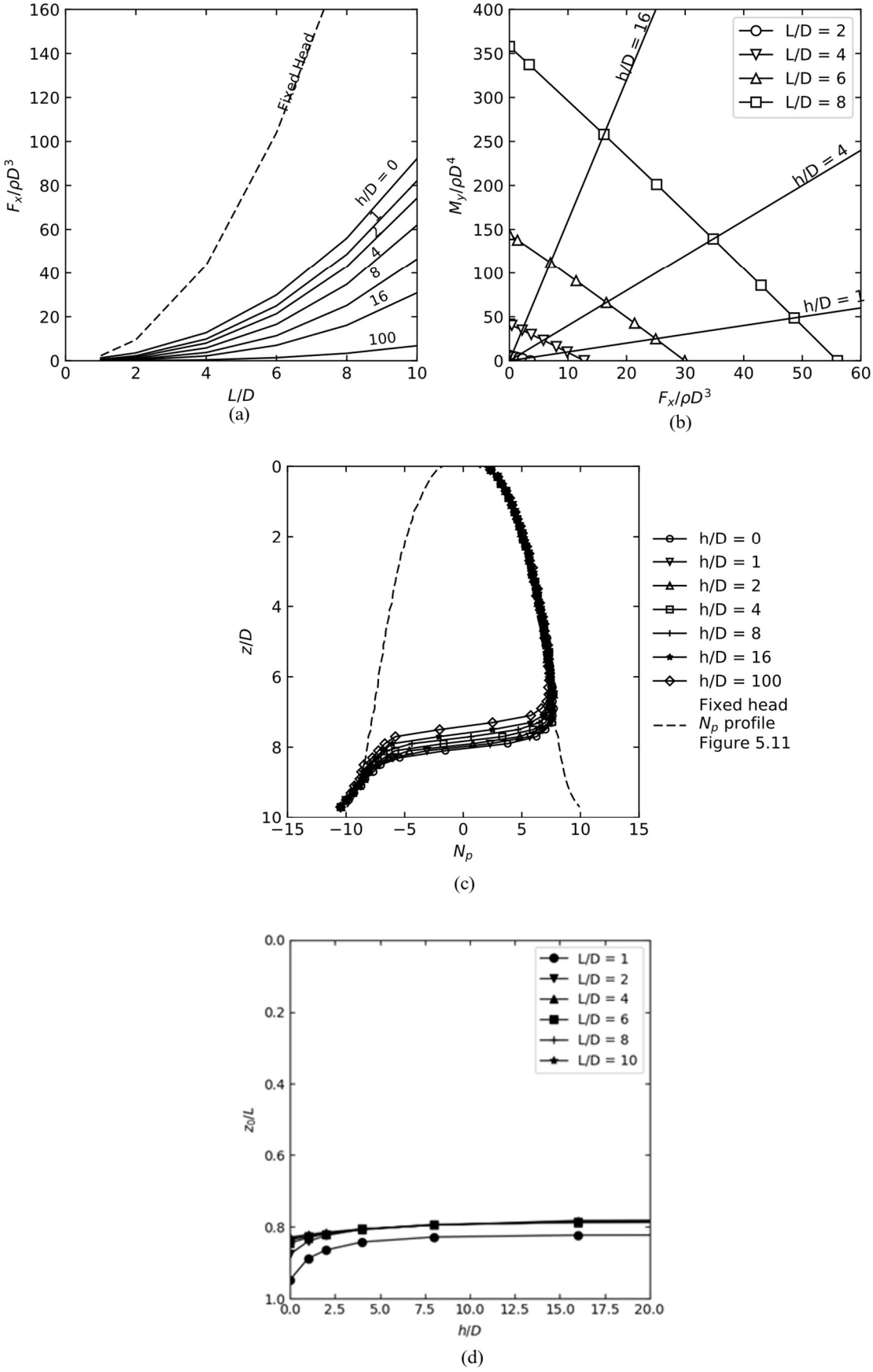

Figure 5.10 - (a) Pile head lateral capacity with varying load application height for LFNWn (b) Lateral load moment envelope for LFNWn (c) Rotation point depth for LFNWn (d) Distribution of mobilised lateral bearing factor for LFNWn

from the corresponding translation modelling, i.e. LXNWn from Figure 5.8. The resistance then transitions from the front to the back of the pile over a depth of approximately 3*D* before following the profile from the translation case down to the toe of the pile. As with the LFTWn case, Figure 5.5 (c), the spread of rotation points depths is approximately 0.6*D* with little variation between the lower values: i.e. h/D = 0, 1, 2, and 4.

5.1.5. Translating pile with no interface tension and varying γ/ρ

This section considers the influence of varying the dimensionless group γ/ρ on the pile response when the pile head is fixed against rotation, i.e. LXNWi. To perform this the unit weight of the soil is set to 1kN/m^3 and ρ has been varied in the range of 0.2 to 5kPa/m: thus giving a range of γ/ρ = 0.2 to 5.

The lateral resistance in these conditions is shown in Figure 5.11. The results from both the LXTWn modelling, from Figure 5.2, and the LXNWn modelling, Figure 5.7, are shown for comparison. As was observed for the homogeneous cases where $\gamma D/s_u$ was varied, see Figure 4.9(a), the result is a set of curves that plot between the full tension case and the no tension weightless case. Figure 5.11 shows that low values of γ/ρ lead to a response close to the LXNWn case, while high values approach the LXTWn case. The latter occurs as the higher ratio of soil weight to strength leads to partial gapping occurring as the soil slumps onto the back face of the pile. This leads to the conditions required for flow-around failure occurring at a shallower depth than the weightless case. As was observed for HXNWi in Figure 4.9(b), this suggests the conditions of full interface tension, and zero interface tension in weightless soil form upper and lower limits to the resistance respectively. The moment reactions developed in these analyses are shown in Figure 5.12. Again it is seen that as γ/ρ varies the moment reactions vary between the LXTWn and the LXNWn cases. The profiles of lateral bearing factor for varying γ/ρ are shown in Figure 5.13. The lower values of γ/ρ show similar results to the LXNWn case. It is interesting to note that quite a high ratio of γ/ρ is required to achieve a similar profile to LXTWn.

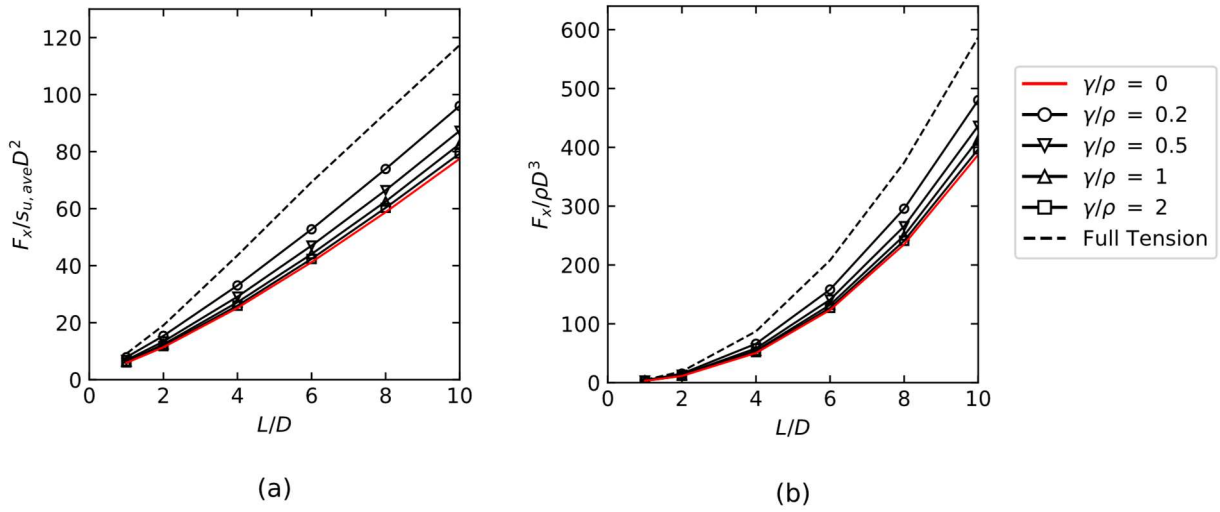

Figure 5.11 - Lateral capacity LXNWi normalising by (a) average shear strength over length of pile and (b) the change of strength with depth

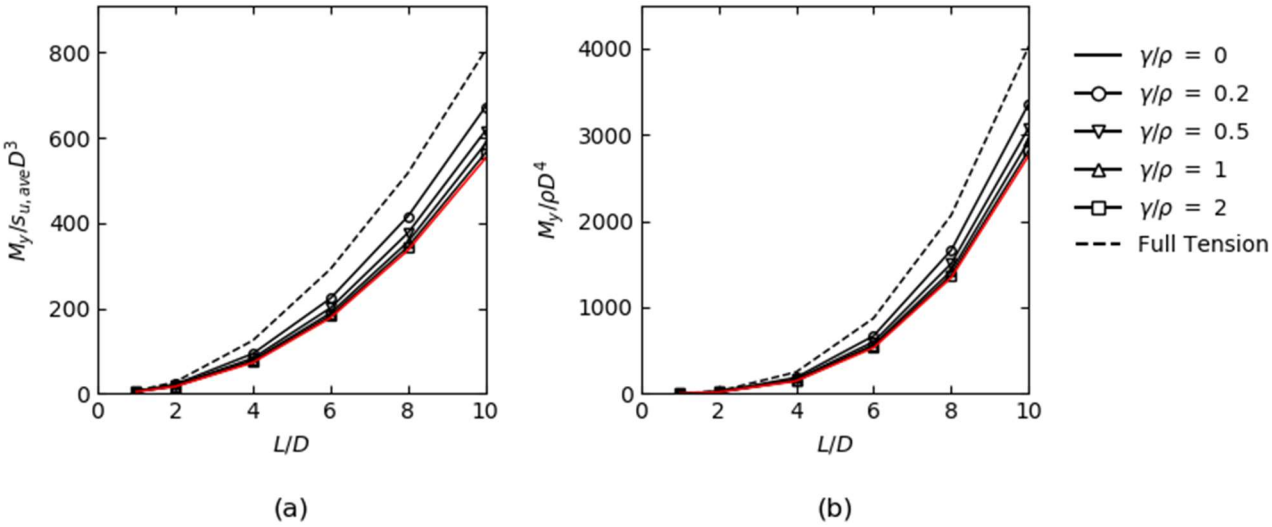

Figure 5.12 - Moment restraint for LXNWi normalised by (a) average shear strength over length of pile and (b) change of strength

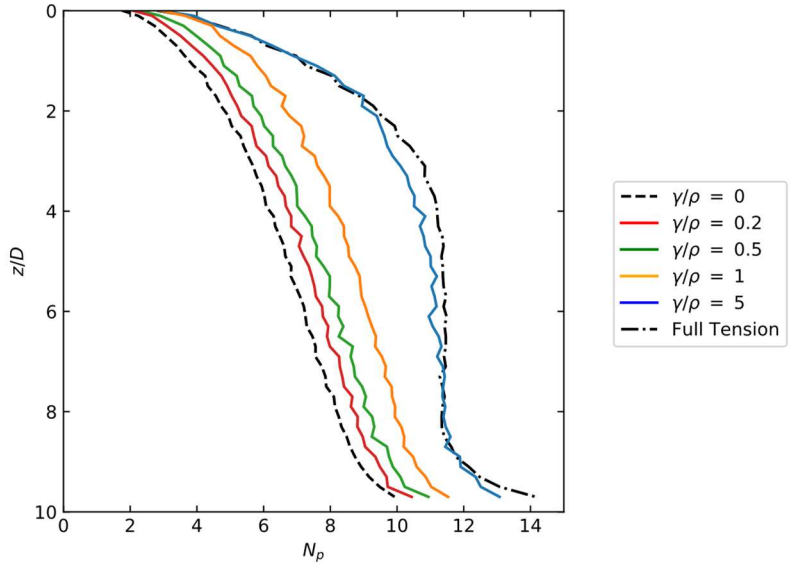

Figure 5.13 - Lateral bearing factor profile for LXNWi

In offshore practice a ratio $\gamma/\rho = 5$, corresponding to a submerged unit weight of 10kN/m^3 and strength gradient of 2kPa, would likely be the highest encountered.

5.1.6. Free head pile with no interface tension and varying γ/ρ

In this section the restraint against pile head rotation is removed and the effect of varying γ/ρ on the response of a pile with no interface tension is investigated; i.e. LFNWi conditions. Figure 5.14 shows the normalised lateral resistance for varying load application heights across four ratios of γ/ρ. As with the LXNWi case (see Figure 5.11) the results in Figure 5.14 are bounded by the full interface tension, LFTWi, and no interface tension, LFNWn, cases as upper and lower limits respectively: these limits are shown on the figure for $h/D = 0$. Each case of γ/ρ gives a variation across the various h/D ratios that can be considered typical across all of the cases reviewed. Similar variation between these upper and lower limits can be seen for the normalised F_x-M_y envelopes, shown in Figure 5.15. The variation of F_x/s_uD with γ/ρ is shown more clearly in Figure 5.16 for a pile with L/D = 10. From this, most of the variation in resistance occurs between approximately $\gamma/\rho = 0.5$ to 5. The lateral resistances for γ/ρ values outside this range are very close to the LFNWn and LFTWn cases.

Figure 5.17 shows the rotation point depth for $\gamma/\rho = 0.2$, 0.5, 1, and 2 and various values of L/D and h/D. The variation of γ/ρ causes very little variation in the rotation point depth except for $L/D = 1$. For $L/D = 1$, the depth varies between the LFNWn (Figure 5.5(a)) and the LFTWn cases (Figure 5.10(a)). The failure mechanisms from various cases of this study are shown in Figure 5.19. From this it becomes more apparent as to why the rotation point depths from the $L/D = 1$ analyses differ from the other L/D ratios. Figure 5.19(a), (b), and (c) show the meshes from $L/D = 1$ for LFTWn, LFNWi with $\gamma/\rho = 1$, and LFNWn (i.e. $\gamma/\rho = 0$). Similarly, Figure 5.19 (d) and (e) show the LFTWn and LFNWn for $L/D = 2$ respectively. Each of the cases for $L/D = 1$ show that there is no rotation of the body of soil exterior to the pile; as opposed to the rotating block of soil that can be seen to form in the $L/D = 2$ (and greater) cases. For $L/D = 1$ a failure surface is extending into the pile; as opposed to occurring at the base of the pile.

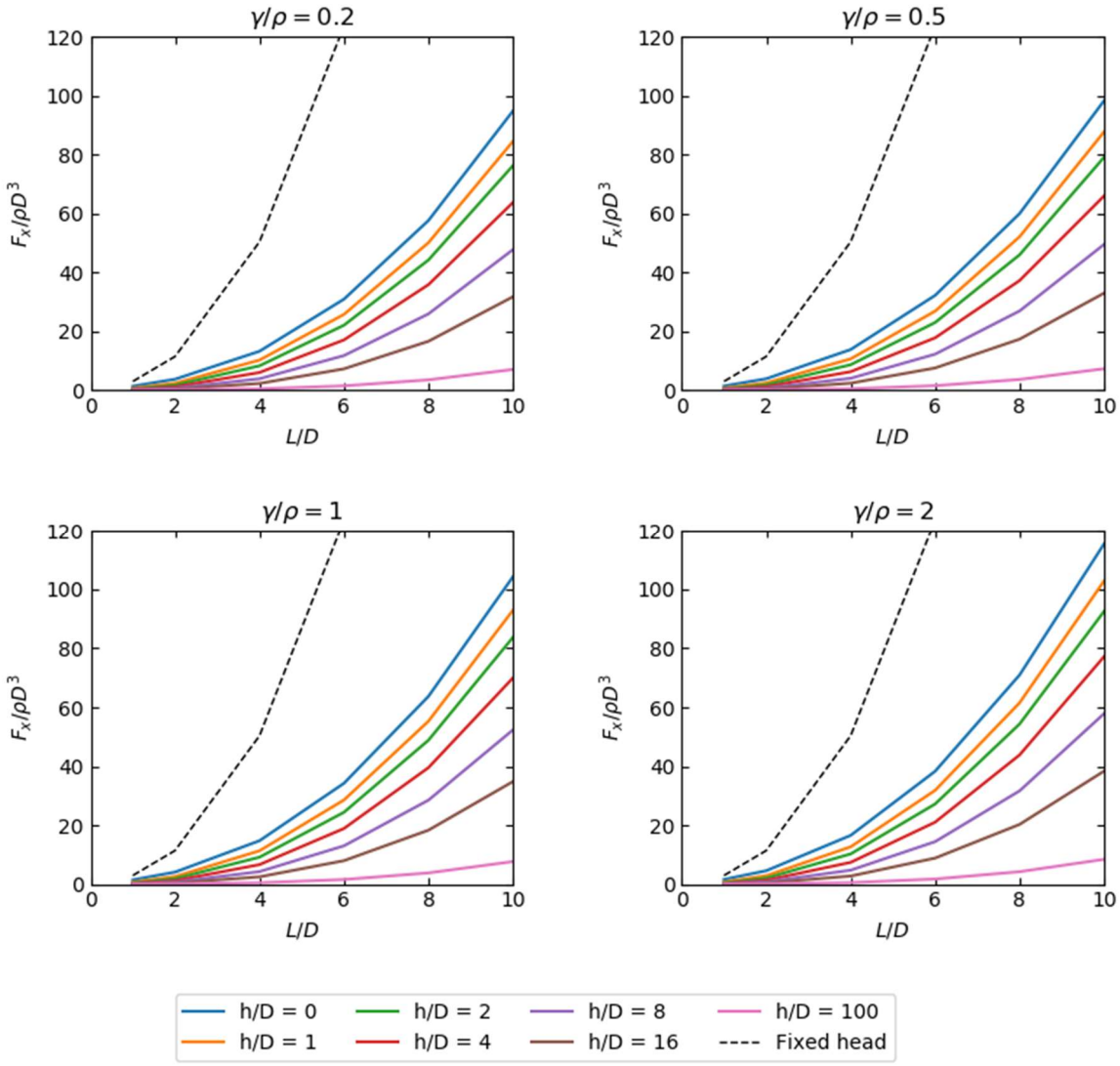

Figure 5.14- Pile head lateral capacity with varying load application height for LFNWi

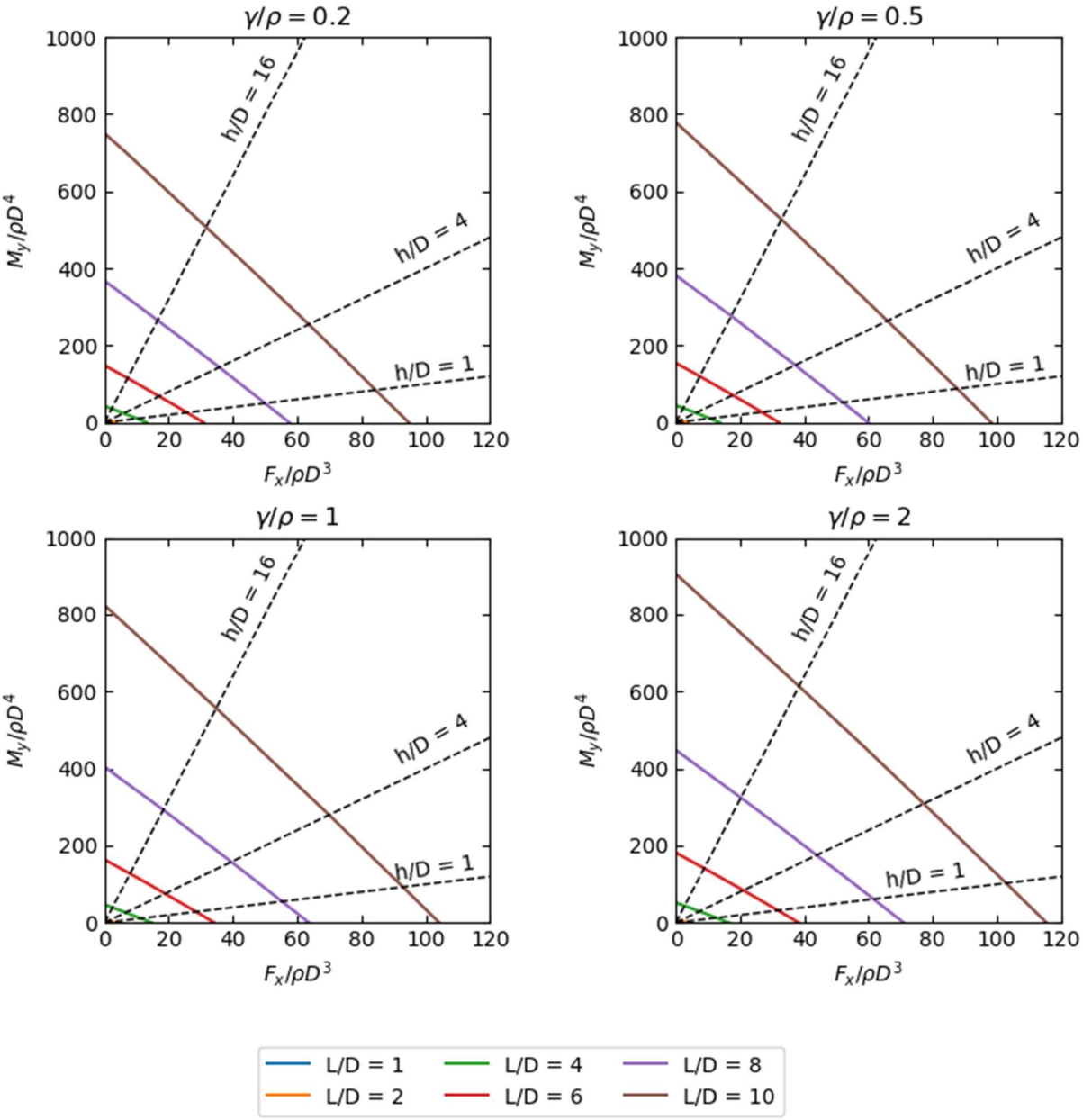

Figure 5.15 - Lateral load moment envelope for LFNWi

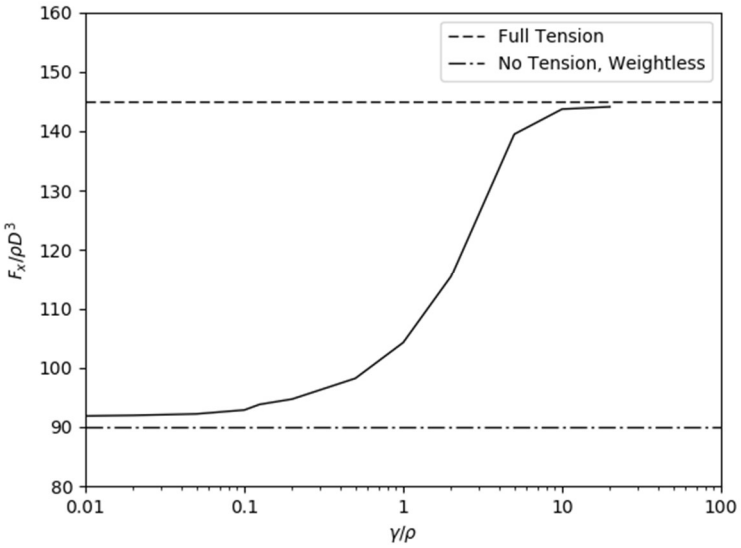

Figure 5.16 - Variation of $F_x/\rho D^3$ with γ/ρ for free head pile with no interface tension for L/D = 10

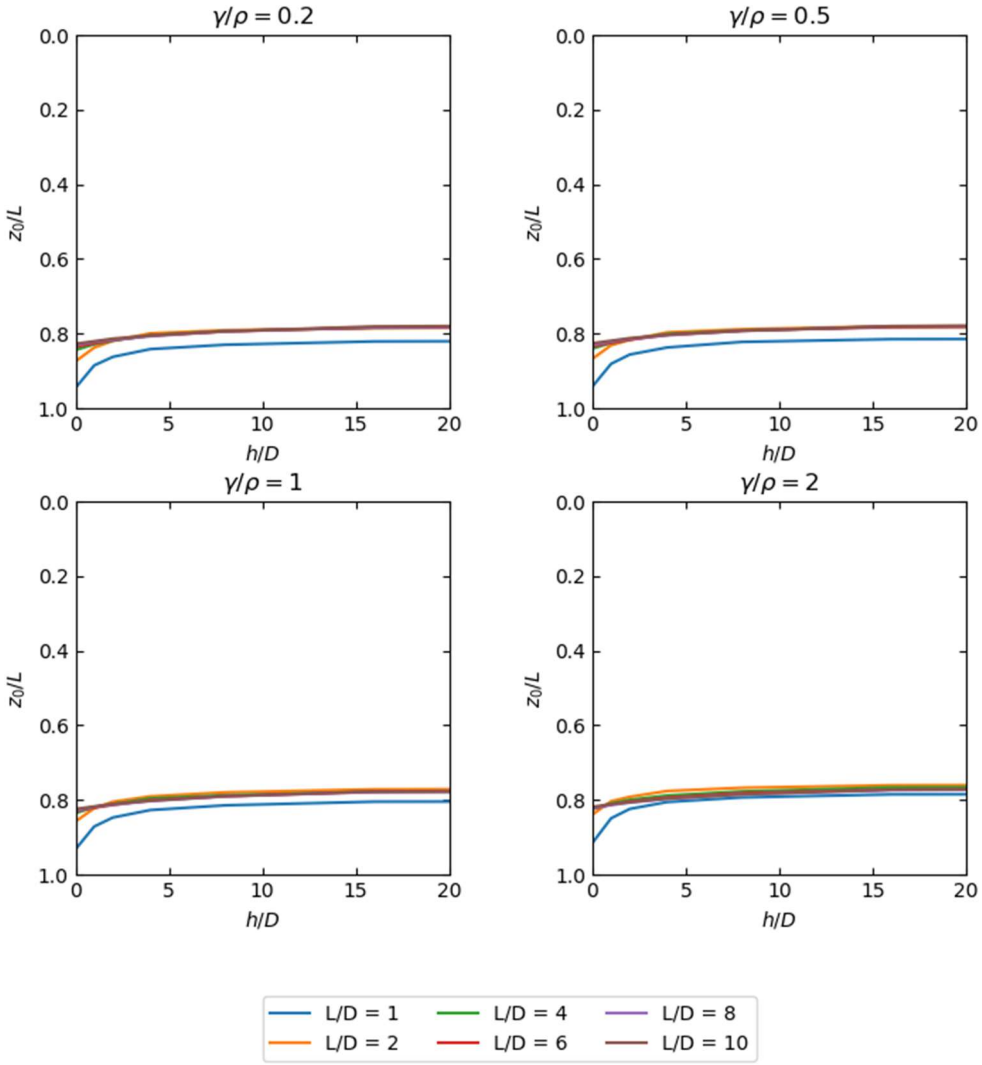

Figure 5.17 - Rotation point depth for LFNWi

The profiles of lateral bearing factor for L/D = 10 and the conditions used in this section are shown in Figure 5.18. The variation of γ/ρ causes no variation of the expected pattern of the mobilised resistance conforming to the N_p profile obtained from the translation case except for the transition zone that occurs around the rotation point of the pile. As with all the other cases, the transition occurs over a depth of approximately 3D centred around the rotation point depth.

5.1.7. Comparison to methods in literature

In this section comparison of N_p profiles obtained from OxLim are made to the three selected literature methods: Matlock (1970), Murff and Hamilton (1993), and Jeanjean et al. (2017). The results from this comparison are shown in Figure 5.20. The comparison has been made using the N_p profiles obtained with the fixed head pile, for the cases of LXTWn and LXNWn, alongside four of the intermediate cases: LXNWi with γ/ρ = 0.2, 0.5, 1, 2. The same set of assumptions have been used in this comparison as for the corresponding homogeneous comparison; these assumptions are outlined in Section 4.2.7. In each case the Matlock approach under-predicts the resistance; however the under-prediction is less than that observed with a homogeneous strength profile; shown in Figure 4.15. This is likely due to the Matlock approach being derived from pile load tests in clay with a similar profile to the linear strength increase being modelled here. It should again be noted that the Matlock approach, and the subsequent recommendations in design standards, assumes a maximum lateral bearing factor of N_p = 9, i.e. smooth pile conditions. Assuming a limiting N_p of 11.5, as has been done for the other methods would lead to a closer match between the OxLim and Matlock results. However, the Matlock approach does predict a linear increase in bearing factor with depth whereas the OxLim results indicate that N_p will have a non-linear change with depth.

In each case the Murff and Hamilton approach overpredicts the resistance, sometimes significantly. For example in the γ/ρ = 1 case, the Murff and Hamilton approach predicts a lateral bearing factor of N_p = 10 will be achieved at around z/D = 4. The OxLim results indicate

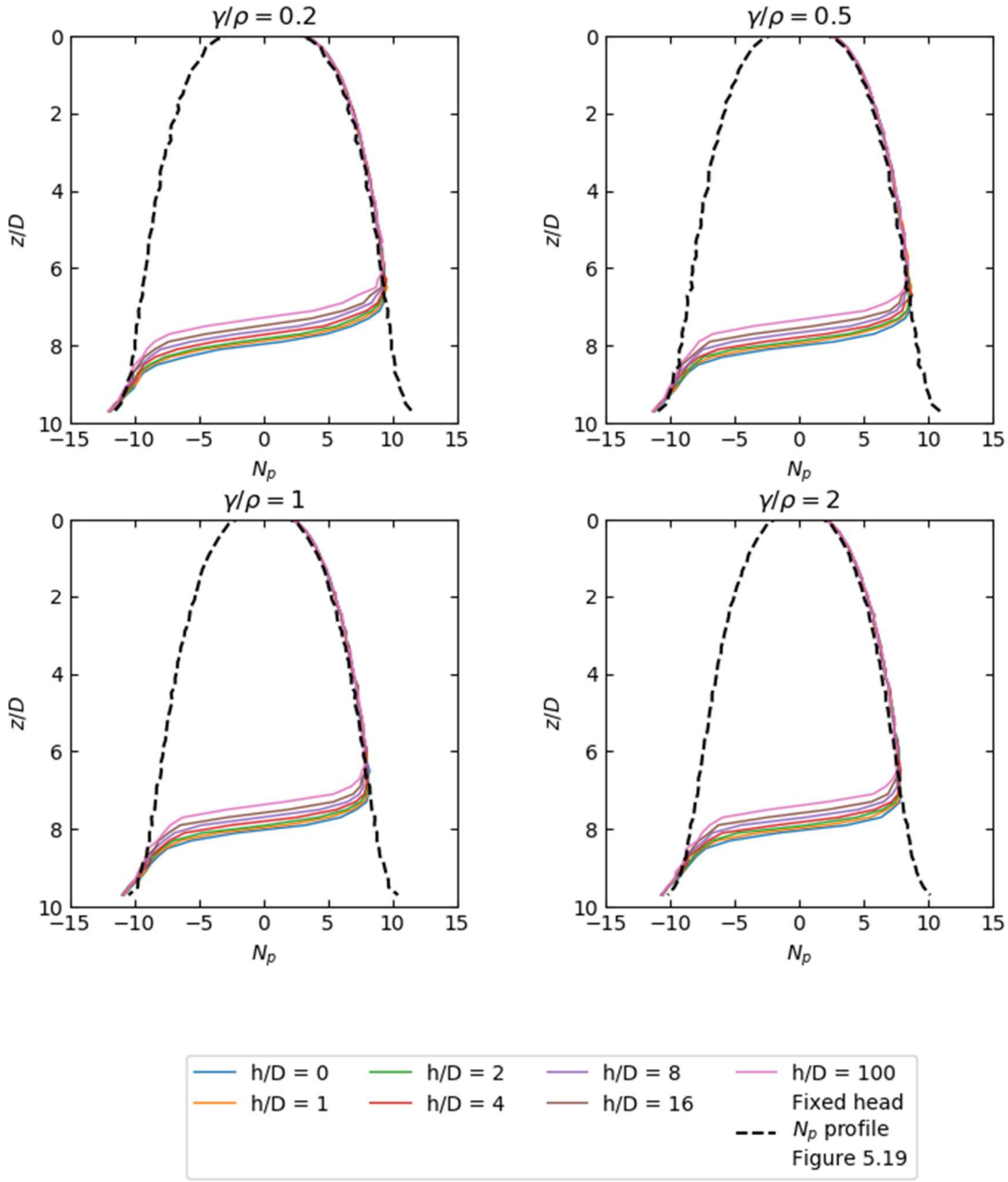

Figure 5.18 - Distribution of mobilised lateral bearing factor for LFNWn

a bearing factor of N_p = 7.5 at this depth indicating that the Murff and Hamilton approach gives a 33% over-prediction of resistance. The Murff and Hamilton approach also predicts the flow-around mechanism to occur at a shallower depth than indicated by the OxLim analysis; for γ/ρ = 1 and 2 the Murff and Hamilton approach predicts the flow-around mechanism to be achieved at z/D = 8.5 and 5.5 respectively. In both these cases the OxLim analysis indicates that the flow-around resistance is not achieved by z/D = 10.

The Jeanjean approach gives a slight over-prediction in every case although the profile shows a good overall match to the shape of the predicted resistance. This occurs from the way the Jeanjean approach is formulated. When the surface shear strength, s_{u0}, is zero or close to zero, as has been modelled here, the formulation used for the Jeanjean approach has a jump in resistance. For s_{u0} = 0kPa the second component in the N_p formulation from Jeanjean, $\gamma z/(s_{u0} + z\rho)$, reduces to γ/ρ. This leads to $N_p = N_{p0}$ at $z = 0$ and $N_p = N_{p0} + \gamma/\rho$ when $z \neq 0$. A second factor to consider is that the Jeanjean approach assumes a set value of the resistance at surface whereas the OxLim results appear to indicate that the resistance at the surface varies with γ/ρ. As the Jeanjean approach is formulated as a variation between upper and lower values of resistance, N_1 and N_2 respectively, starting with a higher surface resistance will lead to a subsequent over-prediction at all depths assuming the same higher value of resistance in both cases, e.g. N_1 equal to the bearing factor for the flow-around mechanisms from OxLim.

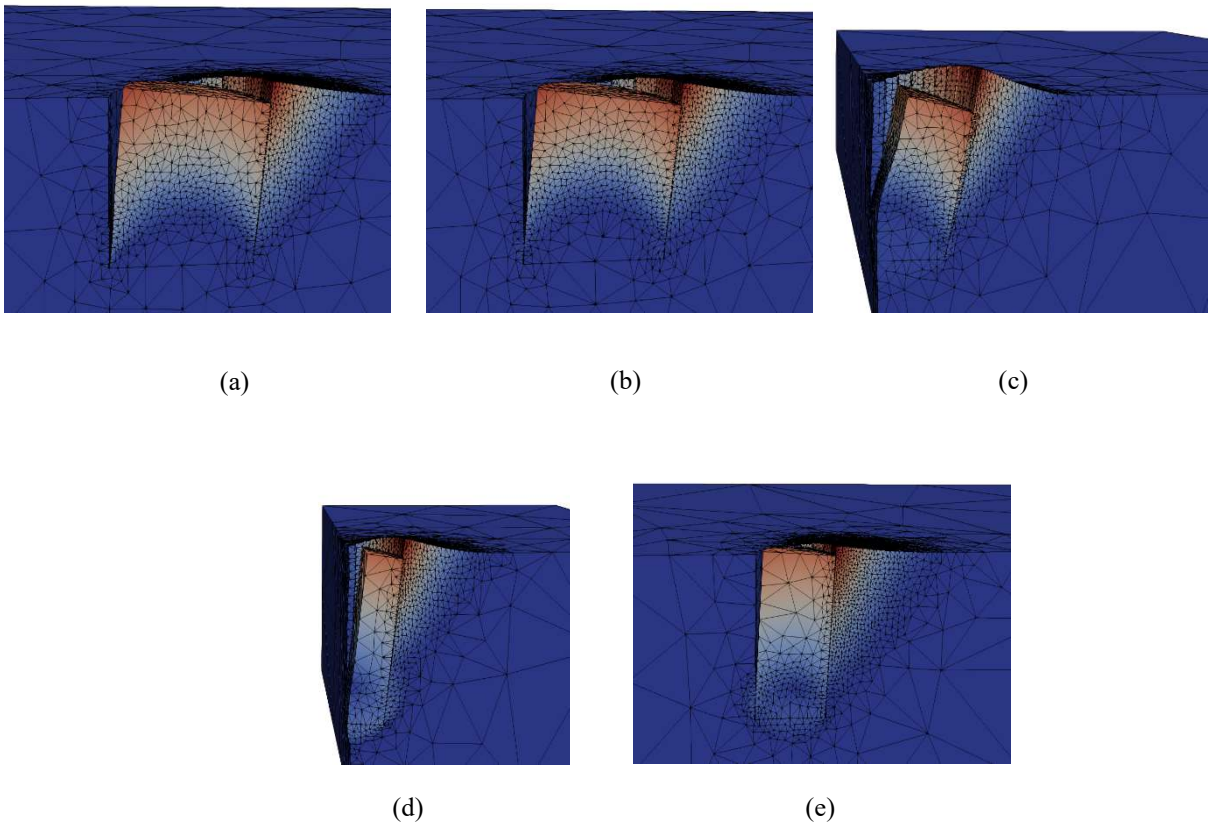

Figure 5.19 - Final deformed meshes of free head piles for (a) LFNWn, γ/ρ = 0, L/D = 1 (b) LFNWi, *γ/ρ* = 1, *L/D* = 1, (c) LFTWn, *L/D* = 1, (d) LFTWn, *L/D* = 2, (e) LFNWn, *L/D* =2, *γ/ρ* = 0

5.1.8. Lateral resistance profile for generalised strength profiles

The work so far has only considered idealised profiles where only either a surface strength or a strength gradient is present. This is suitable for understanding the underlying mechanisms and obtainable resistances within the framework of dimensionless groups outlined in Table 4.1 and Table 5.1 however this does not provide a full indication of the response expected when both surface strength and a strength gradient are present. Having both surface strength and a strength gradient introduces a new dimensionless group $\frac{s_{u0}}{\rho D}$; i.e. λ in the Jeanjean et al. (2017) approach for estimating N_p. A full investigation of the impact of λ on the total response, as has been performed for homogeneous and simple strength gradient conditions, has not been performed.

However, it is important to understand the influence of this dimensionless group and establish whether the existing literature methods for predicting resistance can be improved upon. To do this the Jeanjean (2017) equation N_{p0} has been modified into a parameterised form

$$N_p = N_{p0} + \frac{\gamma z}{s_{u0} + \rho z} \tag{5.10}$$

$$N_{p0} = N_1 - N_2 \left(1 - \left(\frac{z}{dD}\right)^{x_1}\right)^{x_2} \tag{5.11}$$

with

$$d = x_3 - x_4 \log(\lambda) \tag{5.12}$$

The pile soil adhesion component of the Jeanjean et al. (2017) equation has been removed as well. In its place the value of N_2, the lateral bearing factor at the ground surface, has been calculated using

$$N_2 = 1.8 + 2.36\alpha \tag{5.13}$$

This derivation of this relationship is shown in Chapter 6.1. using the relationship for a simple strength gradient; i.e. $\rho \neq 0$kPa/m. In this form, Equation 5.11 could be used in an optimisation

algorithm to find a fit for Oxlim obtained resistance; i.e. with x_1, x_2, x_3, and x_4 as independent variables and an error function, given in Equation 5.14, showing the difference between an OxLim obtained N_p profile and Equation 5.11. Performing a fit to a single model is not particularly useful as the values of x_1 to x_4 will only be appropriate to that particular model. In order to find the appropriate value of the independent variables, the optimisation process needs to be performed across multiple model results. This is achieved by using the objective function, given in Equation 5.15., which the optimisation algorithm will minimise to find the optimal values of x_1 to x_4. The number of models compared to also needs to be sufficiently large along with models performed across a suitable range of parameters to give confidence that the values of x_1 to x_4 are appropriate in all cases. Such an exercise is made possible by the speed that OxLim can resolve plastic collapse loads; an equivalent study using traditional displacement FEA would either take too long or would have to compromise on the number of analyses run which potentially reduces the reliability of the optimisation results. This exercise has been performed using the results from 1,000 OxLim analyses using the parameter space shown in Table 5.2 and the Sequential Least Squares Programming (SLSQP) algorithm in the Scipy Python library. The error and objective functions shown in Equation 5.14 and Equation 5.15 respectively were found to provide reliable results when using with the SLSQP algorithm.

$$W_i = \frac{1}{L}\sum_{z=0}^{L}\left(N_{p,z} - O_z\right)^2 \tag{5.14}$$

$$W_{glob} = \frac{1}{N}\sum_{i=1}^{N} W_i \tag{5.15}$$

Table 5.2 - Parameter space used for optimisation exercise

Parameter	Minimum	Maximum
Surface Shear Strength, s_u	1	50
Strength Gradient, ρ	1	20
Unit Weight, γ	1	20
Pile-soil adhesion, α	0	1
Diameter, D	0.3	6

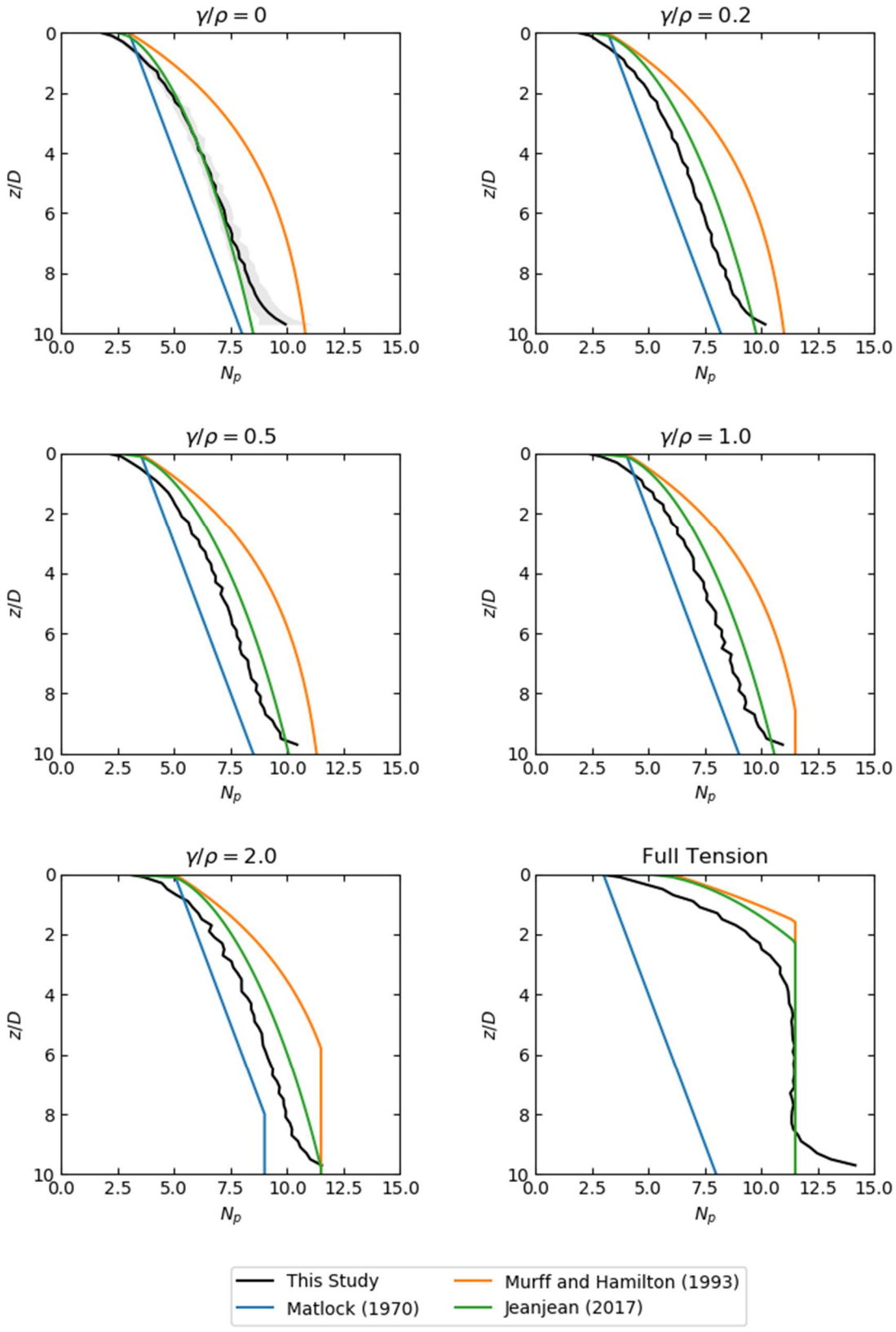

Figure 5.20 - Comparison of OxLim obtained N_p profiles for linearly increasing strength with depth strength to N_p prediction methods in literature: Matlock (1970), Murff and Hamilton (1993), and Jeanjean et al. (2017)

Where W_i is the error for each OxLim model, $N_{p,z}$ is the value of N_p at depth z from Equation 5.10, O_z is the OxLim obtained result at depth z, and N is the number of OxLim models used in the optimisation. The half model of a translating pile has been used to obtain the OxLim results for this study, as such the results obtained from OxLim will include the increase in resistance near the pile toe that has been observed in the homogeneous and simple strength gradient modelling; see Figure 5.3. As such, a modification is needed to the N_p profile obtained using Equation 5.10 to account for this increase. A linear increase in N_p from $1D$ above the pile toe up to a maximum of $1.3N_p$ at the pile toe has been used; see Chapter 6.2 for more details on this modification. This modification will reduce the chance of the optimisation process overpredicting N_p due to the increase at the pile toe.

Performing the SLSQP optimisation on all the OxLim models using Equation 5.15 as the objective function results in

$$x_1 = 0.6 \quad x_2 = 1.87 \quad x_3 = 26.6 \quad x_4 = -2.3$$

resulting in

$$N_{p0} = N_1 - N_2\left(1 - \left(\frac{z}{dD}\right)^{0.6}\right)^{1.87} \tag{5.16}$$

$$d = 26.6 - 2.3\log(\lambda) \tag{5.17}$$

Figure 5.21 shows the value of the error function, Equation 5.14, with λ from this study. The values of the error function when using the Jeanjean et al. (2017) equation is also shown on the figure. The average reduction in the objective function value is 34% across all the results however it is evident from Figure 5.21 that for many cases when $\lambda \leq 2$ that Equation 5.26 provides a more significant improvement in the accuracy of the prediction. Figure 5.22 shows four of the comparisons between OxLim, Jeanjean et al. (2017) and the outcome from the optimisation exercise. For Figure 5.22(a) and (d) the improvement from using Equation 5.26 is

clear with the Jeanjean et al. (2017) approach overpredicting the OxLim results. However as shown by Figure 5.28(b) and (c) there are occasions where the Jeanjean et al. (2017) approach gives a better estimate of the OxLim results. It should be noted however that in both Figure 5.28(b) and (c) the unit weight is below what could reasonably be expected to occur in real clay. There are geotechnical materials that can have low effective unit weight, such as low density chalks or peat, however these materials are not he focus of this thesis and the methods presented in this thesis should not be applied to these materials.

5.2. Two-layer systems

In this section, analysis is performed on models that include two soil layers with an abrupt change in strength across the layer boundary as shown in Figure 5.1(b). This scenario is quite common in the North Sea, where deposits of clay frequently have high variation in strength between different geological units. This can be especially prevalent in some near coastal areas in the UK where paleo-river channels can be present resulting in relatively soft sediments that can be located on top of much stronger glacial deposits.

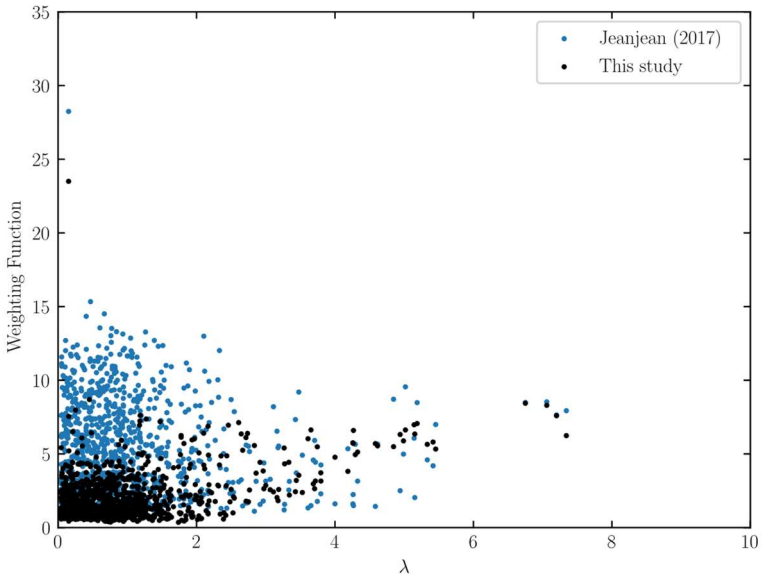

Figure 5.21 - Comparison of objective function value for Jeanjean et al.(2017) approach and Equation 5.15 with λ

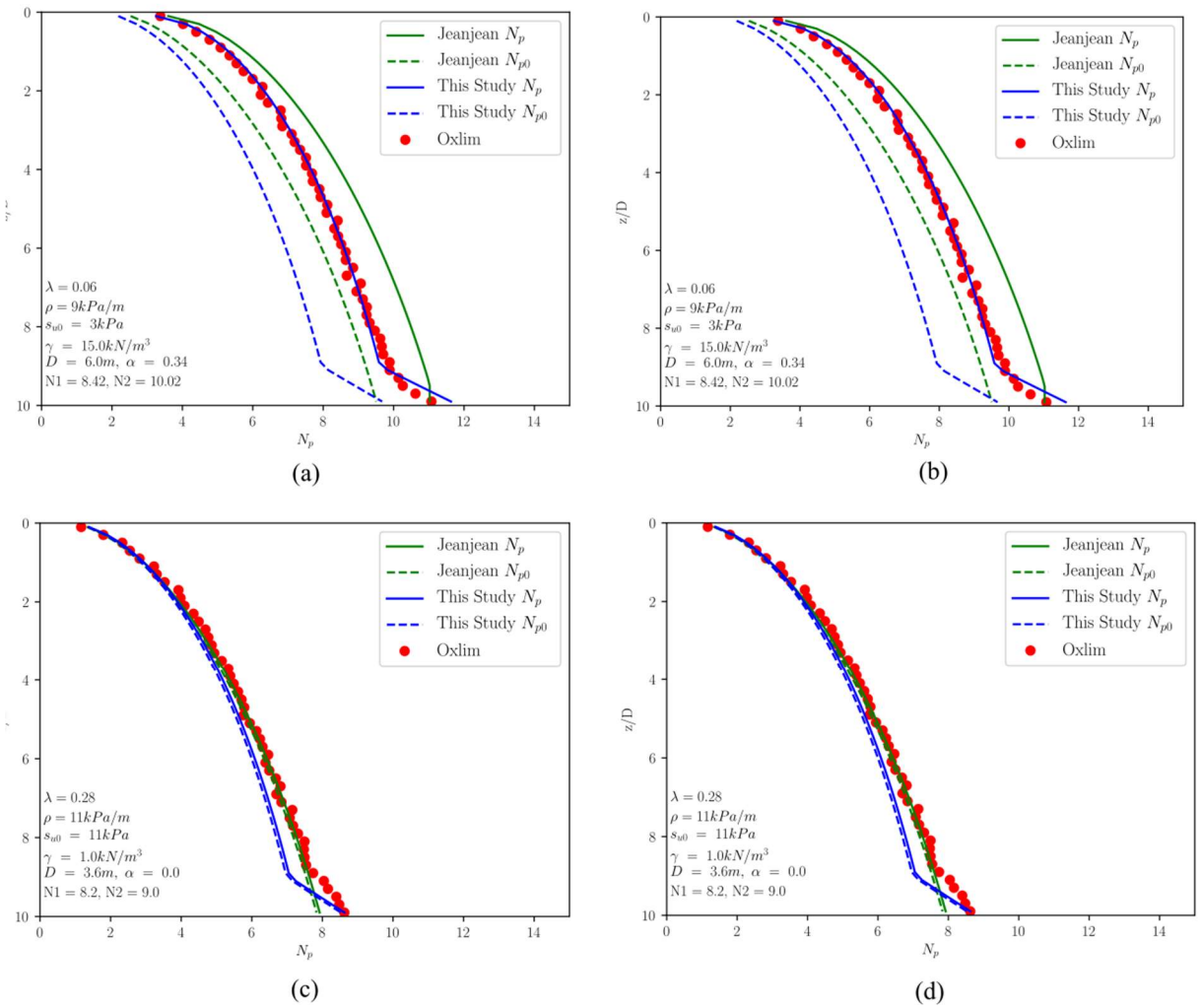

Figure 5.22 - Example comparisons of OxLim, Jeanjean et al. (2017) and proposed empirical approach.

To facilitate this study two new dimensionless groups are required, shown in Table 5.1. These groups represent the ratio of strength between the bottom and top layers and the depth of the layer transition: the latter group only being relevant when the layer boundary is located within the wedge mechanism. A previously used group, $\gamma D/s_u$, is used in a modified form. In this study the ratio of unit weight to strength is presented using the strength of the upper soil unit, i.e. $\gamma D/s_{u1}$. For this study, only the lateral bearing factor N_p is being reviewed. While the overall behaviour of fixed and free head piles in these conditions is a subject of interest, the purpose of this section is instead to show and explain the mechanisms that will affect lateral pile resistance by investigating the effect of soil layering on the lateral bearing factor profile. As such, only models with fixed head conditions, i.e. translation with no rotation, are used in these analyses.

Analysis has been performed on four key scenarios, where the layer boundary occurs:

1. in the flow-around zone
2. in the wedge mechanism with full interface tension
3. in the wedge mechanism with no interface tension and weightless soil
4. in the wedge mechanism with no interface tension and soil with weight

Note that although the third case will not to occur in practice, this case is presented as a reference case for a theoretical lower limit as with the other analyses performed in this thesis.

5.2.1. Results and Discussion

5.2.1.1. Layer boundary in flow-around zone

Initially the influence of a layer boundary in the flow-around mechanism is considered. This is achieved by modelling a translating pile with full interface tension and the top surface of the model as a symmetry boundary condition. This permits use of a quarter model with an anti-symmetry boundary on the Y-Z plane of the model, i.e. similar to the full interface tension modelling performed for the homogeneous and linearly increasing strength studies. To better capture the variation in bearing pressure as the layer boundary is approached, the rigid bodies in the model are created with a height of $0.1D$: as opposed to the $0.2D$ used in the homogeneous and linearly increasing strength models. This has the effect of slightly increasing the bracketing error of each case, although the bracketing error is still considered to be within an acceptable range with the average error across all models being approximately 8%. The increase in bracketing error occurs due to the reduced mesh density away from the pile; the reduced height of the individual rigid bodies in the pile increases the density of the mesh at the pile-soil interface hence reducing the potential for a more refined mesh where the failure mechanisms are occurring in the soil.

The range of s_{u2}/s_{u1} taken is 0.01 to 100. This represents a much greater range than would occur in practice. However modelling such as this presents an opportunity to explore such an extreme parameter space and, as has been shown to occur in the previous studies, exploring such a wide range makes it possible to establish whether the mechanisms being reviewed are limited between specific cases; such as the limits established previously between the full interface tension and no interface tension with weightless soil scenarios. As with previous analyses using a quarter model and full interface tension weightless soil has been adopted in all models.

The model has been set up with $L/D = 15$ and the layer boundary at $z_L/D = 4$. This depth is deep enough to prevent interaction with both the top surface of the model, i.e. the symmetry boundary condition, and the increase in resistance that has been observed to occur at the toe of the pile. The L/D value used is actually much larger than necessary to prevent this interaction with the toe occurring; however it has been set this high to allow full flow-around conditions to exist below the layer boundary as well as above. This permits determination of the lateral bearing factor of the flow-around mechanism, $N_{p,flow}$, that is specific to a given model thus allowing any variation to be normalised by an $N_{p,flow}$ value that accounts for potential deviations due to differences in individual models, e.g. the bracketing error, number of tetrahedra in mesh etc.

An example of the variation of p_{ult} that occurs across a layer boundary in the flow around zone is shown in Figure 5.23(a) for $s_{u2}/s_{u1} = 2$. The variation across the boundary appears continuous with $p_{ult} \approx 15$kN at the layer boundary. Results for varying s_{u2}/s_{u1} in this scenario are shown in Figure 5.24; the results in Figure 5.24 and all subsequent figures in this section are presented in terms of bearing factor, N_p. The variation of the lateral bearing factor across the layer boundary is shown in Figure 5.24 (a) and (b) for $s_{u2}/s_{u1} > 1$ and $s_{u2}/s_{u1} < 1$ respectively. The results show clear increases and reductions of the lateral bearing factors in the weak and strong layers respectively. In the weaker layer, i.e. the lower part of Figure 5.24 (a) and the upper part of Figure 5.24 (b), the variation of N_p is the same in all cases irrespective of whether the layer is above or below the layer boundary. In both cases of $s_{u1}/s_{u2} > 1$ and $s_{u1}/s_{u2} < 1$ the variation

starts with a slight decrease in resistance at a distance of approximately 3D away from the layer boundary. At about 1D from the boundary the resistance starts to increase up to maximum of approximately N_p = 15 at the layer boundary itself. This general pattern of behaviour is mimicked by the change in resistance observed in the stronger layer, however one key difference is that the profile of the resistance changes with varying s_{u2}/s_{u1} ratio. Figure 5.25 shows the ratios of $N_p/N_{p,flow}$ that occur for the pile elements immediately above and below the layer boundary.

Given that the N_p value reached in the weak layer does not vary with s_{u2}/s_{u1} it would be expected that the N_p in the strong layer would change. The actual resistance with depth, i.e. $p_{ult} = N_p s_u D$, seems to change in a continuous manner from one layer to the next, as seen in Figure 5.23, and as such the bearing factor N_p will change in such a way to accommodate this continuous variation.

It should be noted that the results of N_p obtained from OxLim are actually the average N_p over a given depth in the model. As such, immediately above and below the layer boundary the value of N_p obtained is the average N_p over a distance of 0.1D above or below the layer boundary. As such, taking the values directly from the model will not provide a continuous variation of N_p across the layer boundary. However, it is straightforward to work out the value of N_p that would be approached for a given layer if the N_p of the other layer is known. If we let N_{p1} and N_{p2} be the N_p at the layer boundary for the upper and lower layers respectively, and assume that p_{ult} varies continuously across the layer boundary then it follows that

$$P_{ult} = N_{p1} s_{u1} D = N_{p2} s_{u2} D \tag{5.28}$$

Given this and the knowledge that the N_p profile in the weaker layer does not vary with s_{u2}/s_{u1} Equation. 5.28 can be rearranged to

$$N_{p2} = \frac{N_{p1} s_{u1}}{s_{u2}} \text{ for } s_{u2} > s_{u1} \tag{5.29}$$

$$N_{p1} = \frac{N_{p2} s_{u2}}{s_{u1}} \text{ for } s_{u1} > s_{u2} \quad (5.30)$$

with Equation 5.29 and Equation 5.30 representing the weak layer being s_{u1} and s_{u2} respectively. Understanding this is aided by plotting the results normalised by the N_p value of the flow-around mechanism, i.e. showing the proportional increase or decrease from the reference case that would occur if there was no layer boundary. This is shown in Figure 5.24(c) and (d) for $s_{u2}/s_{u1} < 1$ and $s_{u2}/s_{u1} > 1$ respectively. Plotting this way shows that the N_p value for the weaker layer typically approaches a value about 30% above the reference flow-around resistance, i.e. $N_{p1} = 1.3N_{p,flow}$ for $s_{u1} < s_{u2}$ in Figure 5.24 (d). Taking Equation 5.29 for $s_{u1}/s_{u2} = 0.5$ then leads to a value of $N_{p2} = 0.65N_{p,flow}$.

This is marginally below the $N_p/N_{p,flow} \approx 0.75$ seen from the OxLim results, however as mentioned this is due to the OxLim results representing the average N_p over a small depth away from the layer boundary. An error like this will occur in both the weak and strong layers in the Oxlim model and as such the value of $N_p/N_{p,flow} = 1.3$ in the weak layer will likely also include an error due to the process of averaging over a small depth away from the layer boundary.

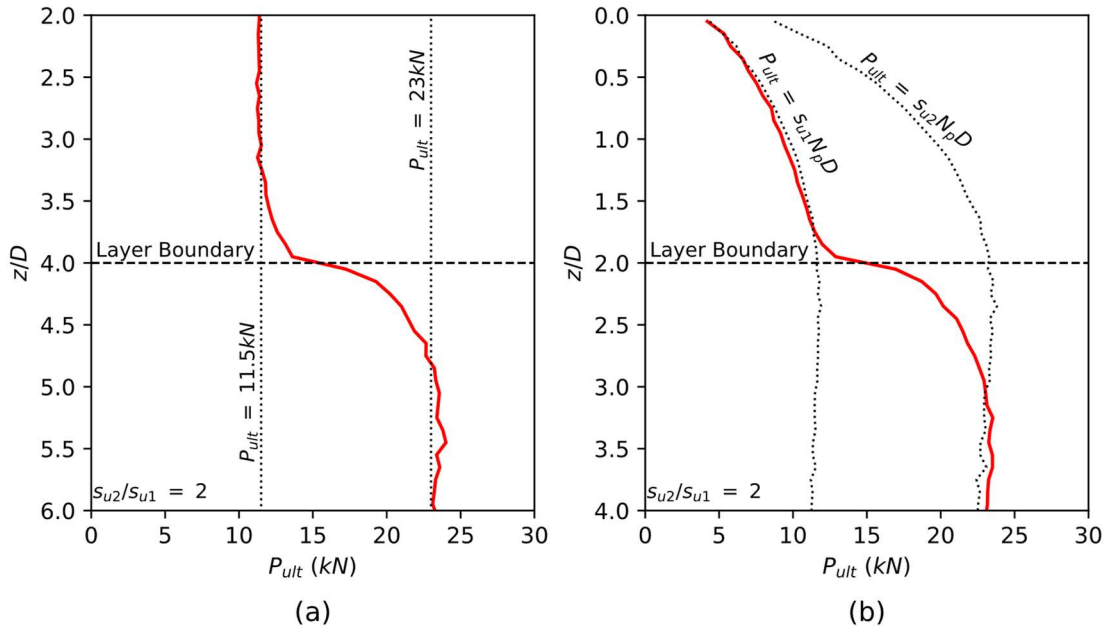

Figure 5.23 - Example variation of P_{ult} across a layer boundary located (a) flow-around conditions and (b) wedge mechanism

The rate of change of N_p as it approaches the layer boundary will be different for the weak and strong layers and as such a simple estimation such as shown above will be unlikely to exactly capture the behaviour at the layer boundary. However, it provides a convenient way of expressing the expected limits of N_p as the boundary is approached.

5.2.1.2. Layer boundary in wedge mechanism with full interface tension

This section and subsequent sections review the influence of having the layer boundary occur in the wedge mechanism. This first part utilises a similar quarter model as the previous section but with the top surface of the model no longer a symmetry boundary but a free surface. From the homogeneous modelling in Chapter 4 it is apparent that the wedge will occur in the top 3D of the pile irrespective of parameter variation, see Figure 4.1(b), as such values of z_L/D have been investigated in the range of z_L/D = 0.5 to 2 with the length of the pile set to L/D = 6. The range of s_{u1}/s_{u2} has been reduced to between 0.1 and 10.

Figure 5.26 and Figure 5.27 show the lateral bearing factor profiles for varying layer boundary depths for $s_{u2}/s_{u1} \geq 1$ and $s_{u2}/s_{u1} \leq 1$ respectively. In each subplot of these figures a reference case of s_{u2}/s_{u1} = 1 is plotted: i.e. the N_p profile that would occur if no layer boundary was present. This profiles is denoted $N_{p,ref}$. The first important observation from the profiles is that for nearly all of them the variation of N_p across the layer boundary exhibits behaviour similar to that observed for the flow-around mechanism, see Figure 5.24. However, it is immediately apparent that the change in N_p across the layer boundary depends on the depth of the layer boundary within in the wedge. For example, Figure 5.26 (a) shows the results for z_L/D = 0.5 for $s_{u2}/s_{u1} \geq 1$. In this profile the increase in resistance in the weak layer, s_{u1} here, above the reference case is either too small to be apparent in the results or does not occur. This is likely due to the proximity of the layer boundary to the ground surface. The modelling of the flow-around mechanism indicated the N_p profile to be influenced out to 3D away from the layer boundary. This influence can be seen in the other layer boundary depths, shown in Figure 5.26 (b), (c),

and (d) for z_L/D = 1, 1.5, and 2 respectively. This suggests that if the layer boundary is very near the surface there will be minimal change of the N_p profile in the upper layer from the reference case.

The profiles of N_p for $s_{u1} \geq s_{u2}$ shown in Figure 5.27 show some similar trends to the $s_{u1} \leq s_{u2}$ cases shown in Figure 5.26. For z_L/D = 0.5, Figure 5.27(a), the upper stronger layer shows little deviation from reference profile. However the lower weaker layer for z_L/D shows a significant increase above the reference profile for all values of s_{u2}/s_{u1} reviewed. For s_{u2}/s_{u1} = 0.2 and s_{u2}/s_{u1} = 0.1 this results in $N_p \geq N_{p,flow}$ at all depths in the weaker layer. The increase above $N_{p,ref}$ is lower for s_{u2}/s_{u1} = 0.1 however the value of N_p near the top of the layer is still relatively close

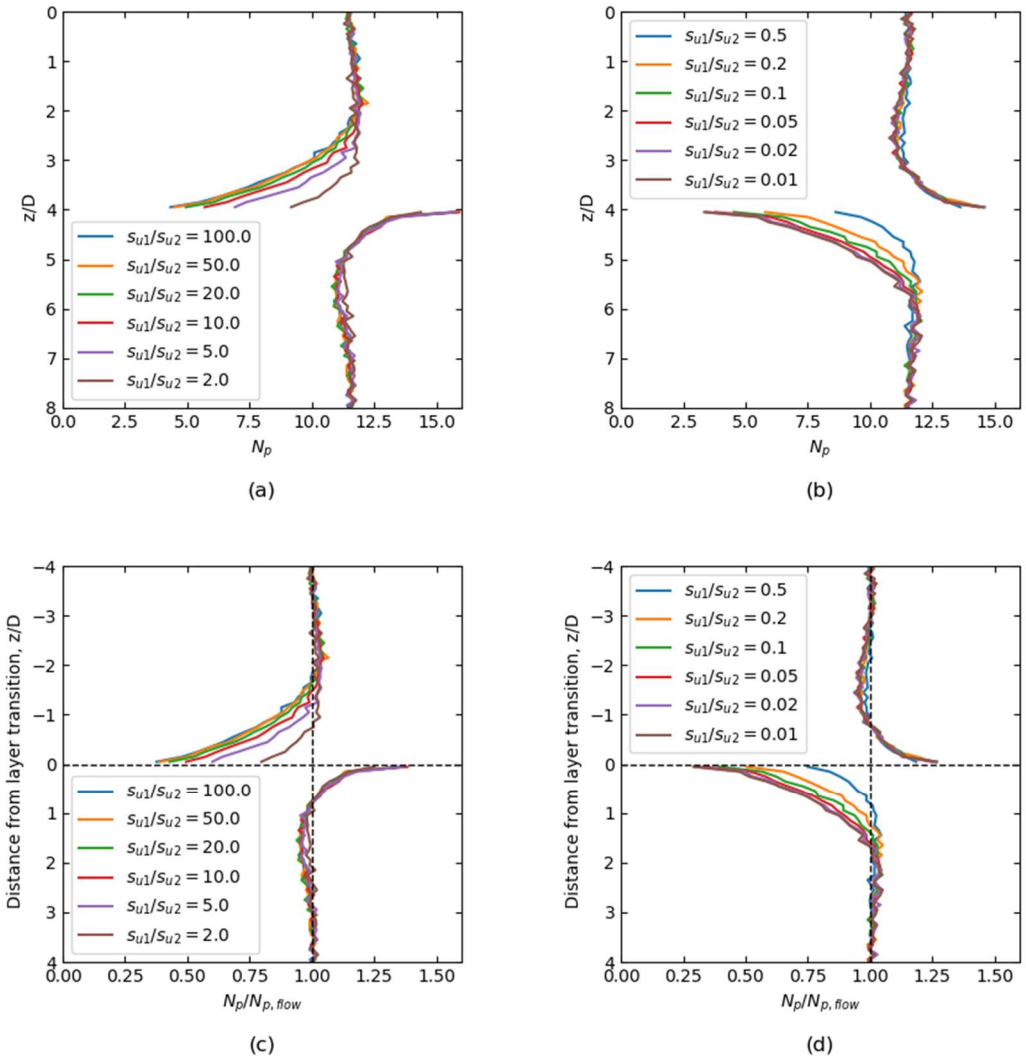

Figure 5.24 - Change of lateral resistance around an abrupt strength change between flow-around mechanisms (a) Lateral bearing factor N_p with normalised depth, $s_{u1}/s_{u2} > 1$, (b) Lateral bearing factor Np with normalised depth, $s_{u1}/s_{u2} < 1$. (c) N_p normalised by flow-around conditions with distance from transition, $s_{u1}/s_{u2} > 1$, and (d) N_p normalised by flow-around conditions with distance from transition, $s_{u1}/s_{u2} < 1$

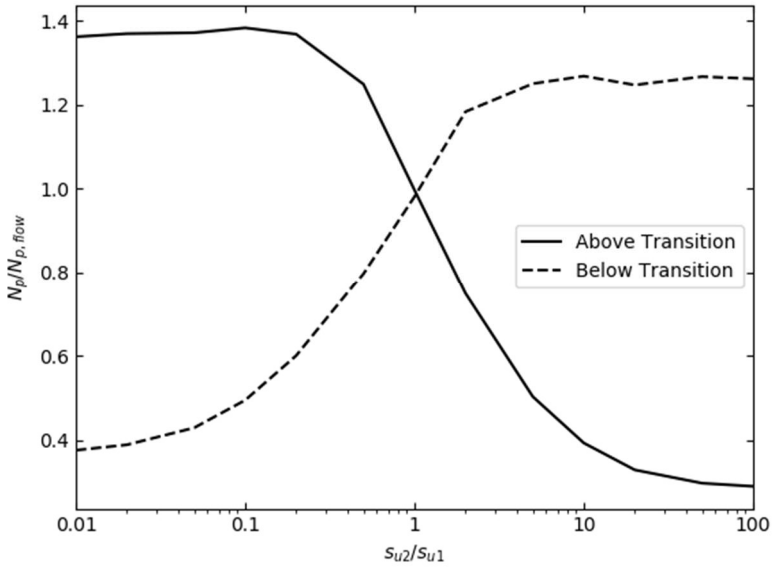

Figure 5.25 - Normalised bearing factor immediately above and below transition for transition located in flow-around mechanisms

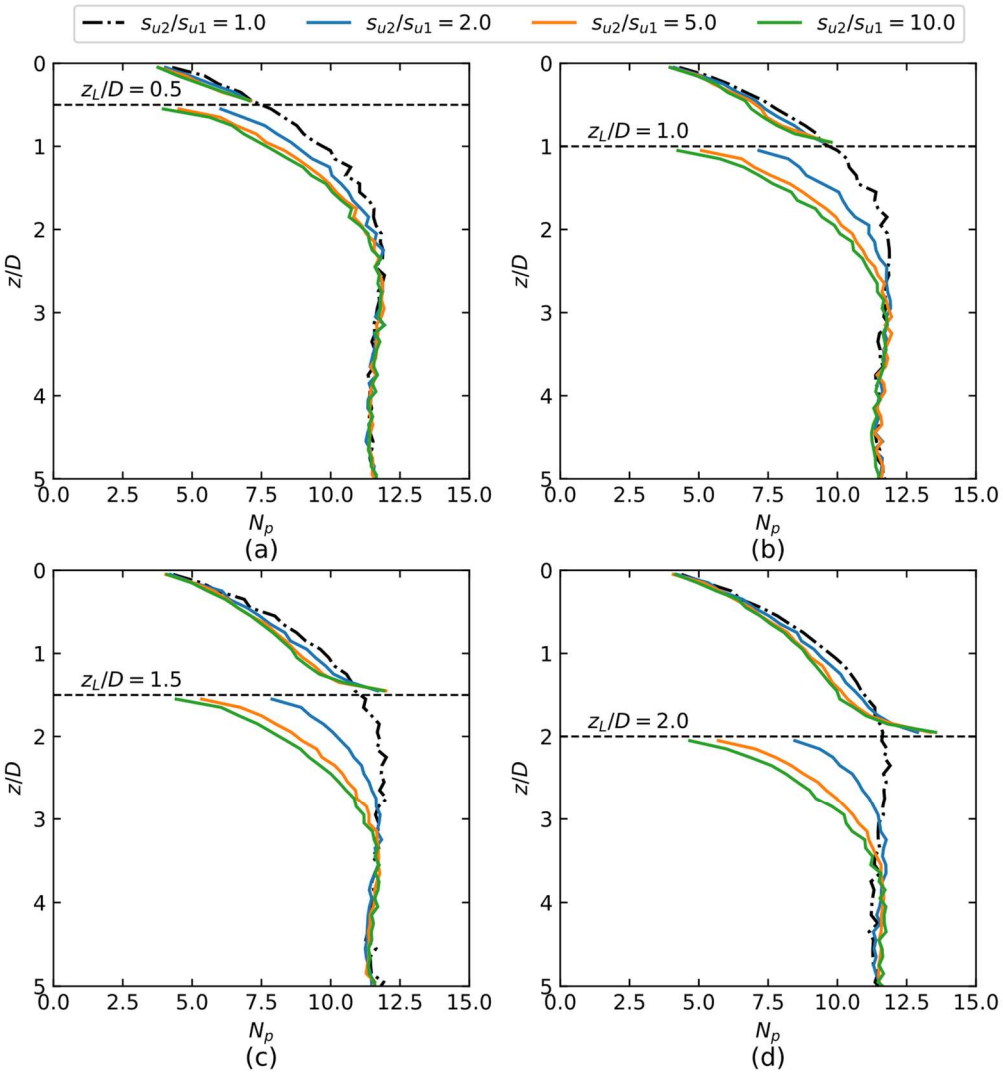

Figure 5.26 - Lateral bearing factor N_p for transition, z_L, located in wedge mechanism when full interface tension occurs for $s_{u2}/s_{u1} \geq 1$ (a) $z_L/D = 0.5$, (b) $z_L/D = 1$, (c) $z_L/D = 1.5$, (d) $z_L/D = 2.0$

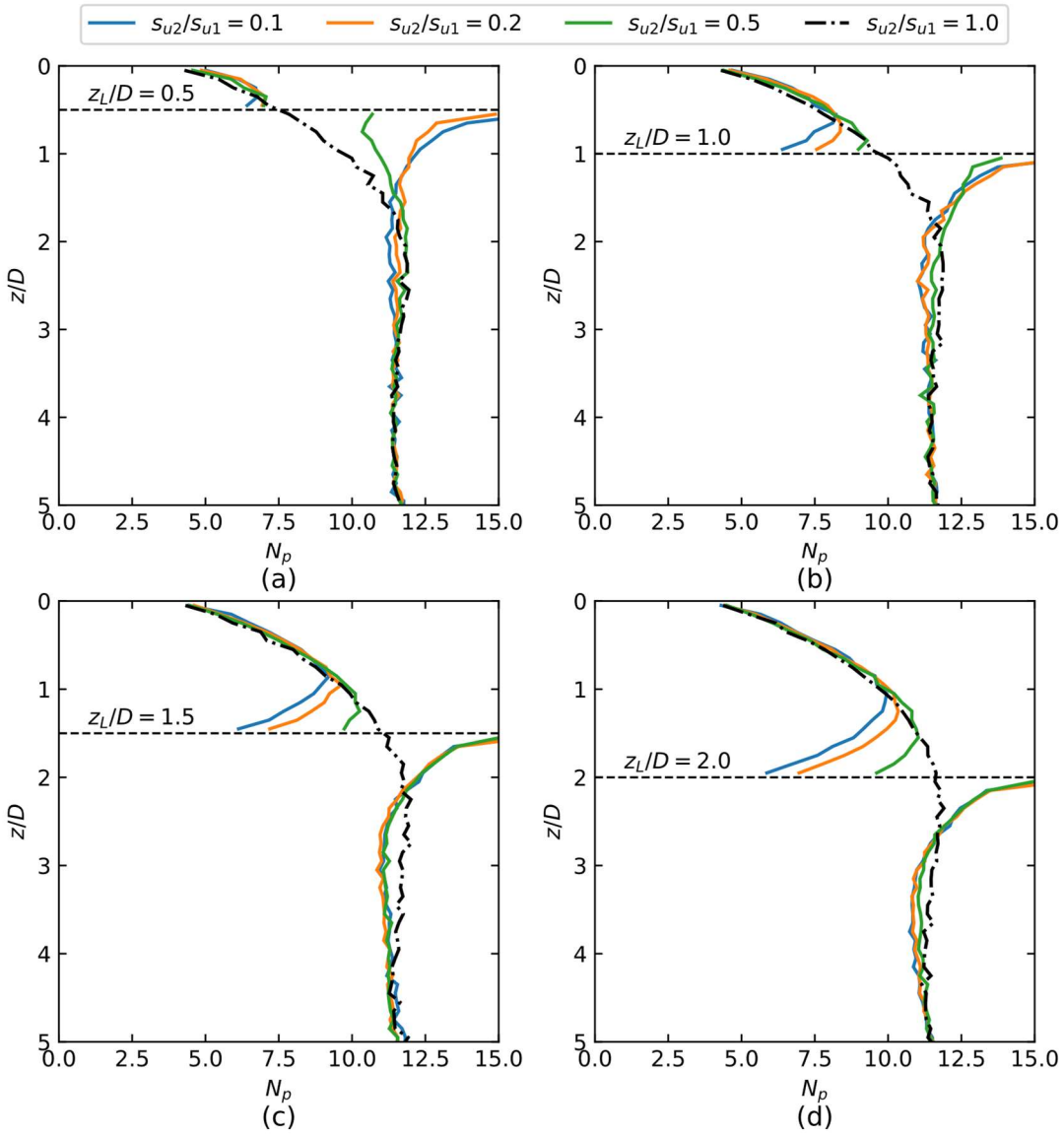

Figure 5.27 - Lateral bearing factor Np for transition, z_L, located in wedge mechanism when full interface tension occurs for $s_{u1}/s_{u2} \geq 1$ (a) $z_L/D = 0.5$, (b) $z_L/D = 1$, (c) $z_L/D = 1.5$, (d) $z_L/D = 2.0$

to $N_{p,flow}$ for this case. As z_L/D increases the profiles of N_p in the lower weaker layer become similar for all values of s_{u2}/s_{u1} assessed.

As the depth of the layer boundary increases, the variation of N_p away from the reference case starts to become similar to that observed in the flow-around case (see Figure 5.24). This is most easily shown by plotting the results normalised by the reference case: i.e. each N_p profile for a given s_{u2}/s_{u1} is normalised by the N_p profile for $s_{u2}/s_{u1} = 1$. This is shown in Figure 5.28 and Figure 5.29 for $s_{u2}/s_{u1} \geq 1$ and $s_{u2}/s_{u1} \leq 1$ respectively. The results in Figure 5.28 show a clear

progression from the case of $z_L/D = 0.5$ in (a) to $z_L/D = 2$ in (d). With each increase in layer depth the increase of $N_p/N_{p,ref}$ in the upper layer is greater until $z_L/D = 2$ where the maximum N_p achieved is similar to that seen in the flow-around mechanism analysis. A key difference for this case is the depth the change in resistance occurs over when the weak layer is the upper layer in the wedge mechanism. In each case the variation in N_p from the reference profile only occurs over a small depth of about $0.5D$. This likely occurs due to the weaker layer having little influence on the overall shape of the failure mechanism in this case: i.e. the response is dominated by behaviour of the failure in the stronger layer. However, it should be noted that the drop in resistance in the lower stronger layer still occurs over a depth of approximately $3D$ with the main change occurring within $2D$ from the layer boundary. Figure 5.29 shows the normalised results for $s_{u1} \geq s_{u2}$. For z_L/D the N_p is approximately twice $N_{p,ref}$ at the top of the lower weaker layer when $s_{u2}/s_{u1} \leq 0.2$. This reduces to $N_p = 1.3N_{p,ref}$ when $s_{u2}/s_{u1} = 0.5$; i.e. similar to the increase seen in the flow around mechanism case presented in Figure 5.24. As z_L/D increases the N_p profiles for each s_{u2}/s_{u1} case become similar to those in Figure 5.24. This suggests that upper stronger layer confines the lower weaker layer causing behaviour similar to flow around case despite the $N_{p,ref}$ profile indicating this depth should still have be part of the wedge failure mechanism. As for $s_{u1} \leq s_{u2}$ the decrease in strength in the stronger layer can be quite significant: a reduction of $N_p = 0.5N_{p,ref}$ occurs for $z_L/D \geq 1$ and $s_{u2}/s_{u1} \leq 0.2$. When $s_{u2}/s_{u1} = 0.5$, the reduction in resistance is less; the results indicating a 5% to 15% reduction from $z_L/D = 1$ to $z_L/D = 2$.

5.2.1.3. Layer boundary in wedge mechanism, with no interface tension and weightless soil

This part of the study on layer boundaries located in the wedge mechanism investigates the response when there is no interface tension and weightless soil. As with the previous studies on homogeneous and linearly increasing strength profiles, the assumption of weightless soil is not representative of actual conditions but is included to provide insight into the potential lower

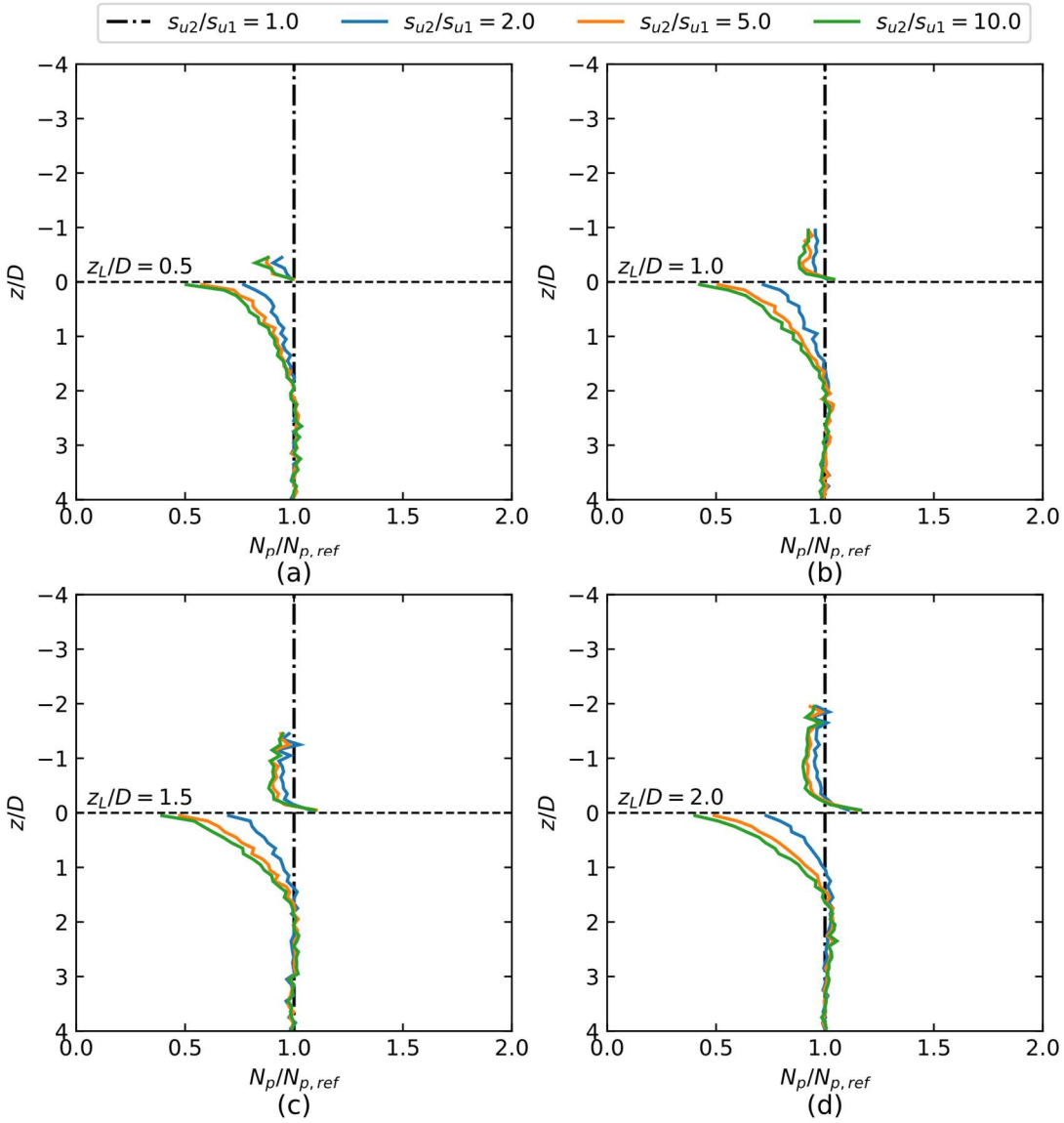

Figure 5.28 - Lateral bearing factor, N_p, normalised by lateral bearing factor for $s_{u1}/s_{u2} = 1$, $N_{p,ref}$, for layer transition z_L in wedge mechanism for full interface tension and $s_{u1}/s_{u2} \leq$ 1(a) $z_L/D = 0.5$, (b) $z_L/D = 1$, (c) $z_L/D = 1.5$, (d) $z_L/D = 2.0$

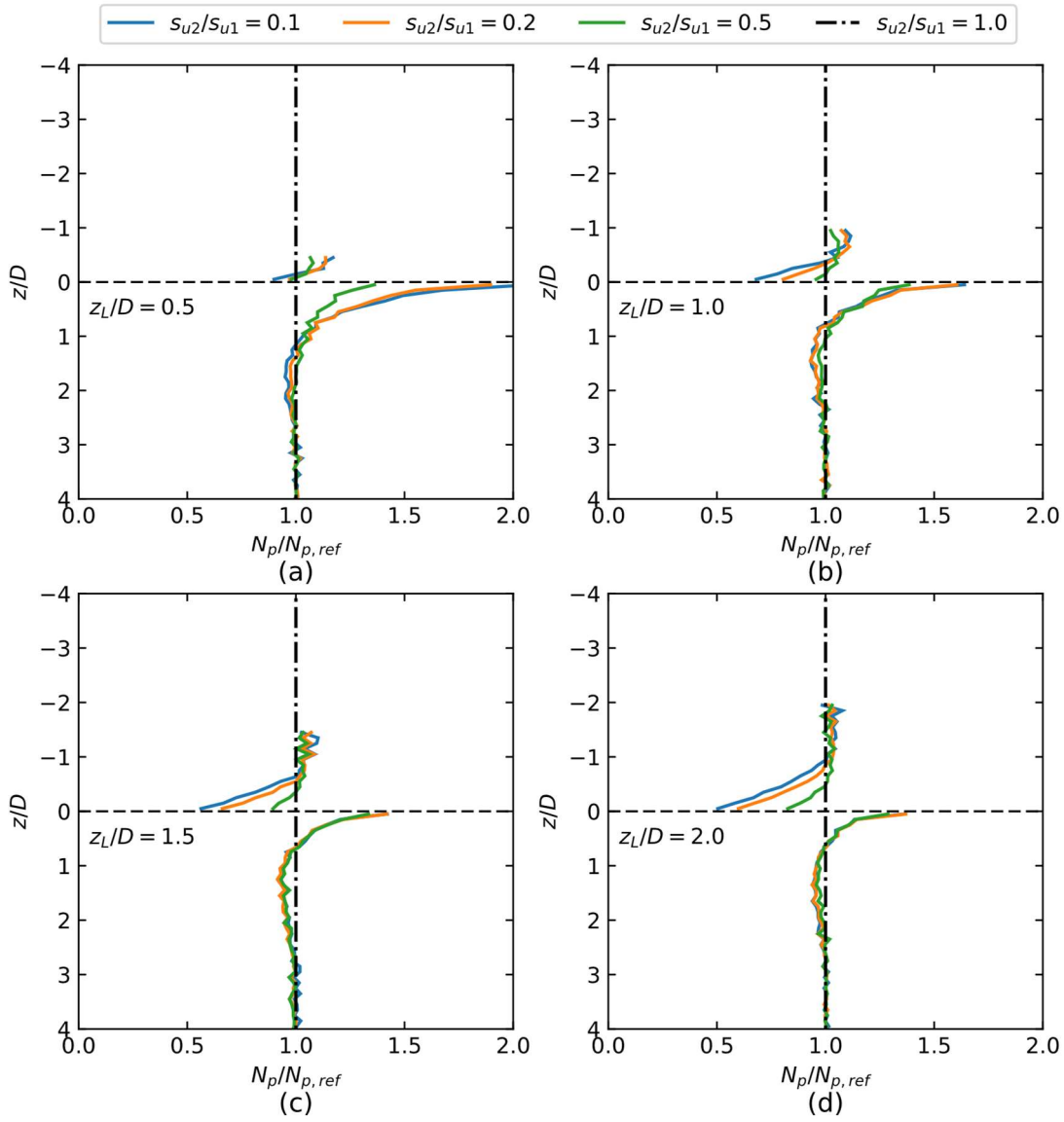

Figure 5.29 - Lateral bearing factor, N_p, normalised by lateral bearing factor for $s_{u1}/s_{u2} = 1$, $N_{p,ref}$, for layer transition z_L in wedge mechanism for full interface tension and $s_{u1}/s_{u2} \leq 1$(a) $z_L/D = 0.5$, (b) $z_L/D = 1$, (c) $z_L/D = 1.5$, (d) $z_L/D = 2.0$

limits of the lateral response. As before when modelling separation between the pile and the soil, a half model needs to be used.

The N_p profiles obtained in two-layer soils with $s_{u1} \leq s_{u2}$ and $s_{u1} \geq s_{u2}$ are presented in Figure 5.30 and Figure 5.31 respectively. It is immediately apparent that these conditions have a significant effect on the depth over which the transition between layers occurs. With the weak layer on top, Figure 5.30, re-joining of $N_{p,ref}$ curve appears to take a minimum of 8D: much greater than the 2D required for the full tension scenario. A similar response is observed when strong layer is on top, i.e. $s_{u1} > s_{u2}$ in Figure 5.31, where in each case the resistance of the lower layer is significantly above $N_{p,ref}$ until near the pile toe. It is important to note that these models have been performed with a pile of finite length using a model with L/D = 10. This was done to give an indication of the effect of the pile toe being located near to the interface. From subplots (c) and (d) in Figure 5.31 it is clear that the pile toe does affect the increase of the resistance with the N_p profiles below the layer boundary not re-joining the $N_{p,ref}$ curve before the increase towards the toe occurs.

5.2.1.4. Layer boundary in wedge mechanism with no interface tension

Finally in this investigation the dimensionless ratio of unit weight to strength is varied to understand the effect this will have on both the depth that the N_p transition occurs over, and the deviation from the reference N_p profile. Figure 5.32 and Figure 5.33 show the results from this scenario with $\gamma D/s_{u1}$ = 1. For $\gamma D/s_{u1}$ = 1 and $s_{u1} \leq s_{u2}$ (Figure 5.32) a similar behaviour to the weightless scenario is observed: i.e. a high z/D is required for the reduced profile in the stronger, lower layer to rejoin the $N_{p,ref}$ curve, with the depth to rejoin varying with the s_{u1}/s_{u2} ratio. The increase above $N_{p,ref}$ in the weaker, upper layer is also very small, with increases typically only 5% above $N_{p,ref}$, as shown in Figure 5.32. The decreases in $N_{p,ref}$ in the stronger, lower layer are of a similar magnitude to the full tension case Figure 5.26 with s_{u2}/s_{u1} = 2 resulting in approximately 70% of $N_{p,ref}$ immediately below the layer boundary.

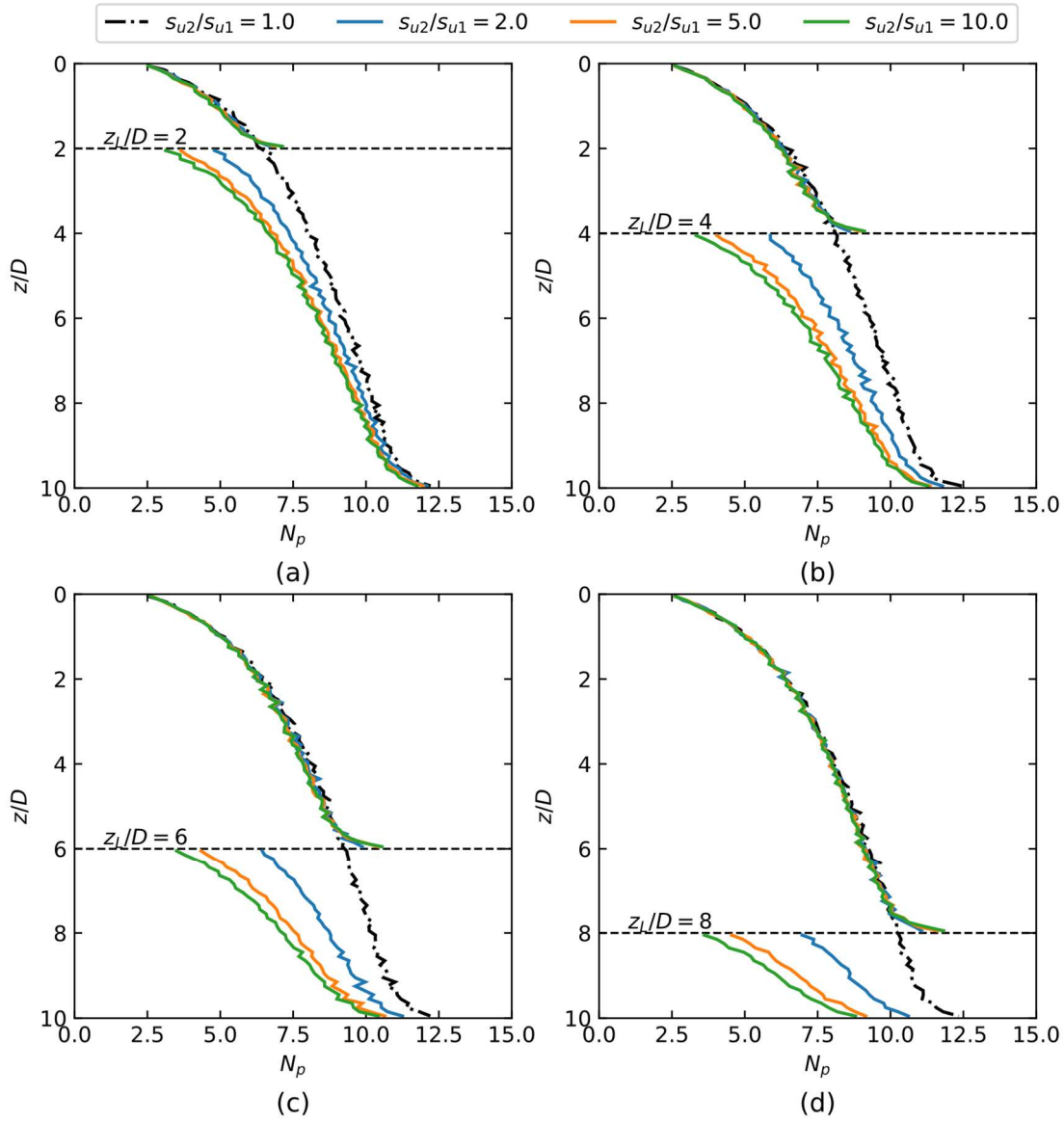

Figure 5.30- Lateral bearing factor Np for transition, z_L, located in wedge mechanism with no interface tension in weightless soil occurs for $s_{u2}/s_{u1} \geq 1$ (a) $z_L/D = 2$, (b) $z_L/D = 4$, (c) $z_L/D = 6$, (d) $z_L/D = 8$

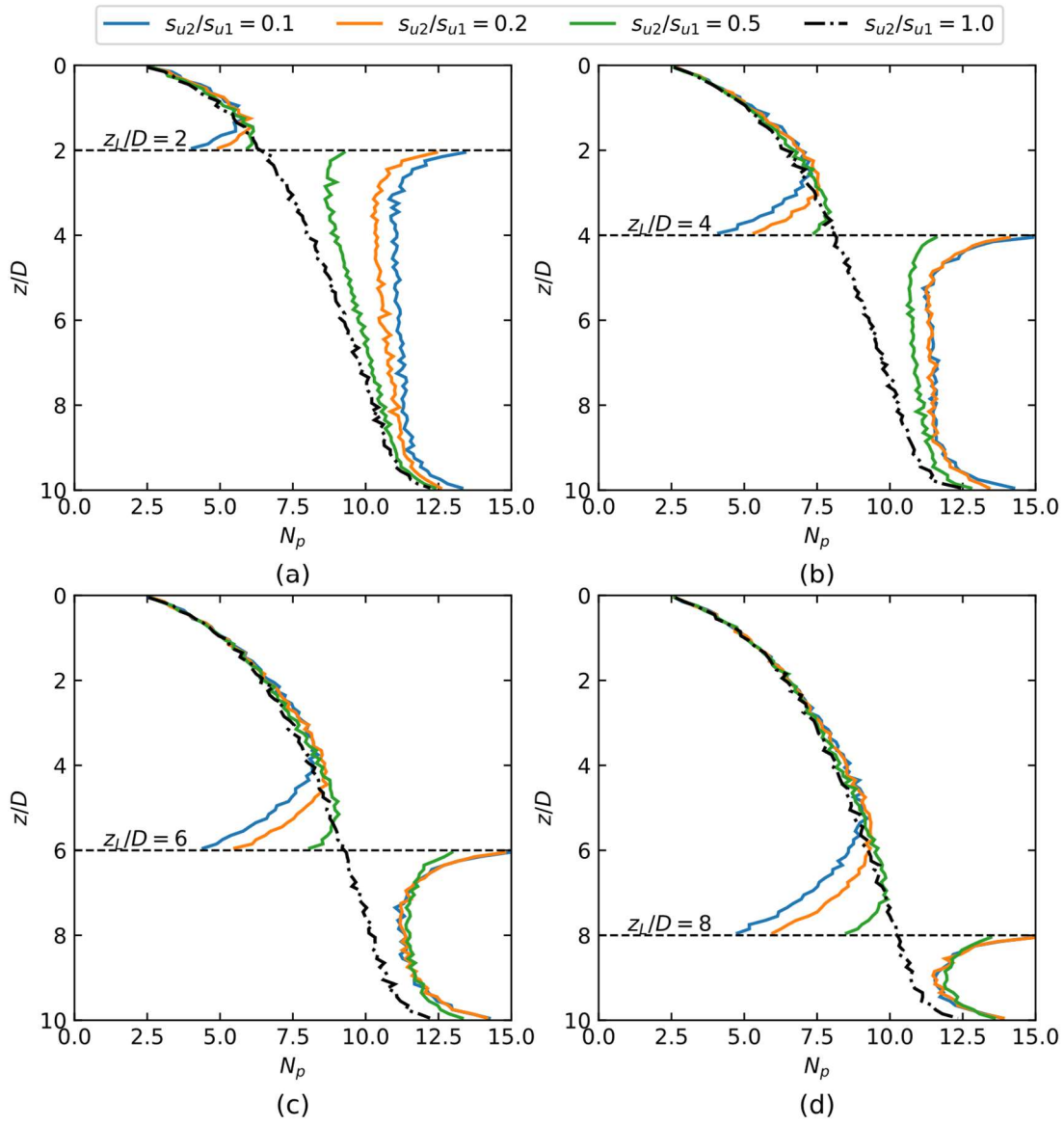

Figure 5.31- Lateral bearing factor Np for transition, z_L, located in wedge mechanism when no interface tension in weightless soil occurs for $s_{u2}/s_{u1} \leq 1$ (a) $z_L/D = 2$, (b) $z_L/D = 4$, (c) $z_L/D = 6$, (d) $z_L/D = 8$

As z_L/D increases the amount N_p increase by in the weaker layer reduces until the profiles normalised by $N_{p,ref}$ start to become similar to the observed change for the layer boundary occurring in the flow-around mechanism. The results for $z_L/D = 4$, shown in Figure 5.33(d), are near identical to the profiles from Figure 5.24(c). The $s_{u2}/s_{u1} = 0.2$ case requires approximately $z/D = 7$, 6, 5, and 4 to rejoin $N_{p,ref}$ for $z_L/D = 1$, 2, 3, and 4 respectively. As with $\gamma D/s_{u1} = 1$, the increase in resistance in the weaker top layer close to the layer boundary is relatively minor except when the layer boundary is at a depth where the flow-around mechanism would normally occur, i.e. the increase for $z_L/D = 4$ in Figure 5.34(d) is only slightly less than has typically been observed for the layer transition in the flow-around mechanism (See Figure 5.24). Plotting the proportional reductions in N_p, Figure 5.34, shows that there is minimal variation in the reductions that occur in the stronger lower layer, with $N_p/N_{p,ref} \approx 0.3$, 0.4 and 0.7 for $s_{u2}/s_{u1} =$ 10, 5, and 2 respectively.

The results for $\gamma D/s_{u1} = 2$ and $s_{u1} \geq s_{u2}$ are shown in Figure 5.35. The results are similar in form to $\gamma D/s_{u1} = 1$ case (Figure 5.33): at low z_L/D the stronger top layer has minimal reduction from the reference profile while the weaker lower layer shows increases similar to that of the layer transition in the flow-around mechanism scenario (Figure 5.24). As with the $\gamma D/s_{u1} = 1$ results the top layer appears to confine the lower layer sufficiently to cause the flow-around mechanisms to occur at shallower depths than the homogeneous case. This is most prominent for $z_L/D = 1$, subplot (a) in Figure 5.33, where the resistance of the lower layer increases significantly from the reference profile: by approximately 50%, 100% and 100% for $s_{u2}/s_{u1} =$ 0.5, 0.2, and 0.1. From Figure 5.33(a) it is apparent that for $s_{u2}/s_{u1} = 0.2$ and 0.1 that the flow-around mechanism has been achieved between $z/D = 2$ and 4: whereas the reference profile shows that flow-around conditions in homogeneous soil start occurring between $z/D = 4$ and 5. As z_L/D increases, the change across the layer boundary becomes similar to the change observed for a layer boundary in the flow-around mechanism; for $z_L/D = 3$ and 4 there is very little difference between the $N_p/N_{p,ref}$ profiles for this scenario and those for the flow-around case.

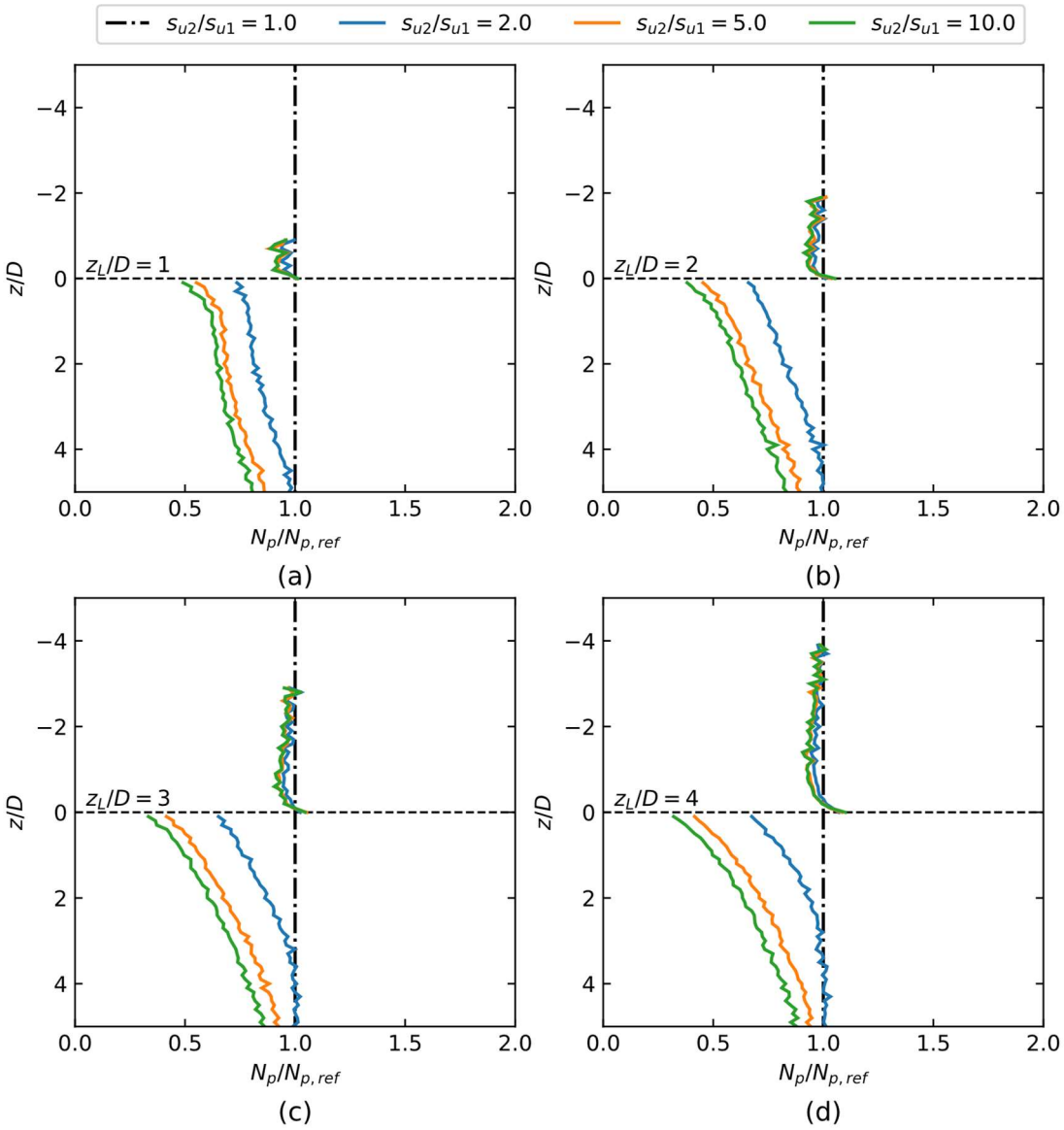

Figure 5.32 - Lateral bearing factor Np for transition, z_L, located in wedge mechanism with no interface tension with $\gamma D/s_{u1} = 1$ for $s_{u2}/s_{u1} \geq 1$ (a) $z_L/D = 1$, (b) $z_L/D = 2$, (c) $z_L/D = 3$, (d) $z_L/D = 4$. Note that the vertical axis refers to the normalised offset from the layer depth

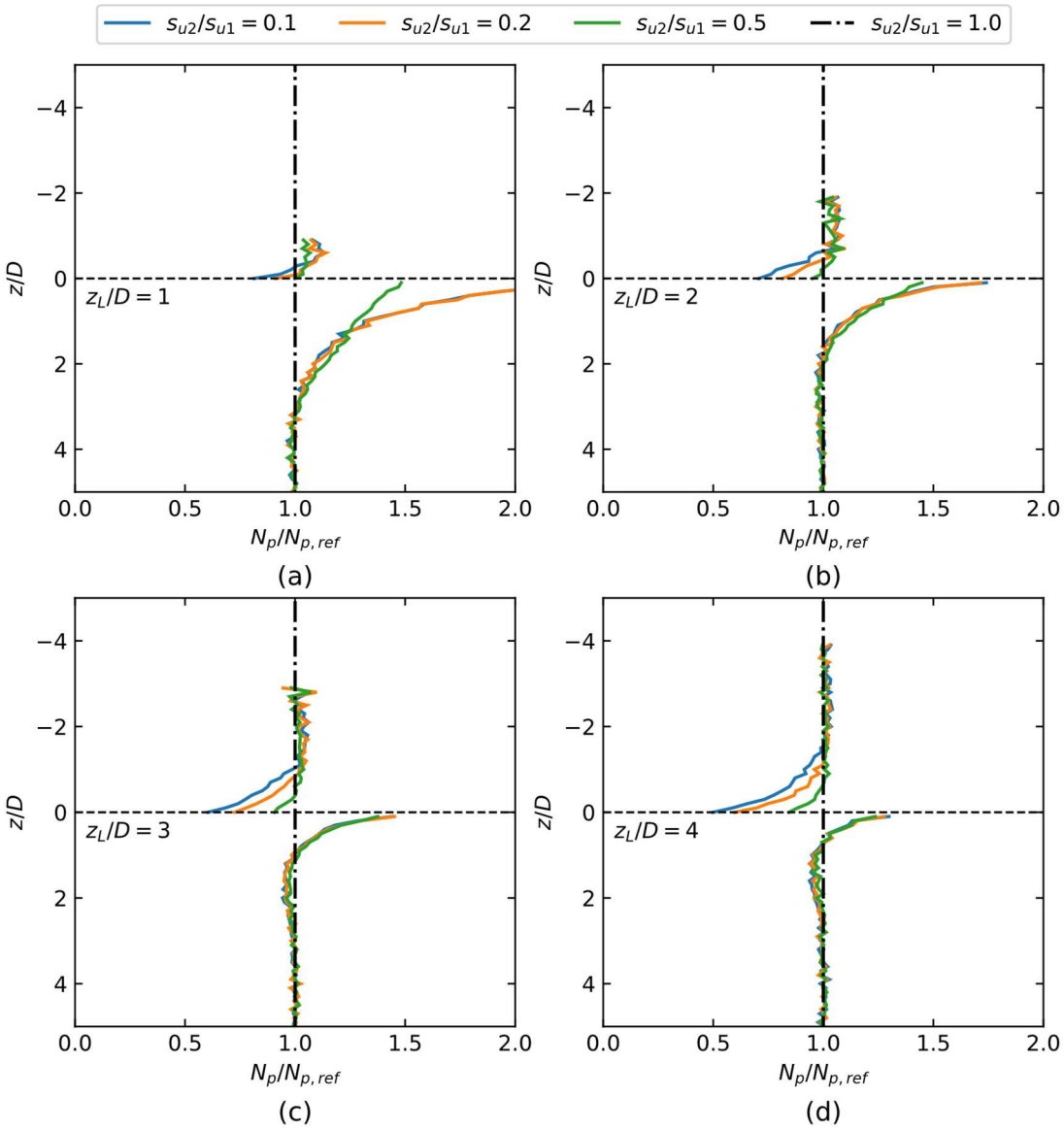

Figure 5.33 - Lateral bearing factor Np for transition, z_L, located in wedge mechanism with no interface tension with $\gamma D/s_{u1} = 1$ for $s_{u2}/s_{u1} \leq 1$ (a) z_L/D 1, (b) $z_L/D = 2$, (c) $z_L/D = 3$, (d) $z_L/D = 4$. Note that the vertical axis refers to the normalised offset from the layer depth

The results from this study indicate that abrupt strength changes can potentially have a significant impact on the lateral resistance of a pile. In cases where a weaker layer is located on top, the reduction in the bearing factor profile in the stronger layer can take multiple pile diameters before it returns to the reference N_p profile for homogeneous soil. For piles with a large L/D ratio this may not be overly significant as the total depth over which the change occurs will likely be relatively small compared to the pile length. However in piles with lower L/D these strength reductions may have a significant impact on the total resistance; monopiles for offshore wind turbines are regularly being designed with diameters between 5m and 8m with concept designs even considering up to 10m. As such, having a simple set of rules to modify N_p profiles, and thus p_{ult} profiles, could be beneficial in early stages of design studies where more complex modelling is not practical.

5.2.2. Implications for Design

Based on the results of this study of a translating pile in two-layer soil, two ways of modifying an N_p profile from its reference homogeneous case have been considered. These are approximating the response as (i) a linear change with depth or (ii) a constant change over fixed depth: both of these are shown schematically in Figure 5.36. To facilitate the proposed modifications, four new parameters are proposed: the depths that the transition occurs over in the weak and strong layers, z_{tw} and z_{ts} respectively, and the proportional change in N_p that occur at the layer boundary in the weak and strong layers, $N_{p,tw}$ and $N_{p,ts}$ respectively. Both $N_{p,tw}$ and $N_{p,ts}$ are represented as a proportion of $N_p/N_{p,ref}$ that occurs at the specified layer depth, z_L/D, i.e.

$$N_{p,tw} = C\frac{N_p}{N_{p,ref}} \tag{5.31}$$

where $N_{p,ref}$ is the N_p that would occur if there was no layer transition, i.e. $N_{p,ref} = N_{p,flow}$ if the layer transition is deep enough to be located in the flow-around mechanism, otherwise it is the

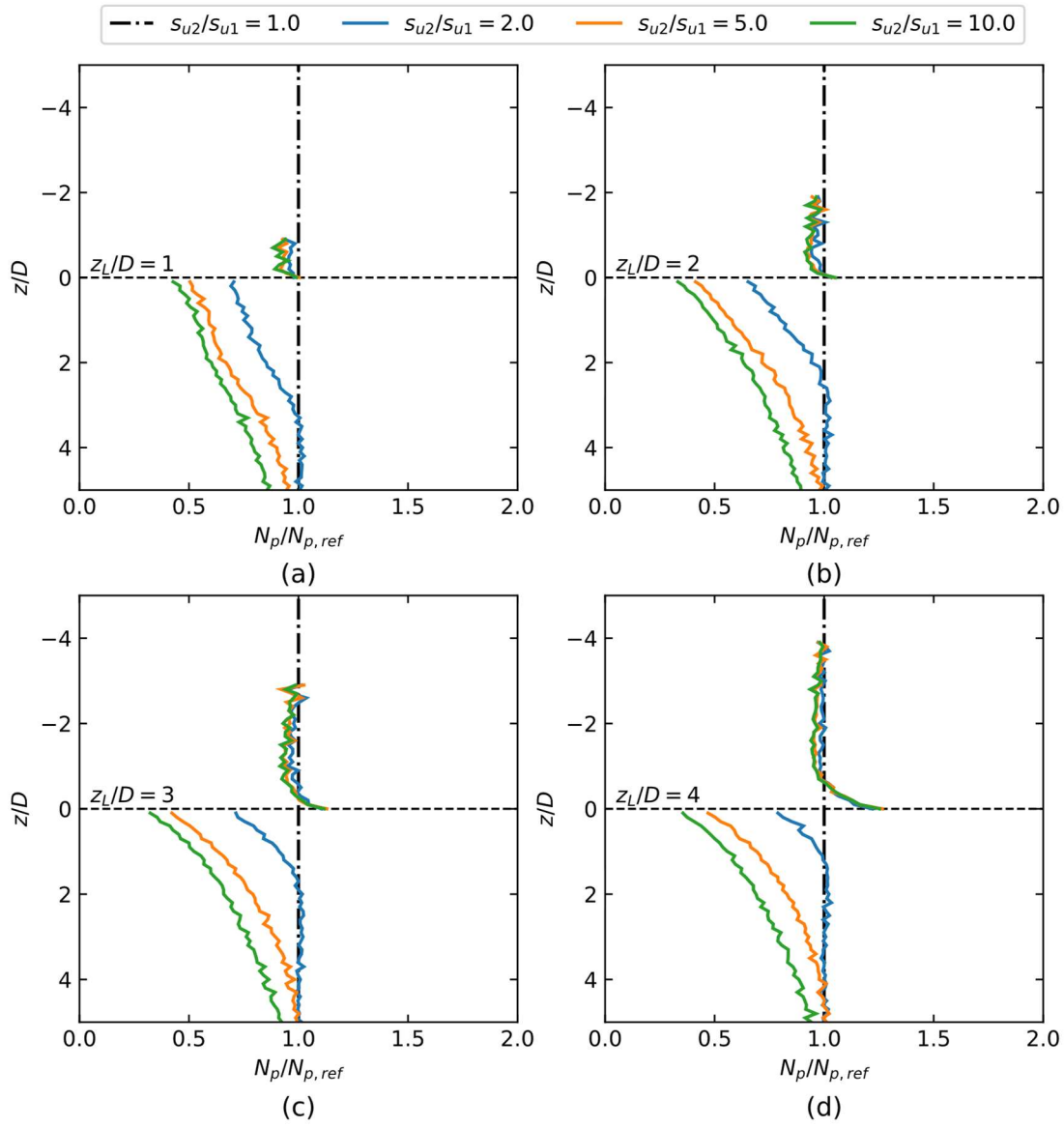

Figure 5.34 - Lateral bearing factor N_p for transition, z_L, located in wedge mechanism with no interface tension with $\gamma D/s_{u1} = 2$ for $s_{u2}/s_{u1} \geq 1$ (a) $z_L/D = 1$, (b) $z_L/D = 2$, (c) $z_L/D = 3$, (d) $z_L/D = 4$. Note that the vertical axis refers to the normalised offset from the layer depth.

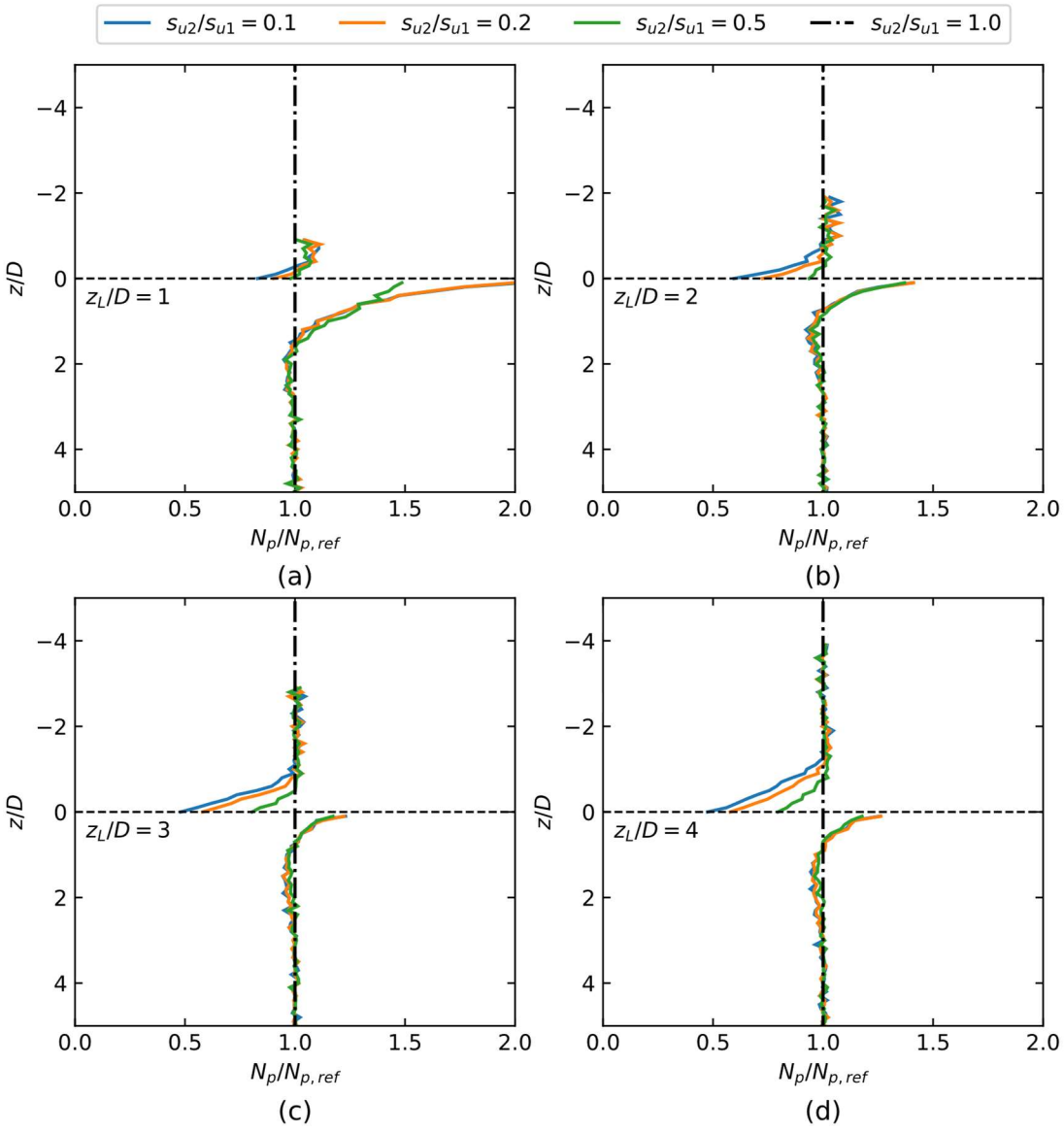

Figure 5.35 - Lateral bearing factor N_p for transition, z_L, located in wedge mechanism with no interface tension with $\gamma D/s_{u1} = 2$ for $s_{u2}/s_{u1} \leq 1$ (a) $z_L/D = 1$, (b) $z_L/D = 2$, (c) $z_L/D = 3$, (d) $z_L/D = 4$. Note that the vertical axis refers to the normalised offset from the layer depth.

N_p for a given z/D in the wedge mechanism. In Equation 5.31, C is the proportional change above $N_p/N_{p,ref}$ for the weak layer, e.g. for a layer boundary in the flow-around zone, as shown in Figure 5.24, the value of C will not vary and is $C = 1.3$ in all cases. For cases where the layer boundary is in the wedge mechanism the value of C depends on the depth of the layer and ratio of weight to strength in the layer: i.e.

$$C = f\left(\frac{z_L}{D}, \frac{\gamma D}{s_{u1}}\right) \tag{5.32}$$

Using the relationship established in Equation 5.30 it can also be seen that

$$N_{p,ts} = N_{p,tw}\frac{s_{u1}}{s_{u2}} = C\frac{N_p}{N_{p,ref}}\frac{s_{u1}}{s_{u2}} \tag{5.33}$$

Based on the results of this study, the depth that the transition occurs over will also typically depend on the depth of the layer boundary and the ratio of soil weight to strength. However unlike N_{pt}, the value of z_t will also depend on the ratio of strength between the layers; e.g. when the strong layer is above the weak layer the strong layer will provide additional confinement to the weaker layer, thus reducing z_t as seen in Figure 5.33 when compared to Figure 5.32. Indicative limits for $N_{p,ts}$ and z_t/D are provided in Table 5.4 and indicative values of z_t/D are provided in Table 5.3.

The first proposed way of modifying N_p, Figure 5.36(b), considers a linear change of N_p from a point z_t away from the layer boundary up to the value of $N_{p,t}$, i.e.

$$N_p = N_{p,ref} + (z_t - \Delta z_t)\left(\frac{N_{p,t} - 1}{z_t}\right) \tag{5.34}$$

where $N_{p,ref}$ is the reference N_p that occurs when no layering is present, and Δz_t is the distance from the layer boundary. $N_{p,t}$ and z_t represent the relevant parameters for the weak and strong layers, $N_{p,tw}$, z_{tw} and $N_{p,ts}$, z_{ts} respectively.

The second proposed way of modifying the N_p profile is by using a constant offset from $N_{p,ref}$ to a prescribed distance away from the layer boundary. This can be achieved by making the total distributed force for this method the same as the total distributed force for the linear approximation used in the other method and then ensuring the equivalent depth this force is applied if it was a point load at is also the same. For a linearly varying resistance profile, the equivalent point load is applied at 1/3 of the height; the height of the loading being z_t/D in this example. As such, the equivalent uniform distribution will need a height of $2/3z_t$, which results in a $3/4N_{p,t}$ to achieve the same total distributed force. This is shown schematically in Figure 5.36(c).

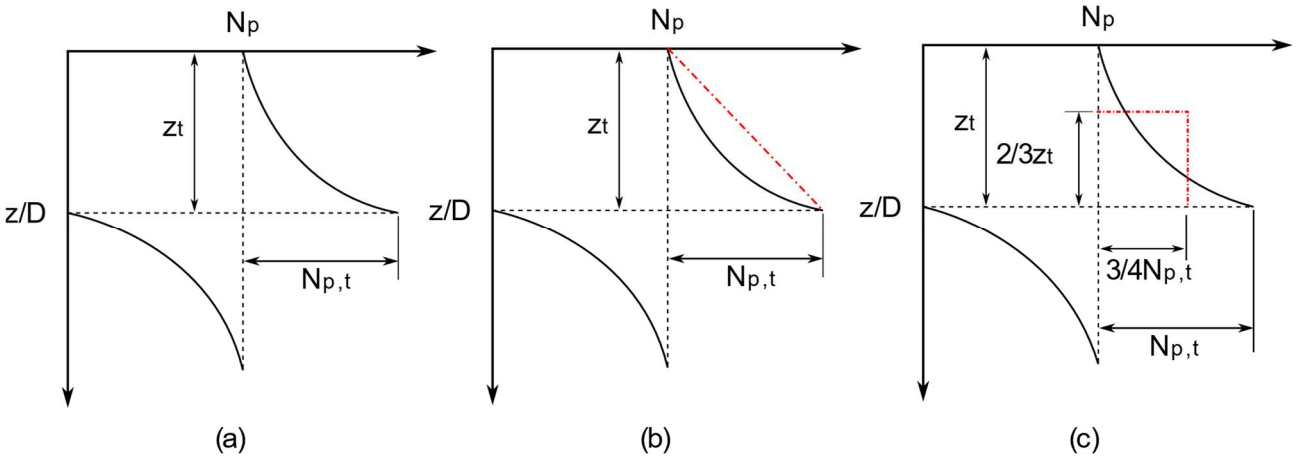

Figure 5.36 - modifying Np to account for a layer boundary

An example of the effect of modifying the resistance for different layer depths using the linear change, Figure 5.36(b), is shown in Figure 5.37 for L/D = 5, α = 1, using no interface tension and across varying $\gamma/s_{u1}D$ and s_{u2}/s_{u1}. The results shown in Figure 5.37 have been calculated using the moment equilibrium method, i.e. Equation 5.7. The results in Figure 5.37 show that this modification can lead to significant reductions in calculated total capacity when $s_{u2} > s_{u1}$ and the layer boundary is near surface; the greatest reduction being 17% when $s_{u2}/s_{u1} = 5$. In contrast to this, there is also the potential for an increase in total capacity when $s_{u2} < s_{u1}$ and the layer boundary is near the surface. However, most of the observed increases in capacity in these results are quite modest with most cases having less than a 5% increase in total capacity. It

should also be noted that these calculations only incorporate the lateral bearing resistance and include no account for the additional resistances that arise from the base shear, base moment or distributed moment. Inclusion of these components of lateral resistances in the moment equilibrium calculation would reduce the overall effect of accounting for the variation of N_p near the layer boundary.

Table 5.3 - Values of z_t/D for layer transition located in the wedge mechanism

		Top Layer				Bottom Layer			
	z_l/D	s_{u2}/s_{u1} **<0.2**	**0.2 to 1**	**1 to 5**	**>5**	s_{u2}/s_{u1} **<0.2**	**0.2 to 1**	**1 to 5**	**>5**
Full Tension	**<0.5** **0.5 to 1** **1 to 2** **>2**	0.5				1		2	
$\frac{\gamma D}{s_{u1}} \geq 2$	**<0.5** **0.5 to 1** **1 to 2** **>2**	0.5 0.75 1		0.5		1		3 2 1.5 1	6 5 5 4
$\frac{\gamma D}{s_{u1}} < 2$	**<0.5** **0.5 to 1** **1 to 2** **>2**	0.5 1		0.5		3 2 1.5 1		5 4 3	8 7 6
Weightless	**<0.5** **0.5 to 1** **1 to 2** **>2**	6 5.5 5 4							

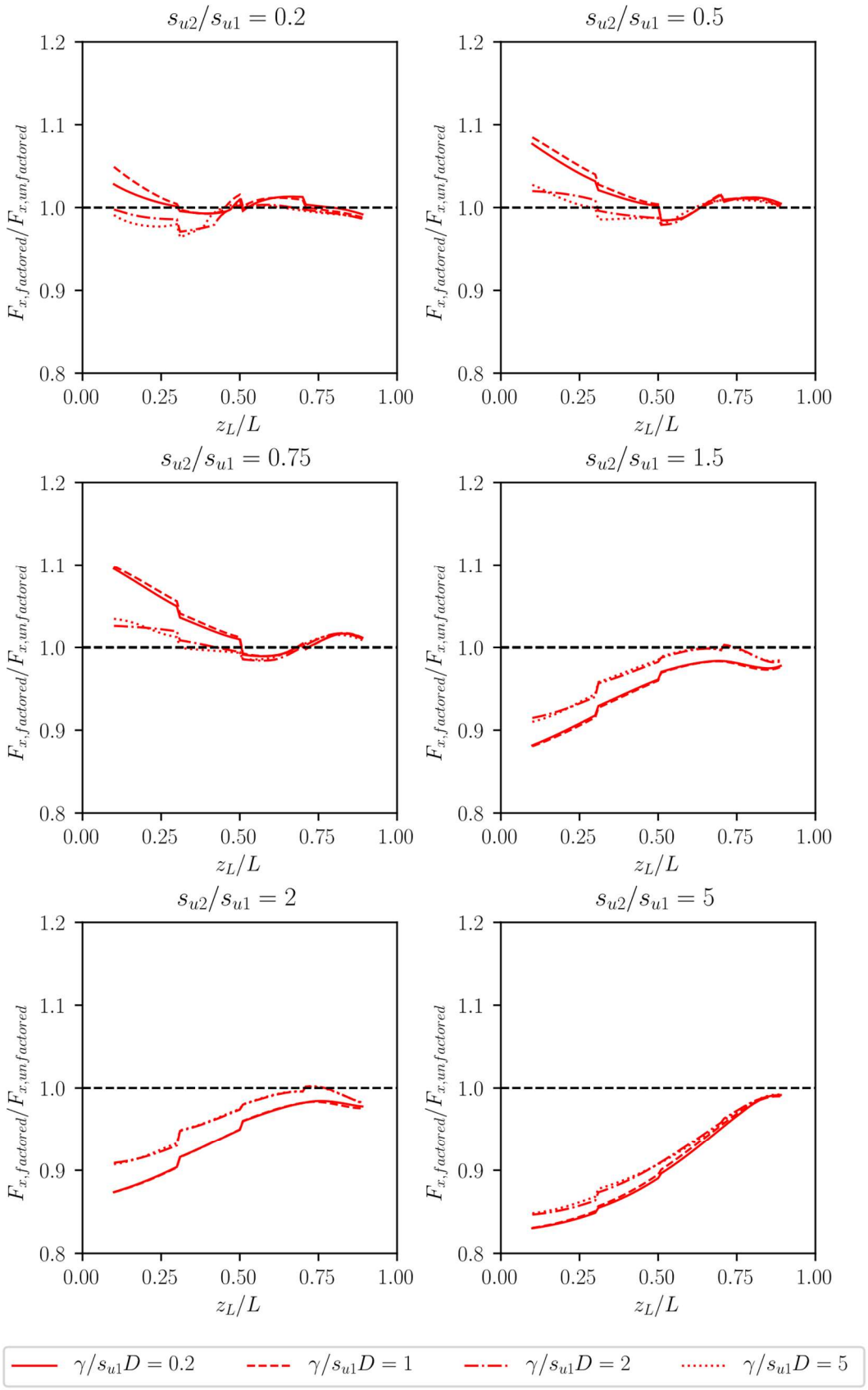

Figure 5.37 - Change in calculated total lateral resistance using a linear increase in resistance and the values of N_{pt} in Table 5.4. Lateral resistance values have been calculated using moment equilibrium, L/D = 5, α = 1, and no interface tension for varying s_{u2}/s_{u1} and $\gamma D/s_{u1}$

Table 5.4 - Summary of limits for N_{ptw} and z_t/D

Parameter	Wedge	Flow-around
$N_{ptw} = C\frac{N_p}{N_{p,flow}}$	$s_{u1} > s_{u2}$	
	$1.3 < C < 2$	$C = 1.3$
	$s_{u1} < s_{u2}$	
	$1 < C < 1.3$	$C = 1.3$
$\frac{z_t}{D}$	$s_{u1} > s_{u2}$	
	$1 < \frac{z_{tw}}{D} < 8$ $0.5 < \frac{z_{ts}}{D} < 1$	$\frac{z_{tw}}{D} = 1$ $\frac{z_{ts}}{D} = 1.5$
	$s_{u1} < s_{u2}$	
	$0.5 < \frac{z_{tw}}{D} < 1$ $1 < \frac{z_{ts}}{D} < 8$	$\frac{z_{tw}}{D} = 1$ $\frac{z_{ts}}{D} = 1.5$

5.3. Embedded Layers

In this section, analyses are performed on soil profiles of a high or low strength layer of soil embedded into homogeneous soil: as shown in Figure 5.1(c). The purpose of this assessment is to provide insight into the effect of having two-layer boundaries close together and the potential for interaction to occur between them. This scenario regularly occurs in areas with a complex depositional history.

In this system there are two additional dimensionless groups to be considered: the relative thickness of the embedded layer, z_e/D, and the relative depth of the layer, z_L/D, where z_e and z_L are the thickness of and depth to the top of the embedded layer respectively. In this assessment, only the effect of an embedded layer in the flow-around zone will be considered: this removes consideration of the second dimensionless group, z_L/D. As was shown in the study on two-layered systems, layer boundaries occurring within the wedge mechanism normalise to be similar to the flow-around case; see Figure 5.24 and Figure 5.33. This similarity increases with

increased normalised depth and as the weight to strength ratio, $\gamma D/s_u$, of the soil increases. As such, limiting the study to the flow-around mechanism will provide enough insight into this scenario to form some basic rules for how N_p profiles can be modified to accommodate this scenario. It should be noted that flow around conditions are unlikely to be achieved for the low L/D monopile foundations used to support offshore wind turbines, and as such the results herein may not be directly applicable to these foundation types. However, the work in the two layer section demonstrated that a high γ/s_uD returned similar variations in the normalised N_p profile to the flow around case and as such applying the findings of this work to monopiles should give some indication of the potential impact of embedded layers to a specific design prior to a bespoke assessment being performed for that foundation.

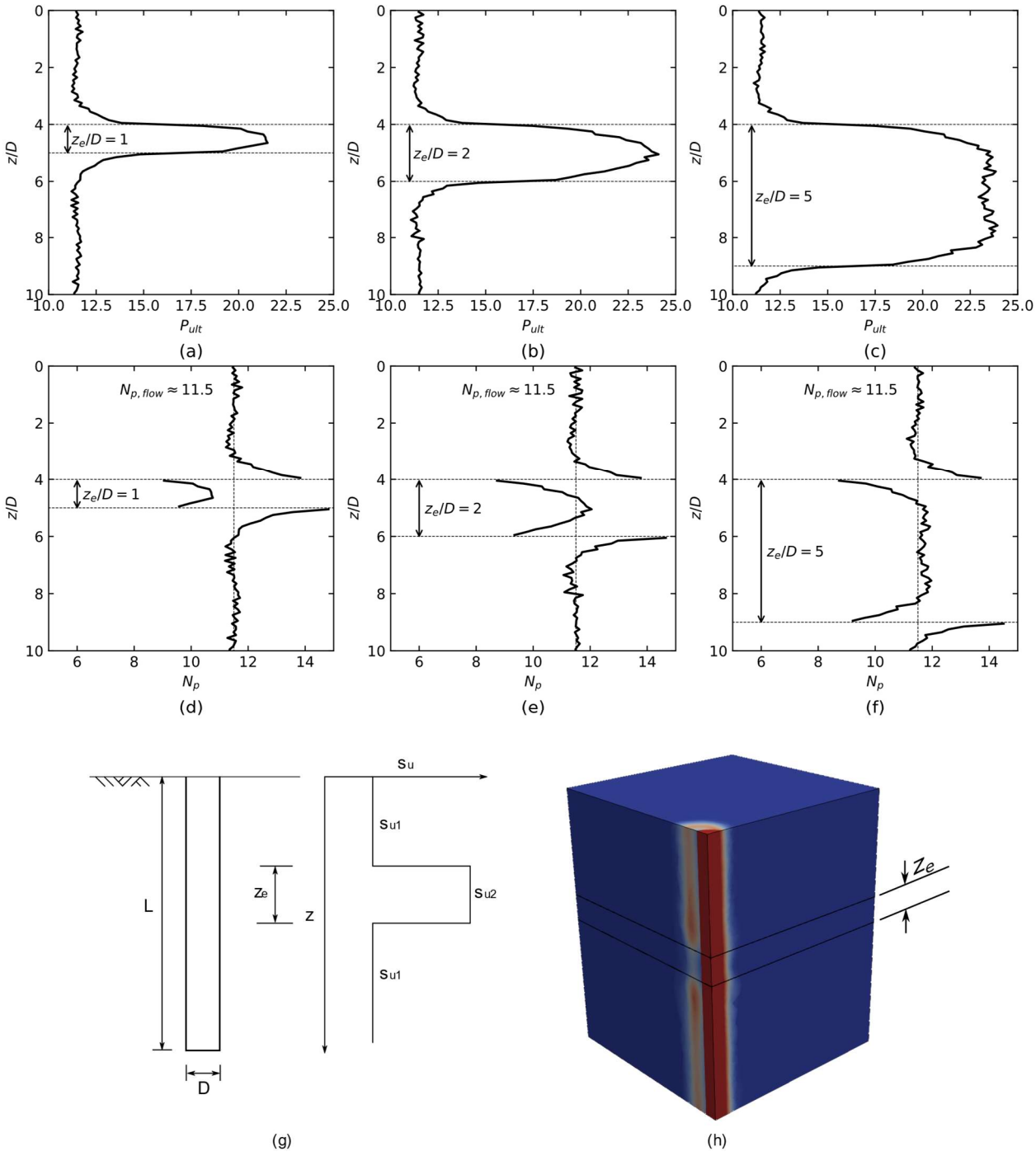

Figure 5.38 - Resistance variation across embedded layer for s_{u2}/s_{u1} = 2. Ultimate resistance, P_{ult}, for (a) z_e/D =1, (b) z_e/D =2 and, (c) z_e/D = 5, Lateral bearing factor N_p for (d) z_e/D = 1, (e) z_e/D = 2 and, (f) z_e/D = 5. Also shown (g) system schematic and (h) final velocity contour for z_e/D = 1

5.3.1. Results and Discussion

There are three distinct cases of N_p variation that occur for an embedded layer in an N_p profile. These cases are shown in Figure 5.38 for p_{ult}, subplots (a) to (c), and N_p, subplots (d) to (f). The results in Figure 5.38 are for $s_{u2}/s_{u1} = 2$, i.e. an embedded layer with twice the strength of the surrounding soil. The first three subplots, (a) to (c), show the distribution of p_{ult} from the analysis. In each case, the variation of p_{ult} is apparently continuous across the layer boundaries with the value of p_{ult} in the embedded layer reaching a maximum resistance of twice that of the surrounding soil. The first potential outcome of having an embedded layer, shown in Figure 5.38 (d), is when the thickness of the layer is relatively small: a normalised thickness of $z_e/D = 1$ is shown in this example. For $s_{u2} > s_{u1}$ this results in a resistance in the embedded layer that is always less than the reference case: for these results the reference case is the resistance of the flow-around mechanism, i.e. $N_p \approx 11.5$ for these analyses. Conversely, for $s_{u2} < s_{u1}$ the resistance in the embedded layer is always above that of the reference case. As z_e/D increases the resistance in the embedded layer increases, or decreases if $s_{u2} < s_{u1}$, until it has resistance at the centre of the embedded layer equal to the reference case. An example of this is shown in subplots (d) of Figure 5.38 where $z_e/D = 2$. For $z_e/D = 2$ the variation of N_p across each layer boundary starts to closely resemble that of an isolated layer boundary, such as those reviewed in the previous section of this chapter (see Figure 5.24). Increasing z_e/D further, such as to $z_e/D = 5$ as shown in Figure 5.38 (f), results in the mechanisms from each layer boundary separating. This leads to the majority of the resistance in the embedded layer being equal to the refence case of $N_{p,flow}$ with the variations at the top and bottom being the same as for the single layer boundary cases.

Similar to the single layer boundary case the ratio of strength between he embedded layer and surrounding soil will have an effect on the amount of change from the reference N_p. Results for $0.2 \leq s_{u2}/s_{u1} \leq 5$ for $z_e/D = 0.5$, 1, 2 and, 5 are shown Figure 5.39 and Figure 5.40 for $s_{u2} > s_{u1}$ and $s_{u1} < s_{u2}$ respectively. As was seen with the single layer boundaries in the previous section,

variation of s_{u2}/s_{u1} has no effect on the increase in resistance that occurs in the weaker layer, i.e. the surrounding soil for $s_{u2}/s_{u1} > 1$ and the embedded layer for $s_{u2}/s_{u1} < 1$. The only exception to this appears to be at $z_e/D = 0.5$ for $s_{u2}/s_{u1} < 1$; shown in Figure 5.40 (a). In this case the analysis is indicating a variation in the obtained N_p profile in the embedded layer, however this variation is very small with variation of N_p between different s_{u2}/s_{u1} ratios being <1%. In all other cases, the N_p profiles in the weak layer show no variation with a maximum increase in resistance to approximately N_p=15, i.e. a 30% increase over the equivalent flow-around resistance ($N_{p,flow} = 11.5$).

In the stronger layer, whether the embedded layer for $s_{u2}/s_{u1}>1$ or surrounding soil for $s_{u2}/s_{u1}<1$, the reduction in resistance that occurs clearly varies with s_{u2}/s_{u1}. At the layer boundaries, the reduction in resistance ranges from 25% to 50% for $s_{u2}/s_{u1} = 2$ to 5 respectively. This reduction is the same as was observed for the single layer boundary case and is consistent across all values of z_e/D. For $s_{u2}/s_{u1} > 1$ the maximum possible resistance in the embedded layer varies with s_{u2}/s_{u1}. At low values of z_e/D, e.g. $z_e/D = 0.5$ shown in Figure 5.39 (a), the variation of the maximum N_p at the centre of the layer between different s_{u2}/s_{u1} values is roughly the same as the variation that occurs at the layer boundary. For $z_e/D = 0.5$ This leads to maximum resistances in the embedded layer of 50% to 75% of $N_{p,flow}$ for $s_{u2}/s_{u1} = 5$ and 2 respectively. As z_e/D increases, the resistance at the centre of the embedded layer starts to converge on the reference N_p value and no longer exhibits the variation observed for lower z_e/D.

The variation of N_p at the centre of the embedded layer for varying layer thicknesses is shown on Figure 5.41: Figure 5.41 (a) shows the results for $s_{u2}/s_{u1} > 1$ while Figure 5.41 (b) shows $s_{u2}/s_{u1} < 1$. For $s_{u2}/s_{u1}>1$ it is evident that $z_e/D < 2$ will lead to a reduced maximum N_p in that layer. Above $z_e/D = 2$ it is interesting to note that the analysis shows a consistent increase above the reference case of $N_{p,flow} = 11.5$. This occurs as the conditions at the centre of the layer have not reached the plane strain state required to cause the minimum resistance that the flow-around resistance represents.

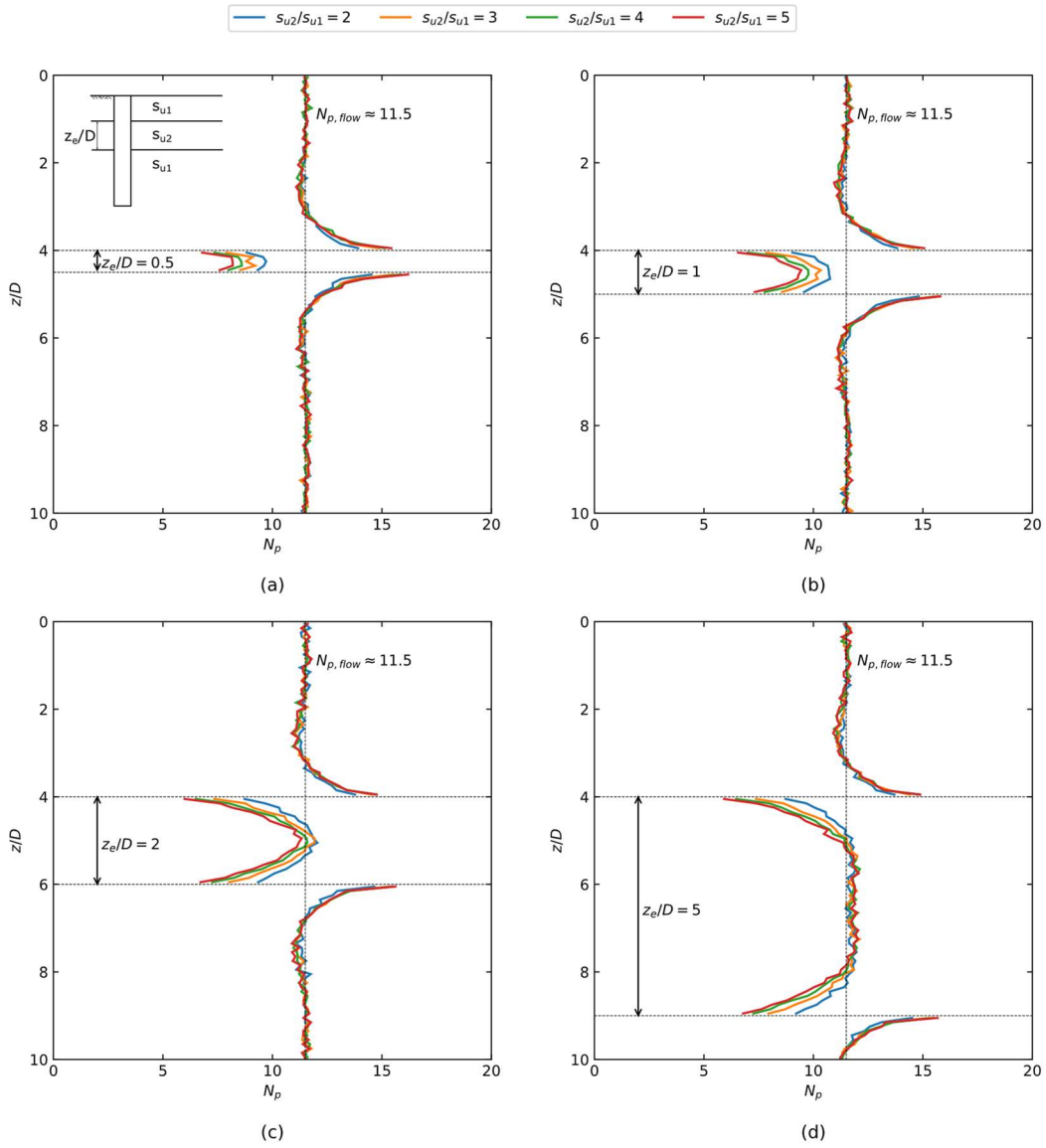

Figure 5.39 - Resistance variation across embedded layer in flow-around mechanism, α = 0.5, $s_{u2} > s_{u1}$ for (a) $z_e/D = 0.5$, (b) $z_e/D = 1$, (c) $z_e/D = 2$ and, (d) $z_e/D = 5$

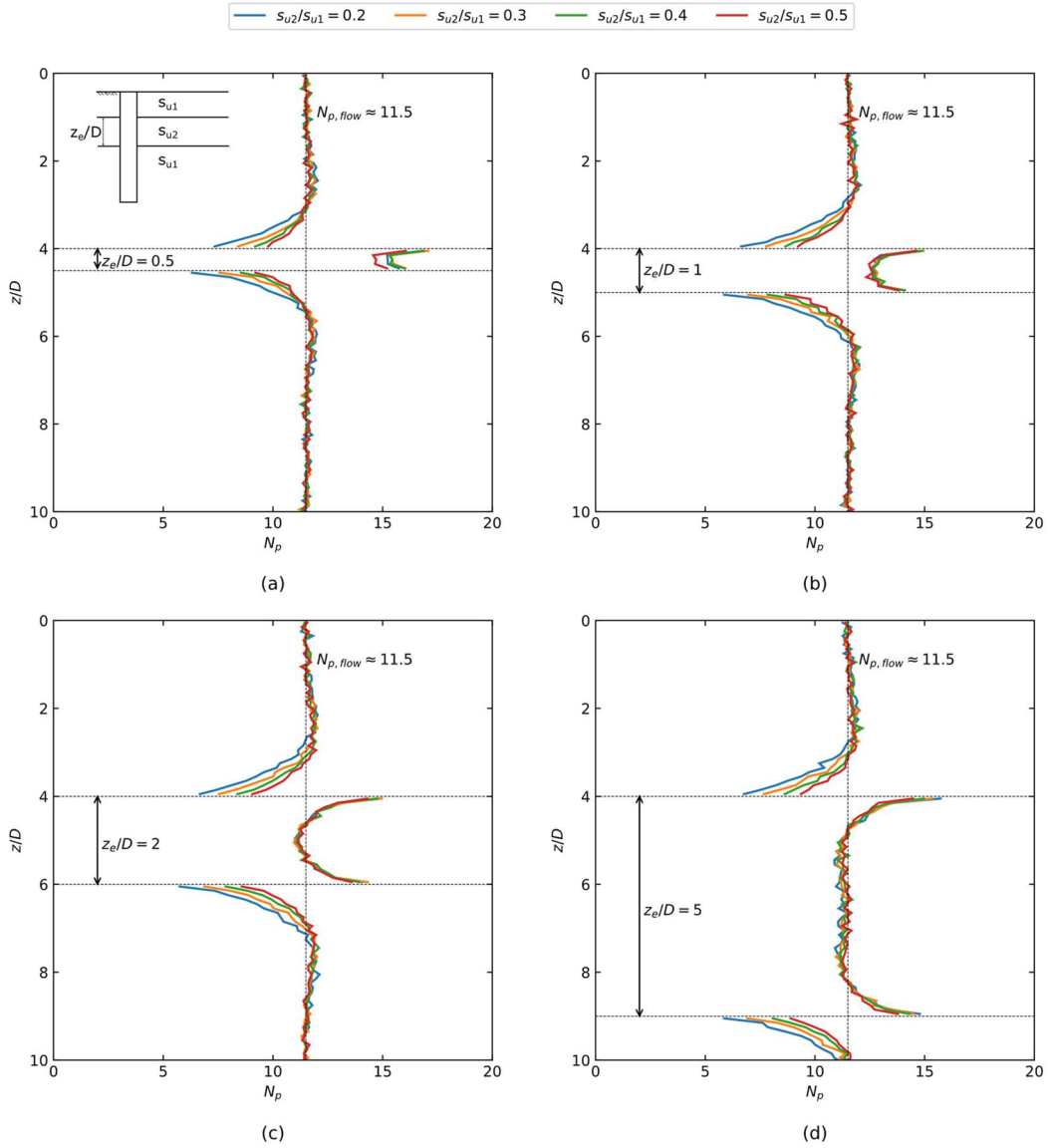

Figure 5.40 - Resistance variation across embedded layer in flow-around mechanism, α = 0.5, $s_{u2} < s_{u1}$ for (a) $z_e/D = 0.5$, (b) $z_e/D = 1$, (c) $z_e/D = 2$ and, (d) $z_e/D = 5$

As was noted in the previous section the deviation of N_p for flow-around conditions near a layer boundary predominantly occurs over $z/D = 1$ away from the boundary. However, at $1D$ and $3D$ away from the boundary a small increase or decrease from the reference N_p is observed for the strong and weak layers respectively; see discussion on Figure 5.24. These observations of the distance from the layer boundary that gets influenced match well with the results shown in Figure 5.41. At $z_e/D = 2$, i.e. twice the depth that most of resistance change occurs over for a single layer boundary, the resistance at the centre of the embedded layer is close to the reference

and either increases or decreases slightly from it as z_e/D increases. At $z_e/D = 6$, i.e. twice the total depth that a layer boundary was observed to affect the N_p profile, the resistance at the centre of the embedded layer matches the resistance of the reference case.

5.3.2. Implications for design

There are several key implications from this study:

- When $z_e/D \geq 2z_t/D$ the embedded layer behaves as though it has two separate layer boundary mechanisms, i.e. the mechanisms are distinct and there is no increase or reduction in capacity.
- For $s_{u2} > s_{u1}$ and $z_e/D < 2z_t/D$, i.e. with $z_t/D = 1$, the capacity in the embedded layer does not reach its maximum value. The reduction in capacity is dependent on the thickness of the layer with thinner layers leading to a greater reduction in capacity. In the surrounding soil, the increase in resistance for both the upper and lower layers matches that of the increase observed for a single layer boundary. This increase is the same irrespective of the thickness of the embedded layer.
- For $s_{u2} < s_{u1}$ and $z_e/D < 2z_t/D$ the capacity in the embedded layer is increased above the reference capacity. As z_e/D decreases this capacity approaches the maximum $N_{p,tw}$ observed for the single layer boundary cases reviewed in the previous section. In the surrounding soil, the decrease in resistance for both the upper and lower layers matches that of the increase observed for a single layer boundary. This decrease is the same irrespective of the thickness of the embedded layer.

From the above it can be seen that embedded layers can be both beneficial and detrimental to a piles capacity. The case presented here is a very simplified version of a much more complicated problem. In reality embedded layers would be representative of other scenarios such as a sand or gravel layer embedded into clay or a system with three distinct shear strengths. The first of these scenarios, i.e. having a granular layer within a cohesive, is currently not possible in

OxLim3D. FELA methods in 3D are currently limited to very simple constitutive models and as such modelling of granular materials is not practical. The latter scenario simply has too many combinations to allow simple presentation of results.

It should also be noted that this study was limited in scope to only the flow-around mechanism. As has been shown in the two-layer study, locating the layer boundaries in the wedge mechanism can lead to even greater reductions in capacity which occur over much greater depths. However, as with the study of layered profiles with three distinct shear strengths, performing a general study on this mechanism becomes impractical to present within the constraints of this thesis.

From the results presented in this section, the following rules can be recommended:

- For embedded layers of thickness $z_e/D > 2z_t/D$, where z_t/D is selected based on Table 5.3, no change in capacity is required and the transitions around the layer boundary can be modelled as separate layer transitions, i.e. using the methods established in Section 5.2.
- For embedded layers of thickness $z_e/D < 2z_t/D$, the capacity should be reduced or increased by the relevant value shown in Figure 5.41. Note that the values provided in Figure 5.40 represent the midpoint value of N_p for an embedded layer as opposed to an averaged resistance over the depth of the embedded layer. As such this will result in a small overprediction for $s_{u2}/s_{u1} > 1$ and an underprediction for $s_{u2}/s_{u1} < 1$.

For all cases not covered by this simple rule, such as the alternate soil profiles noted previously, it is recommended that either FEA or FELA or a translating pile is performed to establish the p_{ult} profile.

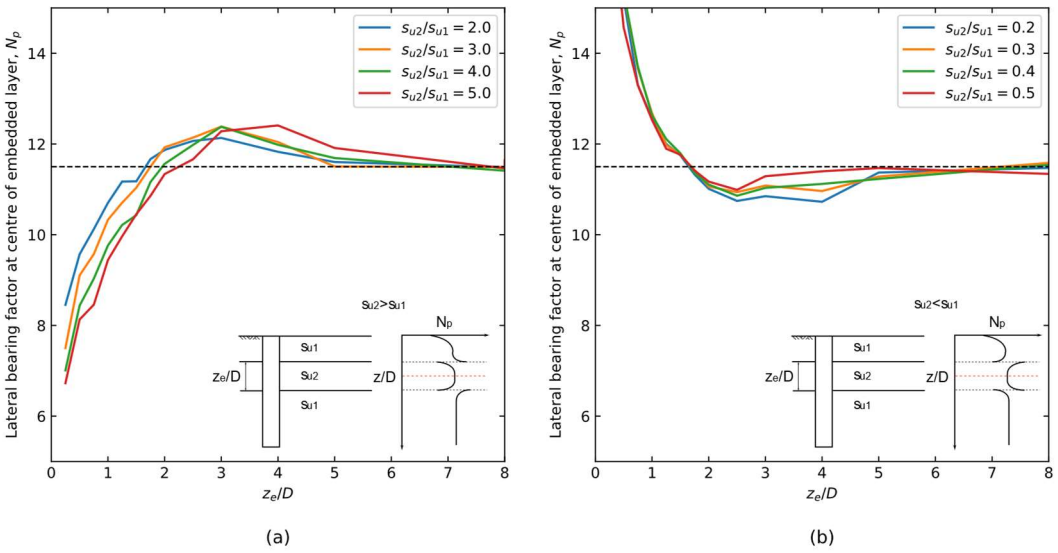

Figure 5.41 - Lateral bearing factor at centre of embedded layer for (a) $s_{u2} > 1$ and (b) $s_{u2} < 1$

Chapter 6

Detailed investigations of components of lateral resistance

This chapter focuses on other resistance features that have an influence on the total capacity of a pile. Some of these features have been discussed briefly in previous chapters, for example the discussion on base shearing in Chapter 4, however the aim of this chapter is to present each case in greater detail and provide insight into how each feature can be accounted for when calculating the capacity of a pile. The four resistance features presented in this chapter are:

(i) the lateral resistance at the ground surface

(ii) the lateral bearing factor increase near the pile toe,

(iii) base shear and moment resistance, and

(iv) distributed moments on the exterior of the pile

6.1. Lateral Resistance at ground surface

This section investigates the lateral resistance that occurs at the ground surface. From the modelling in the previous chapters it is clear that the lateral bearing factor at the ground surface varies, see Figure 4.9(b) and Figure 5.13. The lateral bearing factor at the ground surface, henceforth referred to as $N_{p,surface}$ (see Figure 6.1), can vary significantly depending on the conditions specified; namely whether interface tension occurs and the pile-soil adhesion ratio. The methods in the literature typically take a simplified view with the value at the surface being considered constant irrespective of interface conditions, e.g. the Matlock (1970) approach prescribes a value of $N_p = 3$ at the ground surface. The Jeanjean et al. (2017) approach does not

explicitly consider a change of N_p at the ground surface, i.e. the value of N_2 in the formulation (see Equation 2.17) is taken as $N_2 = 3$ for all cases. However, the Jeanjean formulation (see Equation 2.17) does include a variation at surface from pile-soil adhesion, due to the inclusion of $1 - \alpha$ in the calculation of N_{p0}. This leads to a variation of $2 \leq N_{p,surface} \leq 3$ for $0 \leq \alpha \leq 1$.

To facilitate the assessment of the lateral bearing factor at the ground surface a different parameterised OxLim model to those used previously has been used. This model has the pile extending over the entire depth of the soil domain, i.e. the pile toe is coincident with the base of the soil domain, with a symmetry boundary condition imposed at the base of the model. This allows exclusion of the internal soil column from the model permitting a greater mesh density in the soil around the pile and hence a reduction in bracketing error. Similar to the previous studies, both quarter and half models have been considered depending on the conditions being assessed; i.e. a quarter model is used for full tension modelling and half models for other cases. A schematic of boundary conditions are shown in Figure 6.1(a), of the modelling conditions used is shown in Figure 6.1(b) and an example of one of the adaptively refined meshes for a quarter model is shown in Figure 6.1(c).

Both homogeneous and strength proportional to depth profiles have been considered with the following three scenarios being modelled for each strength profile:

1. Full interface tension
2. No interface tension in weightless soil
3. No interface tension with $\gamma D/s_u$ or γ/ρ as appropriate varying between [0.2, 5]

In each scenario values of α between 0 and 1 (at intervals of 0.1) have been considered. The total depth of the model has been set deep enough to allow the full wedge mechanism to form for each model. For each case investigated in this section the depth used has been based on the results presented in Chapters 4 and 5. For example, for case HXTWn the depth of the model

has been set to 4D based on the results in Figure 4.1. Table 6.1 shows the model depths used for each scenario.

Table 6.1 - Summary of model depths used to investigate N_p at surface

Scenario	Model Depth
HXTWn	5
LXTWn	5
HXNWi ($\gamma = 0$)	10
LXNWi ($\gamma = 0$)	10
HXNWi ($\gamma \neq 0$)	6
LXNWi ($\gamma \neq 0$)	8

In the analyses described in Chapters 4 and 5, the circular cross section of the pile was segmented into 20 facets in the full circle; i.e. 10 facets in the half model and 5 in the quarter model. In this section this amount has been doubled to 40 facets in the full circular section. This has been performed to reduce the potential over-estimation of resistance that occurs from segmenting the pile cross section in this way; see Section 3.2.1. The rigid body representing the pile in the OxLim model has been subdivided vertically into individual sub-elements 0.1D in length.

6.1.1. Results and discussion

Results for $N_{p,surface}$ when full interface tension is used are shown in Figure 6.2(a) and (b) for homogeneous, HXTWn, and strength proportional to depth, LXTWn, conditions. The values shown in Figure 6.2 have been obtained from the top sub-element of the pile and as such represent the average N_p over the top 0.1D of the pile. In practice this will result in a lateral bearing factor slightly above the actual value at ground level. An attempt was made to account for this by performing a curve fit to the results using Equation 6.1, which is a modification of Equation 2.17 (Jeanjean et al., 2017) with the α term removed. The curve fit was performed using the differential evolution optimisation method (Storn and Price, 1997) present in the SciPy Python package.

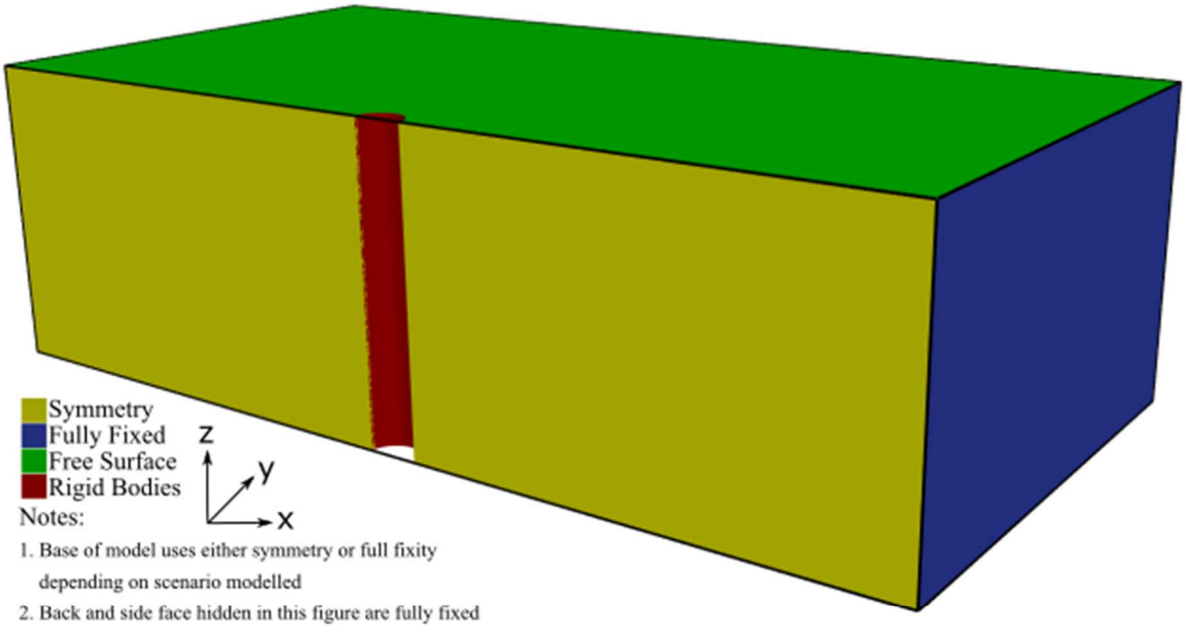

(a)

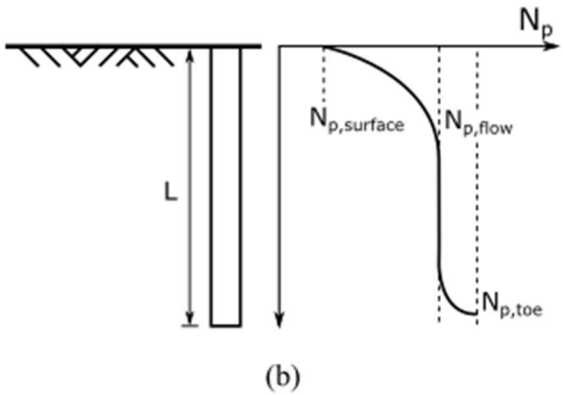

(b)

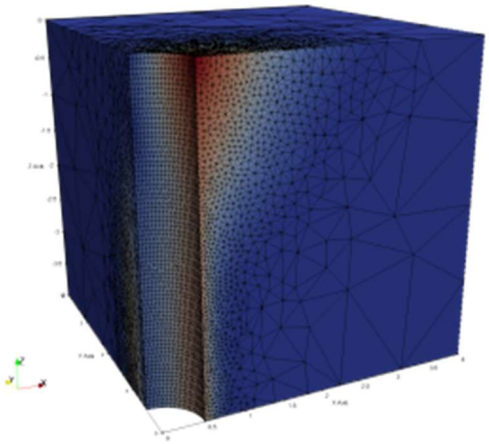

(c)

Figure 6.1 - (a) schematic of boundary conditions for near surface resistance analysis note that the bottom of the model uses a symmetry boundary condition, (b) Schematic showing key values of Np and (c) example mesh with contours of velocity from upper bound analysis

$$N_{p0} = N_1 - (N_1 - N_2)\left(1 - \left(\frac{z}{dD}\right)^{x_1}\right)^{x_2} \tag{6.1}$$

$$d = x_3 - x_4 log(\lambda) \tag{6.2}$$

where x_1, x_2, x_3, and x_4 are optimisation parameters. To perform the curve fit N_1 and N_2 have also been used as optimisation parameters, i.e.

$$\boldsymbol{x} = [x_1, x_2, x_3, x_4, N_1, N_2] \tag{6.3}$$

The optimisation function then takes the following form

$$f(\boldsymbol{x}) = \sum_{i=1}^{N} \frac{1}{N} \sqrt{\left| \frac{OxLim_i^2 - Jeanjean_i^2}{OxLim_i^2} \right|} \tag{6.4}$$

where N is the number of data points from the OxLim modelling, i.e. equivalent to the number of rigid bodies in the depth being assessed (10 times the L/D of the model in these analyses), and $Jeanjean_i$ is the value of Equation 6.1. at the depth of the OxLim data point. Figure 6.3 shows the results of using this curve fit for HXTWn. The curve fit shows a clear reduction in $N_{p,surface}$ compared to using the N_p of the top sub-element. However, this method results in an increased variability when compared to the results from the top sub-element. For HXTWn this variability does not appear to be overly significant, however this variability increases

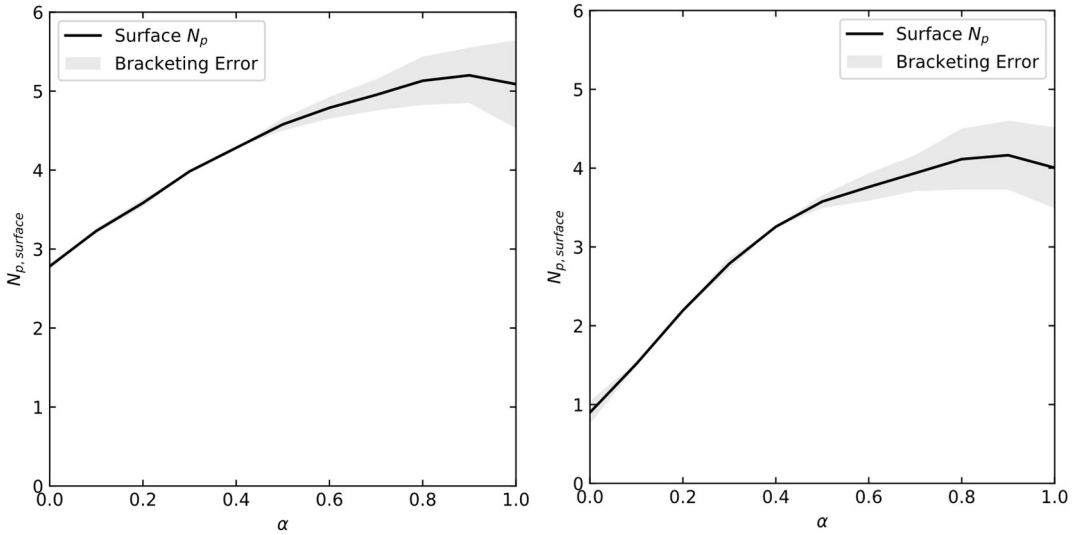

Figure 6.2 - Variation of lateral bearing factor at ground surface, $N_{p,surface}$, for full interface tension in (a) homogeneous conditions and (b) linearly increasing strength

significantly for the other scenarios where a half model is used and the bracketing error is increased from the increased model size and decreased mesh density.

While the reduction in N_p predicted is evident, the increased variability acted to obfuscate the results when no tension and soil with unit weight were considered. As such, all further results in this section will be presented using the N_p from the top sub-element. The comparison to $N_{p,surface}$ from the curve fit in Figure 6.3 suggests that the difference between $N_{p,surface}$ and N_p of the top sub-element, i.e. N_p at 0.05D, is 0.4 to 1.5 and if needed N_p values obtained from the top sub-element could simply be reduced by a value in this range to accommodate this difference; a reduction of 1 is tentatively proposed.

The results in Figure 6.2 indicate that for both cases the pile-soil adhesion has a clear effect on the resistance at the surface. For homogeneous conditions the surface lateral bearing factor varies from $N_{p,surface}$ = 2.78 when α = 0 to $N_{p,surface}$ = 5.2 when α =1. For the linearly increasing strength profiles the surface lateral bearing factor varies between $N_{p,surface}$ = 0.9 when α = 0 to $N_{p,surface}$ = 4.0 when α = 1, though it should be noted that as α starts increasing above 0.5 the bracketing error increases up to 15% when α = 1. The drop in N_p from α = 0.9 to α = 1.0 is likely to be from the larger error and not representative of the actual change in $N_{p,surface}$ as α increases.

Results for varying the unit weight of the soil with no interface tension, characterised by the ratios $\gamma D/s_u$ and γ/ρ, are shown in Figure 6.4(a) and (b) for homogeneous, HXNWi, and strength proportional to depth, LXNWi, conditions respectively. In both cases the results from the full tension modelling shown in Figure 6.2 are included for comparison. For HXNWi the results indicate that variation of $\gamma D/s_u$ has only a minor effect on the resistance at the surface. In Chapter 4 it was shown that $\gamma D/s_u$ = 5 results in a profile of N_p very similar to HXTWn with the transition from wedge to flow-around failure occurring at the same depth in both cases. From

the results in Figure 6.4(a) it is apparent that at the surface the two cases have different lateral bearing factors with $\gamma D/s_u = 5$ having $N_{p,surface} = 1.6$ and 3.7 for $\alpha = 0$ and 1 respectively,

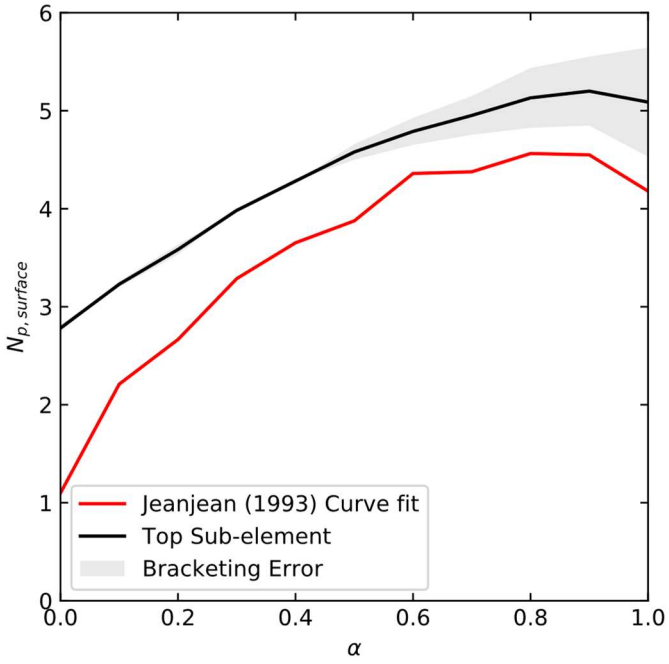

Figure 6.3 - Comparison of curve fit to Jeanjean et al. (2017) method to bearing factor in top sub-element of pile

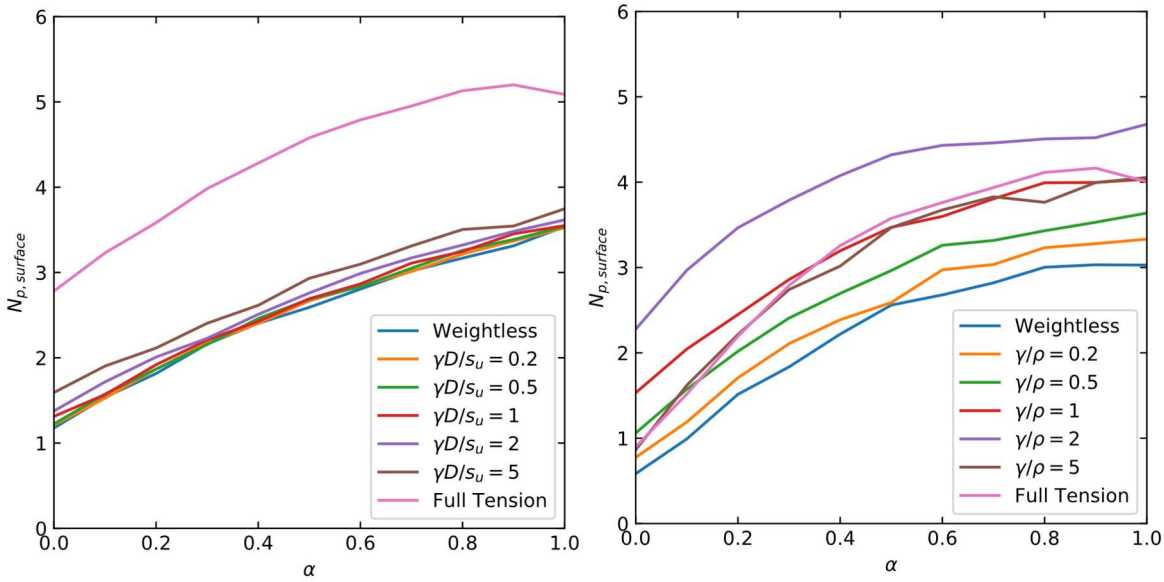

Figure 6.4 - Effect of varying soil unit weight on lateral bearing factor at ground surface for (a) homogeneous conditions and (b) strength proportional with depth

resulting in differences of 1.18 and 1.5 from the full tension case for $\alpha = 0$ and $\alpha = 1$. For $\alpha = 0$ this roughly fits the assumption in Jeanjean et al. (2017) that the full interface tension capacity would be twice that of the no interface tension scenario. For this case, the change in $N_{p,surface}$ with α can be approximated as a linear relationship

$$N_{p,surface} = \begin{cases} 2.78 + 2.42\alpha & Full\ interface\ tesnion \\ 1.6 + 2.1\alpha & No\ interface\ tension \end{cases} \quad (6.5)$$

The effect of varying γ/ρ on the resistance at surface is shown in Figure 6.4 (b). The results show much greater variability than observed for the homogeneous case: both α and γ/ρ show a significant influence on the value of $N_{p,surface}$. Of interest is that for these soil conditions the resistance at the surface is not highest for the full tension case but for no tension with $\gamma/\rho = 2$. It is not clear what mechanism is causing the resistance of some cases to be higher than the full tension case. As with previous analysis it is typically expected that the resistance will be limited to the resistance of the full tension case. Review of the model outputs does not reveal any obvious explanation for this increase in resistance that is related to the modelling process. However it is potentially the case that the increase in resistance above the full tension case is due to the parameter selection, i.e. a strength gradient with no surface strength, resulting in behaviour that is unlikely to occur in practice. Indeed, the deformed mesh for $\gamma/\rho = 5$, shown in Figure 6.5(f), indicates that the soil near the ground surface starts to collapse before the gap lower down the pile starts to close. In practice, both the strength gradient and surface shear strength will be greater than zero and that the variation of $N_{p,surface}$ will vary between the constant shear strength and strength gradient results shown in Figure 6.4. As such the $\gamma/\rho = 2$ and $\gamma/\rho = 5$ are potentially unrepresentative of real conditions.

Deformed meshes and velocity contours for the full tension case and no tension case with $\gamma/\rho = 2$ and $\gamma/\rho = 5$ are shown in Figure 6.5; undeformed meshes with velocity vectors for each case are shown in Figure 6.5(a), (c) and (e) with deformed meshes shown in (b), (d) and (f). The

deformed mesh for HXTWn, shown in Figure 6.5(b), shows the behaviour typical of this scenario with a wedge of soil being pushed up in front of the pile and evidence of the flow-around mechanism being achieved from the vectors pointing towards the left hand side of the figure. If this case was performed using the half model then a wedge of soil being pulled down at the back of the pile would also be evident from the deformed mesh. Figure 6.5(d) shows the deformed mesh for LXNWi, $\gamma/\rho = 2$. In these conditions the gap behind the pile extends deep into the model and the deformation near the ground surface resembles that from the LXNWi $\gamma/\rho = 0$ case, i.e. no tension with weightless soil (see Figure 5.18). For LXNWi $\gamma/\rho = 2$ no deformation is occurring in the soil behind the pile, i.e. the ratio of soil unit weight to strength gradient is not high enough for the soil to start collapsing onto the back of the pile. At some value between $\gamma/\rho = 2$ and $\gamma/\rho = 5$ the ratio becomes large enough for the soil to start collapsing onto the back of the pile, as shown for the deformed mesh of LXNWi $\gamma/\rho = 5$ in Figure 6.5(f). An interesting aspect of the wedge behaviour is that the gap closes at the top of the pile but remains open further down beginning at a depth of approximately $z/D = 2$.

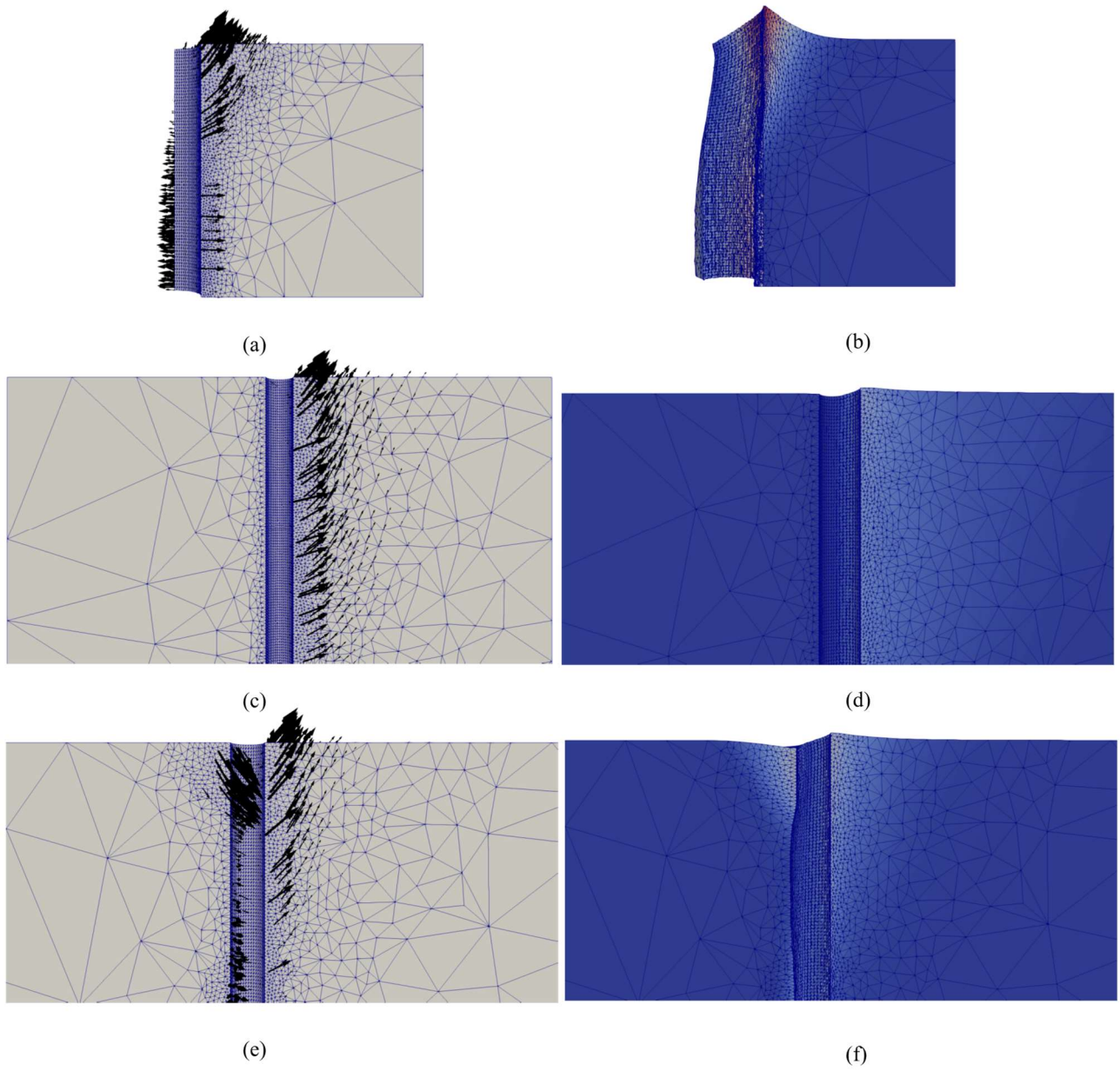

Figure 6.5 – Undeformed mesh with velocity vectors and deformed meshes with velocity contour for (a) and (b) LXTWn, (c) and (d) LXNWi, γ/ρ = 2, (e) and (f) LXNWi γ/ρ = 5

Similarly to Equation 6.5 for the homogeneous case, a linear equation, can be used to approximate the change of $N_{p,surface}$ with α. However, due to the uncertainty around the results greater than the full tension case the linear estimation will exclude the $\gamma/\rho = 2$ and $\gamma/\rho = 5$ results. Taking the average through the remaining results gives

$$N_{p,surface} = 2.56\alpha + 0.9 \tag{6.6}$$

6.2. Lateral bearing factor increase near pile toe

This section presents the analysis, results and conclusions from an investigation of the increase in lateral bearing factor that occurs near the toe of a pile. This feature of resistance was observed in the analyses performed for homogeneous and linearly increasing strength profiles in Chapter 4 and Chapter 5 respectively. This work showed that near the toe of the pile there was a consistent increase in resistance above the reference resistance, i.e. $N_{p,flow}$ when the toe is in the flow-around mechanism or N_p when the toe is in the wedge (see Figures 4.1, 4.5, and 5.13). The only reference in the literature known to the author about this increase in resistance is in Broms (1964) where the author makes a passing statement about the expected resistance based on comparisons to the bearing pressures on rigid footings. For a rigid footing on elastic soil the bearing stress acting on the foundation is known to increase towards the edge of the footing. Broms (1964) reasoned that the same would be true for piles as the toe of the pile was approached. The profile that Broms (1964) theorised would occur are shown in Figure 6.6 for both fixed and free head piles. Subsequent literature does not appear to have revisited this idea however this is predominantly due to a focus in the industry on long slender piles where the increase in lateral resistance near the toe of the pile is typically inconsequential to the total pile resistance.

This investigation focuses on several cases that are representative of the scenarios most likely to occur in practice. These are the increases that occur when the toe of the pile is (i) in the flow-around zone and (ii) near the base of the wedge when no interface separation can occur. No scenarios involving gap formation have been reviewed. While cases of allowing gapping and low $\gamma D/s_{u0}$ or γ/ρ are of technical interest they result in behaviour that is not expected to occur in practice. Modelling with these conditions would potentially lead to gapping on the front face of the pile below the rotation point; a feature observed in the weightless soil modelling in Chapters 4 and 5. This is shown in the deformed meshes in Figure 4.8. In practice the self

weight of the soil will lead to this gap closing; such as shown in Figure 4.14. As such, modelling with full interface tension is considered sufficiently representative to provide a meaningful analysis of this resistance feature.

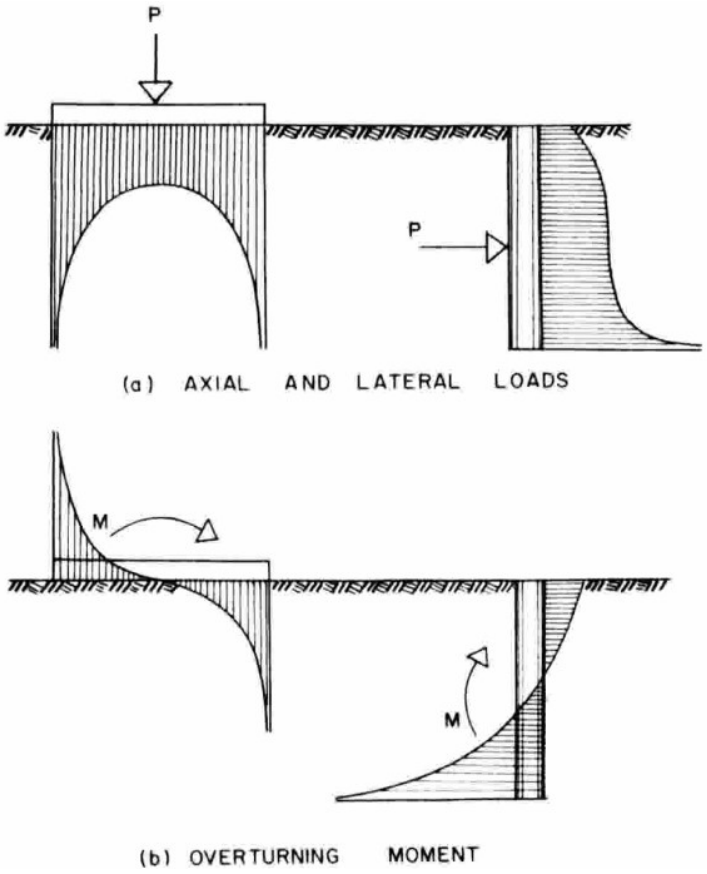

Figure 6.6 - Assumed distribution of soil reactions from Broms(1964) for (a) a fixed head pile and (b) a free head pile. The left hand side of the figure shows the bearing stress distributions for a shallow footing undergoing the equivalent loading case

To perform this study, the same parameterised model used for Section 6.1. has been adopted. However, to enable detailed study of the behaviour near the toe, the boundary conditions have been changed as follows:

- For analysis of the increase in lateral bearing factor that occurs when the toe is in the flow-around mechanism, the top boundary has been changed to a symmetry boundary condition to cause flow-around failure to occur at the top of the model. It should be noted that for cases where the soil strength is increasing with depth, this

is not truly representative of plane strain flow-around conditions: the top boundary symmetry in these soil conditions leads to behaviour similar to the two-layer scenario investigated in Section 5.2. Figure 6.7 shows the resulting change in resistance from using this boundary condition for a model with depth 6*D*. The aim of using this boundary condition is to increase the density of the mesh around the pile, thus ensuring a higher degree of accuracy when investigating local mechanisms. The depth that this boundary condition affects is approximately 2*D* from the top of the model. The depth that the toe kick mechanism occurs over is approximately 1*D*, meaning a total model depth of 6*D* is needed to minimise the potential for interaction between the top and bottom mechanisms. The alternative would be to have a free surface at the top of the model thus allowing the wedge mechanism to form. The model would have to be sufficiently long to ensure no interaction between the base of the wedge and increase near the toe; a depth of 8*D* would be likely needed at a minimum based on the observations in Chapter 5. This would lead to either a 30% increase in the number of tetrahedral elements required in the model, assuming the same mesh density, or a reduction in the mesh density resulting in an increase in the bracketing error.

- The base boundary has been changed from a symmetry boundary condition to a fixed boundary. This results in a rough interface at the base of the model which produces similar behaviour to models where the 'base' soil block (below the level of the pile toe) is included in the model geometry. As before, modelling this way allows the mesh to be created without the internal soil column; this significantly increases the number of tetrahedral mesh elements that can be located exterior to the pile.

It is typical in the literature for the flow-around mechanism to be treated as giving the maximum N_p that can be achieved, such as is done in Murff and Hamilton (1993) and Jeanjean et al.

(2017). However, it must be remembered that the flow-around mechanism is in fact the minimum collapse load that occurs under a specific set of conditions, i.e. plane strain. As has been shown in the analyses of an abrupt strength change in the flow-around zone (Section 5.2) having conditions that deviate from plane strain can cause significant increases or

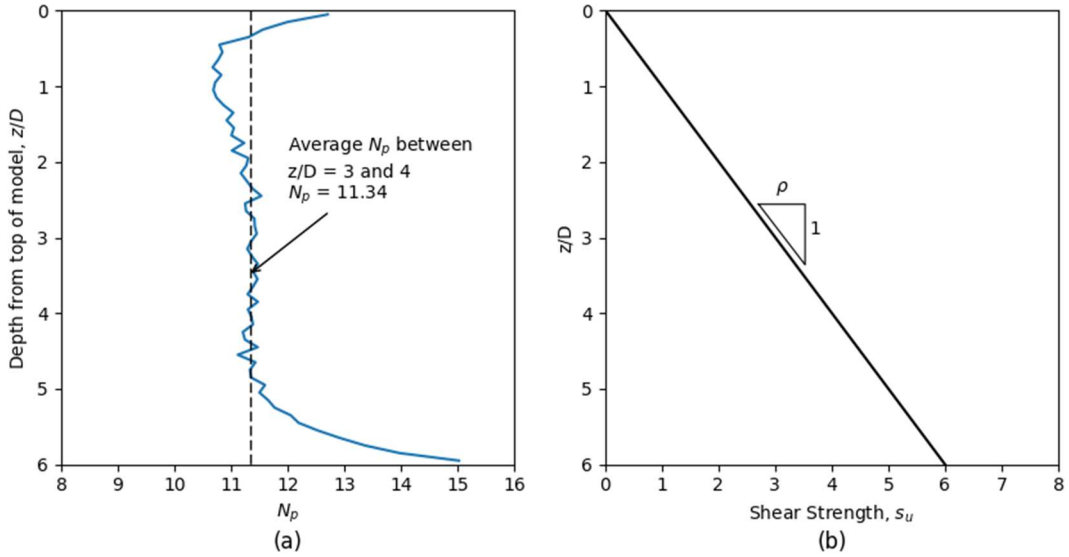

Figure 6.7 - Effect of using symmetry at top of model when using a strength gradient (a) resultsing N_p profile (b) shear strength profile

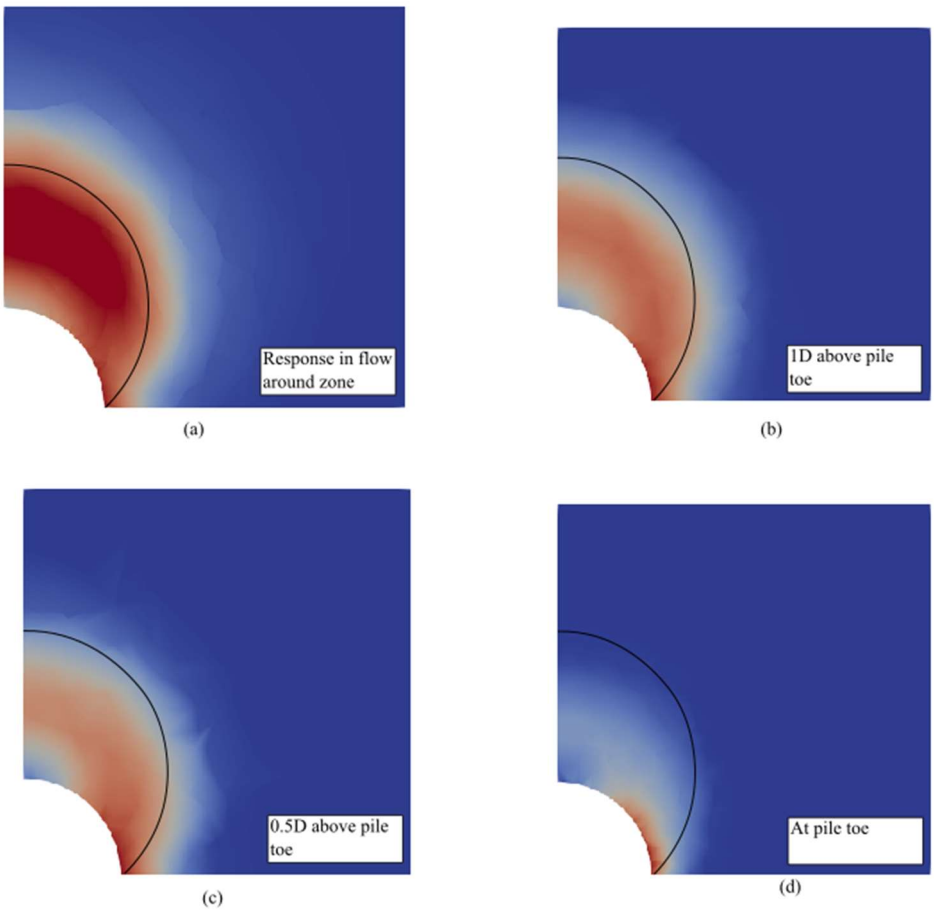

Figure 6.8 - Contours of velocity for (a) flow-around mechanism, (b) 1D above pile toe, (c) 0.5D above pile toe, and (d) at pile toe. Each subplot shows the approximate extents of the flow-around mechanism for comparison

decreases in N_p. In Section 5.2 the deviation from plane strain flow-around was caused by the change in soil strength. A similar situation occurs at the pile toe; as the pile toe is approached the soil behaviour no longer behaves in plane strain. At the pile toe, the deviation from plane strain conditions arises from the soil near the toe of the pile and beneath the pile transitioning from the flow-around mechanism to a state where there is no displacement in the soil. This is demonstrated in Figure 6.8 which shows the velocity contour on the X-Y plane at various depths from the model used to create Figure 6.7. Figure 6.8 shows how the velocity contours change from the flow-around mechanism in subplot (a) to a different mechanism at the pile toe in subplot (d). As the pile toe is approached the size of the mechanism and velocity of the soil around the pile decreases.

6.2.1. Results and discussion

Figure 6.9 shows the resulting profiles of N_p near the pile toe when the length of the pile is sufficient to locate the toe in the flow-around mechanism. Results are shown for HXTWn and LXTWn in Figure 6.9(b) and Figure 6.9 (c) respectively. Analysis has been performed using pile-soil adhesion values between 0 and 1. The increase at the toe is clear in these results with the amount of increase and the depth of the increase consistent across all values of α. Figure 6.9(d) shows all of the results normalised by the value of $N_{p,flow}$ for each case: $N_{p,flow}$ has been calculated here by taking the average resistance over the upper part of the model where N_p is constant. When normalised this way, it is clear that α has no influence on the relative increase of resistance near the toe of the pile. The results show very little deviation from the average value, marked on the figure as a red line, with the increase starting approximately z_b = 1D above the pile toe and N_p reaching a maximum increase of about 40% above $N_{p,flow}$.

For linearly increasing strength profiles, a dimensionless group that may influence the results is $\rho D/s_{u,base}$, i.e. the ratio of the strength gradient to the strength at the base. It should be noted that for simple linearly increasing strength profiles this parameter can be rewritten as

$$\frac{\rho D}{s_{u,base}} = \frac{\rho D}{s_{u0} + \rho L} \tag{6.7}$$

This implies that the group will have a range of $0 \leq \rho D/s_{u,base} \leq$ D/L with the upper limit of D/L occurring when s_{u0} = 0. Figure 6.10 shows the effect of varying this group on the lateral resistance near the toe. For these results a model using L/D = 8 was required to prevent interaction with the top surface at low $\rho D/s_{u,base}$: resulting in $0 \leq \rho D/s_{u,base} \leq 0.125$. The results show minimal variation of N_p with this dimensionless group; however this may be in part due to the narrow range of values that have been considered. Though based on the results obtained,

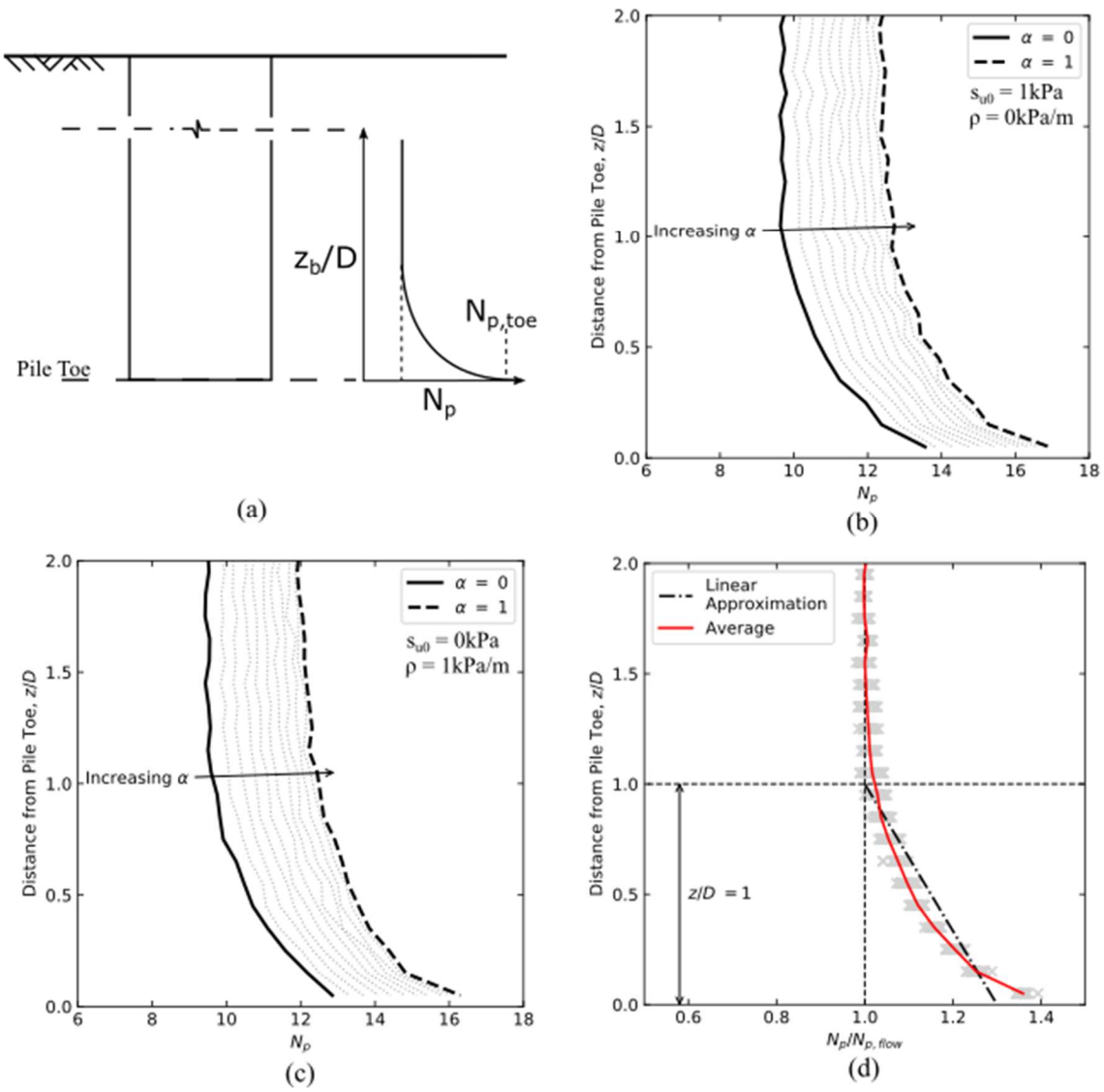

Figure 6.9 - Increase in lateral resistance acting on shaft near pile toe (a) expected case, (b) results for varying α in HXTWn, (c) results for varying α in LXTWn, and (d) method of approximating increase

it is not expected that an increased $\rho D/s_{u,base}$ will have a significant influence on the variation of N_p near the toe of the pile.

Results for the pile toe located in the wedge mechanism with full interface tension are shown in Figure 6.11. Figure 6.11 (a) and (c) show the N_p profiles for L/D = 2 and 3 respectively as dashed lines with the reference N_p profiles shown as a solid line. Results for both homogeneous and linearly increasing strength profiles are shown. Figure 6.11 (b) and (d) show the same

results when normalised by $N_{p,ref}$, focusing on the bottom 2D of the pile. The results indicate that the increase above $N_{p,ref}$ at the pile toe is consistent for the two strength profiles for both L/D ratios. There is a slight difference in the total increase at the pile toe between L/D = 2 and 3 with increases of approximately $N_p/N_{p,ref}$ = 1.25 and 1.3 for L/D = 2 and 3 respectively. Both of these are lower than the $N_p/N_{p,ref}$ = 1.4 observed for the pile toe in the flow-around mechanism: Figure 6.9 (d). As with previous studies, it is likely that the flow-around mechanism presents a limiting value for the increase in resistance; in this case a maximum possible increase. Results for L/D = 1, 2, 3, 4 and 5 with α between 0 and 1 are shown in Figure 6.12. The results show a significant amount of variation when compared to the flow-around case presented in Figure 6.10. This scatter is predominantly from changing L/D with some variation from pile-soil adhesion. The increase in resistance at the pile toe varies between $N_p/N_{p,ref}$ = 1.25 to 1.35 and as with the increase in the flow-around case occurs over a distance of z_b = 1D from the pile toe.

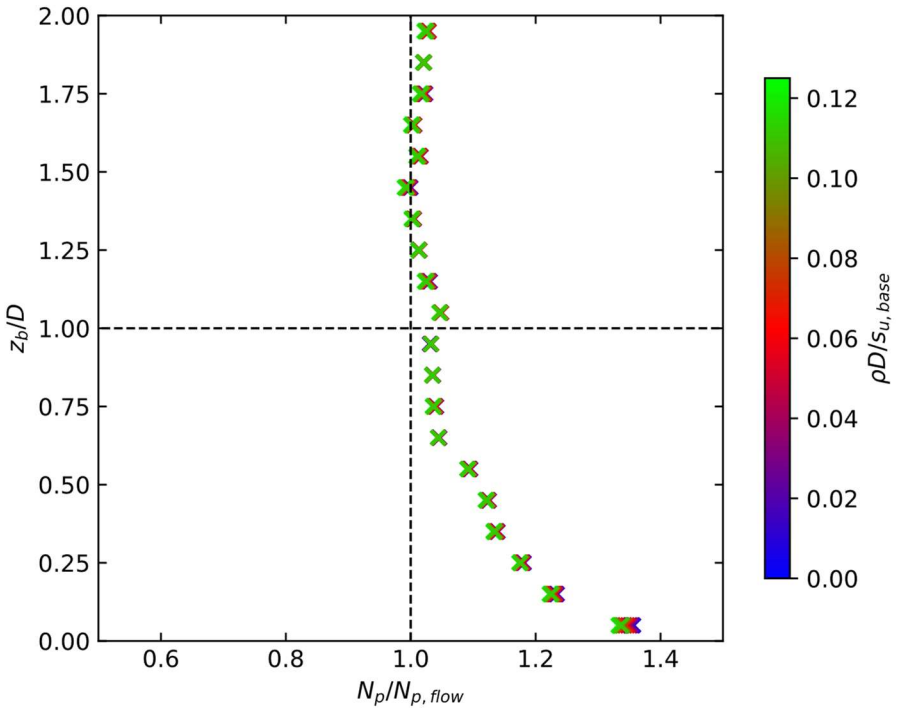

Figure 6.10 - N_p profile near pile toe located in flow-around mechanism with varying $\rho D/s_{u,base}$

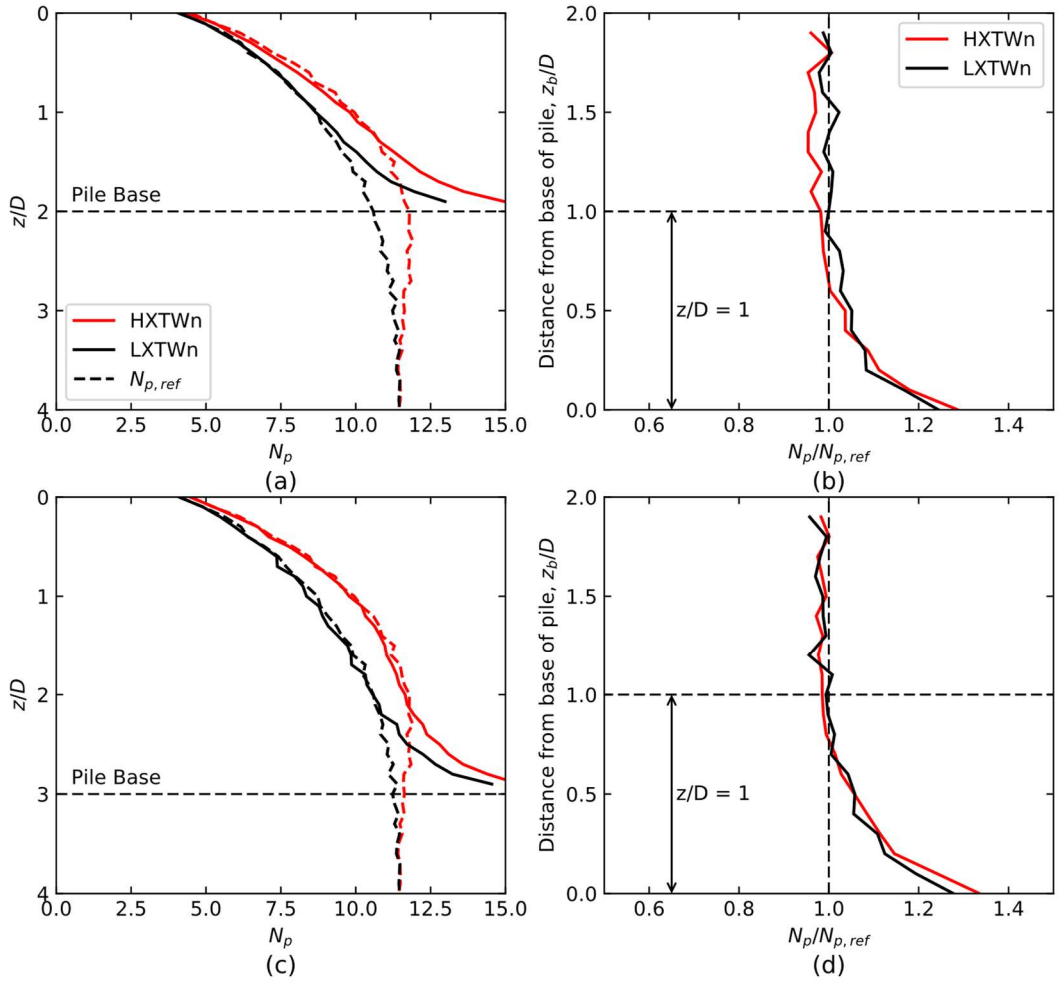

Figure 6.11 - Increase in lateral shaft resistance near pile toe when in wedge mechanism (a) L/D = 2, N_p (b) L/D = 2 normalised, (c) L/D = 3, N_p, and (d) L/D normalised

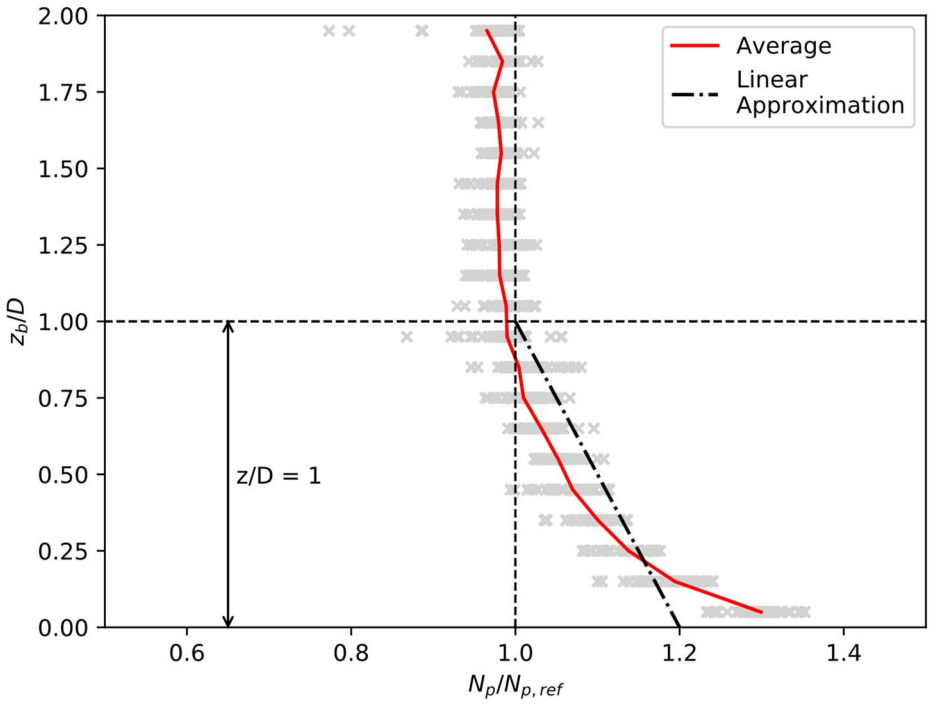

Figure 6.12 - Average N_p near pile toe and linear approximation when pile toe in wedge mechanism

6.2.2. Implications for design

The increase in N_p towards the pile toe has a very similar profile to that observed in Section 5.2 for the transition of N_p from a weak layer to a strong layer. As such, similar approaches to those proposed in Chapter 5 can be used to approximate the variation in resistance; i.e. either a constant increase over a set depth from the pile toe or by using a linear approximation, see Figure 5.46. Linear approximations for the pile toe in the flow-around and wedge zones are shown in Figure 6.9 and Figure 6.12 respectively. The results from OxLim indicate that $N_{p,t}$ = 1.3 and $N_{p,t}$ = 1.2 give suitable estimates for the flow-around and wedge cases respectively. As such, the rules presented in Table 6.2 are the recommended approaches for estimating the increase in N_p near the pile toe.

Table 6.2 - Methods of predicting increase in N_p near pile toe

Case	Linear	Step
Flow	$N_p = N_{p,flow}\left(1 + 0.3\left(1 - \frac{L-z}{D}\right)\right)$ $for\ \frac{L-z}{D} \leq 1$	$N_p = 1.225N_{p,flow}$ $for\ \frac{L-z}{D} \leq \frac{2}{3}D$
Wedge	$N_p = N_p\left(1 + 0.2\left(1 - \frac{L-z}{D}\right)\right)$ $for\ \frac{L-z}{D} \leq 1$	$N_p = 1.15N_p$ $for\ \frac{L-z}{D} \leq \frac{2}{3}D$

6.3. Base shear and moment resistance

This section investigates the lateral and moment resistance that occurs at the base of the pile. These resistances are considered distinct from the resistance outlined in Section 6.2. as they result from the summation of forces acting on the interior of the pile; as opposed to the resistance feature outlined in Section 6.2. which is acting on the exterior of the pile. The work in this section follows on from the work in Chapter 4 where it was shown that that the lateral base shearing does not show much variation except at low *L/D* ratios; see Figure 4.1(d) and

4.5(d). The variation of the lateral resistance at the base for low L/D occurs due the rotation point of the pile being closer to the pile toe as L/D decreases. At high L/D the bulb of soil that rotates with the pile is located such that the failure surface along the base of the pile is relatively flat; as shown in Figure 6.13(a) for $L/D = 8$ for HFTWn conditions. As discussed in Chapter 4, this leads to a lateral shearing resistance at the base of the pile of $F_{base}/s_u D^2 = \pi/4$. As L/D decreases the shape of the failure surface changes as the base of the bulb of soil that rotates with the pile moves deeper as the rotation point moves closer to the pile toe; Figure 6.13 (b) shows this for $L/D = 1$. When the pile is rotating about the pile toe, i.e. the depth of rotation z_r equals the pile length, the failure surface becomes hemispherical in shape as shown in Figure 6.13(c). For shallow foundations it is known that the lateral and moment resistance are coupled. Given the similarity between the mechanisms it is prudent to assume that the same coupling between lateral and moment resistance will occur at the pile toe. Another aspect that is of interest to this investigation is the distribution of forces on the interior of this pile. Knowledge of this distribution and in particular where forces are concentrated near the toe of the pile will aid in structural assessment of stresses in the pile wall and any potential implications for deformation and fatigue.

The modelling for this section utilises the same parameterised model geometry used in Chapter 4 and Chapter 5. Both full interface tension cases and no interface tension cases are considered with the latter involving variation of $\gamma D/s_u$ or γ/s_u as appropriate. Ratios of $\gamma D/s_u$ and γ/ρ of 0, 1, 2, and 5 have been used. In all models pile soil adhesion is set to $\alpha = 0.5$; analyses performed in Chapter 4 and Chapter 5 (for example see Figure 4.2, Figure 4.4 and Figure 5.24) has shown the internal soil column to move with the pile as a rigid block and as such α will have minimal influence on the resistance at the toe of the pile. An $L/D = 5$ has been used for this assessment; this value has been selected based on review of the final deformed meshes of the analyses in Chapter 4 and Chapter 5. This L/D ratio ensures both scenarios of a gap or no gap forming will occur within the range of $\gamma D/s_u$ and γ/ρ selected.

To obtain a range of lateral force and moment responses at the pile toe the rigid joint, i.e. the point that all rigid bodies in the model move in relation to, in the OxLim model has been fixed against translation in the x-direction with a unit moment applied. The height of the rigid joint has then been varied; this forces the pile to rotate about a given point of the model irrespective of load applied. Modelling this way permits results that would be otherwise unachievable if the rigid joint is free to translate. One example of this is shown in Figure 6.13(c) where the pile rotates about the pile toe; achieved by setting $h = -L/D$ in the model.

6.3.1. Results and discussion

The total lateral resistance at the pile toe is obtained by summing the total lateral reaction acting on all the rigid bodies that face into the pile. The resulting lateral resistance at the pile toe for HXTWn and HXNWi are shown in Figure 6.14(a). As seen in Chapter 4 (Figure 4.1(d)) the results are close to $F_{base}/s_uD = \pi/4$, i.e. the resistance across a circular area. As previously discussed, the reduction in resistance arises from the discretisation of the pile cross section into a regular polygon (See Chapter 4, Section 4.3.2). The results indicate a difference between the resistance obtained for HXTWn and HXNWi with HXTWn having $F_{base} = 0.767$ and HXNWi having F_{base} varying between 0.732 and 0.755. The difference between F_{base} for HXTWn and the average HXNWi is only 2% and may simply be from the use of a quarter model for HXTWn and a half model HXNWi; i.e. the mesh density for HXTWn is higher leading to a more reliable answer. The distribution of lateral reactions on the interior of the pile is shown in Figure 6.14(b) for HXTWn. All of the internal forces are located in the bottom $1D$ of the pile with a near linear increase in force from zero at $1D$ above the pile toe to $F_{x,local}/s_uD = 0.2$ at the pile toe.

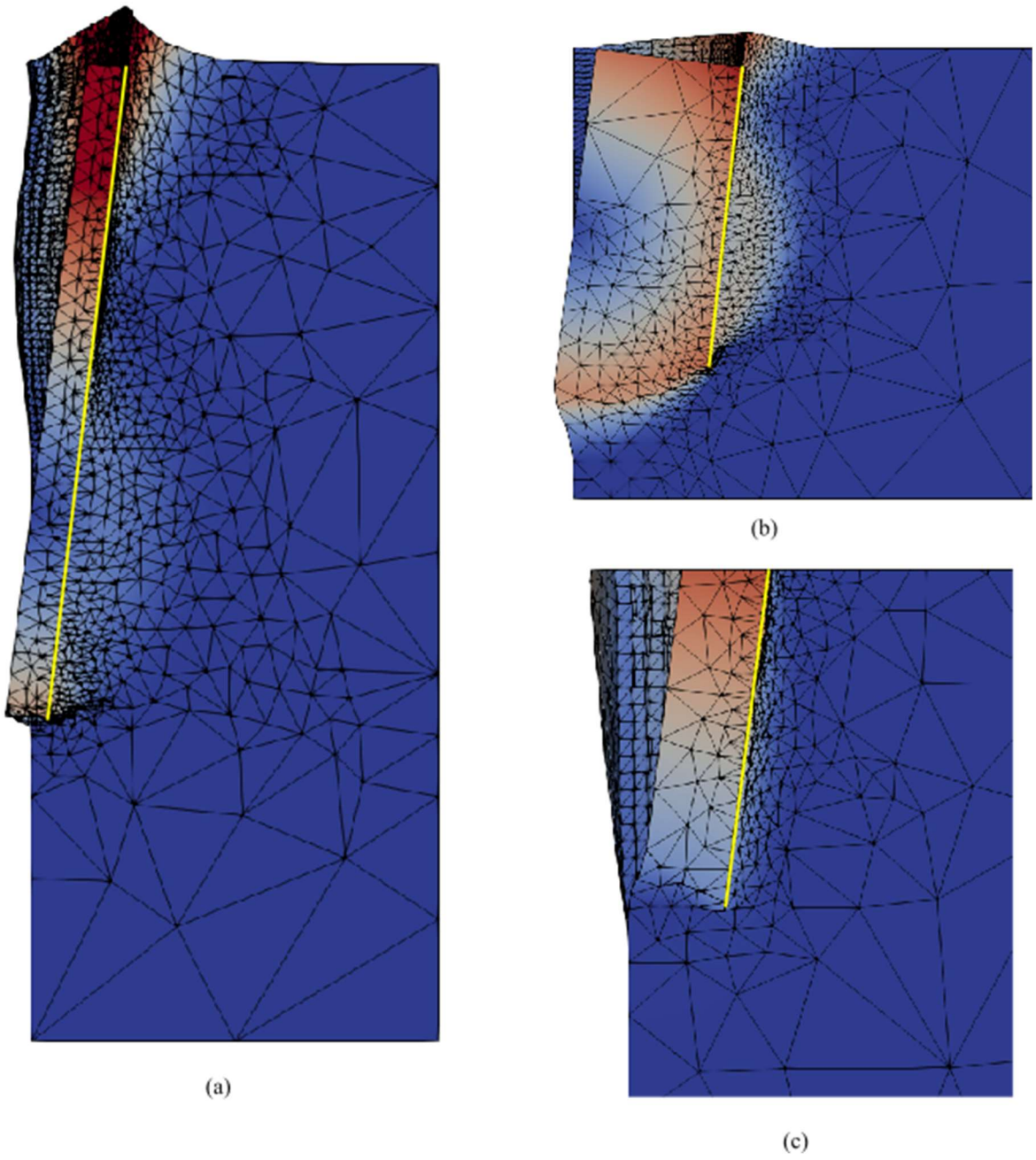

Figure 6.13 - Deformed meshes showing response at base for (a) L/D = 8, (b) L/D = 1, and (c) L/D = 5 (note only bottom 2D shown). Yellow line indicates position of pile wall

Of interest is the behaviour of the upper and lower bounds; the value of each bound relative to the average changes, i.e. the upper bound changes from being above the average to below, just above the pile toe leading to the lower bound to be locally higher than the upper bound at the pile toe. This behaviour seems counter intuitive when considered in the context of plasticity theory, however it should be remembered that these values of resistance are at a local level in the model. Globally, the lower bound response is still below the upper bound response at the pile toe it is evident that there is some difference between the upper and lower bound cases that

changes the behaviour. It should be noted as well that the local bracketing error is 100%; this occurs due to the use of zero thickness elements to represent the pile. Figure 6.14(c) shows the internal force distribution for each $\gamma D/s_u$ assessed: there is no discernible variation between each of the cases. One interesting thing to note is that despite the high bracketing error that occurs at the pile toe each of the different cases give approximately the same result; suggesting that the average may well be reliable here despite the high difference between upper and lower bound.

The lateral response at the pile toe for strength gradient cases are shown in Figure 6.15. The results for $F_{base}/s_{u,base}D$, Figure 6.15(a), show similar results to the homogeneous case, Figure 6.14(a). The resistance for the strength gradient cases is normalised by the strength at toe of the pile; i.e. $s_{u,base} = \rho L$ for these analyses. The resistance for LXTWn is $F_{base}/s_{u,base}D = 0.766$ which is only 0.1% difference from HXTWn; suggesting that when undergoing no rotation the resistance at the pile toe is only affected by the strength of the material immediately at the pile toe. Distribution of internal forces for LXTWn and LXNWi models are shown in Figure 6.15(b) and Figure 6.15(c). The response is similar to the homogeneous case shown in Figure 6.14; the majority of the resistance occurs 1D from the pile toe with a normalised response of $F_{x,local}/s_uD = 0.2$ at the pile toe.

Envelopes of the lateral and moment resistance at the base of the pile, F_{base} and M_{base} respectively, are shown in Figure 6.16. These envelopes have been obtained by forcing the pile to rotate about a given point in the model; for example, pure moment resistance at the pile base is achieved by forcing a rotation about the centroid of the pile base area. The results indicate that there is very little variation in the resistance obtained for both HFNWn, Figure 6.16(a), and LFNWn, Figure 6.16(b), with varying $\gamma D/s_u$ or γ/ρ. Similarly varying the L/D ratio of the pile has little effect on the obtained resistance; only $L/D = 1$ for LFNWi, shown on Figure 6.16(d), shows a significant deviation.

This deviation at $L/D = 1$ likely occurs due to the short length of the pile allowing the open top of the pile to influence the resistance at the base. As previously noted, the lateral force distribution inside the pile occurs over a length of pile 1D from the pile toe. One key difference between the resistance envelopes for HFNWi and LFNWi is when $F_{base}/s_uD \geq 0$. For HFNWi this results in a slightly flattened curve whereas for LFNWi the envelope is closer to having symmetry with the $F_{base}/s_uD \leq 0$ envelope.

Envelopes like this can be fit using an ellipse of the form

$$a\left(\frac{F_{base}}{s_u D^2}\right)^2 + b\left(\frac{M_{base}}{s_u D^3}\right)^2 = 1 \tag{6.8}$$

has been fitted to the results using a least squares regression analysis on all of the results obtained resulting in

$$1.45\left(\frac{F_{base}}{s_u D^2}\right)^2 + 1.62\left(\frac{M_{base}}{s_u D^3}\right)^2 = 1 \tag{6.9}$$

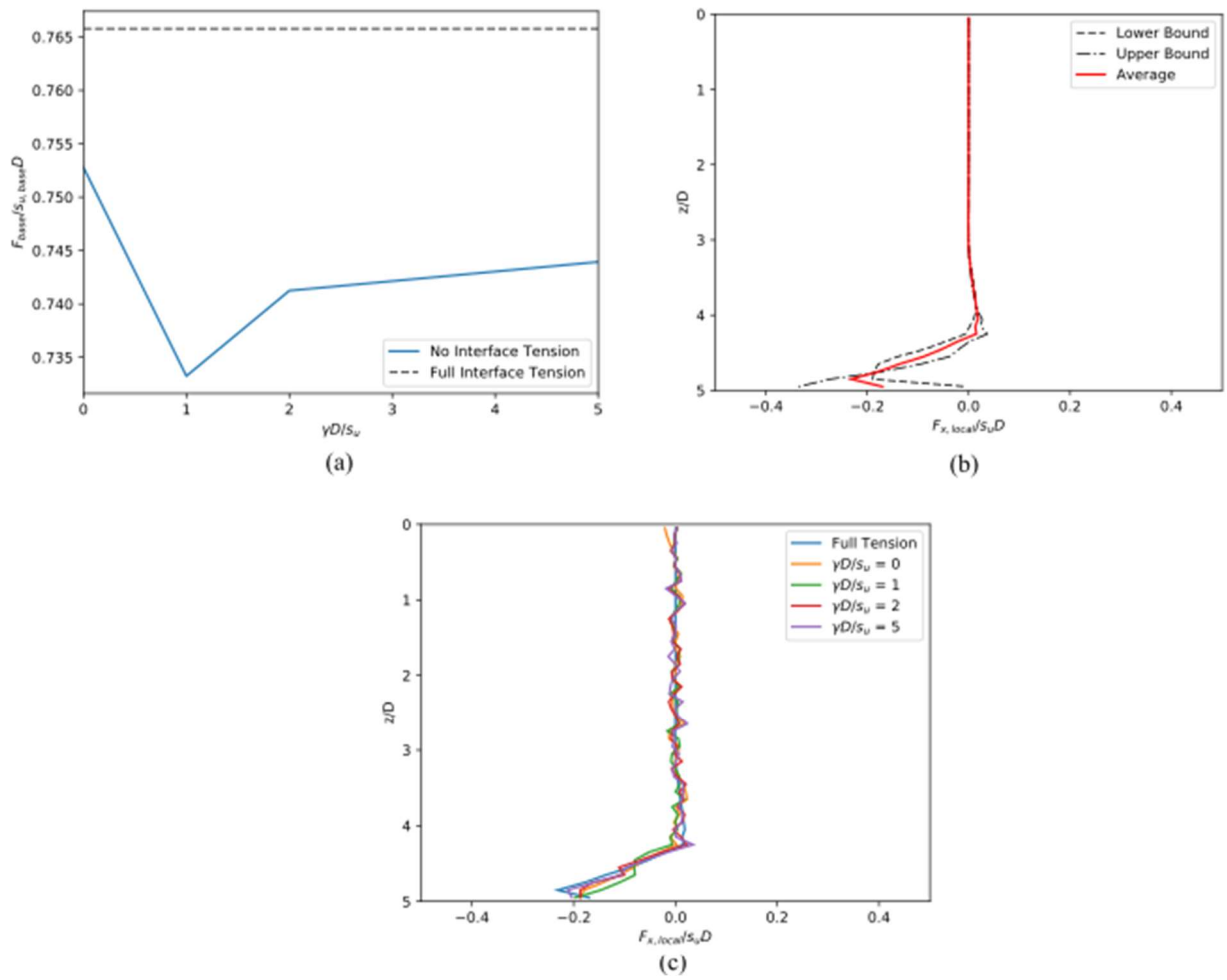

Figure 6.14 - Base resistance and internal lateral force distribution for homogeneous soil (a) variation with γD/s_u, (b) distribution of internal forces with upper and lower bounds, and (c) distribution of internal forces with varying γD/s_u

While obtaining an envelope of resistance is useful if the loads are known, they are of limited use for calculating the total capacity of a pile unless the influence of the displacement and rotation on the pile base resistance is known. One way of achieving this is expressing the resistance of the pile with respect to the distance from the rotation point; as is shown in Figure 6.16(e) and (f) for lateral and moment resistance respectively. In Figure 6.16(e) and (f) a value of $(L - z_0)/D = 0$ represents the rotation point being at the toe of the pile; i.e. achieved in this modelling by setting the rigid joint, the point that all rigid bodies move relative to, to the centroid of the pile toe and applying fixity against horizontal and vertical translation while applying a unit rotation about this point. Values of $(L - z_0)/D > 0$ represent cases where the rotation point of the pile is above the pile toe while values of $(L - z_0)/D < 0$ represent cases

where the rotation point is below the pile toe. The latter of these two cases will not occur for a single pile under general loading but may be relevant when a pile is subject to a forced displacement and rotation from the structure it is supporting.

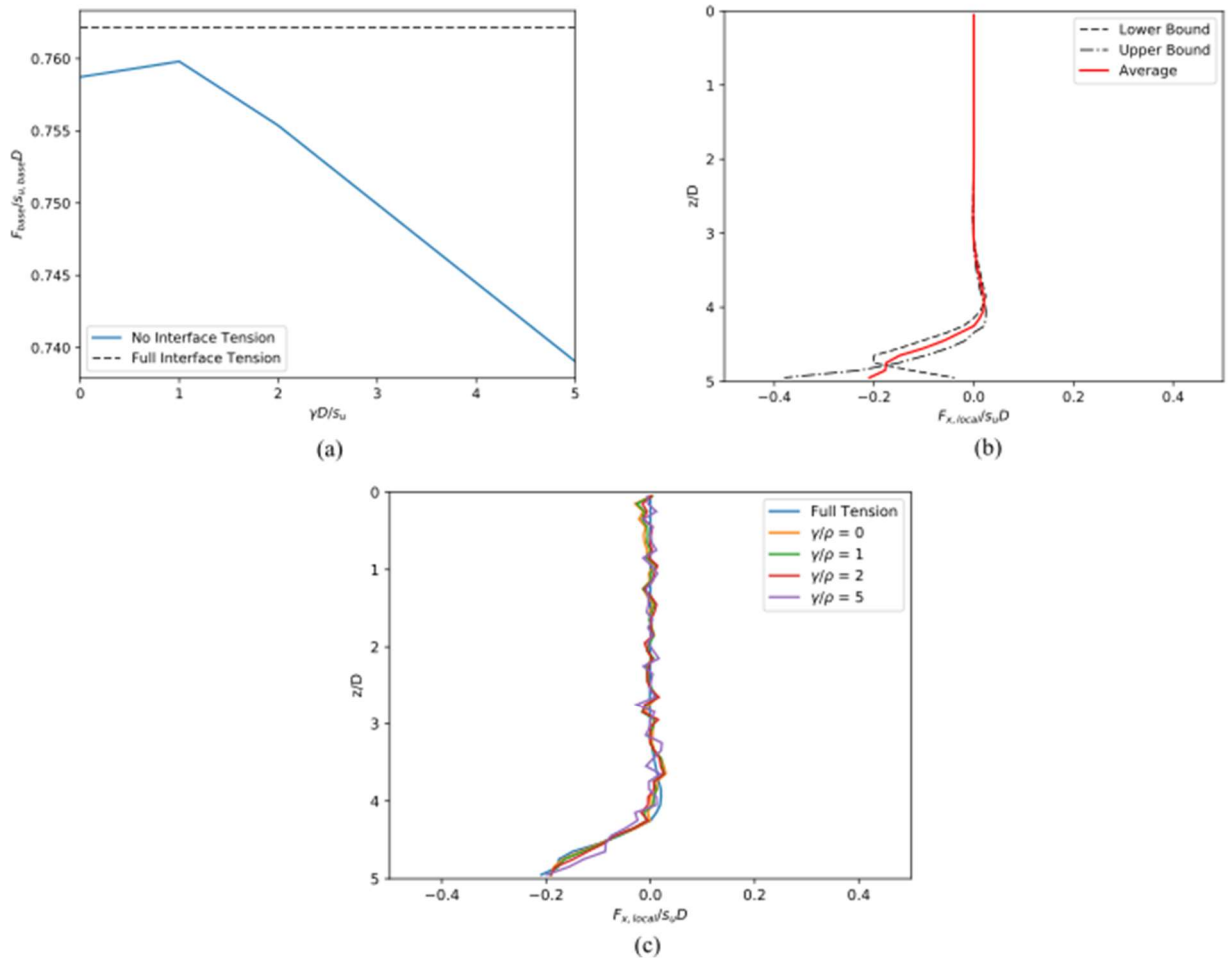

Figure 6.15 - Base resistance and internal lateral force distribution for homogeneous soil (a) variation with γ/ρ, (b) distribution of internal forces with upper and lower bounds, and (c) distribution of internal forces with varying γ/ρ

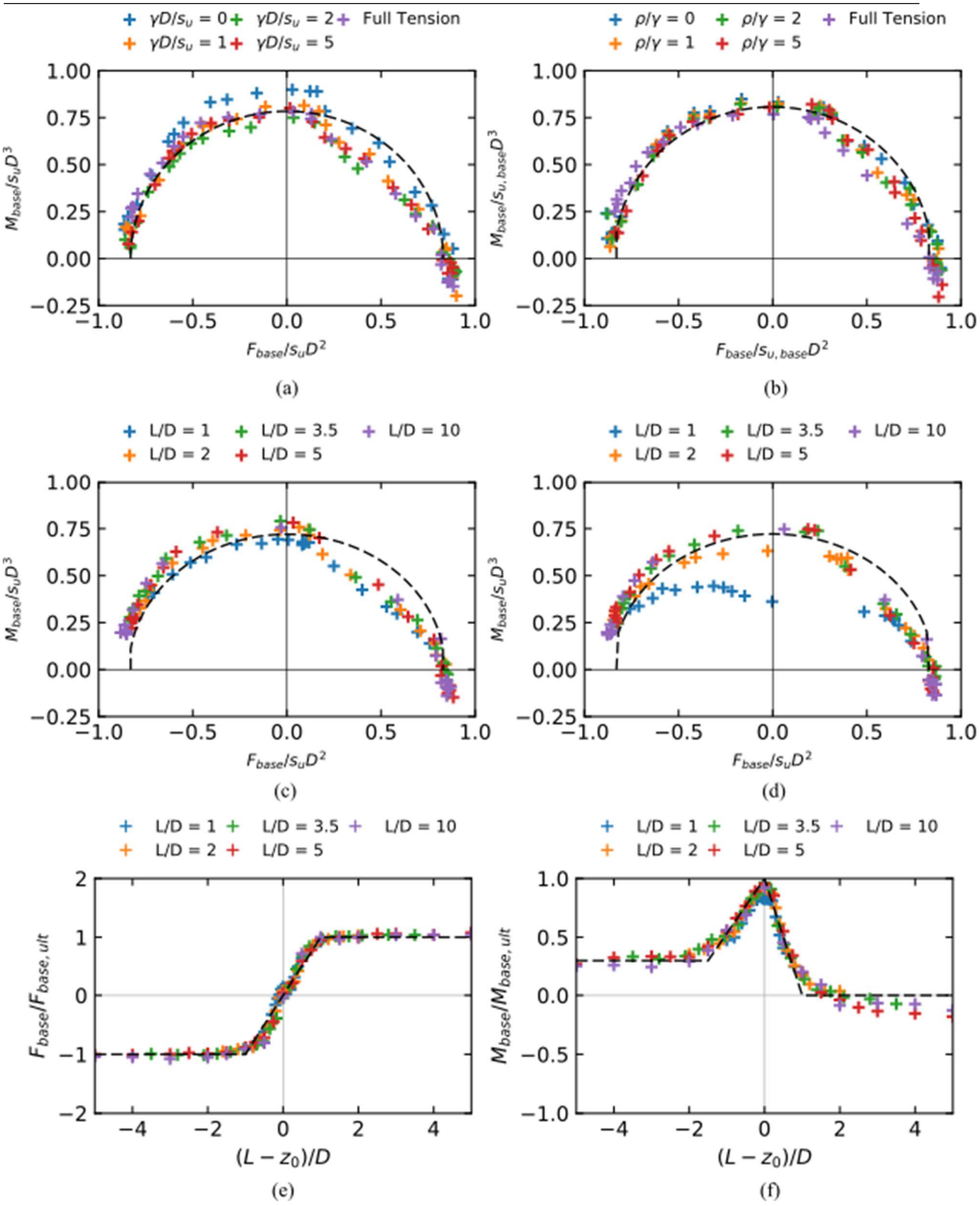

Figure 6.16 - F_{base}-M_{base} envelopes for (a) HFNWn varying $\gamma D/s_u$ (b) LFNWn varying γ/ρ (c) HFNWn varying L/D (d) LFNWn varying L/D (e) F_{base} with distance from rotation point and (f) M_{base} with distance from rotation point

Normalising by the ultimate resistance and diameter allows a simple multi-linear fit to be performed for both resistances.

$$\frac{F_{base}}{F_{base,ult}} = \begin{cases} -1 & for\ \frac{L-z_0}{D} \leq -1 \\ \frac{L-z_0}{D} & for -1 < \frac{L-z_0}{D} < 1 \\ 1 & for\ \frac{L-z_0}{D} \geq 1 \end{cases} \tag{6.10}$$

$$\frac{M_{base}}{M_{base,ult}} = \begin{cases} 0.3 & for\ \frac{L-z_0}{D} \leq -1.5 \\ \frac{0.47(L-z_0)}{D} + 1 & for -1.5 < \frac{L-z_0}{D} < 0 \\ 1 - \frac{L-z_0}{D} & for\ 0 < \frac{L-z_0}{D} < 1 \\ 0 & for\ \frac{L-z_0}{D} \geq 1 \end{cases} \tag{6.11}$$

The value of $F_{base,ult}$ has already been shown to be around π/4 regardless of soil conditions; i.e. equivalent to integrating the shear strength at the pile toe over the area of the pile. The limit $M_{base,ult}$ can be established in a similar way by assuming that a hemispherical surface would provide the maximum moment resistance. For homogeneous conditions the resistance is the following

$$M_{ult,base} = 4 \int_{\psi=0}^{\frac{\pi}{2}} \int_{\theta=0}^{\frac{\pi}{2}} s_u r^3 \cos(\psi)\, d\theta d\psi \tag{6.12}$$

where s_u is the soil strength, r is the pile radius, and ψ and θ are the angle about and inclination from the pile centreline along the vertical axis. This results in

$$M_{ult,base} = \frac{4 s_u r^3 \sin\left(\frac{\pi}{2}\right)\pi}{2} = 2 s_u r^3 \pi = \frac{s_u D^3 \pi}{4} \tag{6.13}$$

with a normalised expression of the base moment as

$$\frac{M_{ult,base}}{s_u D^3} = \frac{\pi}{4} \tag{6.14}$$

6.3.2. Results and discussion

For piles where the rotation point will likely be further than 1*D* away from the pile base only the additional base shear resistance need be considered. Based on the analysis performed in Chapter 4 and Chapter 5, this is likely to be the case for piles with length over *L*/*D* > 3 where the rotation point will typically be 1*D* to 1.5*D* away from the pile base. The lateral shear resistance at the base of a pile can be assumed to be $\frac{\pi}{4}\mathrm{s_{u,base}D^2}$ at a maximum irrespective of soil conditions. For a freely rotating pile this resistance acts in the same direction as the applied force at the pile head. This resistance can be incorporated into the calculation of a piles ultimate resistance by adding an additional term to Equation 5.7 for predicting ultimate resistance, i.e.

$$F_x(h+z_0) = \int_{z=0}^{z_0} P_{ult}(z)(z_0 - z)dz - \int_{z=z_0}^{L} P_{ult}(z)(z - z_0)dz \; - \frac{\pi}{4} s_{u,base} D^2 (L - z_0) \quad (6.15)$$

For piles where the rotation point is likely to be closer to the pile toe, i.e. *L*/*D* < 3, then the following equation should be used:

$$F_x(h+z_0) = \int_{z=0}^{z_0} P_{ult}(z)(z_0 - z)dz - \int_{z=z_0}^{L} P_{ult}(z)(z - z_0)dz \; - F_{base}(L - z_0) + M_{base} \quad (6.16)$$

where F_{base} and M_{base} are obtained from Equation 6.10 and 6.11 respectively.

6.4. Distributed moment resistance

This section investigates the distributed moment resistance. This feature of resistance for piles has not been reviewed extensively in the past with literature seemingly limited to Lam and Martin (1986) and the recent PISA investigation (Byrne et al, 2019). The distributed moment resistance occurs from vertical shearing on the pile as it rotates. The moment resistance per unit length of pile is calculated by integrating these resistances around the perimeter of the pile, i.e.

$$m_y = \int_{\psi=0}^{2\pi} r^2 cos(\psi)\tau_v(\psi)\, d\psi \tag{6.17}$$

where ψ is the angle about the vertical axis, $rcos(\psi)$ is the distance from the pile centroid along the direction of loading, $rd\psi$ is the arc length and $\tau_v(\psi)$ is the vertical shear stress at ψ.

To investigate this resistance, modelling has been performed using both OxLim and Plaxis 3D; OxLim is used to investigate a range of parameters for full interface tension cases while Plaxis is used to verify the outputs from OxLim and provide insight into the effect that gapping has on the distributed moment. The use of Plaxis in this investigation is to account for the limitations of OxLim with respect to interface behaviour. OxLim assumes a rigid plastic interface with the permissible stress states shown in Figure 6.18, an issue with this assumption is that for $\alpha > 0$ this can lead to a phenomenon known as "phantom shears". This phenomenon results in shear stresses occurring on the soil-structure interface when separation has occurred leading to an artificial increase in resistance. For previous investigations in this thesis, the amount of additional resistance should be relatively minor as either interface separation has only occurred over a small part of the model or the response has been driven by the normal stresses acting on the pile. However, this will not be the case for the distributed moment where resistance will be predominantly from the shear stresses on the pile wall. As such, using OxLim may not provide a reliable indication of the distributed moment response when interface separation occurs. To investigate this effect a different parameterised OxLim model has been used; referred to as the iterative model which is described further in section 6.4.1.

Half models have been used for both Plaxis and OxLim using the boundary conditions as the analyses in Chapters 4 and 5. The Plaxis 3D modelling has been performed following the steps outlined in Chapter 3.

In OxLim, the distributed moment can be obtained directly from the output file without integration of stresses on the pile face. The software returns the 6 degree of freedom forces for

each rigid body specified in the model. However, it should be noted that the moments shown in the OxLim results refer to the moment of that rigid body about the rigid joint; i.e. for a pile loaded at mudline the rigid joint is located at x = 0, y = 0, z = 0 and all moments in the outputs are the moments around this point. As such, the moments output need to be adjusted to account for the influence of the local force. In this modelling, we are only interested in the moments about the y-axis as modelling the pile using a half model means it is restrained against rotations about the x-axis and z-axis. For each rigid body m_y is calculated as

$$m_{y,oxlim} = m_{y,total} - f_z \Delta x + f_x \Delta z \tag{6.18}$$

where $m_{y,total}$ is the moment obtained in OxLim, f_x and f_z are the forces in the x and z directions and Δx and Δz are the offset between the rigid joint location and rigid body centroid along the x and z axes respectively.

In Plaxis 3D, stresses at the interface are obtained as two shear stress components, τ_1 and τ_2, and a normal stress, σ_n. These stresses can be obtained for either the nodal positions or stress point locations for the structural element and are expressed in the local coordinate system; i.e. they would typically need to be transformed from the elements local coordinate system into the global coordinate system before they can be used. Conveniently for this investigation it is possible in Plaxis to align the local axis to the global axis; this results in τ_1 in the Plaxis outputs being shear stress in the global z direction.

Modelling in Plaxis 3D has been performed using the Tresca soil model with input parameters, such as shear strength and pile-soil adhesion ratio, set to the same as the OxLim model that is being compared against. For each Plaxis 3D model, pile geometry and soil properties are set to match the OxLim model the comparison is being performed against. All other model conditions are set as outlined in Chapter 3.

6.4.1. Modelling approach for interface separation analysis

As previously stated, a modified modelling approach using OxLim has been adopted to investigate the influence of phantom shears. The key differences between this modified approach and the approach outlined in Chapter 3 is how the rigid bodies are defined in the model and that additional iterations of the model beyond mesh refinement are performed. In the standard modelling approach, the pile is split vertically into rings with each ring representing a single rigid body. This approach is ideal for obtaining all the resistances reviewed in this thesis thus far as this approach results in OxLim directly outputting a profile of resistance with depth. In the iterative modelling approach, each of the rings defined in the standard model are further subdivided into a number of rigid bodies of equal size. As such, resistances are now calculated based on the sum of all resulting forces across the rigid bodies at each depth. The distributed moment is then the sum of m_y values calculated using Equation 6.18 for each group of rigid bodies down the length of the pile.

The second modification involves an additional set of calculation stages where the behaviour of the interface of each rigid body is toggled on where required. This toggling is performed by initially having the α value for all interfaces set to zero. This results in rigid bodies only having a reaction force in the outputs if there is a normal force acting on the body; i.e. if interface separation has occurred then the resulting force should be zero in the outputs. Where a rigid body has resulting forces in the OxLim outputs, the value of α for that rigid body is switched to the required value. Once this has been performed the model is rerun to obtain the final results. The iterative model has the following steps:

1. Model geometry defined and initial mesh created with Tetgen (Si, 2015)
2. OxLim data file set up with $\alpha = 0$ for all rigid bodies
3. OxLim models run with successive mesh refinement as described in Chapter 3
4. New OxLim data file created with α values toggled as required

5. Refined mesh geometry from $\alpha = 0$ models copied and run with the new OxLim data file.

6.4.2. Results and discussion

To understand the likely profiles of distributed moment that can be expected, a set of calculations of varying α and L/D was performed; the output of which is shown in Figure 6.17. Using HFTWn as a base analysis, results for $\alpha = 0$, 0.25, 0.5, 0.75, and 1.0, and $L/D = 1$, 2, 4, 6 and, 8 have been obtained using OxLim. Results have also been obtained from Plaxis for 4 cases with different L/D and α values in each case. The results from Plaxis and OxLim show a good match across most of the profiles. However it is evident that there is some variability in the results obtained from the two methods; mostly occurring close to the depth of the rotation point for high values of α. It is likely that this difference arises from the difference between the constitutive models used; while both cases utilise the Von-Mises Yield surface the assumptions on pre-yield behaviour are very different. This leads to cases where the overall resistance of a given scenario may be the same but distribution of local resistances may differ as seen here. It should also be noted that the bracketing error around the rotation point is typically the highest in the model; this is most easily seen in the bracketing error shown for $L/D = 8$, $\alpha = 1$. In this case, the global bracketing error was 8% while locally the bracketing for this resistance mechanism was over 50% at the depth of the rotation point. This increased error can also been seen in the results for $\alpha = 0$. Given that the resistance being assessed in these assessments should arise entirely from shear stresses on the pile wall then the profile for $\alpha = 0$ should be equal to zero at all depths. However, around the rotation point the upper bound solution deviates from this leading to the bump in the average resistance; the lower bound solution remains close to zero at all depths. It should be noted that a distributed moment may also arise from an imbalance of normal forces acting over the vertical length of a rigid body. However as the modelling process for the results in Figure 6.17 assumes full interface tension the normal forces on the

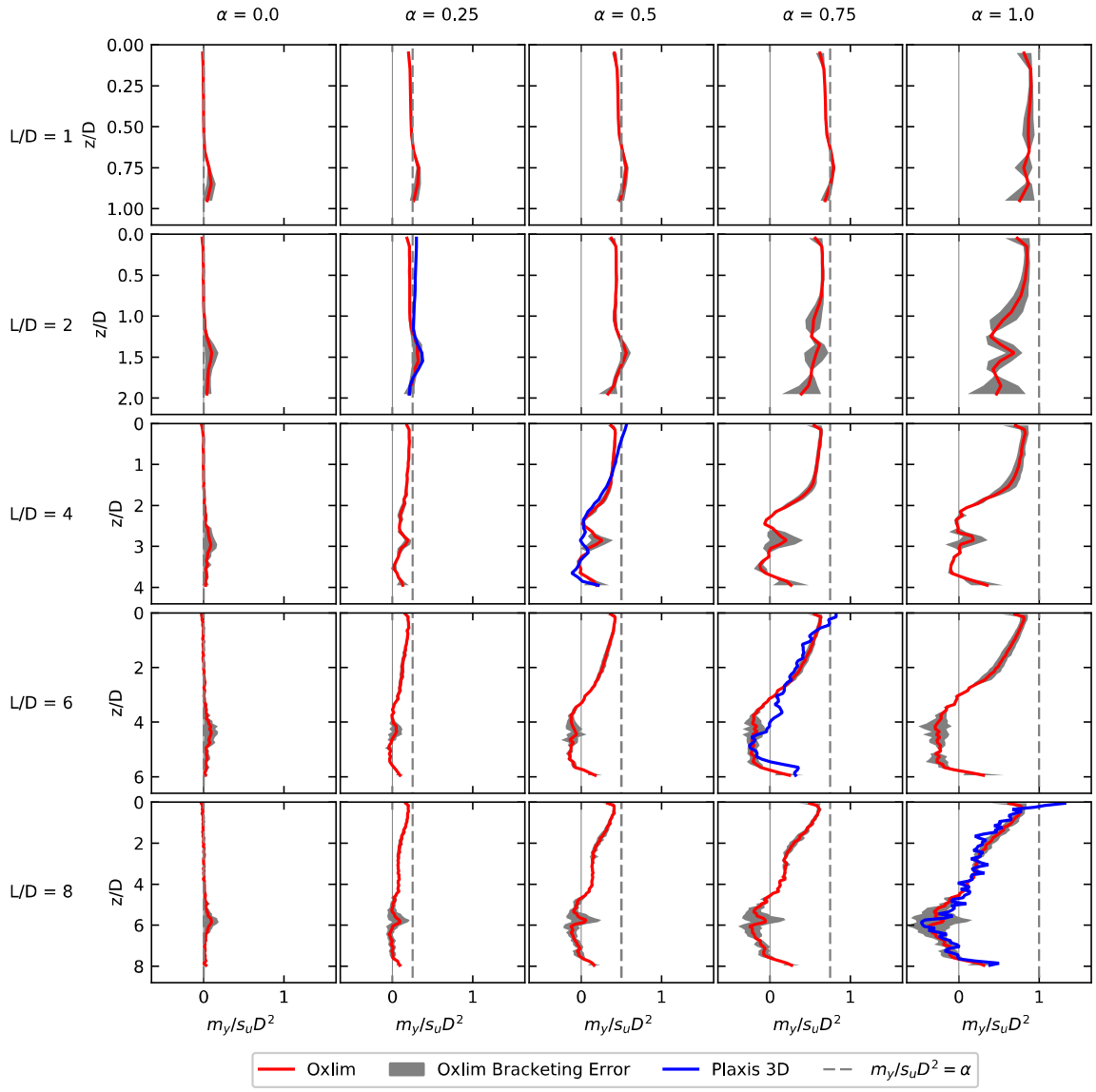

Figure 6.17 - Profiles of distributed moment from HFTWn modelling in OxLim and Plaxis 3D

back face of the pile will be equal to the forces acting on the front face of the pile albeit acting in the opposite direction. As such, these forces on the front and back of the pile should counteract each other.

The first observation from the results is that for $L/D = 1$ the profile of resistance is almost constant with depth and is almost equal to α. To understand why this occurs it is convenient to compare this to the theoretical maximum moment that could occur from vertical shear stresses.

This maximum assumes that the maximum shaft friction can be mobilised in the vertical direction at every point around the circumference of the pile. Taking this assumption and limiting the maximum stress to $\tau = \alpha s_u$ results in Equation 6.17 becoming

$$m_{ult} = 4 \int_{\psi=0}^{\frac{\pi}{2}} r^2 cos(\psi) \alpha s_u \, d\psi = 4r^2 \alpha s_u = D^2 \alpha s_u \tag{6.19}$$

Which then results in

$$\frac{m_{ult}}{s_u D^2} = \alpha \tag{6.20}$$

This limiting case is apparent across all the results obtained.

The second observation from the results is that similarly to the N_p profile the distribution of resistance can be broken down into distinct zones. Firstly, the resistance in the wedge zone

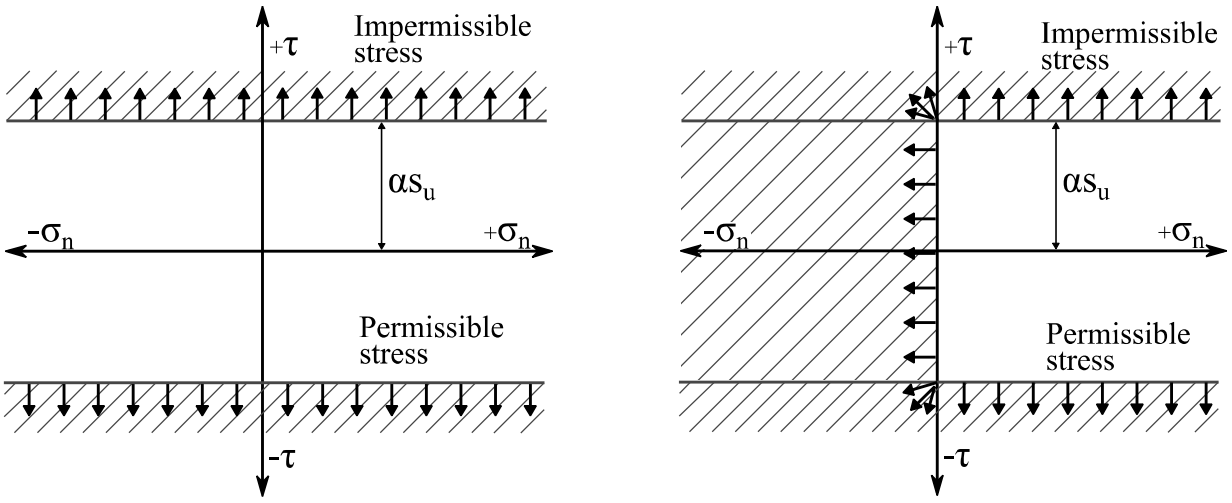

Figure 6.18 - Permissible stress states for rigid plastic interface for (a) full interface tension and (b) no interface tension

shows a decrease from close to m_{ult} at ground surface to either zero or a constant value below the wedge. For HFTWn, the wedge mechanism typically extends to a depth of approximately 3D: most easily seen in the results for $L/D > 6$ and $\alpha > 0.5$ in Figure 6.17. For $L/D = 2$ and 4 the depth this occurs over is reduced: this occurs from the depth the wedge mechanism occurs over being truncated by the rotating bulb of soil. This can be seen when reviewing the velocity contours for selected models shown in Figure 6.19. For $L/D = 8$ both the soil wedge and soil

bulb can be considered fully formed as the mechanisms are completely separated. For $L/D = 4$ and $L/D = 1$ the pile is sufficiently short for the mechanisms to interact, for both cases this leads to each mechanism being restricted to half of the pile length.

The second resistance zone extends from the base of the wedge mechanism to approximately $0.5D$ above the toe of the pile. This resistance zone encompasses the rotation point and bulb of soil rotating about the pile. The resistance in this zone is clearly dependent on both α and L/D with the profile varying from a small increase at the rotation point ($L/D = 4$, $\alpha = 0.25$) to a sizeable negative response for about $1D$ above and below the rotation point ($L/D = 8$, $\alpha = 1.0$). The latter negative response only occurs for the $L/D \geq 6$ in the modelling. It is not clear what mechanism is causing the distributed moment to be negative in these results: be it an actual failure mechanism or an product of the rigid plastic modelling approach of Oxlim (and the high stiffness modelling performed in Plaxis to approximate this behaviour). This resistance only seems to occur when the soil bulb is fully separated from the wedge mechanism and thus presumably able to move independently from the wedge (i.e. at lower L/D the upward motion of the wedge of soil in front of the pile may be influencing the way the bulb mechanism moves). Similar behaviour is present in the HFNWi and LFTWn modelling (in Figure 6.20 and Figure 6.21 respectively) albeit to a lesser extent in the LFTWn cases. The negative resistance is not observed in the LFNWi modelling, Figure 6.21, however the resistance does drop to zero in this zone. It is encouraging that the FELA and FEA results are giving similar results. While the methods use the same criterion to define soil failure, the methods they each use to reach a collapse load are very different. As such, there remains the possibility that this is an accurate representation of the distributed moments that occur between a pile and the soil within the bulb mechanism when it is moving independently of other failure mechanisms in the soil.

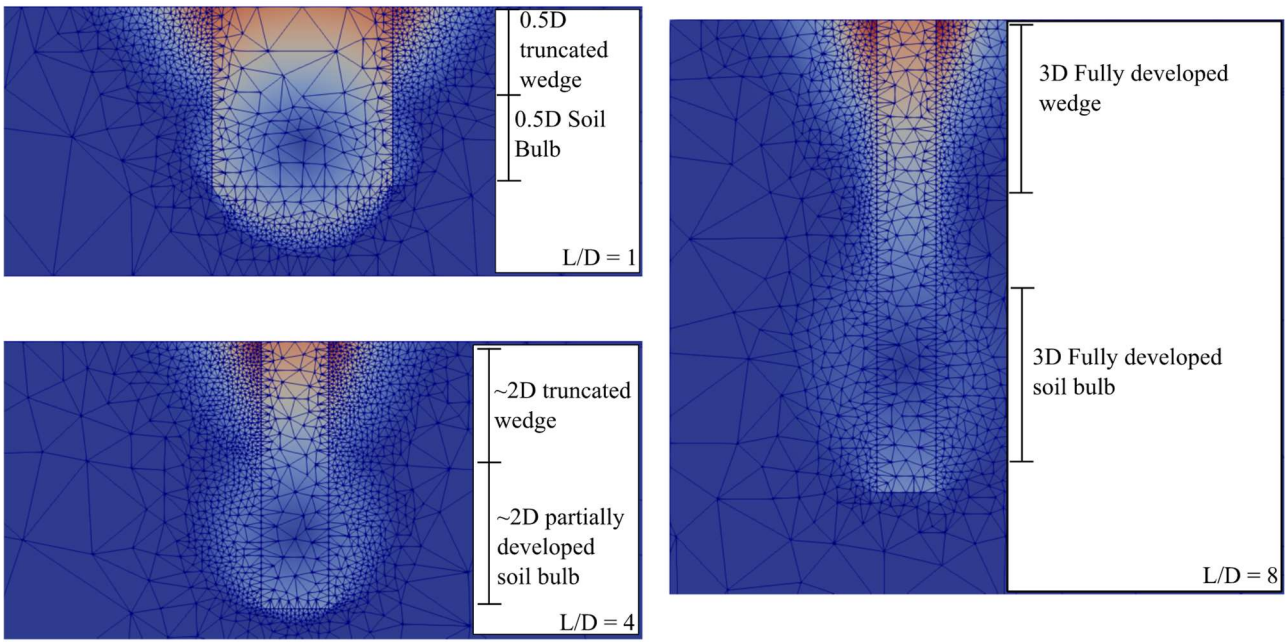

Figure 6.19 - Images of velocity contour and mesh on X-Z plane of symmetry for L/D = 1, 4 and 8 from HFTWn models.

The third resistance zone is close to the toe of the pile where, as with the N_p profile, this is a noticeable increase in resistance as the toe is approach. The resistance scales with α resulting in

$$\frac{m_y}{s_u D^2} \approx 0.25\alpha \tag{6.21}$$

for all profiles where $L/D \geq 4$. For $L/D = 1$ and 2 this increase does not occur; likely due to the rotating bulb of soil encompassing the toe of the pile (see Figure 6.19) and preventing this resistance arising.

Plaxis models have been run for a selection of the cases shown in Figure 6.17 with results obtained. The results from Plaxis show a good match across all cases. One variation between OxLim and Plaxis results that occurs in all cases is the resistance at the ground surface. In OxLim, the results show a small decrease away from $m_y/s_u D^2 = \alpha$ whereas the Plaxis results instead show the resistance is at a peak value at the ground surface. This likely arises from the

different constitutive modelling behaviour, i.e. rigid-plastic and linear elastic-perfectly plastic, used in the two modelling approaches.

As stated previously, the assumed interface behaviour in OxLim will be detrimental to any assessment where shear stresses form the main component of a resistance mechanism and interface separation occurs. The effect this assumption has on the obtained distributed moment profiles is shown in Figure 6.20 where results from both the default OxLim behaviour and the iterative modelling approach described earlier in Section 6.4.1. are shown. Results from Figure 6.17 are shown as well for comparison. It is apparent that using the default modelling case in OxLim, i.e. no iteration to adjust interface properties, results in resistances in the wedge zone similar to that from the full tension modelling for L/D = 1 and 2. For higher L/D ratios there is some reduction from the full tension case however it typically is not by a significant amount. In all cases, the distributed moment profile obtained from the iterative modelling approach is lower than the non-iterative approach in the wedge. This suggests that phantom shear stresses are being mobilised in the model and are contributing to the distributed moment resistance. The difference in resistance ranges from a 27% to 48% reduction from non-iterative to iterative results suggesting that for this mechanism using a rigid plastic interface can lead to a significant over prediction in the available distributed moment resistance.

As with the HFTWn analysis, Plaxis 3D models have been run for four cases. Both the L/D = 6, α = 0.75 and L/D = 8, α = 1.0 analysis show a very good match between the iterative OxLim models and Plaxis analysis: the only apparent difference occurring near the base of the wedge where Plaxis obtains a lower resistance than OxLim. At this depth, the profile of m_y/s_uD^2 obtained from Plaxis deviates from the OxLim obtained no tension results and starts to match the full tension results.

Away from the wedge mechanism, there is little to no deviation between the two profiles. This is due to closure of the gap at these depths; arising either due to the soil collapsing under self-

weight onto the back of the pile or the rotation point being reached and the direction of pile displacement reversing. This latter case leads to the jump in resistance profile at the rotation point observable in the results for L/D = 1 and 2 for the iterative modelling approach.

Similar behaviour is observed when a strength gradient is used; shown in Figure 6.21. The LFTWn results when normalised by the local shear strength, i.e. $s_u = s_{u0} + \rho z$ show a profile very similar to the HFTWn results shown in Figure 6.17. The LFNWi results show a different behaviour to that seen for HFNWi; this is due to large gap depth that forms under these conditions. This results in similar profiles between the high and low L/D cases shown here. Increasing γ/ρ would lead to the m_y/s_uD^2 profile becoming increasingly similar to the full tension profile; i.e. similar behaviour to that observed for N_p profiles in Chapter 4 and Chapter 5 (see Figure 4.9(b) and Figure 5.13). As for the HFNWi analysis, using the iterative model for LFNWi leads to a decrease in the obtainable ultimate distributed moment. The magnitude of this decrease is very similar to that observed in the HFNWi analyses and ranges between a 24% and 48% reduction from the normal modelling approach to the iterative approach. Table 6.3 shows a summary of the percentage decrease for each model at $z/D = 0.5$. As with the HFNWi results, all the results obtained for HFNWi adhere to $m_y/s_uD^2 < \alpha$. However, for this scenario the maximum resistance achieved is at the depth of the rotation point in all cases; similar to the resistance observed for $L/D = 1$ and 2 for HFNWi in Figure 6.20.

In both the HFNWi, Figure 6.20, and LFNWi, Figure 6.21, modelling some of the values of m_{ult} obtained from Oxlim and Plaxis exceed the theoretical maximum of α. This typically occurs at the depth of the rotation point and is likely due to the increased error at that depth (as shown for the HFTWn results in Figure 6.17). Similar to the HFTWn results in Figure 6.17, the HFNWi and LFNWi results both have non-zero distributed moments at the rotation point depth when $\alpha = 0$. In each case the lower bound Oxlim results give $m_y/s_uD^2 = 0$, thus showing agreement with Equation 6.19 which gives zero moment resistance when $\alpha = 0$. This implies that the lower

bound solution from Oxlim may give a better representation of this component of the lateral resistance than the upper bound.

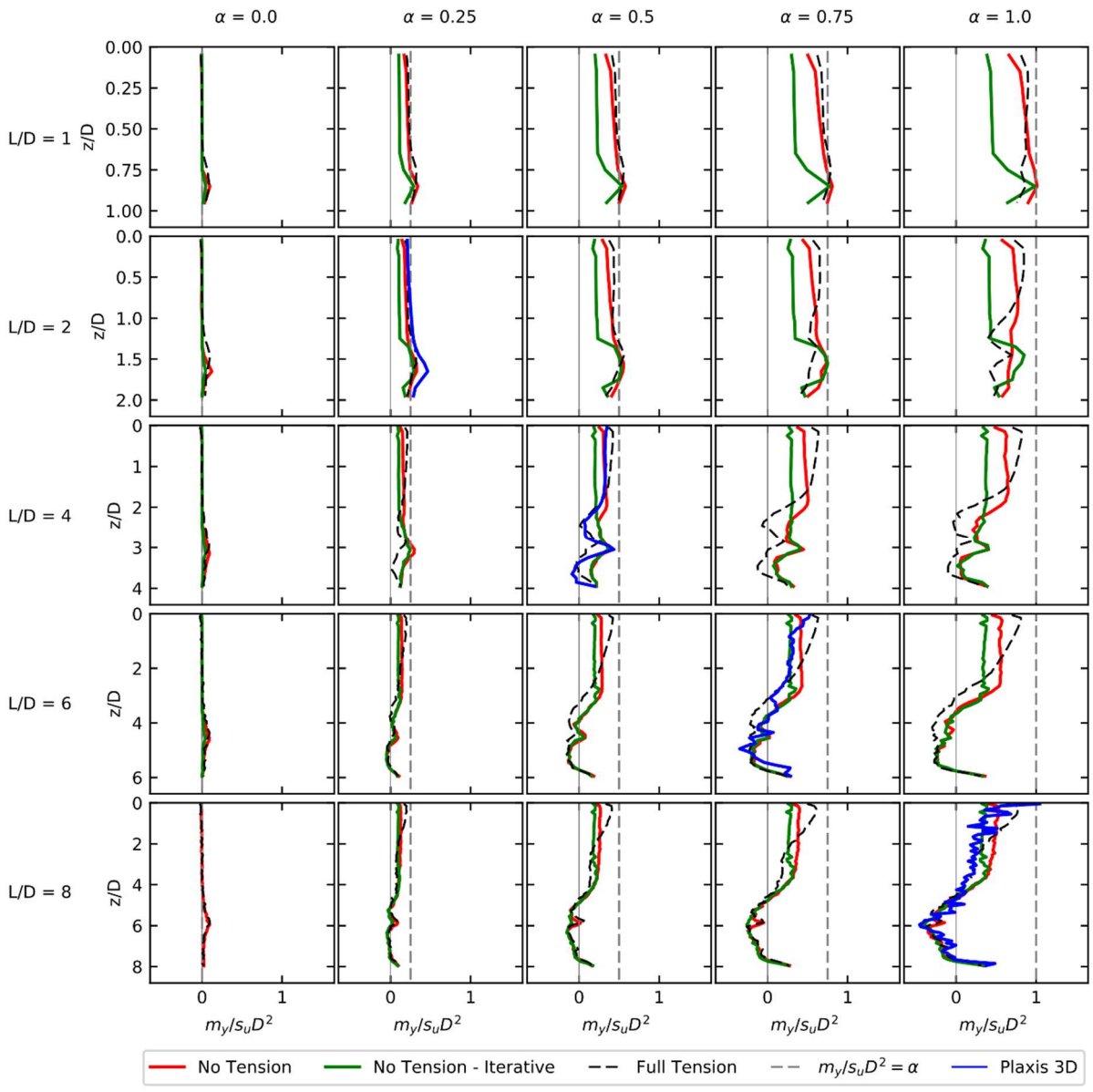

Figure 6.20 - Profiles of distributed moment for HFNWi with L/D = 1, 2, 4, 6, and 8, α = 0, 0.25, 0.5, 0.75, and 1.0, and $\gamma D/s_u = 1$. Results obtained from OxLim 3D and Plaxis 3D

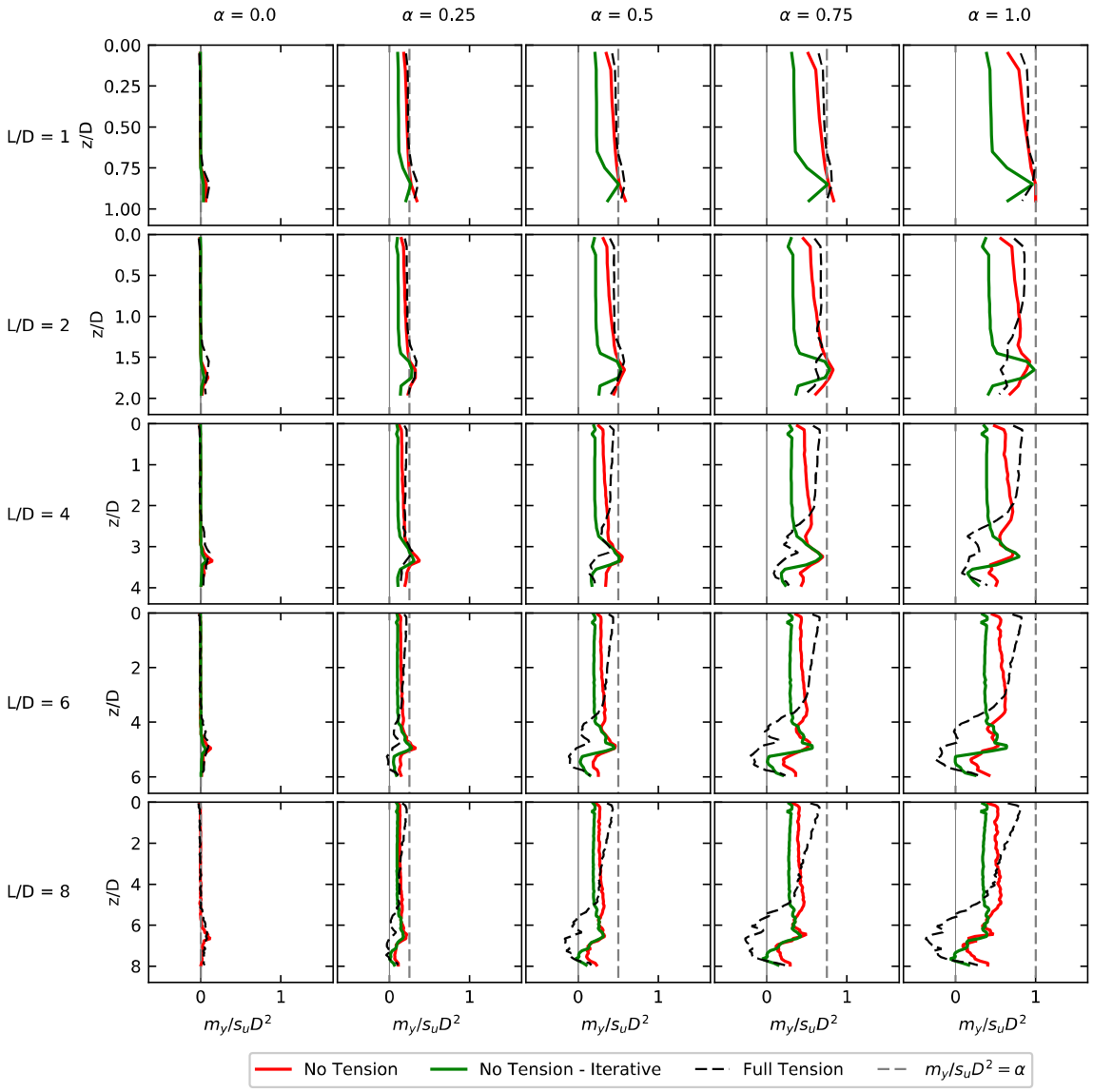

Figure 6.21 - Profiles of distributed moment for LFNWi and LFTWn with L/D = 1, 2, 4, 6, and 8, α = 0, 0.25, 0.5, 0.75, and 1. LFNWi performed with γ/ρ = 1 Results obtained from OxLim3D

Table 6.3 - Values of m_y/s_uD^2 for normal and iterative modelling approaches with percentage reduction for HFNWi and LFNWi

	HFNWi (Normal/ Iterative/ % reduction)			
L/D	α = 0.25	0.5	0.75	1.0
2	0.21/0.11/48%	0.43/0.22/48%	0.65/0.34/48%	0.88/0.45/49%
4	0.18/0.10/41%	0.36/0.21/42%	0.55/0.31/43%	0.74/0.41/44%
6	0.15/0.10/33%	0.31/0.20/34%	0.46/0.30/34%	0.62/0.39/38%
8	0.14/0.10/27%	0.28/0.20/28%	0.41/0.29/28%	0.56/0.38/32%

	LFNWi (Normal/ Iterative/ % reduction)			
L/D	α = 0.25	0.5	0.75	1.0
2	0.22/0.11/48%	0.44/0.23/48%	0.66/0.34/48%	0.86/0.44/48%
4	0.18/0.11/41%	0.37/0.22/41%	0.56/0.32/42%	0.73/0.41/43%
6	0.15/0.11/31%	0.31/0.21/32%	0.47/0.31/34%	0.62/0.40/36%
8	0.14/0.10/24%	0.28/0.21/26%	0.42/0.31/26%	0.55/0.39/29%

As stated earlier, the effect of phantom shears on other resistance mechanisms has not been considered thus far. However, the difference in moment capacity due to phantom shears does raise the question of how much of an effect it is likely to have on the other resistance mechanisms. As mentioned in section 6.3, the base shear and base moment resistances are independent of the pile-soil adhesion and as such phantom shears should not affect these mechanisms. However the same is not true for the lateral bearing acting on the pile. While the majority of the lateral bearing on the pile will come from normal stresses acting on the pile wall, an increasingly large portion will be due to lateral shear stresses as the pile-soil adhesion increases. This will be most prominent in cases where a significant amount of gapping will occur, i.e. low $\gamma D/s_{u0}$ or γ/ρ. Figure 6.22 shows the difference in total capacity for the HFNWi results shown in Figure 6.20. Greater reductions in total resistance occur at lower L/D corresponding to the higher proportion of total resistance that the distributed moment will form for shorter piles. For the more typically seen pile geometries between $L/D = 4$ and $L/D = 8$ the reduction in total capacity due to using the iterative modelling approach is less than 8%. Figure 6.23 shows the N_p profile for the $L/D = 4$, $\alpha = 1$, and $\gamma D/s_{u0} = 1$ case for both the iterative and normal modelling approaches. The difference in N_p is up to 10% locally with the greatest difference being near the ground surface and decreasing as the rotation point is approached.

The implication for this is that using a rigid plastic interface will almost always provide an unconservative result however for many scenarios the error from using this assumption will be relatively small. It is apparent that more work is required to understand the impact of this modelling assumption especially with respect to shorter piles or caissons. The method presented in this chapter of using an iterative modelling approach provides some means of accounting for phantom shears. However this approach will only provide an approximation of the resistance and the process will likely introduce some additional error into the model results. Ideally the accounting for phantom shears should be done within the interface element of the FELA modelling and further work is required in this area.

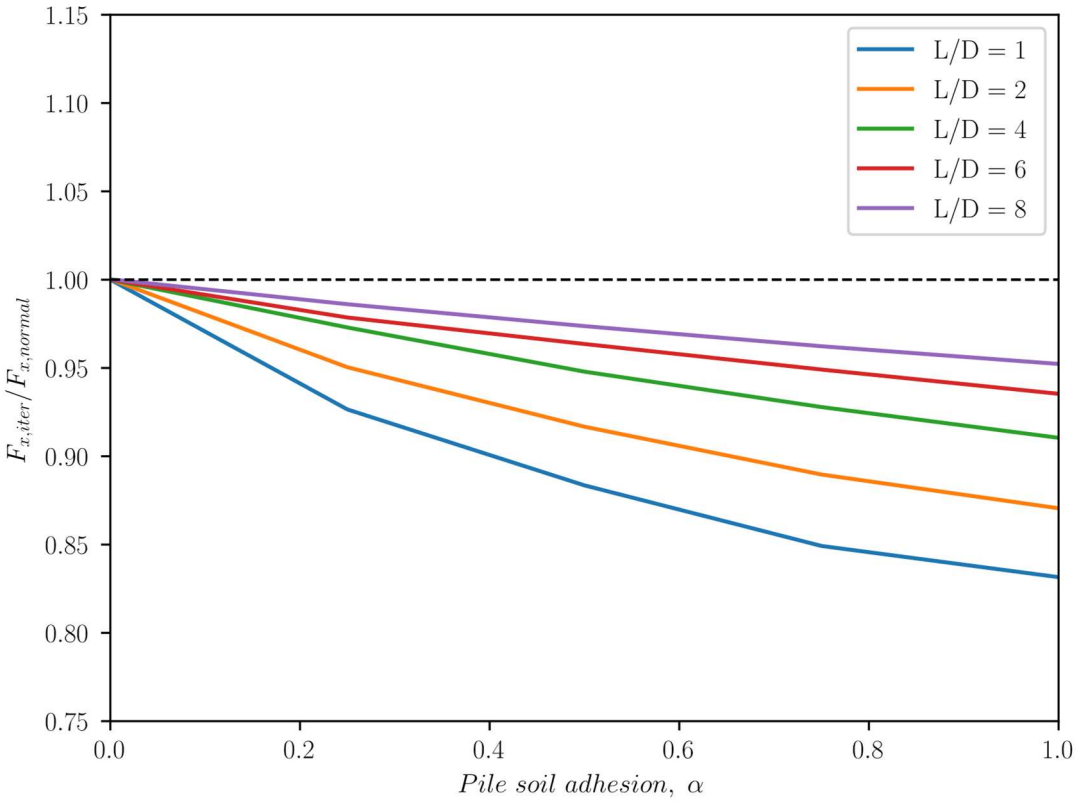

Figure 6.22 - Change in total lateral capacity for HFNWi with $\gamma D/s_u$ = 1for varying L/D and α. $F_{x,inter}$ and $F_{x,normal}$ are the total lateral capacity from the iterative and normal modelling approaches respectively

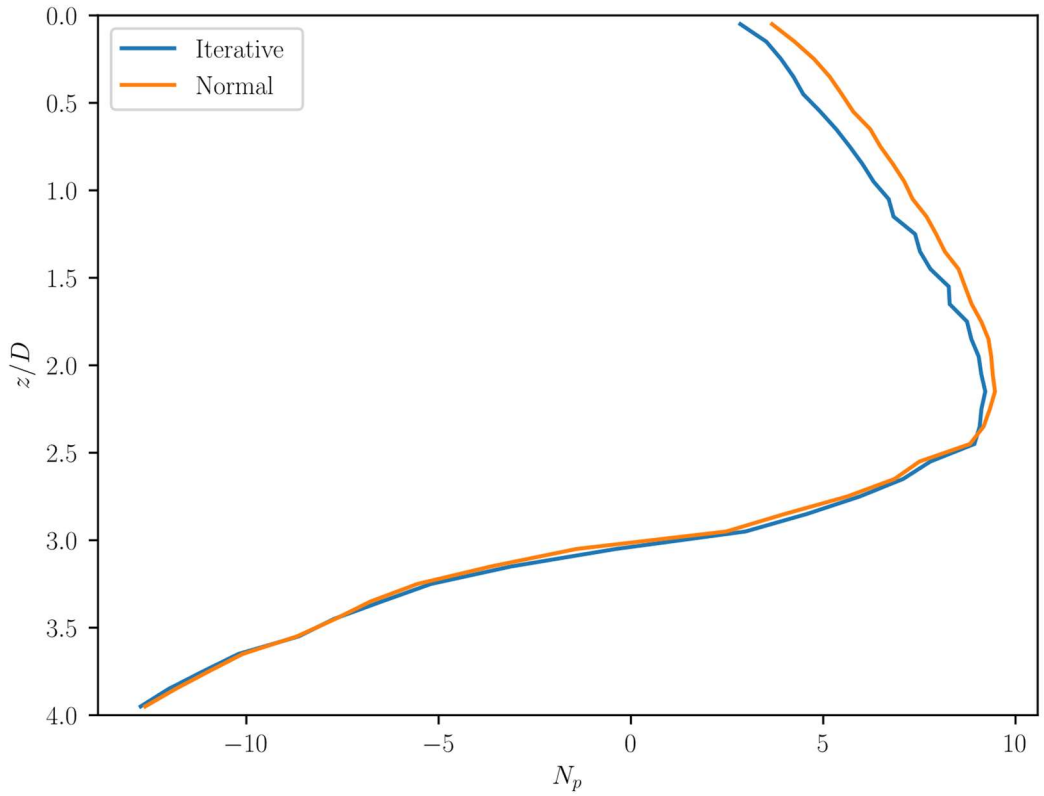

Figure 6.23 - Change in N_p when using the iterative modelling approach for HFNWi with L/D = 4, α = 1, and $\gamma D/s_{u0}$ = 1

6.4.3. Implications for design

The results obtained from Plaxis and OxLim show a consistent set of responses across all cases investigated. From the analysis of higher *L*/*D* ratios it is evident that there are several key components that form the distributed moment profile and that it is possible to relate these components to some easily obtainable features of the overall pile response, for example the depth of the rotation point and α. As such it is possible to express the profiles as a simple set of rules relating to these parameters; similar to what has previously been performed for lateral resistance with obtaining N_p profiles. The consistency of profiles seen in this assessment suggests that it is reasonable to introduce a bearing factor for distributed moments; similar to how p_{ult} is expressed for piles in undrained clay are typically expressed in terms of $p_{ult} = N_p s_u D$. Following the existing convention from lateral resistance this would result in distributed moments being expressed as

$$m_{ult} = N_m s_u D^2 \tag{6.22}$$

Defining a profile of N_m with depth allows Equation 6.16 to be extended to include distributed moment resistances resulting in

$$F_x(h + z_0) = \int_{z=0}^{z_0} p_{ult}(z)(z_0 - z)dz - \int_{z=z_0}^{L} p_{ult}(z)(z - z_0)dz - F_{base}(L - z_0) + M_{base} + \int_{z=0}^{L} m_{ult}(z)dz \tag{6.23}$$

As stated previously, for higher L/D ratios the N_m profile can be separated into three distinct sections located over the depth of the wedge mechanism and above the rotation point, within $0.5D$ of the pile toe and between these two mechanisms. The first of these cases has two distinct scenarios to consider; behaviour with and without interface separation. The primary factor that will affect whether a gap forms are the weight to strength ratios $\gamma D/s_u$ and γ/ρ. The effect of varying these ratios is shown in Figure 6.24. As with the other resistance features reviewed in this thesis, the distributed moment is bounded by the full tension and no-tension weightless soil cases as upper and lower limits respectively. The profiles of distributed moment shown in Figure 6.24 show little deviation from these two limiting cases for most of the weight to strength ratios used; at depths where no separation occurs the profile matches that of the full tension case and when separation does occur the profile matches that of the weightless scenario. This can be seen for a few cases in Figure 6.24; e.g. the $\gamma D/s_u = 2$ profile in Figure 6.24(a) which matches the weightless case down to $z/D = 2$ then matches the full tension profile to the toe of the pile. Similarly the $\gamma/\rho = 5$ profile in Figure 6.24(b) shows this behaviour.

Some deviation from the full tension and weightless cases occurs around the rotation point. For HFNWi this occurs for $\gamma D/s_u < 0.5$ and for LFNWi for $\gamma/\rho < 2$; both of these correspond to cases where the gap stays open for most of the pile length. For most real cases a gap would likely not

form below the rotation point as such the profile for the full tension scenario is appropriate for obtaining N_m at these depths.

An issue with creating a set of rules for N_m from this work is the current uncertainty surrounding the negative distributed moments that occur in the HFTWn, HFNWi and LFTWn modelling. It is unclear at present what is causing the distributed moment to be negative in these models and further work is needed to understand whether this is representative of the actual distributed moments that would occur or are something that occur due to the specific modelling conditions used. At this stage, it is felt that inclusion of the negative distributed moments in creating design profiles is prudent. Should later work demonstrate that the negative moments are not representative and positive distributed moments do occur than the current inclusion of negative distributed moments as part of the recommendations in this work will provide a conservative result. It should be noted that the negative moments only occur for high L/D ratios. As such, any global error introduced by use of incorrect distributed moments should be diminished as the distributed moment represents a smaller proportion of the total capacity as L/D increases. It should also be noted that as L/D increases the likelihood of a pile having a rigid response at failure is diminished and as such the applicability of applying these distributed moments that have been derived assuming a rigid pile response is lessened.

From these results simple rules can start to be established to represent N_m for piles with $L/D >$ 4, i.e. pile dimensions where the wedge and soil bulb are expected to not interact.

- Firstly for full tension, $\gamma D/s_u \geq 5$ and $\gamma/\rho \geq 10$ a linear approximation of $N_m = 0.8\alpha$ at surface decreasing to $N_m = 0.4\alpha$ at $z/D = 2$ for HFTWn conditions and $z/D = 5$ for the LFTWn conditions shown in Figure 6.24(b). For piles with lower $L/D < 8$ the depth will be limited to $1D$ above the rotation point. For $\gamma D/s_u < 5$ and $\gamma/\rho < 10$ a constant value of $N_m = 0.4\alpha$ should be used instead. This constant value extends to the greater of the full tension wedge depth or the depth of the gap behind the pile,

which can be expressed as $z_g = -0.785C + 5.5$ where C is γ/ρ or $\gamma D/s_u$ as appropriate; shown in Figure 6.25. This is again limited to 1D above the rotation point.

- Below this the N_m profile decreases to $N_m = -0.25\alpha$ at 0.5D above to rotation point; i.e. at $z/D = 5$ for HFTWn and $z/D = 6$ for LFTWn for the results shown in Figure 6.24.
- The value of N_m then remains constant down to 0.5D below the rotation point before increasing up to 0.25α at the pile toe.

For low L/D ratios, such as $L/D = 1$ and L/D = 2 as analysed in this work, a simpler set of assumptions can be used to construct an N_m profile. For full interface tension, simply using $N_m = \alpha$ appears adequate to estimate the resistance. This will lead to an overprediction when $\alpha = 1$, however in most design scenarios α is taken as less than 1. When interface separation occurs, $N_m = 0.5\alpha$ provides a suitable estimate down to 0.25D above the rotation point. The resistance then increases up to $N_m = \alpha$ at the rotation point before decreasing back to $N_m = 0.5\alpha$ at the pile toe. These rules are summarised in Table 6.4

Table 6.4 - Summary of method for estimating distributed moment bearing factor N_m

L/D ≤ 4	$N_m = \alpha$ Full Tension, $\gamma D/s_u \geq 5$ or $\gamma/\rho \geq 10$ $N_m = 0.5\alpha$ otherwise

	Full Tension, $\gamma D/s_u \geq 5$ or $\gamma/\rho \geq 10$		$\gamma D/s_u < 5$ or $\gamma/\rho < 10$	
	z/D	N_m	z/D	N_m
L/D > 4	0	0.8α	0	0.3α
	H[1]: min(2, z_0/D - 1D) L[2]: min(5, z_0/D-1D)	0.3α	H[1]: min(max(z_g[3], 2,) z_0/D - 1D)) L[2]: min(max(z_g[3], 5), z_0/D - 1D))	0.3α
	z_0/D – 0.5D	-0.25α		
	z_0/D + 0.5D	-0.25α	As for full tension	
	L/D	0.25α		

Notes:
1. Applicable to profiles with homogeneous strength
2. Applicable to profiles with a strength gradient
3. $z_g = -0.785\gamma/\rho + 5.5$ or $z_g = -0.785\gamma D/s_u + 5.5$

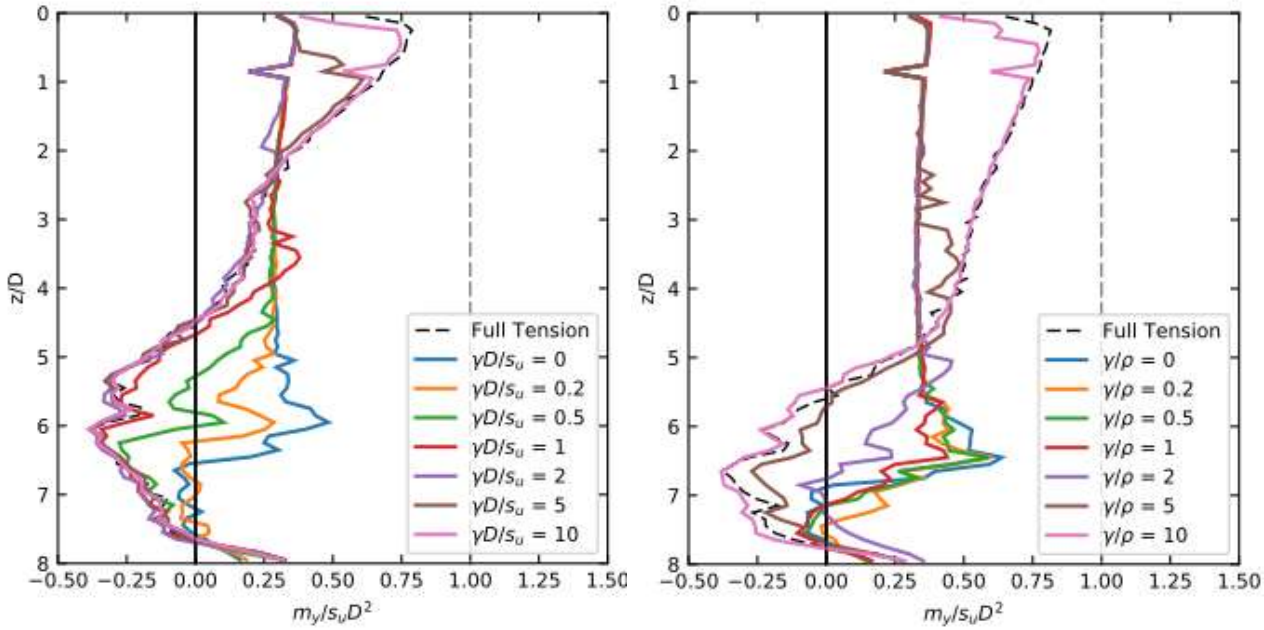

Figure 6.24 - Distributed moment profiles with varying weight to strength ratios , α = 1 and L/D = 8 for (a) HFTWn and HFNWi, and (b) LFTWn and LFNWi

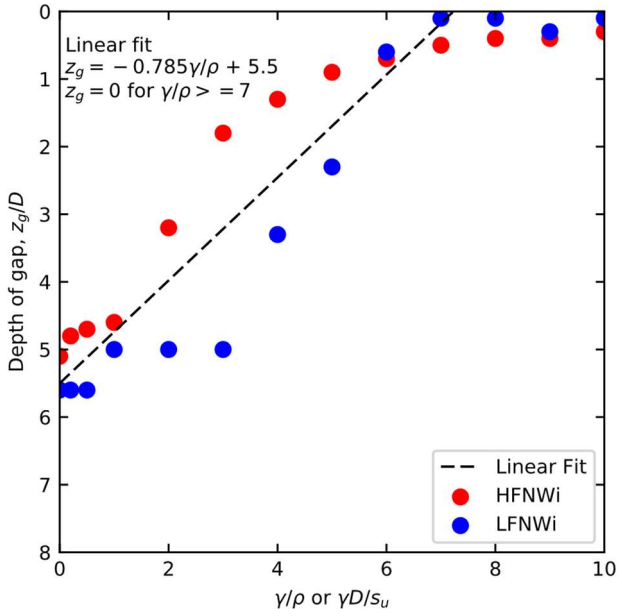

Figure 6.255 - Variation of gap depth with γ/ρ and γD\sᵤ for L/D = 8 and α = 1

Chapter 7

Comparison to Displacement Finite Element Analysis

This chapter presents an investigation comparing the rigid-plastic FELA modelling of OxLim to linear elastic, perfectly plastic modelling performed using the displacement Finite Element Analysis (FEA) software PLAXIS3D. As shown in Chapter 3 and other work, see Dunne (2017), modelling using FELA has certain advantages over traditional FEA techniques; principally the significant reduction in time required to assess a plastic collapse problem. However, a potential drawback of FELA is the necessary assumption of a rigid structural body. This limits the use of FELA to applications where it is demonstrable that the structure being assessed has enough rigidity relative to the soil strength for the structure not to deform significantly under loading. This is investigated in this chapter by performing a parametric study in PLAXIS3D where the rigidity of a pile is varied across a range of soil conditions and L/D ratios.

To investigate the influence of pile rigidity a dimensionless parameter to represent the relative flexibility is needed. Typically when investigating pile flexibility a dimensionless group relating soil stiffness to pile rigidity is used. However, in this investigation where the collapse load of the soil is a more practical dimensionless group would involve the soil shear strength. In undrained clays, the flexibility of the pile can be expressed as either

$$\kappa = \frac{EI}{s_u D^4} \tag{7.1}$$

or

$$\kappa = \frac{EI}{\rho D^5} \tag{7.2}$$

where E is the Young's modulus and I is the second moment of area of the pile. This permits comparison to the rigid model structural model used in OxLim which can be considered to represent $\kappa = \infty$. In this investigation open ended, tubular piles have been considered, for which the second moment of area can be calculated using

$$I = \pi r^3 t \tag{7.3}$$

Where t is the wall thickness of the pile and r is the pile radius. To give an idea of the range of values that could be expected, contours of κ are shown in Figure 7.1 alongside some reference cases from the literature. The API RP 2GEO (API, 2011) range of values corresponds to the minimum recommended wall thicknesses with an assumed upper estimate of twice the minimum value. This suggests that κ will typically be in the range of about $7x10^4$ to $4x10^6$. Values outside this range can be expected when the undrained shear strength of the soil is extremely high or low, as can occur in heavily overconsolidated or recently deposited materials respectively. However, for a practical consideration of the impact of pile flexibility the range estimated from Figure 7.1 will suffice. It should be noted that this range is specific to open ended tubular steel piles; piles made of other materials or with different cross sections may deviate from this range of κ.

The work in this chapter investigates four key cases:

- HFTWn – Free head pile in homogeneous soil with full interface tension and no soil weight
- LFTWn – Free head pile in soil with a strength gradient, full interface tension and no soil weight
- HFNWi – Free head pile in homogeneous soil with no interface tension and soil weight included

- LFNWi – Free head pile in soil with a strength with no interface tension and soil weight included

Within each of these cases a range of κ has been explored for L/D between 2 and 10. The lower values are outside the range of practical interest however the results obtained using these values provide an interesting insight into the variation of lateral pile resistance as pile flexibility varies.

7.1. Outline of modelling

Modelling has been performed in both PLAXIS3D and OxLim. The PLAXIS modelling has been performed by creating a parameterised PLAXIS model similar in form to the parameterised OxLim half-pile models used throughout this thesis. This parameterised model consists of a Python script that generates the geometry, performs the calculation and extracts results to a summary file. The steps used by this model are outlined in the following subsections. The OxLim modelling has been performed using the non-iterative model used in Chapters 4 and 5.

7.1.1. Geometry Creation

A rectangular soil domain centred on the origin and extending 20D in the positive X, negative X, and positive Y directions is created. Model symmetry occurs on the X-Z plane and as such only half of the soil domain and pile are modelled. Refer to Figure 7.2 for the global coordinate system used. The vertical height of the model is set by creating a borehole object with a single layer; the bottom of this layer is set to be the greater of 3D and 1.5L. As per Chapter 3 this ensures there is no interaction between the model boundaries and the deforming soil. Model boundary conditions are set to symmetry at the lateral extents of the model, full fixity at the base of the model and a free surface at the top of the model.

7.1.2. Soil Model

Soil behaviour is defined using the Mohr-Coulomb soil model with Undrained C parameters; i.e. a total stress analysis. This model requires undrained parameters of undrained Young's modulus, E_u, undrained Poisson's ratio, ν_u, and undrained shear strength, s_u, with friction and dilation angles set to zero; i.e. $\phi = \psi = 0°$. This reduces the yield surface to the Tresca criterion. The use of Tresca here will lead to a small overprediction in capacity when compared to the OxLim models, see Chapter 3, however the effect is not significant in the context of this investigation; as seen later in Table 7.3 the predicted resistance from PLAXIS models with a high κ is typically within 5 - 10% of the OxLim predictions. Soil parameters used for each analysis are presented in Table 7.1.

7.1.3. Structural elements, interface elements and loading

The pile geometry is created by specifying an 180º arc with radius 0.5D centred on the origin at depth z = 0m which is then extruded to the required length to create a surface. This surface is then used to create positive and negative interfaces (exterior and interior facing to the pile respectively) along with plate elements to represent the structural behaviour of the pile. The plate elements consist of 6-node triangular plate elements using Mindlin's plate theory (Bathe and Saunders, 1984). The elastic plate model with the parameters shown in Table 7.2 has been used assuming isotropic behaviour.

The positive and negative interfaces use PLAXIS built-in interface model. These consist of 12-node elements that pair with the 6-node triangular faces of the plate and soil elements. The interface elements are zero thickness; i.e. the pile wall has no geometric thickness within the model. The interface elements use a copy of the soil constitutive model, as shown in Table 7.1, with a change to tension cut off as required; i.e. set to no interface tension for HFNWi and LFNWi and left unchanged for HFTWn and LFTWn. For all models, interface behaviour has

been set with the strength reduction factor, R_{inter}, set to α: in this investigation $\alpha = 1$ has been used.

The plate elements have been defined with a wall thickness of $t = 0.01D$, resulting in a second moment of area for the pile of

$$I = \pi \times 0.5^3 \times 0.01 = 0.0039 \tag{7.5}$$

and a thus a flexural rigidity of

$$EI = 0.0039E \tag{7.6}$$

Loading in this investigation is applied through application of a line displacement applied to the pile at ground level. This line displacement is specified with a prescribed displacement in the x-direction and $u_{x,start} = 0.1D$; i.e. each model is performed to a final pile head deflection of $0.1D$.

7.1.4. Mesh

The mesh is generated using PLAXIS' inbuilt meshing tools to create a mesh of 10-noded tetrahedral elements. A 'relative element size factor', r_e, is used to specify the relative coarseness or fineness over the whole mesh. This parameter specifies a target element size based on the size of the model using

$$I_e = \frac{r_e}{20}\sqrt{(x_{max} - x_{min})^2 + (y_{max} - y_{min})^2 + (z_{max} - z_{min})^2} \tag{7.7}$$

where I_e is the average element size and x_{max}, x_{min}, y_{max}, y_{min}, z_{max}, and z_{min} are the model extents. In this investigation $r_e = 0.7$ has been used.

Mesh refinement in PLAXIS is performed by assigning a coarseness factor to each geometry object in the model. This coarseness factor specifies the target size of tetrahedra within the geometry object relative to the global r_e value. To ensure a higher degree of accuracy in pile

models the mesh around the pile should consist of smaller elements with larger elements located further away from the pile. To achieve this, a cylindrical solid element 3D in diameter and 1.25L in length is created. The following coarseness factors are then applied:

- 0.06 to the plate elements in the pile section
- 0.25 to the cylindrical volume around the pile
- 8 to the remaining soil volume away from the pile

Figure 7.2 shows the model geometry with these areas shaded to represent the coarseness factors used. This results in a mesh with refined elements close to the pile where the deformation occurs in the soil with coarse elements further away from the pile where there is little deformation. These coarseness factors combined with $r_e = 0.7$ result in element counts between 16,495 and 74,903 depending on L/D. Higher L/D models have higher element counts as the average element size is similar across all models. The average element size I_e varies between 1.94 and 2.05 for $L/D = 2$ and $L/D = 10$ respectively. An example mesh for $L/D = 6$ is shown in Figure 7.3.

7.2. Influence of pile flexibility

Plots of pile displacement with depth for HFNWi models with $L/D = 4$ and $L/D = 8$ are shown in Figure 7.4. Both fully flexible and essentially rigid pile deformations are evident in the results. For example, for $L/D = 4$, Figure 7.4 (a), the $\kappa = 3.9 \times 10^3$ case shows no lateral displacement below $z/D = 2.5$ suggesting a flexible response, whereas the $\kappa \geq 3.9 \times 10^5$ cases show no discernible bending deformation of the pile suggesting a rigid response. For both $L/D = 4$ and $L/D = 8$ there are cases where some deformation of the pile occurs, but the response is not fully flexible; i.e. there is no depth after which zero deformation occurs. This can be seen in the $\kappa = 3.9 \times 10^4$ for $L/D = 4$, Figure 7.4 (a), and $\kappa = 3.9 \times 10^5$ for $L/D = 8$, Figure 7.4 (b). It is these intermediate cases that are of interest in this study because bending deformation in the pile may

reduce the mobilised soil resistance. Deformed meshes from three of the L/D = 8 PLAXIS models where fully flexible, intermediate and rigid behaviour occurs are shown in Figure 7.5(a) to (c). An OxLim model for this geometry, Figure 7.5(d), shows the mesh deformed by the velocity from the upper bound solution. Figure 7.5(a) shows fully flexible behaviour with no deformation of the pile below 5D; see Figure 7.4 (a) for the lateral displacement profile. Figure 7.5(b) shows fully flexible behaviour verging on intermediate. Near the toe of the pile there is a very small displacement suggesting that the depth below which negligible pile displacement occurs is slightly deeper than 8D in this case. Figure 7.5(c) shows the intermediate behaviour when $\kappa = 3.9 \times 10^5$, as seen in Figure 7.4 (b) there is some deformation of the pile however it is small relative to the geometry of the pile.

Figure 7.6 shows the variation of total lateral capacity with normalised stiffness for the four scenarios investigated. As stated, each model has been run to a ground level displacement of 0.1D; i.e. a value typically considered when assessing pile ULS capacity from pile testing. This value of ground level displacement provides a reference case to compare the results in a context suitable to pile design. This means that the resistances obtained for lower values of κ do not represent the maximum capacity of the pile, however in these cases it is likely that the total displacement required to achieve the maximum capacity is beyond the range considered appropriate for pile design. Each case shows a similar variation of normalised lateral resistance with changing normalised stiffness. For each L/D ratio investigated the lateral resistance decreases with decreasing normalised stiffness once a threshold value has been reached; e.g. for L/D = 6 with HFNWi, Figure 7.6 (a), the potential lateral resistance is lower when $\kappa < 3.9 \times 10^4$. Above this threshold the resistance does not increase and is close to the OxLim results; i.e. above the threshold the behaviour is either close to rigid or pile deformation is sufficiently small to not reduce the lateral capacity. In both the homogeneous strength cases when full interface tension is allowed, Figure 7.6 (a), the PLAXIS analysis indicates that a lateral resistance equal to the rigid response can be expected up to L/D = 10 for the range of κ expected

for steel tubular piles. This does not indicate that the pile will not deform under these conditions: rather that the limiting resistance is the same as the rigid pile case. For example, for HFNWi, L/D = 4 and κ = 3.9 x 10^3 the lateral resistance from PLAXIS is 5% above the OxLim average resistance. This is despite the pile undergoing significant deformation; as shown in Figure 7.4(a). With interface tension removed, Figure 7.6(b), L/D = 8 and L/D = 10 result in capacities below the OxLim average; approximately 7% and 12% lower than the OxLim average respectively.

Similar responses to the homogeneous case occur when a strength gradient is used except with a higher κ required to match the rigid case from OxLim; shown in Figure 7.6(c) and (d). Within the range of κ of practical interest, $L/D \geq 6$ results in a resistance lower than the OxLim resistance. The percentage reduction in resistance, listed in Table 7.3, range between 5% and 80% lower than the OxLim result with the greatest difference occurring for L/D = 10.

As stated, each model has been run to a ground level displacement of 0.1D; i.e. a value typically considered when assessing pile ULS capacity from pile testing. This value of ground level displacement provides a reference case to compare the results in a context suitable to pile design. This means that the resistances obtained for lower values of κ do not represent the maximum capacity of the pile, however in these cases it is likely that the total displacement required to achieve the maximum capacity is beyond the range considered appropriate for pile design.

It is interesting to note that the resistance below the threshold stiffness of each L/D ratio is the similar across all L/D ratio for a given κ: this is expected based on the concept of critical length (Randolph and Gourvenec, 2011) where increasing the length of a pile beyond a certain length will provide no increase in resistance. In Randolph and Gourvenec (2011) the critical length is expressed relative to the soil stiffness as

$$L_{crit} = 4\left(\frac{(EI)_p}{k_{P-y}}\right)^{\frac{1}{4}} \tag{7.8}$$

where $(EI)_p$ is the flexural rigidity of the pile and $k_{P\text{-}y}$ is sub-grade reaction modulus which can be estimated from the soil shear modulus using $k_{P\text{-}y} \approx 4G$. An indicative relationship using the normalised stiffness can be established using the results from this investigation. Figure 7.7 shows the length required to transition from fully flexible to rigid behaviour for each normalised stiffness investigated. The data for this plot is based on inspection of the results shown in Figure 7.6. Each datapoint represents the value of κ at which the pile capacity first matches, or is close to matching, the average Oxlim result, i.e. greater than this value of κ rigid behaviour is expected. A simple fit to this data results in

$$\frac{L_{crit}}{D} = 1.97\log(\kappa) + 0.98 \tag{7.9}$$

where κ is the normalised stiffness; either EI/s_uD^4 or $EI/\rho D^5$ as appropriate. Equation 7.1 and 7.2 can to be used to identify when the assumption of a rigid pile is valid for estimating total capacity (e.g. Broms, 1964); i.e. when L/D is less than the ratio L_{crit}/D obtained from equation 7.9 the pile behaviour can be considered rigid.

Figure 7.8 shows a comparison between profiles of lateral bearing factor, N_p, obtained from both PLAXIS3D and OxLim 3D for HFTWn. For the OxLim results both the free head and translation cases are shown. The PLAXIS3D results are obtained using a method similar to that outlined in Chapter 6 Section 4 where the profiles of distributed moment are obtained. However, where Chapter 6 Section 4 uses the shear stress acting vertically, τ_1, to find the resistance, the other two components of interface stress are used here; the normal stress, σ_n, and the shear stress acting perpendicular to τ_1 and σ_n, termed τ_2. The lateral resistance, and hence N_p, is obtained from these stresses using Equation 7.10.

$$p = 2\int_{\psi=0}^{\pi} (\sigma_n cos\psi + \tau_2 sin\psi)\, r d\psi \tag{7.10}$$

where p is the distributed lateral force, in kN/m, ψ is the angle about the pile circumference from the axis coincident to the direction of loading and r is the radius. The mesh generated in PLAXIS results in an unstructured mesh of triangular elements for the pile; in order to apply Equation 7.10 to the stresses obtained from PLAXIS some post processing is required. First, the X, Y, Z coordinates for each stress point in the interface elements are converted to cylindrical coordinates r, z, ψ; i.e. pile radius, depth and rotation about centroid. As r is constant in these assessments this permits the position of each stress point to be represented in a 2-dimensional system of z, ψ; thus, allowing a 2D interpolation method to be used to convert the unstructured grid of PLAXIS stress points to be converted to set of stresses on a regular grid. In this work a linear interpolation using the griddata function in the Python Scipy library has been performed. Assuming a regular grid is created with 2N points about the circumference of the pile; Equation 7.10 can then be applied to this interpolated grid at each depth z by using Equation 7.11.

$$p = 2\sum_{i=0}^{N}\left(\sigma_{n,i}cos\psi + \tau_{2,i}sin\psi\right)\Delta z\frac{\pi}{n} \tag{7.11}$$

where Δz is the vertical spacing between the points on the grid; i.e. a regular vertical spacing of M points would result in a spacing of $\Delta z = L/(M\text{-}1)$.

The results in Figure 7.8 show a good match between the high rigidity piles modelled in PLAXIS and the rigid piles in OxLim 3D. For the lower rigidities, $\kappa = 3.9\text{x}10^0$ to $3.9 \text{ x } 10^2$ the N_p from PLAXIS starts approximately the same as the OxLim profile and matches it for some depth before reducing to zero. The depths where the $N_p = 0$ first occur match those where no lateral displacement first occurs in the profiles of lateral displacement shown in Figure 7.4. Below this first point of zero displacement the resistance acts in the same direction as the direction of loading; this corresponds to the depth where the deflects away from the direction

of loading. The three flexible cases shown in Figure 7.8, κ = 3.9 x 10^0, 3.9 x 10^1, and 3.9 x 10^2, show an increasing maximum N_p in this zone with increasing κ. This occurs due to the increased pile rigidity leading to a higher deflection, and hence greater mobilised resistance, over this depth.

One important feature to note of the PLAXIS3D profiles in Figure 7.8 is the resistance at the pile surface and pile toe. Similar to how the error in the OxLim models is greatest near the toe due to the assumption of a zero thickness structural body the results from PLAXIS indicated a similar potential error at both ends of the pile. Review of the normal stresses output at the lowest interface elements in the model showed that some of the elements, notably the interfaces at the leading and trailing edge of the pile, were an order of magnitude above or below the stresses acting on elements further away from the toe. In the N_p profiles this potential error materialises as a sharp change in resistance near the pile head and toe. The issue of unrealistic stresses at the end of embedded interfaces or interfaces wrapped around corners of solid elements is one that addressed in Chapter 5.6.7. of PLAXIS where some suggestions are made on how to smooth results near the end of interfaces. However, it should be noted that the impact of this on the overall response of the models performed in this investigation, and hence on the outcomes of this investigation, is negligible due to how localised the issue is relative to the pile size. As such, no additional modelling to account for this effect has been performed.

A factor that has not been addressed in this investigation so far is the potential for a plastic hinge to form in the pile and limit the lateral resistance. The modelling of the structural elements in this investigation has assumed elastic behaviour which allows the limiting geotechnical behaviour to be established. Including plastic deformation in the formulation of the plate elements, through methods such as through use of an elastoplastic constitutive model, may lead to a reduction in the lateral capacity as the structural capacity of the pile may be smaller than the geotechnical capacity in some circumstances; particularly for high L/D ratios. An

assessment of the full influence of a pile buckling under lateral loading is outside the scope of the assessments in this chapter. The modelling of piles buckling under lateral loading is a complex topic in its own right and warrants a comprehensive study to determine the limits formation of plastic moment would apply to a pile.

A simple way of understanding the limiting effect of plastic hinge formation on the capacity of a pile is to compare the moment in the pile to the theoretical plastic moment limit. The theoretical limit is obtained from assuming the axial stress in the pile wall is at yield across the entire cross section. Following Randolph and Gourvenec (2011) this leads to a plastic moment capacity of

$$M_p = \sigma_y D^2 t \tag{7.12}$$

where σ_y is the yield stress. The value of plastic moment can then be compared to moments obtained through a numerical assessment using elastic plate elements to represent the pile; such as has been performed in this Chapter. The moment in the pile cross section can be calculated from the axial forces that occur within the plate element in the PLAXIS model; these forces are termed N_1 and N_2 in the plate elements used in PLAXIS and are expressed in terms of force per unit length of plate element. As with the shear stresses in the interface elements, see Chapter 6.4, the axial forces in the plate elements can be aligned with the global Z axis by specifying an orientation of (0, 0, 1) when creating the geometry for the pile. This ensures no conversion from local to global coordinate systems is needed when processing results. The axial force can be converted to an axial stress by dividing by the width of the plate element, i.e.

$$\sigma_a = \frac{N_1}{t} \tag{7.13}$$

where σ_a is used to represent the axial stress in the plate element. The maximum fibre stress in bending is found using

$$\sigma = \frac{My}{I} \tag{7.14}$$

where M is applied moment, y is the distance from the sections centroid which is the pile radius, r, in this work, and I is the second moment of area, i.e. Equation 7.3 for thin walled cylinders. This can be rearranged and combined with Equation 7.13 to obtain the moment in the pile cross section from the axial force in PLAXIS' plate elements. Thus

$$M = \frac{N_1 I}{tr} \tag{7.15}$$

can be used to obtain a profile of moment with depth when N_1 is taken from nodes or stress points at the leading or trailing edge of the pile. Profiles of moment with depth for L/D = 6 and 8 are shown in Figure 7.9. The assessments performed thus far have relied on parameters selected as part of dimensionless groups as opposed to correlation to parameters for real materials. Yield strength of steel can vary significantly depending on the composition of the steel and is not intrinsically related to the elastic stiffness, as such assessing the effect of plastic hinge formation with a dimensionless group that fits within this assessment without modifying the modelling process to incorporate the yield strength, i.e. as part of an elasto-plastic constitutive rule governing the plate behaviour, is not possible. In lieu of this modification, a simplistic comparison is made the yield strength of S275 structural steel, e.g. σ_y = 275MPa, which is commonly used when fabricating piles. With the geometry used in this assessment this leads to a plastic moment limit of M_p = 2.75MNm using Equation 7.12. In each case the plastic limit is significantly greater than the moment obtained from PLAXIS suggesting that if an elastoplastic rule had been used none of these models would have undergone plastic deformation in the plate elements. However there are several things that need to be considered here. Firstly, as previously stated here the model parameters have been selected in order to achieve consistent dimensionless groups however the group chosen, κ, may not be suitable for understanding plastic hinge formation as the length will likely be a key variable in whether a

plastic hinge will form. This is especially pertinent when comparing to 'real' parameters such as the yield stress for steel. The low undrained shear strengths used in the models (i.e. s_{u0} = 1kPa or ρ = 1kPa/m) do not provide a high enough resistance to cause high enough moments to compare against a realistic value of yield stress. To obtain cases where a plastic hinge is likely to form the parameters and dimensionless groups would need to be selected in an appropriate range; for this assessment the range of parameters was based on the achieving a range of different pile flexibilities and as such is likely not appropriate for assessing plastic hinge formation. Secondly, each of the models was performed to a pile head deflection of 0.1D to ensure a reasonable comparison. For many of the models using a lower κ it is likely that a greater resistance would have been achieved if a greater final displacement at the pile head was specified. This would also lead to a higher moment in the pile for each case where a capacity close to the rigid case was not achieved. Finally, each of these models was performed with h = 0m; i.e. loading at ground level with no applied pile head moment. Applying a moment at the pile head would increase the maximum moment that occurs over the length of the foundation and would be more likely to result in cases where the plastic moment capacity of the pile was reached. Any assessment of plastic hinge formation would need to include consideration of having a combination of lateral load and moment applied at pile head.

Table 7.1 - Soil and interface constitutive model parameters used in PLAXIS3D analysis

Parameter		**Value**
Soil Model		Tresca
Drainage		Undrained C
Cohesion	c	1kPa (HFNWi, HFTWn) 0kPa (LFNWi, LFTWn)
Strength Gradient	ρ	0kPa/m (HFNWi, HFTWn) 1kPa/m (LFNWi, LFTWn)
Unit Weight	γ	1kN/m^3
Youngs Modulus	E	1000kPa
Poissons Ratio	ν	0.495
RInter		1

Table 7.2 - Plate constitutive model properties used in PLAXIS3D

Parameter		Units	Value
Young's Modulus	E	*kPA*	10^i: *i=1, 2, 3, 4, 5, 6, 7*
Plate Thickness	t	m	0.01D
Poisson's Ratio	ν	-	0.3

Note: All other elastic properties used derived based on the above. See Brinkgreve et al. (2016) for derivations

Table 7.3 – Percentage difference between lateral capacity of a free head pile modelled in PLAXIS and Olxim with varying normalised stiffness

HFNWi

		L/D				
		2	4	6	8	10
	3.9×10^1	-69%	-86%	-91%	-94%	-95%
	3.9×10^2	-15%	-60%	-76%	-84%	-88%
	3.9×10^3	12%	-16%	-50%	-65%	-74%
κ	3.9×10^4	15%	4%	-7%	-32%	-49%
	3.9×10^5	15%	5%	-3%	-8%	-15%
	3.9×10^6	15%	5%	-2%	-7%	-12%
	3.9×10^7	15%	5%	-2%	-7%	-12%

HFTWn

		L/D				
		2	4	6	8	10
	3.9×10^1	-67%	-84%	-91%	-93%	-95%
	3.9×10^2	-14%	-60%	-75%	-82%	-86%
	3.9×10^3	27%	-11%	-46%	-61%	-70%
κ	3.9×10^4	30%	19%	9%	-21%	-38%
	3.9×10^5	31%	20%	17%	17%	12%
	3.9×10^6	31%	20%	18%	18%	16%
	3.9×10^7	31%	20%	18%	18%	16%

LFNWi

		L/D				
		2	4	6	8	10
	3.9×10^1	-84%	-96%	-98%	-99%	-99%
	3.9×10^2	-37%	-82%	-92%	-96%	-97%
	3.9×10^3	5%	-46%	-77%	-87%	-92%
κ	3.9×10^4	9%	1%	-39%	-67%	-79%
	3.9×10^5	10%	5%	-5%	-23%	-48%
	3.9×10^6	10%	5%	-2%	-10%	-20%
	3.9×10^7	10%	5%	-2%	-9%	-17%

LFTWn

		L/D				
		2	4	6	8	10
	3.9×10^1	-85%	-96%	-98%	-99%	-99%
	3.9×10^2	-35%	-82%	-92%	-96%	-98%
	3.9×10^3	26%	-46%	-77%	-87%	-93%
κ	3.9×10^4	35%	1%	-39%	-67%	-80%
	3.9×10^5	36%	5%	-5%	-23%	-47%
	3.9×10^6	36%	5%	-2%	-10%	-5%
	3.9×10^7	36%	5%	-2%	-9%	1%

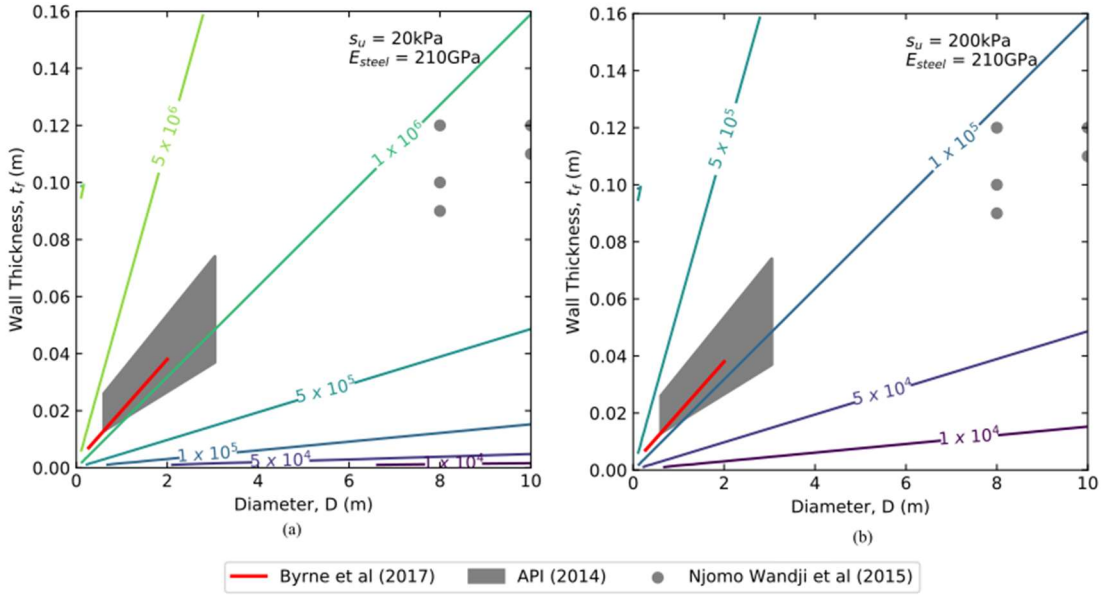

Figure 7.1 - Contours of EI/s_uD^4 for E_{steel} = 210GPa (a) s_u = 20kPa and (b) s_u = 200kPa across a range of diameters and wall thicknesses. Note that the values shown from the literature refer to the geometry investigated in the literature and do not account for soil strength.

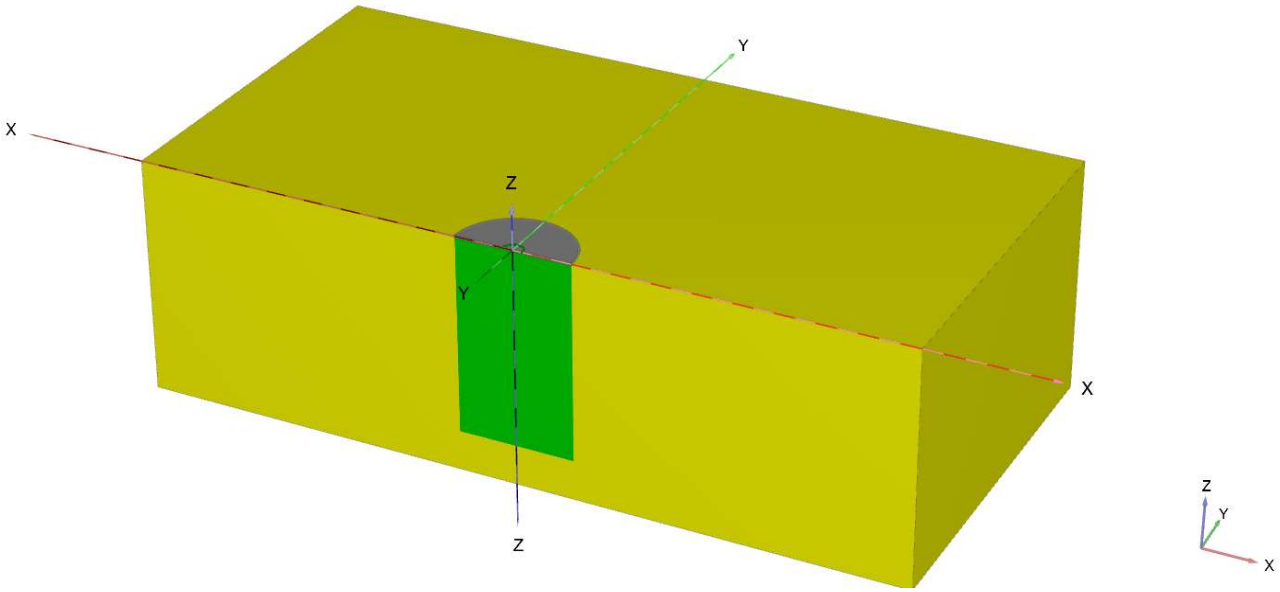

Figure 7.2 - Model geometry for L/D = 6 with global coordinate system shown. Colouring represents coarseness factor of geometry; yellow region is coarseness factor of 8 and green is coarseness factor of 0.25.

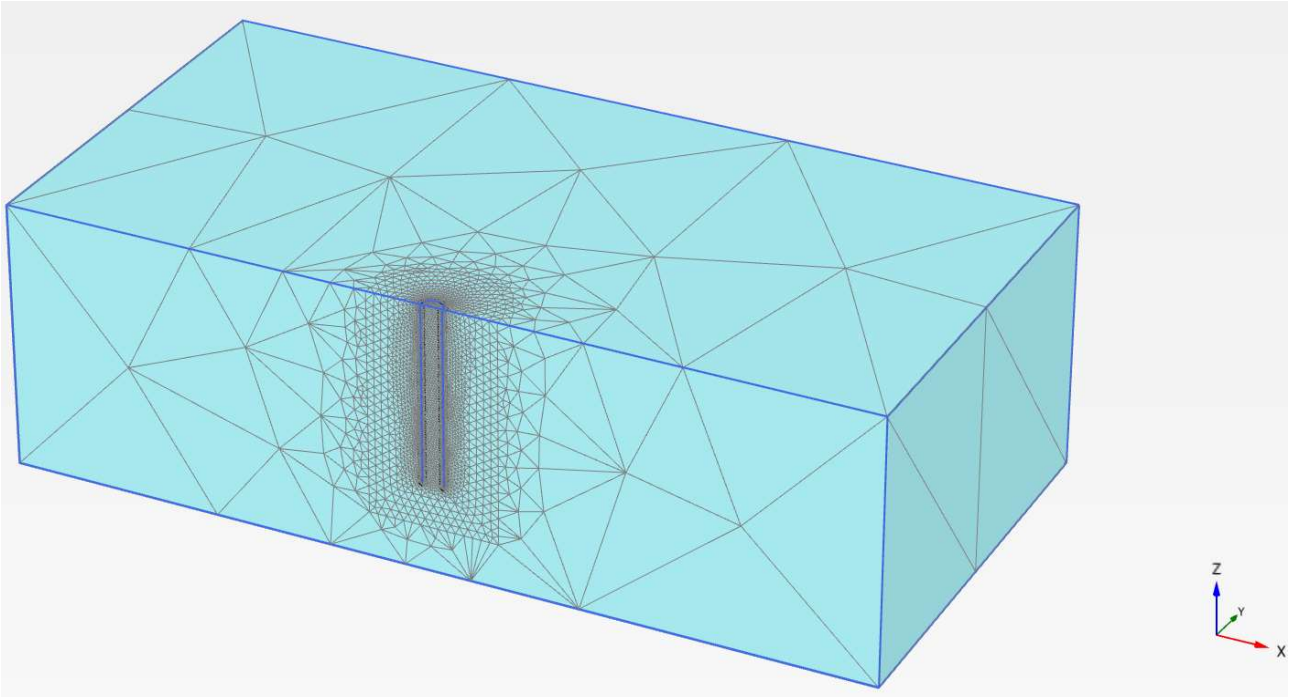

Figure 7.3 - Plaxis3D mesh for L/D = 6

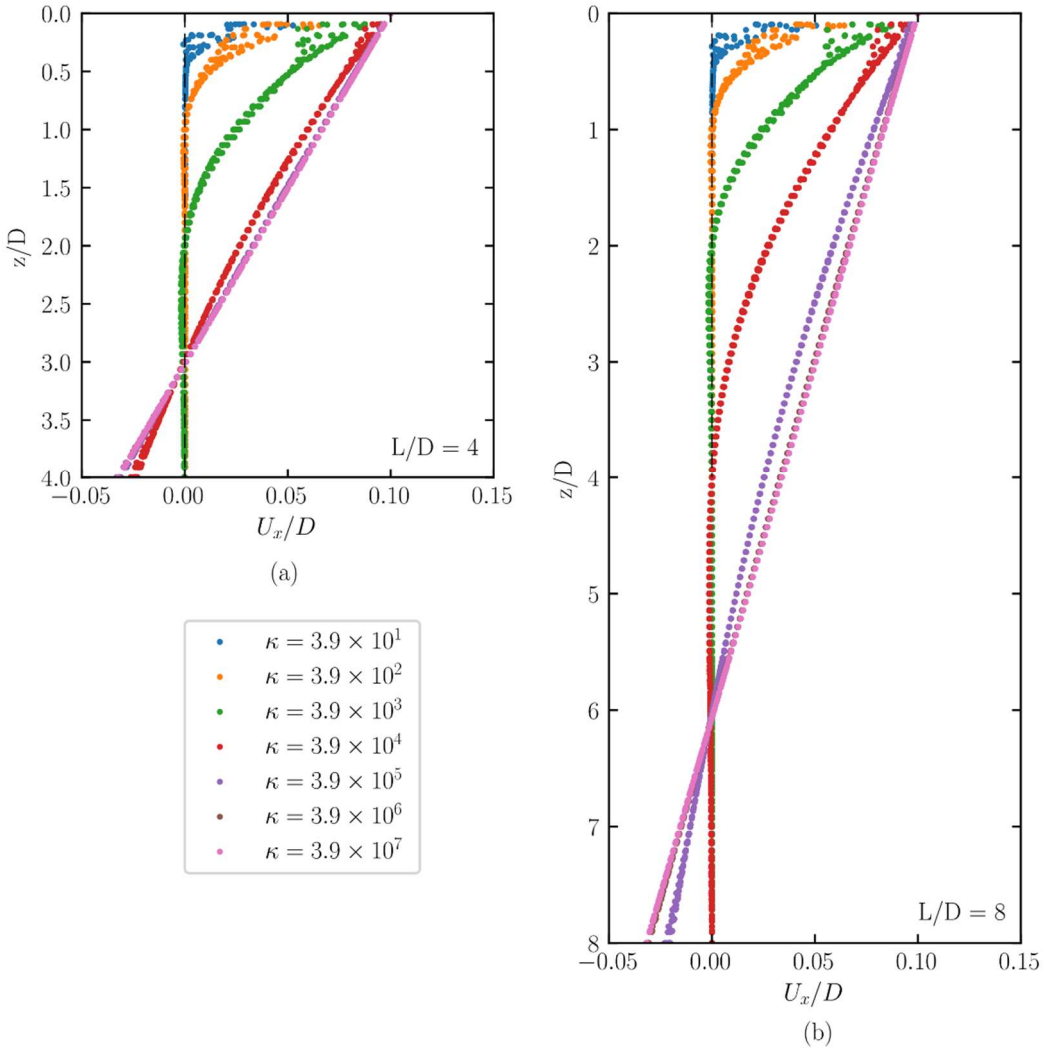

Figure 7.4 - Lateral displacement with depth for HFNWi models with (a) L/D = 4, and (b) L/D = 8. Modelling performed in PLAXIS using Mohr-coulomb model with total stress parameters

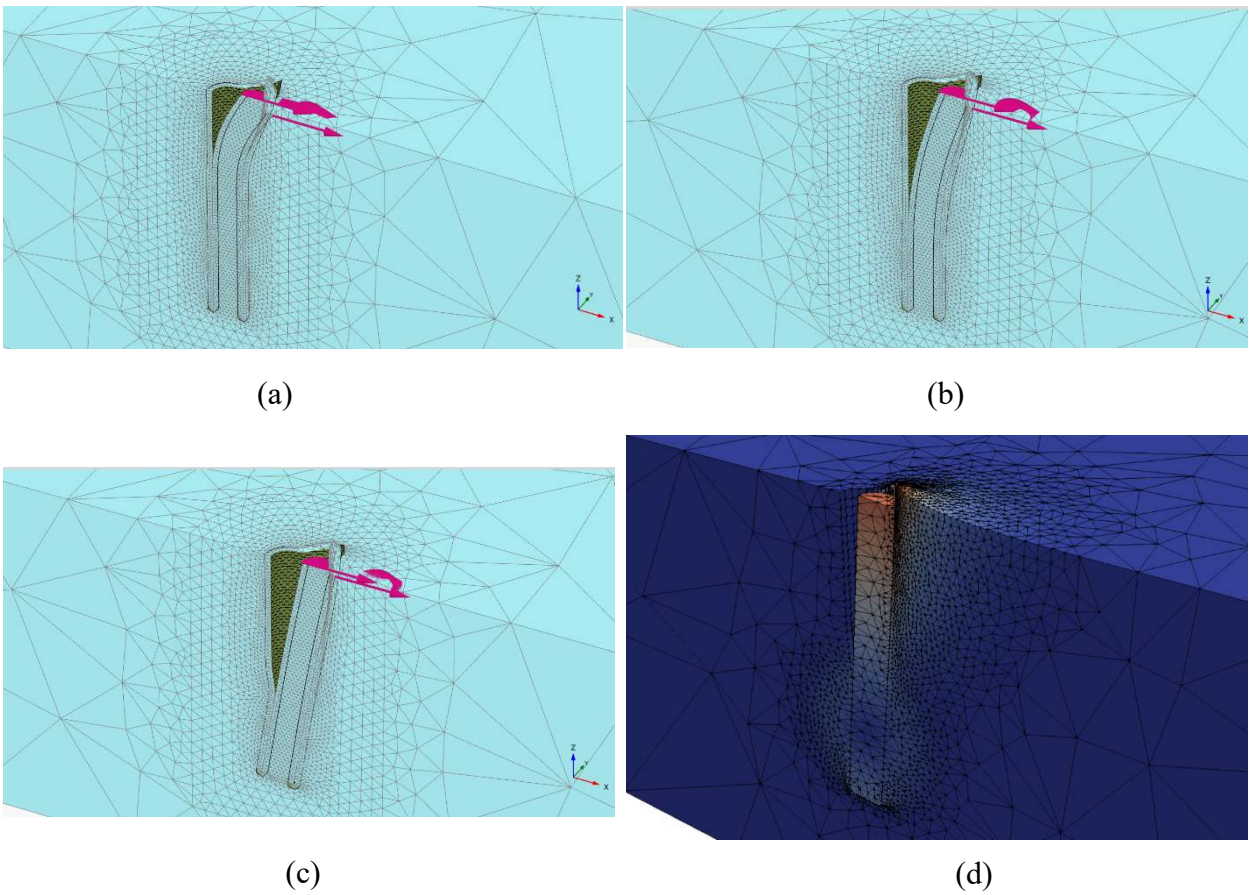

(a) (b)

(c) (d)

Figure 7.5 - Deformed meshes for HFNWi PLAXIS3D model of L/D = 8. Mesh deformation scale set to 10x displacement (a) κ = 3.9 x 10^3, (b) κ = 3.9 x 10^4 ,(c) κ = 3.9 x 10^5,(d) OxLim 3D mesh deformed by nodal velocities from UB analysis

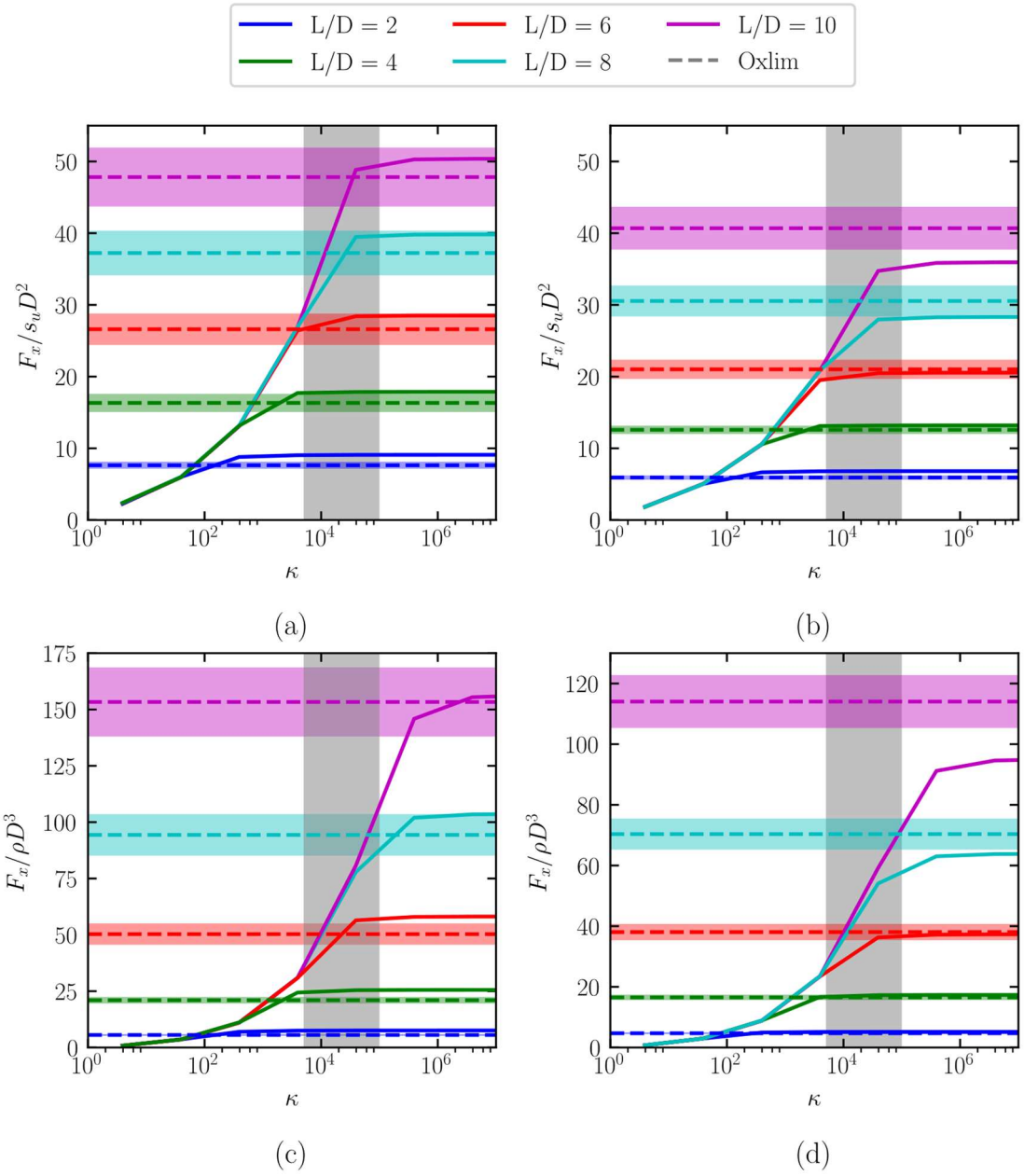

Figure 7.6 - Normalised lateral pile capacity with normalised pile rigidity, κ, for (a) HFTWn, (b) HFNWi, (c) LFTWn, and (d) LFNWi. Solid lines are PLAXIS3D results at 0.1D ground level displacement and dashed lines are OxLim 3D average results. Grey shaded region shows the expected range of κ for tubular steel piles and coloured shaded regions show the range of the upper and lower bound solutions for the relevant OxLim 3D analysis.

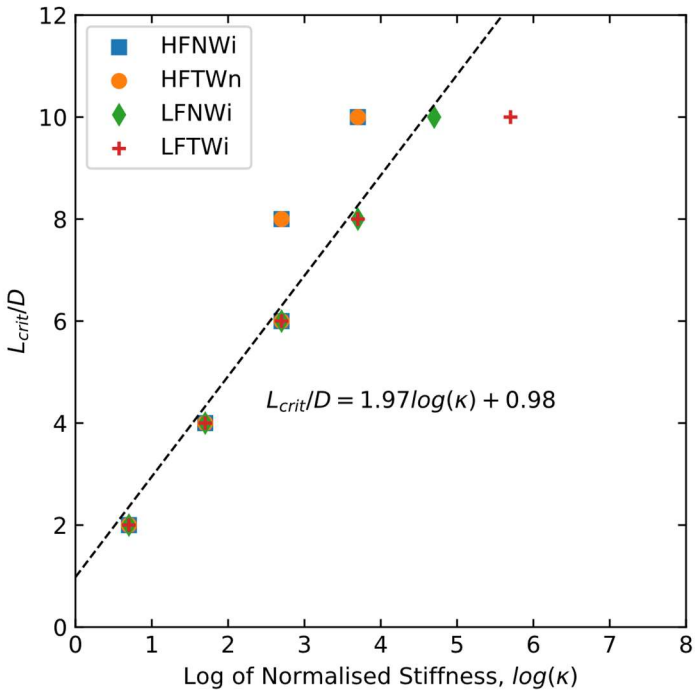

Figure 7.7 - Normalised critical length, L_{crit}/D, for varying normalised pile rigidity, κ, based on PLAXIS3D investigation for HFTWn

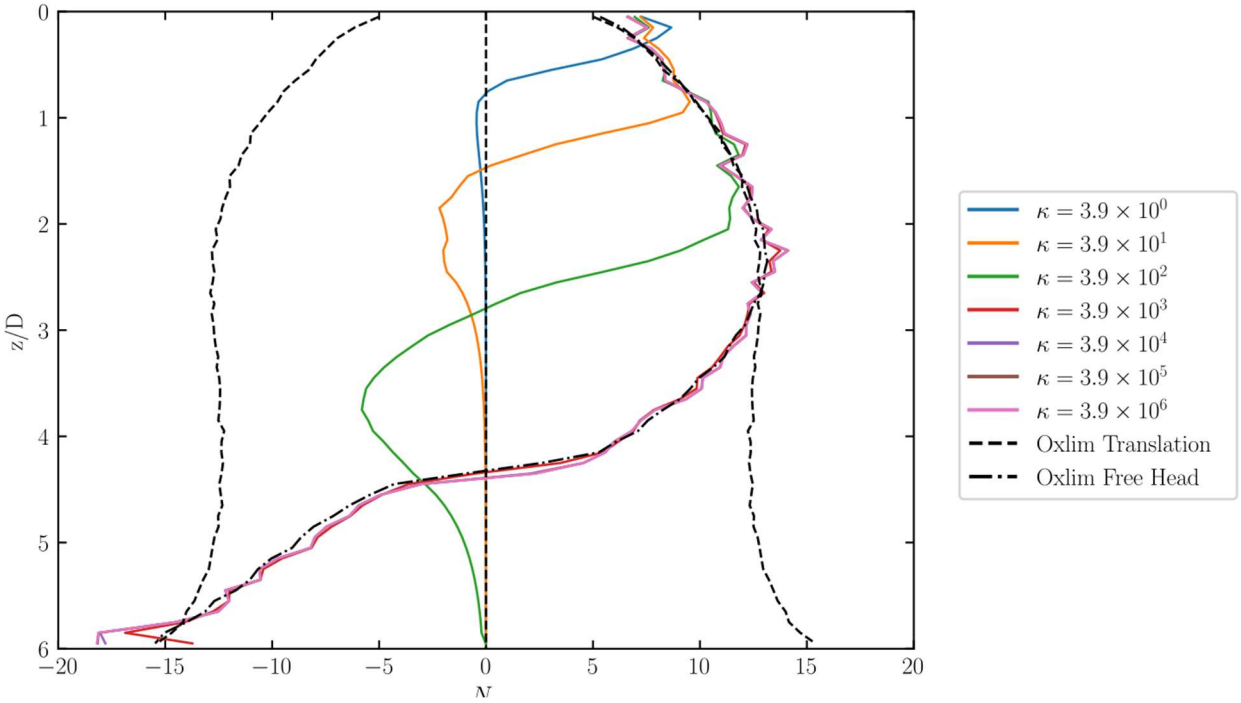

Figure 7.8 - Comparison of lateral bearing factor N_p obtained from PLAXIS3D and OxLim 3D for HFTWn

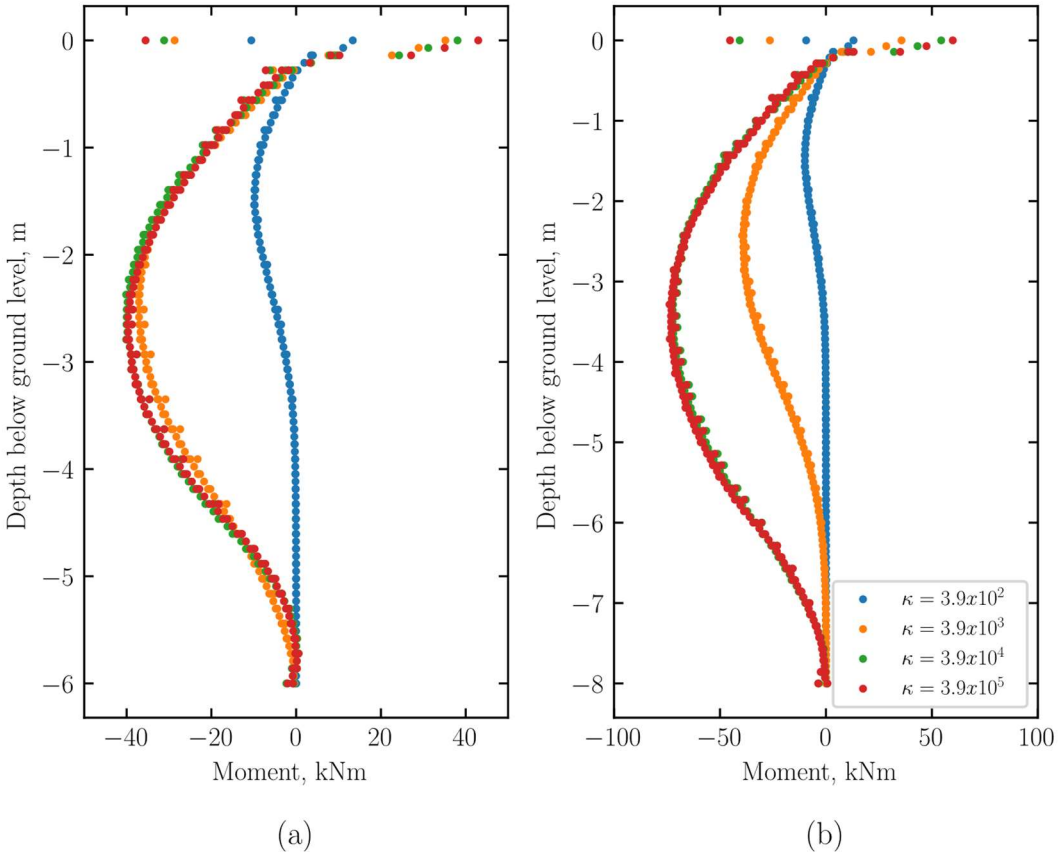

Figure 7.9 - Profiles of moment with depth obtained from PLAXIS modelling for (a) L/D = 6 and (b) L/D = 8

Chapter 8

Design Recommendations and Case Studies

This chapter summarises all the recommendations outlined in this thesis then presents several case studies outlining how the recommendations could be applied in practice.

8.1. Components of lateral resistance

This section outlines the recommendations for each component of ultimate lateral resistance presented in this thesis.

8.1.1. Distribution of lateral resistance

The distributed lateral force can be estimated using the following equations. Equation 8.3 is based on the fitting exercise described in Chapter 5.

$$p_{ult} = N_p s_u D \tag{8.1}$$

$$N_p = min\left(N_{p0} + \frac{\gamma z}{s_{u0} + \rho z},\ N_1\right) \tag{8.2}$$

$$N_{p0} = N_1 - (N_1 - N_2)\left(1 - \left(\frac{z}{dD}\right)^{0.6}\right)^{1.87} \tag{8.3}$$

Where N_1 is the bearing factor at depth, i.e. equivalent to $N_{p,flow}$, and can be estimated using Equation 8.4. (from Chapter 3).

$$\mathrm{N_1} = 9 + 3\alpha \tag{8.4}$$

N_2 is the bearing factor at surface from Equation 8.5 (from Chapter 6.1)

$$N_2 = \begin{cases} 0.6 + 2.1\alpha & No\ interface\ tension, constant\ strength\ at\ surface \\ 1.78 + 2.42\alpha & Full\ interface\ tension, constant\ strength\ at\ surface \\ 0.91 + 2.56\alpha & Any\ interface\ condition, strength\ gradient\ at\ surface \end{cases} \quad (8.5)$$

and d is given by Equation 8.6

$$d = 26.6 - 2.3log\lambda \quad (8.6)$$

with

$$\lambda = \frac{s_{u0}}{\rho D} \quad (8.7)$$

Near the toe of the pile and layer boundaries one of the modifications shown in Figure 8.1can be applied. Table 8.1 (from Chapter 6.2) shows the values of z_t and N_{pt} for the increasing resistance near the pile toe.

Table 8.2 outlines the appropriate values of C to obtain N_{ptw} which can then be used to find N_{pts} (see notes in Table 8.2). For most applications using C = 1.3 will provide suitable results. Care should be taken when $s_{u2}/s_{u1} > 1$ and $z_L/D < 1.5$ as using C = 1.3 may provide unconservative results, for example see results in Figure 5.25 where there is minimal increase in the lower strength layer while the higher strength layer still shows a reduction from the reference N_p profile. Consideration should be given to lower values of C, alternative methods of estimating the reduction on the higher strength layer or performing a bespoke FEA or FELA analysis of the soil profile. Table 8.2 also outlines the typical ranges that z_{tw}/D and z_{ts}/D have, suggested values of each of these variables can be found in Table 8.3. Table 8.3 outlines the appropriate values of z_t to use with varying s_{u2}/s_{u1} and z_L/D. The values in Table 8.3 are intended to be applied across the range of z_L/D and s_{u2}/s_{u1} specified.

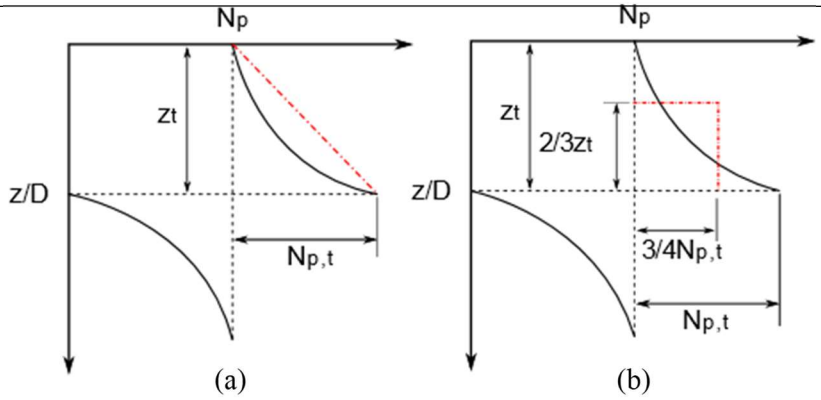

Figure 8.1 - Methods of increasing resistance near the toe of a pile or layer boundaries: (a) linear increase with depth and (b) constant increase

Table 8.1 - Modifications to lateral bearing factor near pile toe

Case	Linear	Constant
Flow	$N_{p,t} = 0.3\left(1 - \frac{L-z}{D}\right)$ $z_t = D$	$N_{p,t} = 0.225$ $z_t = \frac{2}{3}D$
Wedge	$N_{p,t} = 0.2\left(1 - \frac{L-z}{D}\right)$ $z_t = 1$	$N_{p,t} = 0.15$ $z_t = \frac{2}{3}D$

Notes:

1. N_p from Equation 8.2

Table 8.2 - Summary of limits of z_t and N_{pt} near a layer boundary

Parameter	Wedge	Flow-around
$N_{ptw} = C\frac{N_p}{N_{p,ref}}$	$s_{u1} > s_{u2}$	
	$1.3 < C < 2$	$C = 1.3$
	$s_{u1} < s_{u2}$	
	$1 < C < 1.3$	$C = 1.3$
$\frac{z_t}{D}$	$s_{u1} > s_{u2}$	
	$1 < \frac{z_{tw}}{D} < 8$ $0.5 < \frac{z_{ts}}{D} < 1$	$\frac{z_{tw}}{D} = 1$ $\frac{z_{ts}}{D} = 1.5$
	$s_{u1} < s_{u2}$	
	$0.5 < \frac{z_{tw}}{D} < 1$ $1 < \frac{z_{ts}}{D} < 8$	$\frac{z_{tw}}{D} = 1$ $\frac{z_{ts}}{D} = 1.5$

Notes:

- N_{ptw} refers the modified bearing factor in the weaker layer with N_{pts} as the modified bearing factor in the stronger layer with $N_{pts} = N_{ptw}\frac{s_{u1}}{s_{u2}}$
- z_{tw} and z_{ts} refer to the depths the change occurs over for the weaker and stronger layers respectively

Table 8.3 - Values of z_t/D for a layer transition located in the wedge mechanism

		Top Layer				Bottom Layer			
	z_l/D	s_{u2}/s_{u1} **<0.2**	**0.2 to 1**	**1 to 5**	**>5**	s_{u2}/s_{u1} **<0.2**	**0.2 to 1**	**1 to 5**	**>5**
Full Tension	**<0.5**	0.5				1		2	
	0.5 to 1								
	1 to 2								
	>2								
$\frac{\gamma D}{s_{u1}} \geq 2$	**<0.5**	0.5		0.5		1		3	6
	0.5 to 1	0.75						2	5
	1 to 2	1						1.5	5
	>2							1	4
$\frac{\gamma D}{s_{u1}} < 2$	**<0.5**	0.5				3		5	8
	0.5 to 1					2		4	7
	1 to 2	1		0.5		1.5		3	6
	>2					1			
Weightless	**<0.5**	6							
	0.5 to 1	5.5							
	1 to 2	5							
	>2	4							

8.1.2. Distributed Moment profile

For rigid piles the distributed ultimate lateral moment resistance, m_{ult}, can be estimated using Equation 8.8.

$$m_{ult} = N_m s_u D^2 \tag{8.8}$$

Where N_m is a moment bearing factor that can be estimated using the relationships in Table 8.4.

Table 8.4 - Values of moment factor N_m for a rigid pile

L/D ≤ 4	Full Tension, $\gamma D/s_u \geq 5$, $\gamma/\rho \geq 10$	$N_m = \alpha$
	No tension	$N_m = 0.5\alpha$
L/D > 4	Full Tension, $\gamma D/s_u \geq 5$, $\gamma/\rho \geq 10$	$N_m = \begin{cases} 0.8\alpha \ for \ 0 < \frac{z}{D} \leq \min\left(z_g, \frac{z_0}{D} - 1D\right) \\ 0.3\alpha \ for \ \min\left(z_g, \frac{z_0}{D} - 1D\right) < \frac{z}{D} \leq \frac{z_0}{D} - 0.5D \\ -0.25\alpha \ for \ \frac{z_0}{D} - 0.5D < \frac{z}{D} \leq \frac{z_0}{D} + 0.5D \\ 0.25\alpha \ for \ \frac{z_0}{D} + 0.5D < \frac{z}{D} \leq \frac{L}{D} \end{cases}$ $z_g = \begin{cases} 2 \ for \ homogenous \ strength \\ 5 \ for \ a \ strength \ gradient \end{cases}$
	No tension	$N_m = \begin{cases} 0.3\alpha \ for \ 0 < \frac{z}{D} \leq \min\left(z_g, \frac{z_0}{D} - 1D\right) \\ 0.3\alpha \ for \ \min\left(z_g, \frac{z_0}{D} - 1D\right) < \frac{z}{D} \leq \frac{z_0}{D} - 0.5D \\ -0.25\alpha \ for \ \frac{z_0}{D} - 0.5D < \frac{z}{D} \leq \frac{z_0}{D} + 0.5D \\ 0.25\alpha \ for \ \frac{z_0}{D} + 0.5D < \frac{z}{D} \leq \frac{L}{D} \end{cases}$ $z_g = -0.785\eta + 5.5 \ with \ \eta = \frac{\gamma}{rho} or \frac{\gamma D}{s_u} \ as \ appropriate$

8.1.3. Prediction of Base shear and Moment

The limiting shearing resistance on the base of the pile can be estimated using Equation 8.9. If the distance to the rotation point is known, e.g. when performing moment equilibrium for a rigid pile, then Equation 8.10 can be used to determine a reduced lateral base resistance arising from the rotation at the toe of the pile.

$$\frac{F_{ult,base}}{s_u D^2} = \frac{\pi}{4} \tag{8.9}$$

$$\frac{F_{base}}{F_{base,ult}} = \begin{cases} -1 & for\ \frac{L-z_0}{D} \leq -1 \\ \frac{L-z_0}{D} & for -1 < \frac{L-z_0}{D} < 1 \\ 1 & for\ \frac{L-z_0}{D} \geq 1 \end{cases} \tag{8.10}$$

The limiting moment resistance the base of the pile can be estimated using Equation 8.11. If the distance to the rotation point is known, e.g. when performing moment equilibrium for a rigid pile, then Equation 8.12 can be used to determine a reduced moment resistance arising from the lateral displacement at the pile toe.

$$\frac{M_{ult,base}}{s_u D^3} = \frac{\pi}{4} \tag{8.11}$$

$$\frac{M_{base}}{M_{base,ult}} = \begin{cases} 0.3 & for\ \frac{L-z_0}{D} \leq -1.5 \\ \frac{0.47(L-z_0)}{D} + 1 & for -1.5 < \frac{L-z_0}{D} < 0 \\ 1 - \frac{L-z_0}{D} & for\ 0 < \frac{L-z_0}{D} < 1 \\ 0 & for\ \frac{L-z_0}{D} \geq 1 \end{cases} \tag{8.12}$$

8.1.4. Moment Equilibrium

Equation 8.13 shows the moment equilibrium equation that can be used to calculate the lateral and moment resistance of a rigid pile. The equation incorporates the recommendations for distributed moment, base shear and base moment.

$$F_x(h+z_0) = \int_{z=0}^{z_0} p_{ult}(z_0 - z)dz - \int_{z=z_0}^{L} p_{ult}(z)(z - z_0)dz - F_{base}(L - z_0)$$

$$+M_{base} + \int_{z=0}^{L} m_{ult}dz \tag{8.13}$$

Where p_{ult} is the distributed lateral resistance from Equation 8.1, F_{base} is from Equation 8.10, M_{base} is from Equation 8.12 and m_{ult} is obtained from Equation 8.8.

8.1.5. Modification near rotation point

A final modification that can be made to the profile of lateral resistance is the reduction in resistance that occurs at depths were the pile has no lateral displacement: i.e. the rotation point for rigid piles or inflection points for flexible piles. This reduction is only applicable when using Equation 8.13 to predict ultimate resistance and should not be used if using Equation 8.1. to estimate resistance for p-y curves or other displacement based methodologies. It should also be noted that this modification to p_{ult} will not have a significant impact on the total pile capacity if there is not a significant variation of p_{ult} near the rotation; as would occur in homogeneous soil. However there are some scenarios where this modification may be useful to understand a pile's behaviour; such as near a layer boundary with an abrupt change in p_{ult}. The reduction to p_{ult} can be performed by multiplying Equation 8.1 by an additional factor C where

$$C = \min\left(\frac{|z - z_0|}{D}, 1\right) \tag{8.14}$$

8.2. Case Study 1 - Simple London Clay Profile

In this section, the methods outlined in Section 8.1. are used to calculate the capacity of a pile embedded into a simple ground model consisting of a strength gradient with a non-zero surface shear strength. Soil properties are based on clays from the London Clay Formation (Hight et al., 2003) An example calculation is performed for a pile with a diameter of 6m and a length of 24m; resulting in $L/D = 4$. The results from this comparison are compared to an OxLim model using the same geometry and soil conditions. A breakdown of the contribution of each component of resistance, i.e. p_{ult}, m_{ult}, F_{base}, and M_{base}, are shown alongside a comparison of each component to the value obtained from the OxLim model.

8.2.1. Soil properties

Ground conditions for this case study are based on those commonly encountered in the London Clay formation. This formation is prevalent both onshore in the South-East of England and Offshore in the Southern North sea. The London Clay formation typically consists of silty to very silty clays that can be up to 150m thick. The London Clay formation is encountered frequently in civil engineering projects in the South-East of England, such as Heathrow Terminal 5 (Hight et al., 2003) and the Galloper Offshore Windfarm (ABPmer, 2011). As such, geotechnical data for this geological unit is widely available. For the purpose of this case study, reference is made to the bulk density and undrained shear strength data presented in Hight et al. (2003). For the purpose of this case study only two parameters are needed to represent the soil; the unit weight and the undrained shear strength. The data from Hight et al. (2003) indicates bulk density of approximately $\rho_b = 2\text{Mg/m}^3$; corresponding to a bulk unit-weight of $\gamma_b = 19.62\text{kN/m}^3$. For this case study it is assumed that any gap that forms will remain dry as such the bulk unit weight is used for calculations. The estimated undrained shear strength profile from Hight et al. (2003) can be summarised as

$$s_u = \begin{cases} 40 + 6.4z & for\ z \leq 25 \\ 125 + 5z & for\ 25 < z \leq 45 \\ 600 & for\ z > 45 \end{cases} \quad (8.1)$$

This is shown in Figure 8.2. However, for this case study a simpler profile that avoids the jumps in strength present in Equation 8.1 is used. This profile is given by Equation 8.2 and marked onto Figure 8.2.

$$s_u = 50 + 6z \quad (8.2)$$

For this case study a pile-soil adhesion ratio of $\alpha = 1$ has been assumed.

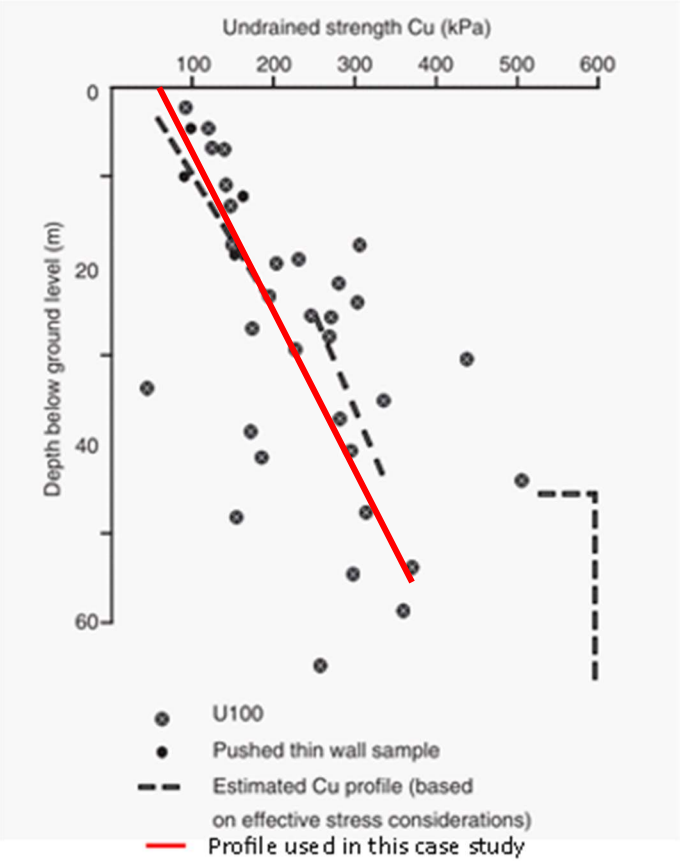

Figure 8.2 - Undrained shear strength with depth for London Clay from Undrained Unconsolidated (UU) testing on clay (Hight et al, 2003) with strength profile

8.2.2. Comparison of simple methods to OxLim

Both OxLim and the simple methods outlined in Section 8.1 have been used to calculate the various components of ultimate capacity. The capacity for the simple method has been

calculated using a python script that calculates the components of lateral resistance outlined in Section 8.1. then solves Equation 8.13. through changing the rotation point. Comparisons of the two methods for the distributed lateral and moment reactions are shown in Figure 8.3; in each case OxLim results are shown as the average with a shaded region to represent the region between the lower and upper bound solutions. A summary of the results is provided in Table 8.5.

Table 8.5 - Summary of case study 1 simple method and OxLim obtained resistances

Component	Simple Method	OxLim LB	OxLim UB	OxLim AVG	Percentage Difference[1]		
Total Lateral Capacity	45101kN	44583kN	49385kN	46984kN	1.1%	-9.5%	-4.2%
Base shear	3931kN	4531kN	4749kN	4640kN	-15.6%	-21.1%	-18.3%
Base Moment	9324kNm	5799kNm	9179kNm	7849kNm	37.8%	1.6%	15.8%
Rotation point depth	19.7m		19.1m			3.0%	

Notes:
1. Percentage difference refers to the increase of decrease of the simple method results from the respective OxLim result

To get the distributed lateral resistance using the simple method first N_p has been calculated using Equation 8.2 to Equation 8.7. This results in the N_p profiles shown in Figure 8.3(a). The distributed lateral resistance can then be calculated from the N_p profile using Equation 8.1. This includes modification near the toe of the pile using the linear increase in the wedge mechanism from Table 8.1 and linear scaling to $N_p = 0$ at the rotation point, z_0, from ±0.5D from the rotation point. The moment contribution from p_{ult} is then calculated, i.e. the first two components of the RHS of Equation 8.13, resulting in the profile shown in Figure 8.3(c). The profiles of lateral resistance obtained from both the simple method and OxLim match well over the entire depth of the model. There is a more noticeable difference that occurs near the toe of the pile; this is due to the proximity of the rotation point to the toe of the pile. In the simple method, the reduction in resistance applied above and below the rotation point is always applied over a fixed

depth of ±0.5D as a best approximation across all the cases reviewed in this thesis. The influence of the rotation point on the nearby mobilised resistance does extend some distance further than ±0.5D and as such can influence the results as seen here. However, the influence shown here is minimal with a maximum local difference of 10% only occurring over a small depth.

The distributed moment has been calculated using the approach outlined in Table 8.4. As L/D ≤ 4, no interface tension is allowed in the model, $\gamma D/s_{u0}$ = 2.36, and γ/ρ = 3.28 a value of N_m = 0.5α is used. With α = 1 this results in N_m = 0.5; as shown in Figure 8.3(d). The distributed moment, m_{ult}, is then calculated using Equation 8.8 resulting in the profile shown in Figure 8.3(e). The distributed moment profiles from OxLim have been extracted using the methodology outlined in Chapter 6.4. and are also shown on Figure 8.3(d) and Figure 8.3(e). The difference between the simple approach and OxLim obtained results is much more apparent than for the distributed lateral resistance. This is due to the relatively simple method adopted for the simple approach for $L/D \leq 4$. However, the average N_m over the depth of the pile is N_m = 0.52; very close to the estimate of 0.5α of the simple method. This means that while locally the OxLim and simple methods may deviate significantly the global contribution, i.e. as used for calculating the contribution of distributed moment in Equation 8.13., is similar between both methods.

The base shear and moment have been calculated using Equations 8.9 to 8.12. This gives ultimate resistances of $F_{base,ult}$ = 5,485kN and $M_{base,ult}$ = 32,911kNm. These values are then used in the moment equilibrium analysis as part of Equations 8.10 and 8.12. Performing moment equilibrium analysis with the resistance profiles shown in Figure 8.3 and the base resistances resulted in a rotation point of z_0 = 19.7m. This results in $\frac{L-z_0}{D}$ = 0.717 and as such the reduced base shear resistance in the simple model is F_{base} = 0.717$F_{base,ult}$ = 3,931kN. With z_0 = 19.7m this results in the base shear contributing 23,586kNm to the moment equilibrium calculation (Equation 8.13). Similarly to the base shear, the base moment resistance gets modified using

Equation 8.12 to M_{base} = (1-0.717)$M_{base,ult}$ = 9324kNm. These compare to the average results from OxLim of F_{base} = 4,640kN and M_{base} = 7,849kNm. These are -18.3% and +15.8% difference of the simple results from the OxLim. This difference is predominantly due to the difference in rotation point depth predicted between OxLim and the simple method. The rotation points in the simple method and OxLim are 19.7m and 19.1m respectively; a difference of 0.6m. The investigation in Chapter 6 showed that the base shear and moment scale linearly with the distance from the rotation point over a distance of 1D. A change of rotation point depth of 0.6m for a 6m diameter pile suggests a 10% change based on Equations 8.10 and 8.12.

The total lateral capacity obtained from the simple method is 45,101kN. As shown in Table 8.5 this results in a resistance 4.6% lower than the average from the OxLim results. It should be remembered that the OxLim results are expected to be slightly higher than the true value due to the segmentation of the pile cross section resulting in a higher flow around bearing factor; see Chapter 3. This segmentation results in an increase of $N_{p,flow}$ of approximately 5% for the OxLim model used in this case study. However, as can be seen in Figure 8.3(a) the limiting resistance of the flow around mechanism is not achieved within the 24m length of the pile. As such, the difference in N_p profiles between the two methods will only account for a part of the difference. The remainder of the difference likely arises from the different rotation point depths obtained from the two approaches which leads to the significant differences in the base resistances.

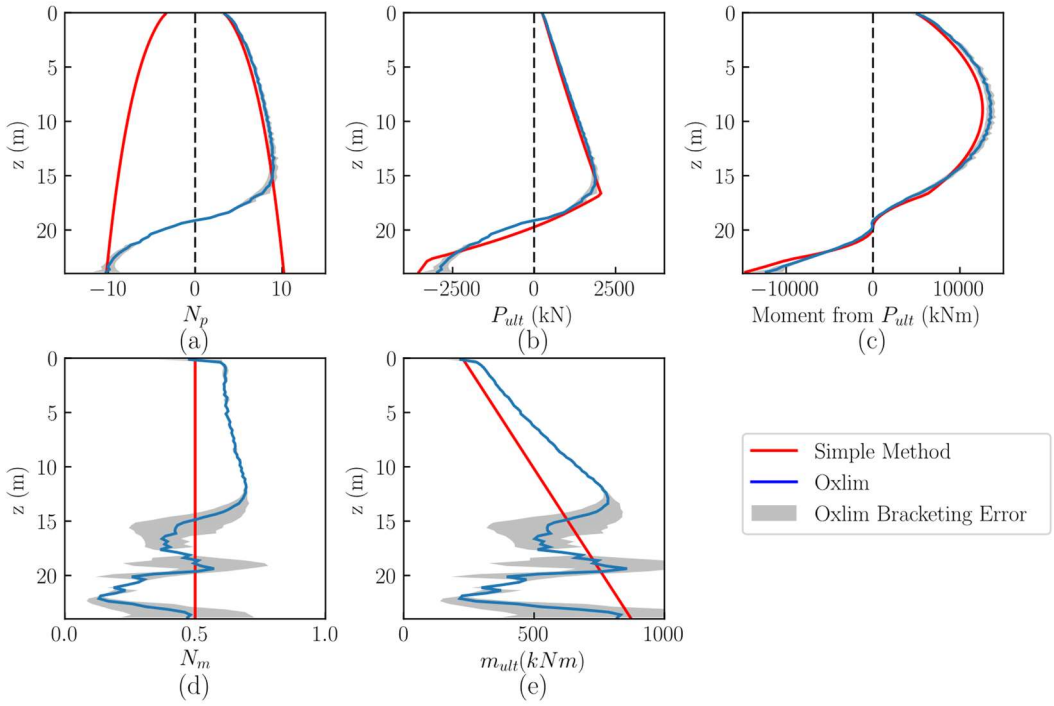

Figure 8.3 - Comparison of distributed lateral and moment resistance using simple method and OxLim (a) N_p, (b) p_{ult}, (c) moment arising from p_{ult}, (d) N_m, and (e) m_{ult}

8.3. Case Study 2 - London Clay with high strength variation

In this section, a case study is performed comparing the simple method to OxLim for a strength profile with an abrupt increase in strength. Soil properties are based on the same data used for Case Study 1 (Hight et al., 2003) but with a different assumed strength profile to represent a jump in strength at 20m depth. In this case study, a diameter of 6m is used and L/D is varied between 2 and 6 to show the effect of the strength change on the contribution of each mechanism.

8.3.1. Soil Properties

In this case study the strength profile shown in Figure 8.4 is used. This strength profile is summarised as

$$s_u = \begin{cases} 100kPa\ for\ z < 20m \\ 250kPa\ for\ z \geq 20m \end{cases} \tag{8.3}$$

resulting in

$$\frac{s_{u2}}{s_{u1}} = 2.5$$

In this case study a typical effective unit weight of γ' = 10kN/m^3 is assumed, i.e. a value representative of typical offshore conditions Equation 8.3. and this unit weight result in

$$\frac{\gamma' D}{s_{u1}} = 0.6$$

Pile-soil adhesion of α = 0 and α = 1 is used in this case study to demonstrate the effect of this parameter on the contribution of each component to the overall capacity.

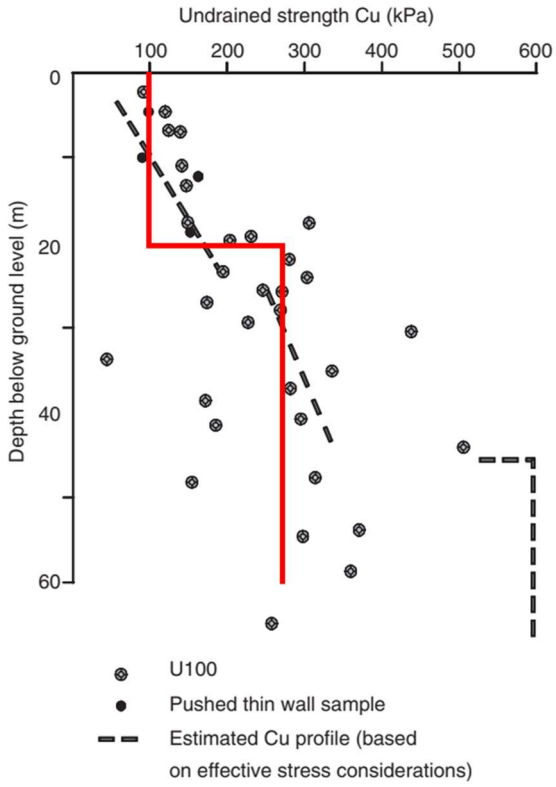

Figure 8.4 - Strength profile for case study 2

8.3.2. Comparison of the simple and OxLim methods

To calculate the total capacity using the simple method with modifications for a layer boundary, the following steps are taken:

1. Unfactored N_p profiles are calculated for both layers using Equation 8.2 and Equation 8.3.
2. The depth the transition occurs over, z_{ts} and z_{tw} for the strong and weak layer respectively, and N_{pt} are estimated from Table 8.2 and Table 8.3. The parameters used to select these values are s_{u2}/s_{u1} = 2.5, $\gamma D/s_u$ = 0.6, and z_L/D =3.3. The values of z_L/D and s_{u2}/s_{u1} are between those shown in Figure 5.35(c) and (d). These parameters mean that N_{pt} = 1.3 can be used from Table 8.2 as z_L/D is sufficiently high to minimise the risk of a strength overprediction in the lower strength layer. The values of z_{tw}/D and z_{ts}/D are obtained from the 'Top Layer' and 'Bottom Layer' columns respectively in Table 8.3 as $s_{u2} > s_{u1}$ (i.e. the stronger layer is the bottom layer). Reading from the $\gamma D/s_u < 2$ row, z_{tw}/D = 0.5 and z_{ts}/D = 3 are obtained for z_L/D = 3.3 and s_{u2}/s_{u1} = 2.5.

   In summary:

   a. N_{pt} = 1.3
   b. z_{tw}/D = 0.5
   c. z_{ts}/D = 3

3. The N_p profile is then modified using the linear approximation shown in Figure 8.1(a) using the previously obtained values of N_{pt}, z_{tw}/D and z_{ts}/D.
4. Additional modifiers for the increase near the toe, Table 8.1, and near the rotation point, Equation 8.14, prior to performing moment equilibrium for a defined z_0, are applied. The modification near the toe is performed using the linear increase method for a toe within the wedge mechanism depth (i.e. increasing N_p by a factor of 1.2 at the toe itself.)
5. The distributed lateral resistance, p_{ult}, for both layers is then calculated using Equation 8.1 using the N_p profile calculated in steps 1 to 4.

6. The profile of N_m for the distributed moment is obtained using the relevant no tension equations in Table 8.4 for the L/D ratio being assessed.
7. Base shear and moment resistance are calculated using Equations 8.9, 8.10, 8.11 and 8.12.
8. Moment equilibrium using Equation 8.13 is performed with z_0 varied until the minimum resistance is found. Note that with each iteration of z_0 variation steps 6 and 7 need to be repeated to obtain a new distributed moment profile and new base resistances as the rotation point has changed.

Using the simple method to generate lateral resistance profiles for L/D = 3.5 to 6 results in the profiles shown in Figure 8.5. The simple method for predicting the change of N_p near a layer boundary gives a good match in the majority of cases shown here. However, it is clear that the combination of factoring methods, i.e. reduction near rotation point, increase at toe, etc., does not provide a fully accurate representation of the soil behaviour when the layer boundary is located near the toe or rotation point. For example, for L/D = 4.5 the rotation point depth z_0 = 22.3m which puts the layer boundary within 0.5D of the rotation point and within the depth influenced by the reduction factor for N_p for the rotation point. The simple method does not appear to correctly capture the change in p_{ult} near the layer boundary, however the resulting p_{ult} profile is close enough to the OxLim case that this will have minimal effect on the predicted ultimate resistance.

For L/D > = 5, i.e. Figure 8.5 (d), (e), and (f), the simple method gives a very good match to the OxLim predicted profile. At the layer boundary the jump in p_{ult} is calculated correctly with the layer boundary factor leading to a good representation of the change in p_{ult} caused by the proximity to the layer boundary. This can be best seen when plotting both the factored and unfactored N_p from the simple method which is shown in Figure 8.6(a). The unfactored N_p profile shows a discrete jump from the bearing factor in the top layer to the bearing factor in the bottom layer; in this case a decrease from N_p = 9.5 to N_p = 8.5. This compares to the OxLim

results where N_p = 11.6 just above the layer boundary and N_p = 6.9 just below the layer boundary. Once modified using the rules outlined at the start of this chapter the N_p values at the layer boundary better match the OxLim results; being N_p = 12.3 and N_p = 6.8 above and below the boundary respectively. Below the layer boundary it is also evident that the unfactored profile overpredicts the resistance with the unfactored N_p being consistently higher than the OxLim obtained results. The proposed system of factoring N_p results in a better match to the OxLim results down to z = 26m where the reduction due to the proximity to the rotation point starts affecting the N_p profile. Figure 8.6(b) and (c) show the p_{ult} and moment arising from p_{ult} for L/D = 6 in this case study; again showing a good match between OxLim and the simple method.

Figure 8.6(d) and (e) show the comparison between OxLim and the simple method for the distributed N_m and m_{ult}; estimated using the methodology in Section 8.1.2. A reasonable estimate is obtained over the entire depth of the pile with the increase in m_{ult} at the layer boundary being represented well in the simple method. It is interesting to note that at the depth of the layer boundary there is only a small increase and decrease in N_m. The work done in Chapter 6 did not consider the potential effect of a layer boundary on N_m however based on this, and the other N_m profiles that were obtained in the course of this case study but not shown here, it could be reasonably construed that no modification is needed for a jump in soil strength when estimating N_m. However there are many other factors that may influence this, such as pile-soil adhesion, whether the layer boundary is in the wedge or flow mechanisms etc., and as such this is an aspect of the resistance that warrants further investigation.

Table 8.6 shows the calculated total capacities for each of the L/D values investigated by both OxLim and the simple method. As with the first case study, the simple method results in a capacity approximately 5% below that of the OxLim capacity. Note that the bracketing error of the higher L/D models is relatively high at greater than 10% however it is interesting to note that the simple method still gives a similar match to the average of the lower and upper bound.

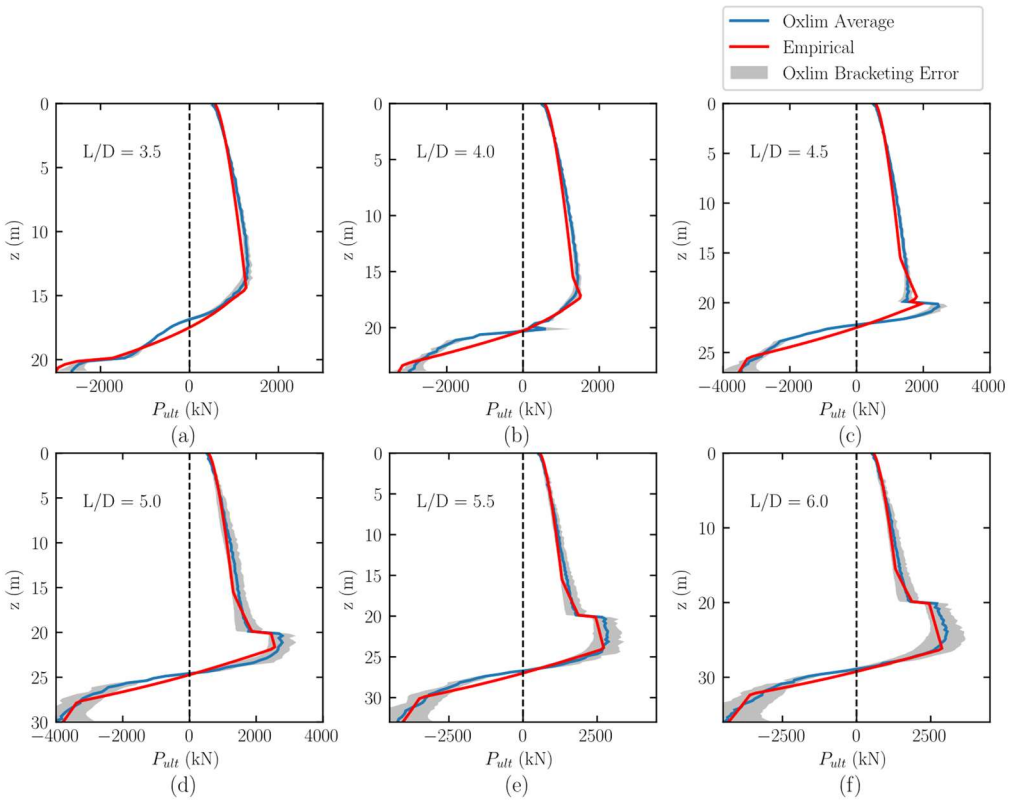

Figure 8.5 - Lateral resistance profiles calculated using OxLim and the simple method for s_{u2}/s_{u1} = 2.5, γ = 10kN/m³, α = 1, D = 6m for (a) L/D = 3.5, (b) L/D = 4, (c) L/D = 4.5, (d) L/D = 5, (e) L/D = 5.5, and (f) L/D = 6

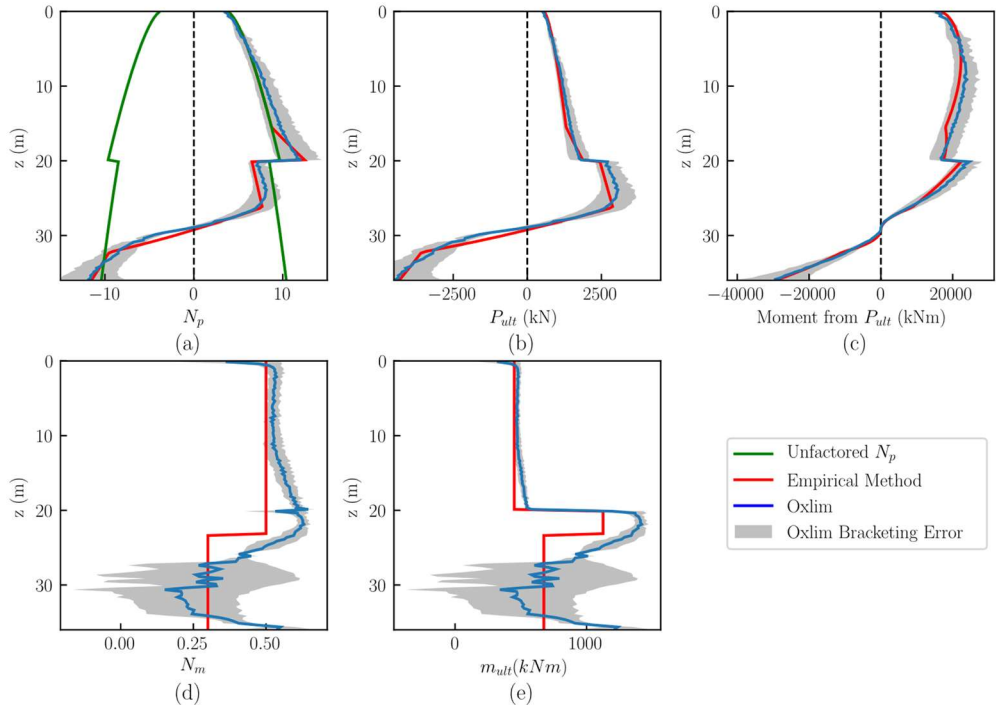

Figure 8.6 - Comparison of distributed lateral and moment resistance using simple method and OxLim with D=6m, L/D = 6, γ = 10kN/m³, α = 1, s_{u2}/s_{u1} = 2.5, (a) factored and unfactored N_p , (b) p_{ult}, (c) moment arising from p_{ult}, (d) N_m, and (e) m_{ult}

Table 8.6 - Summary of total lateral capacity obtained using OxLim and simple methods for Case Study 2

	OxLim					
L/D	Lower Bound	Upper Bound	Bracketing Error	Average	Simple	Difference[1]
3.5	38,190kN	42,725kN	5.3%	40,457kN	38,942kN	-3.7%
4	46,630kN	51,628kN	4.8%	49,129kN	46,562kN	-5.2%
4.5	55,099kN	61,014kN	4.8%	58,056kN	54,250kN	-6.6%
5	58,978kN	77,457kN	11.9%	68,217kN	63,848kN	-6.4%
5.5	64,438kN	88,601kN	11.4%	78,519kN	74,556kN	-5.0%
6	76,543kN	104,163kN	13.3%	90,353kN	86,251kN	-4.5%

Notes:
[1] Difference between the simple method and the OxLim average results

8.4. Case study 3 - Cowden Till

This final case study will use the methods outlined in at the start of this chapter to predict the lateral capacity of the piles tested at Cowden as part of the PISA project (Byrne et al. 2017). The PISA programme included extensive pile testing at the Cowden site with an aim of providing test data to calibrate 3D FEA and a numerical method of predicting the pile load-displacement response. The testing programme included monotonic load tests on piles with diameters between 0.762m and 2m. L/D ratios between 3 and 10 were tested. A summary of the pile tests is provided in Byrne et al. (2019) with key information summarised in Table 8.8. Table 8.8 also includes estimates of the lateral capacity from the pile tests based on the load-displacement responses provided in Byrne et al. (2019). In each case, the lateral capacity of the pile listed in Table 8.8 refers to the lateral resistance at $0.1D$ displacement. While some of the pile tests show resistance still increasing at displacements beyond $0.1D$, taking the resistance at $0.1D$ provides a systematic way of comparing to the simple method and OxLim. It should be remembered that in both the simple method and OxLim there is no consideration of pile had displacement.

The ground conditions at Cowden, outlined in Zdravkovic et al. (2019), consist of stiff overconsolidated clays typical of the clay formations found in the North Sea. The profile of

undrained shear strength at Cowden is shown in Figure 8.7 with a summary of the strength profile and other key parameters given in Table 8.7. It should be noted that the strength profile at Cowden is considerably more complex than the profiles so far considered in this Thesis. While the Cowden profile contains two distinct features, the 4m thick high strength 'crust' of soil near surface and the simpler strength gradient that occurs below this, the change in strength between these features is different from the abrupt changes outlined in this Thesis. Work by Grajales et al. (2017) provided insight into the effect of layer such as this where neighbouring layers have different strength gradients but the same strength at the layer boundary. In this case study, no modification near the boundaries of the layers is made, such as previously in this Thesis been done for abrupt changes in strength. As has been pointed out in Section 8.3, the modification of the N_p profile near layer boundaries does not always effect the overall capacity of the pile due an averaging effect that can occur between the increase and decrease in resistance in the weak and strong layers respectively. It is thought by this author that the overall effect of layering will be greatest when the difference in strength between two layers is high. In the case of Cowden, there is no abrupt changes of strength but quite significant changes in the strength gradient.

This case study is split into two parts. Part one of the case study will compare the capacities obtained from the pile load tests to both OxLim and the simple method. Part two will then use the 1D method proposed by PISA and compare the results of this to the pile capacities obtained using OxLim and the simple methods.

Table 8.7 - Summary of soil parameters used in this case study

Top Depth	Bottom Depth	Surface shear strength, s_{u0}	Strength gradient, ρ	Bulk Unit weight, γ	Effective Unit Weight, γ'
m	m	kPa	kPa/m	kN/m^3	kN/m^3
0	2	50	55	21.19	11.19
2	2.5	160	0	21.19	11.19
2.5	4	243.3	-33.3	21.19	11.19
4	-	87.5	5.625	21.19	11.19

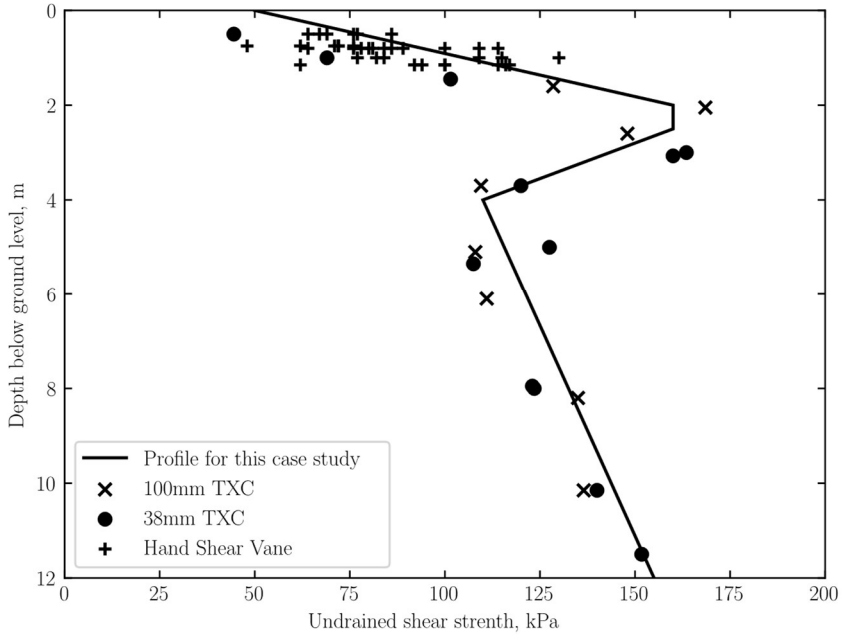

Figure 8.7 - Triaxial (TXC) compression testing and Hand Shear Vane strength data from PISA with strength profile used in this case study (Zdravkovich et al. (2019))

8.4.1. Comparison of OxLim and simple method to PISA pile load tests

Table 8.8 summarises the results from comparing OxLim to the pile load tests. OxLim calculations have been performed using the iterative model outlined in Chapter 6 Section 4. For each test three values of pile-soil interface strength ratio of α = 0, 0.5, and 1 have been used. While the PISA numerical modelling used $\alpha = 1.0$ it is not clear if this is an appropriate value. It is generally accepted that in clays the installation of the pile should create a region of remoulded material at the pile interface with a lower strength than the surrounding intact material. However the magnitude of this strength reduction is not readily definable. This is further complicated by the loading of the soil at the pile-soil interface being different when a pile is laterally loaded when compared to an axially loaded pile. As such is an area where further work is required to understand the implications. A summary of the results is shown in Figure 8.8 with Figure 8.8 (a) showing the ratio of OxLim obtained capacity to PISA test result against *L*/*D* and Figure 8.8 (b) showing the ratio of capacities for each test. OxLim overpredicts the

capacity in every case. There are a couple of potential reasons for this. Firstly, it should be noted that all the PISA results in Table 8.8 and Figure 8.8 refer the capacity obtained at 0.1D ground level displacement which is common practice when performing lateral pile testing. However, the capacity obtained in OxLim represents the plastic collapse load of the soil, something that might not have occurred at 0.1D deflection. The effect of this can be seen in Figure 8.8(a) where it is evident that greater over predictions occur for higher L/D ratios. This fits with the observations from Chapter 7 whereby higher L/D ratios needed a larger EI/s_uD^4 to equal the OxLim capacity. It was also observed that greater deflection was required in these Plaxis models to obtain a resistance similar to OxLim (see Figure 7.6). A similar response is likely occurring here and as such the PISA tests are not showing the ultimate soil resistance at 0.1D. Review of the load deflection behaviour of the piles at Cowden, shown in Byrne et al. (2019) supports this. For example for CM2 and CM9, which have L/D = 3 and L/D = 5.25, respectively the response appears to plateau at or just above 0.1D whereas the response CM3, which has L/D = 10, looks like it would have further increasing resistance beyond 0.1D. The OxLim analysis overpredicts the resistance of CM2 and CM9 by 30% to 100% depending on α while the overprediction for CM3 is 80% to 136%.

Another factor to consider in this comparison is that the strength profile used has been predominantly derived from consolidated anisotropic undrained compression (CAUc) triaxial tests. It is widely recognised that the shear strength of clay can be stress path dependent. In the PISA 3D numerical modelling (Zdravkovic et al., 2019) this was accommodated through use of a generalised yield and plastic potential surfaces (Van Eekelen, 1980) to the constitutive model which resulted in strength variation with varying lode angle; i.e. the soil would have different strengths when loaded in compression and extension. In OxLim, the Drucker Prager model does not account for Lode angle dependency; i.e. when a strength profile based only on compression tests is used the model will overpredict the strength in areas of the model where the soil is in extension. The work by Jeanjean et al. (2017) included an attempt to modify the

p_{ult} profile by a factor to account for the expected loading conditions with depth; i.e. reduced strength near surface where extension is expected. The efficacy of this factor is not tested herein, however it is accepted that further review of the effect of soil strength anisotropy on pile lateral resistance is required. Caution is advised when deriving a shear strength profile for use in calculating lateral resistance and that if possible consideration should be given to the use of consolidated anisotropic undrained extension (CAUe) testing where possible.

A final consideration is that soil is fundamentally a highly variable material. The strength profile presented is based on tests performed at multiple locations across the Cowden site, as is common practice for geotechnical investigations. A drawback to this is that it introduces a potential error to each calculation as local conditions may differ from the assumed profile. This is most relevant to the smaller pile tests which will typically be more sensitive to local strength variations due to the smaller pile geometry; i.e. while the estimated capacity of a larger pile will be affected by a local strength variation the overall effect on the capacity may not be significant if the variation only occurs over a small depth of a pile.

Comparisons of the simple method to the PISA test results is shown in Figure 8.9 alongside a summary table of the obtained capacities. The results show a better match to the PISA test results predominantly due to the reasons outlined in Section 8.3.2 and 8.3.3 for the simple method giving lower resistances than the OxLim models. The simple method still leads to over predictions in most cases however the results are now much closer to parity with the PISA test results; the over prediction for $\alpha = 0.5$ for CL1 and CL2 is now only 15% compared to the 42% overprediction for $\alpha = 0.5$ from OxLim.

Table 8.8 - Summary of PISA pile test results and OxLim capacities

Test Pile	Diameter	L/D	$H_{0.1D}$	Installed length	Gap Depth	h	OxLim		
							α = 0	α = 0.5	α = 1.0
	m	-	kN	m	m	m	kN	kN	kN
CS1	0.27	5.25	7.63	1.4	-[1]	5	10.5	13.1	14.8
CS2	0.27	5.25	4.01	1.4	-[1]	5	10.5	13.1	14.8
CS3	0.27	8	14.5	2.2	1.47	5	33.8	40.7	45.4
CS4	0.27	10	21.5	2.7	1.17	5	53.3	63.8	70.8
CM2	0.76	3	31.8	2.2	1.65	10.06	42.6	55.9	64.0
CM8	0.76	3	-[2]	2.3	1.5	9.92	47.9	62.5	71.4
CM6	0.76	5.25	-[2]	4.1	2.3	9.98	169.2	211.7	239.0
CM9	0.76	5.25	116.2	4.1	2.2	9.98	169.2	211.7	239.0
CM1	0.76	5.25	-[2]	4.1	-[1]	9.98	169.2	211.7	239.0
CM3	0.76	10	392.2	8	3.66	10.01	704.6	835.5	927.4
CL1	2	5.25	2096	10.3	5	10.1	2460	2995	3370
CL2	2	5.25	2217	10.6	6.15	10.1	2597	3151	3544

Notes:
1. Gap depths not presented for these tests in Byrne et al. (2019)
2. Lateral resistance at 0.1D not presented for these tests in Byrne et al. (2019)

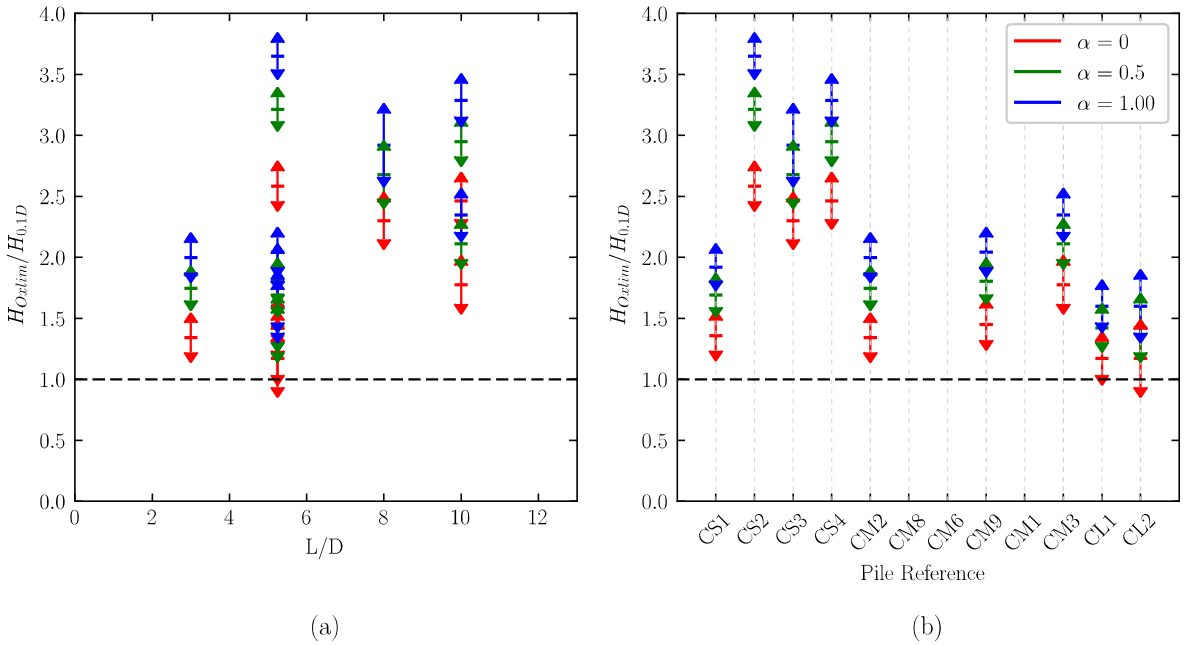

Figure 8.8 - Ratio of OxLim obtained capacity to H0.1D pile test result (a) with L/D, (b) for each test pile

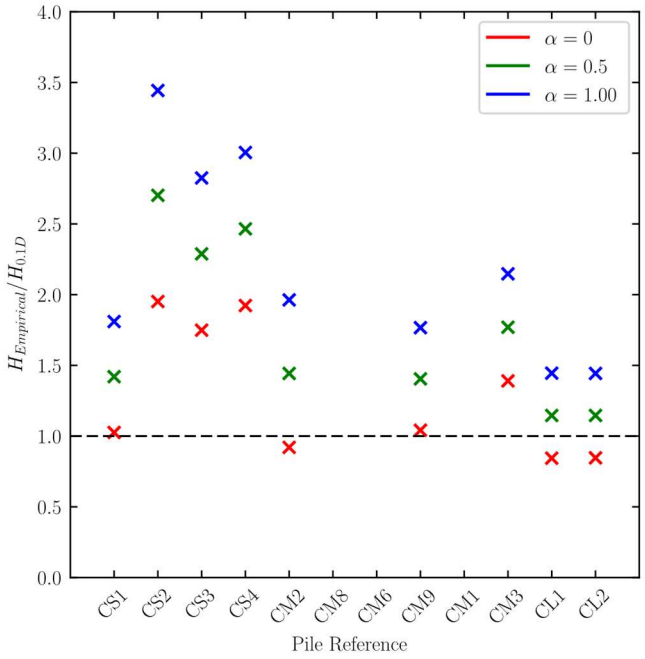

Test Pile	H_{simple} α = 0 kN	α = 0.5 kN	α = 1.0 kN
CS1	7.83	10.84	13.81
CS2	7.83	10.84	13.81
CS3	25.36	33.18	40.97
CS4	41.35	53.0	64.61
CM2	29.27	45.88	62.42
CM8	33.11	51.49	69.76
CM6	121	163.2	205.2
CM9	121	163.2	205.2
CM1	121	163.2	205.2
CM3	545.2	694.0	842.1
CL1	1768	2401	3028
CL2	1876	2540	3199

Figure 8.9 - Ratio of simple method obtained capacity to $H_{0.1D}$ pile test result for each test pile with summary table of simple method capacities

8.4.2. Using the simple method and OxLim in the PISA 1D approach

In order to understand the difference between the ultimate capacity of a pile and the capacity at 0.1*D* the 1-Dimensional modelling approach proposed in PISA has been used (Byrne et al., 2017). This has been performed using the OxPile software. OxPile consists of a library of Matlab code developed at the University of Oxford that performs the 1D numerical model developed on the PISA project. An outline of the theory and application of the 1D method OxPile uses can be found in Byrne et al. (2020) and Burd et al. (2020) for clays and sands respectively. The comparison performed herein has been performed using the 1D parametric model described in Byrne et al. (2020). This model utilises soil reactions derived through a calibration exercise using 3D FEA for a range of pile geometries in conditions similar to the glacial clays encountered at the Cowden site. The reader is directed to Byrne et al. (2020) for a description of the derivation and application of the soil reactions in the 1D modelling approach OxPile uses.

Figure 8.10 shows the pile head load displacement response obtained using the PISA 1D method for pile tests CS2, CM2, CM9, CL1 and CL2. The resistance at 0.1D from the pile tests, from Table 8.8, is less than the maximum resistance for each tests. In each case, the maximum resistance from the 1D approach is close to that predicted by the simple method using $\alpha = 1$; results from the 1D method are typically within 5% of the simple $\alpha = 1$ capacity. It should again be noted that the OxPile models have been calibrated based on the 3D FEA performed as part of PISA. The 3D FEA was performed to large displacements and as such the comparison here is not an extrapolation outside the calibration range of the soil reactions in OxPile. However these displacements are much greater than the 0.1D the pile testing was performed to so some caution is still needed in interpreting the results. However the close match between the simple method derived using OxLim and the OxPile results at high displacement is encouraging.

One approach that can be used to obtain the resistance at 0.1D displacement is to divide the capacity obtained using the simple method by a factor; such as has been done in Figure 8.11 for the simple method capacities shown in Figure 8.9. The factors in this figure have been derived by dividing the maximum resistance from the 1D approach by the resistance at 0.1D displacement. It is likely that factors like these could be related to the L/D, EI/s_uD^4 and a dimensionless group relating pile flexibility to soil stiffness. However a study to find such a relationship is outside the scope of this case study.

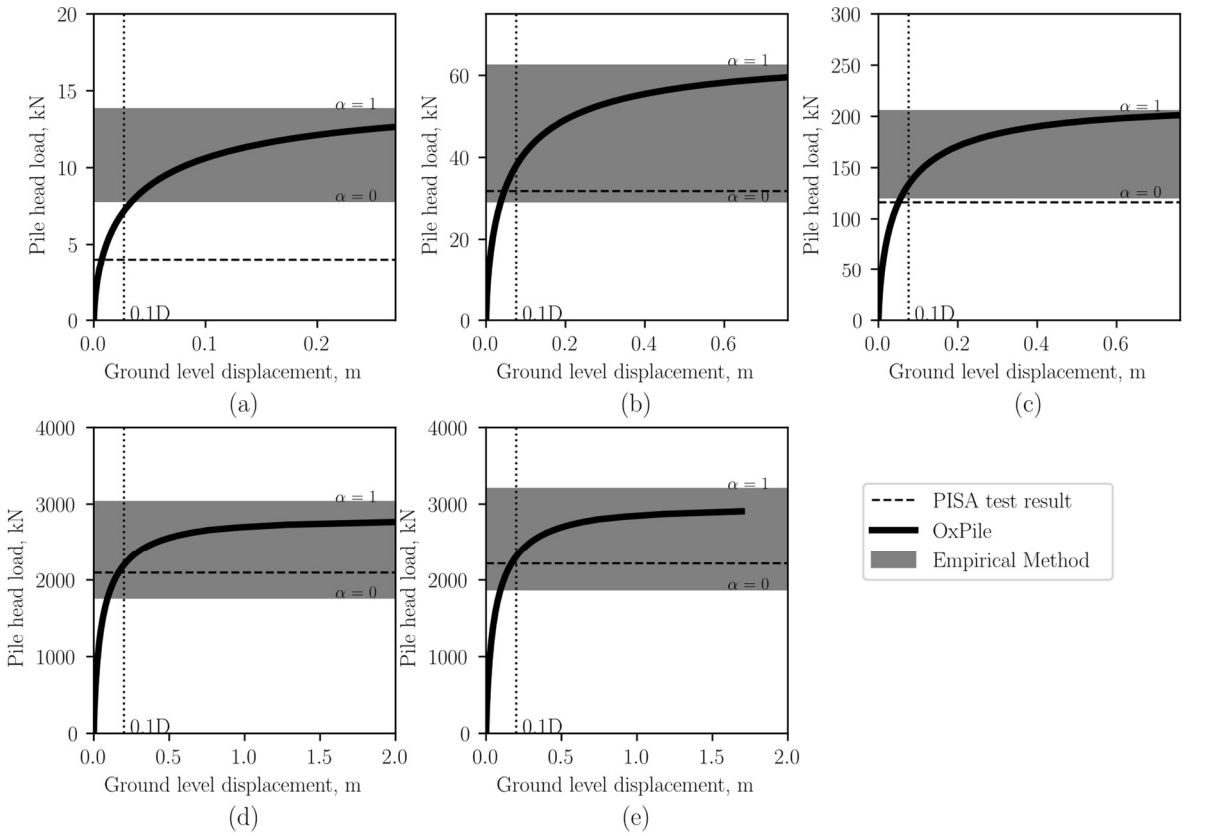

Figure 8.10 - Load against lateral deflection at ground level using 1D numerical model for PISA tests (a) CS2, (b) CM2, (c) CM9, (d) CL1, and (e) CL2

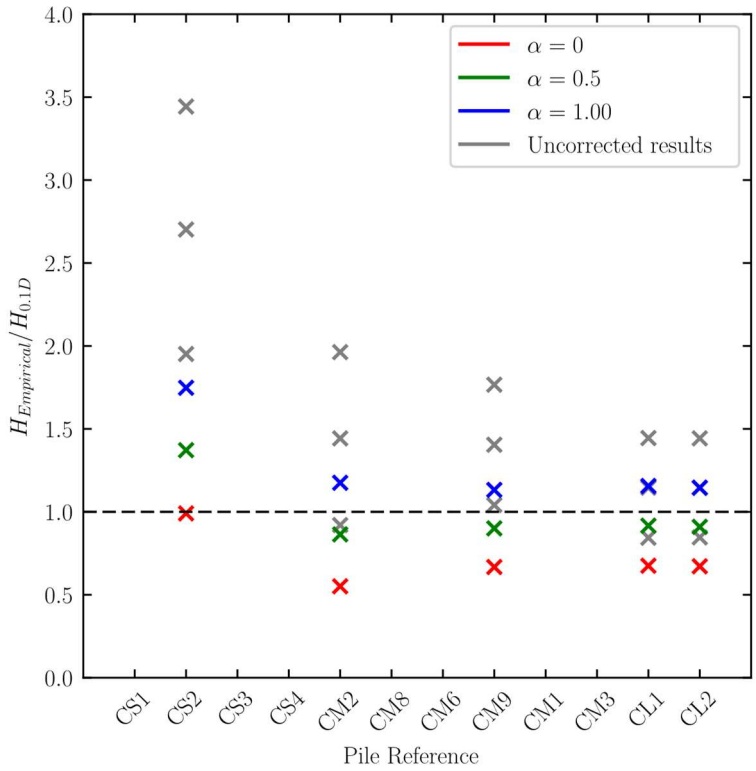

Figure 8.11 - Simple lateral capacities corrected to $H_{0.1D}$ based on 1D load-deflection response

Chapter 9

Conclusions and Further Work

In this thesis finite element limit analysis (FELA) has been used to investigate the capacity of laterally loaded piles in clay. This investigation has been performed using the software Oxlim; a set of solvers capable of producing upper and lower bound plasticity solutions for 2D and 3D geotechnical problems. This chapter summarises the key findings and conclusions from the work performed in this thesis along with potential areas of further research.

9.1. Conclusions

In Chapter 4, the mechanisms that contribute to a piles lateral capacity were investigated for homogenous soils conditions. Oxlim was used to find rigorous upper and lower bound solutions for a piles lateral capacity with varying L/D, interface tension conditions and $\gamma D/s_u$. Charts of normalised lateral load and moment capacity were provided. It was demonstrated that the conditions of weightless soil with no interface tension and full interface tension provide lower and upper limits to a pile capacity with high ratios of $\gamma D/s_u$ resulting in resistance close to that of the full tension case. Methods of predicting the distribution of lateral resistance with depth, i.e the profile of N_p, from the available literature were compared to the Oxlim results. It was seen that the Jeanjean (2016) method provided a reasonable estimate when compared to the Oxlim obtained results however it was evident that there were some potential shortcomings to the method.

In Chapter 5 the investigation was expanded to non-homogenous conditions: simple strength gradient conditions, abrupt changes in strength and embedded layers of higher strength

materials. The first part of Chapter 5 focusing on simple strength gradients demonstrated that the principles established in Chapter 4 were applicable to soil where strength is proportional to depth. Charts relating lateral capacity to L/D and h/D were presented and a comparison to the literature methods of predicting N_p was again made. It was again shown that the Jeanjean (2017) method of predicting N_p provided a reasonable estimate of N_p however similar shortcomings to those identified in Chapter 4 were shown: i.e. over prediction at high γ/ρ and full interface tension along with a greater dependence on pile-soil adhesion ratio, α, than observed from the Oxlim results. A parameterised form of the Jeanjean (2017) equation was made and an optimisation exercise was performed against a large set of Oxlim results. The resulting equation from this exercise was shown to give a better prediction of N_p for the majority of cases. As such it is recommended to use this updated equation to predict N_p.

In the second part of Chapter 5 the effect of an abrupt change in soil strength was investigated. It was demonstrated that an abrupt change in strength can impact the lateral bearing factor to a considerable distance away from the layer boundary. For layer boundaries in flow around conditions the change in resistance extended to $1D$ away from the layer boundary and with an increase in strength in the weaker layer to approximately $1.3N_p$ near the boundary. The decrease in strength in the stronger layer was shown to be roughly proportional to the ratio of layer strengths s_{u2}/s_{u1}. Similar behaviour was observed when the strength change occurred within the wedge mechanism with simple rules provided for estimating the extent and magnitude of this effect.

The final part of Chapter 5 investigated the effect of having a thin layer of higher strength material embedded in a homogenous soil. It was shown that for embedded layers above $1D$ thickness the changes in resistance near the layer boundaries behaved independently with the resistance near the centre of the embedded layer reaching $N_{p,flow}$. For thinner layers the reductions in N_p resulted in the maximum N_p in the layer being lower than $N_{p,flow}$. The maximum resistance in the embedded layer was shown to be independent of s_{u2}/s_{u1} however s_{u2}/s_{u1} did

impact on the available resistance in the layer by reducing N_p near the layer boundaries as s_{u2}/s_{u1} increased.

In Chapter 6 investigations were performed in other aspects that effect a piles lateral resistance, namely: the value of N_p at the ground surface, an increase in N_p that occurs at the pile toe, the shear and moment resistance across the pile toe and the distributed moment down the length of the pile. In the first study it was demonstrated that N_p at the ground surface could be expressed as linear relationship with the pile-soil adhesion ratio α. The second study demonstrated that an increase in N_p near the pile toe does occur for rigid piles. It was shown that this increase was independent of any dimensionless groups, occurred in both the flow around and wedge mechanisms and could be represented by a simple linear increase in resistance near the pile toe. In the third part of Chapter 4, it was demonstrated that the shear and moment capacities could be calculated using simple equations utilising the pile geometry and soil strength. It was also shown that the shear and moment that occur at the pile base are interdependent and could be expressed as an envelope of shear and moment resistance. This envelope can be expressed as a function of distance to the rotation point and can be used in a moment equilibrium equation for calculating pile capacity. Finally in Chapter 6, the distributed moment acting on the pile shaft was investigated. This investigation was performed using an iterative methodology with Oxlim and demonstrated the effect that phantom shears can have on the resistance, i.e. invalid shear stresses occurring on the pile-soil interface when separation has occurred. The Oxlim results were compared to distributed moments obtained using displacement based Finite Element Analysis (FEA) with both methods showing that for rigid piles some simple rules could be used to estimate the resistance. The maximum distributed moment that occurs was shown to be related to α and rules for both full interface tension and interface separation cases were presented.

In Chapter 7 an investigation into the effect of pile flexibility on lateral resistance was performed by comparing the results from FEA to the rigid pile capacities obtained using Oxlim.

The lateral capacity estimated using FEA was performed using a pile head deflection of 0.1*D*: a common practice when performing laterally loaded pile tests. It was shown that lower pile flexibility would lead to Oxlim overpredicting pile capacity for $L/D > 6$ when compared with the FEA obtained capacity.

In Chapter 8 several case studies were performed to demonstrate the application of recommendations from this Thesis. The first case study showed the moment equilibrium equation presented by Brinch-Hansen (1954) could be extended to incorporate the aspects of resistance investigated in this thesis; such as the base moment and shear, and the distributed moment. When performed for a simple strength profile this empirical equation showed a very close match to the Oxlim obtained results. In the second part of Chapter 8 these methods were applied to a strength profile with an abrupt change in strength to demonstrate the use of the rules presented in Chapter 5. A good match between the Oxlim capacity and the empirical method was again shown. Finally, a comparison was made to the recently performed PISA pile tests at Cowden (Byrne et al. 2019). The first part of comparison looked at a direct comparison of the empirical methodology and Oxlim obtained results to the pile tests results (which were performed to 0.1*D* pile head deflection). It was shown that this resulted in an overprediction from both Oxlim and the empirical method; this overprediction occurring due to the PISA test piles not being at their ultimate resistance when at 0.1D displacement. In the second part of this case study, the Oxpile software was used to estimate the ultimate lateral capacity of each of the piles (which typically occurred around 1D pile displacement). Comparing the Oxpile obtained capacity to the empirical method lead to a good estimate of the pile capacity when using $\alpha = 1$ in the empirical method.

9.2. Further Work

While this thesis has covered an extensive range of topics relating to lateral pile resistance there are stills a few areas where additional work could be performed. One area that has not been

covered is the effect that vertical loading will have on the available lateral capacity. It has been shown for other foundation types that vertical loads will influence the available lateral load and piles are no exception. This is something that could readily be performed using Oxlim in order to establish the how much a reduction that vertical loading causes to the lateral and moment capacity. This could readily be performed for each resistance mechanism that has been investigated in this thesis and rules established to reduce each mechanism by some factor related to V/V_{ult}; i.e. the proportion of applied vertical load to the piles ultimate vertical capacity.

In this work, only resistance in clay has been investigated. The current implementation of Oxlim3D utilises Second Order Cone Programming as it's solver routine. This approach is only suitable for total stress problems such as those defined using the Von-Mises yield criterion. An important piece of further work to this thesis would be to perform a similar investigation in granular materials; i.e. through use of the Mohr Coulomb yield surface or similar. Such an approach may be possible using Semi-Definite Programming. An important consideration here is whether the behaviour observed in Chapter 5 for abrupt changes in shear strength would also occur when a soil profiles contains both sand and clay materials. It's not uncommon in the North Sea to encounter dense sand next to lightly overconsolidated clay.

A final area where further work would be beneficial is a more detailed investigation using FEA to try and establish relationships between $H_{0.1D}$ and a piles ultimate capacity. As has been shown in Chapter 8, the empirical methodology presented in this thesis can potentially provide a very good estimate of the ultimate lateral capacity of a pile. However, it is important when designing a pile to understand the difference between these two values of resistance and what would be most appropriate to use during design. This is especially important considering the wide range of differences that were shown to occur in the PISA testing; with ultimate capacities being between 1.3 and 3 times $H_{0.1D}$. A comprehensive FEA study of this would permit rules to be established that would allow designers to be better informed of a piles expected lateral capacity; especially when using L/D in the intermediate range where the behaviour is neither rigid or

fully flexible. Such as study could also readily incorporate further analysis into the limiting case of plastic hinge formation through using of an elastoplastic constitutive rule for the structural elements.

References

ABPmer, 2011, The Galloper Wind Farm – Coastal Processes Assessment Report, Accessed From infrastructure.planninginspectorate.gov.uk on 8/04/19 (full link: http://www.galloperwindfarm.com/assets/images/documents/GWF%20Environmental%20Statement/ES_Appendices_Technical_Appendix_1_Part_2.pdf)

Achmus, M., Abdel-Rahman, K. and Kuo, Y. S. (2007) 'Behavior of Large Diameter Monopiles Under Cyclic Horizontal Loading', in *International Colloquium on Structural and Geotechnical Engineering*.

Achmus, M., Abdel-Rahman, K. and Peralta, P. (2005) 'On the design of monopile foundations with respect to static and quasi-static cyclic loading', *Copenhagen Offshore Wind*, pp. 1–9.

Ahmadi, M. M. and Ahmari, S. (2009) 'Finite-element modelling of laterally loaded piles in clay', *Proceedings of the Institution of Civil Engineers: Geotechnical Engineering*. Thomas Telford Ltd, 162(3), pp. 151–163. doi: 10.1680/geng.2009.162.3.151.

Ahn, J., Lee, H. and Kim, Y. T. (2014) 'Holding capacity of suction caisson anchors embedded in cohesive soils based on finite element analysis', *International Journal for Numerical and Analytical Methods in Geomechanics*. Wiley Online Library, 38(15), pp. 1541–1555. doi: 10.1002/nag.2268.

American Petroleum Institute (2011) API RP 2GEO Geotechnical and foundation design considerations', *American Petroleum Institute, Washington, DC, USA*, p. 120.

Aubeny, C. and Murff, J. D. (2005) 'Simplified limit solutions for the capacity of suction anchors under undrained conditions', *Ocean Engineering*. Elsevier, 32(7 SPEC. ISS.), pp. 864–877. doi: 10.1016/j.oceaneng.2004.10.006.

Aubeny, C. P., Han, S. W. and Murff, J. D. (2003) 'Inclined load capacity of suction caissons', *International Journal for Numerical and Analytical Methods in Geomechanics*. Wiley Online Library, 27(14), pp. 1235–1254. doi: 10.1002/nag.319.

Aubeny, C. P., Murff, J. D. and Moon, S. K. (2001) 'Lateral undrained resistance of suction caisson anchors', *International Journal of Offshore and Polar Engineering*. International Society of Offshore and Polar Engineers, 11(3), pp. 211–219.

Bang, S., Preber, T., Cho, Y., Thomason, J., Karnoski, S. R. and Taylor, R. J. (2000) *Suction piles for mooring of mobile offshore bases*, *Marine Structures*. doi: 10.1016/S0951-8339(00)00012-5.

Bathe, K. J. and Saunders, H. (1984) 'Finite Element Procedures in Engineering Analysis', *Journal of Pressure Vessel Technology*, 106(4), pp. 421–422. doi: 10.1115/1.3264375.

Bhattacharya, S., Carrington, T. M. and Aldridge, T. R. (2006) 'Design of FPSO piles against storm loading', in *Offshore Technology Conference 2006: New Depths. New Horizons*, pp. 295–303.

Bottero, A., Negre, R., Pastor, J. and Turgeman, S. (1980) 'Finite element method and limit analysis theory for soil mechanics problems', *Computer Methods in Applied Mechanics and Engineering*. Elsevier, 22(1), pp. 131–149. doi: 10.1016/0045-7825(80)90055-9.

Brinch Hansen, J. (1961) ‘The Ultimate Resistance of Rigid Piles Against Transversal Forces’, *Bulletin No. 12, Geoteknisk Institut (The Danish Geotechnical Institute)*, (12), pp. 5–9.

Brinkgreve, R. B. J., Kumarswamy, S., Swolfs, W. M., Waterman, D., Chesaru, A., Bonnier, P. G. (2016) ‘Plaxis 2014’, *PLAXIS bv, the Netherlands*.

British Standards Institution (2004) ‘BS EN 1997-1:2004+A1:2013 Eurocode 7. Geotechnical design. General rules’. BSI London, UK. Available at: http://shop.bsigroup.com/ProductDetail/?pid=000000000030272167.

Broms, B. (1964) ‘Lateral Resistance of Piles in Cohesive Soils’, *Journal of the Soil Mechanics and Foundations Division*. ASCE, 90(3), pp. 123–158.

British Standards Institute (2004) ‘BS EN 1997-1: 2004: Eurocode 7: Geotechnical design--Part 1: General rules’. BSI London, UK.

Burd, H. J., Beuckelaers, W. J. A. P., Byrne, B. W., Gavin, K., Houlsby, G. T., Igoe, D., Jardine, R. J., Martin, C. M., McAdam, R. A., Muir Wood, A., Potts, D. M., Skov Gretlund, J., Taborda, D. M. G. and Zdravković, L. (2019) ‘New data analysis methods for instrumented medium-scale monopile field tests’, *Géotechnique*. ICE Publishing, pp. 1–28. doi: 10.1680/jgeot.18.pisa.002.

Burd, H. J., Taborda, D. M. G., Zdravković, L., Abadie, C. N., Byrne, B. W., Houlsby, G. T., Gavin, K. G., Igoe, D. J. P., Jardine, R., J., Martin, C. M., McAdam, R. A., Pedro, A. M. G., and Potts, D., M. (2020). PISA design model for monopiles for offshore wind turbines: application to a marine sand. *Géotechnique,* https://doi.org/10.1680/jgeot.18.P.277.

Byrne, B. W., McAdam, R., Burd, H. J., Houlsby, G. T., Martin, C. M., Zdravković, L., Taborda, D. M. G., Potts, D. M., Jardine, R. J., Sideri, M., Schroeder, F. C., Gavin, K., Doherty, P., Igoe, D., Muirwood, A., Kallehave, D. and Skov Gretlund, J. (2015) ‘New design methods for large diameter piles under lateral loading for offshore wind applications’, in *Frontiers in Offshore Geotechnics III - Proceedings of the 3rd International Symposium on Frontiers in Offshore Geotechnics, ISFOG 2015*, pp. 705–710.

Byrne, B. W., McAdam, R. A., Burd, H. J., Houlsby, G. T., Martin, C. M., Gavin, K., Doherty, P., Igoe, D., Zdravkovic, L., Taborda, D. M. G., Potts, D. M., Jardine, R. J., Sideri, M., Schroeder, F. C., Wood, A. M., Kallehave, D. and Gretlund, J. S. (2015) ‘Field testing of large diameter piles under lateral loading for offshore wind applications’, *Geotechnical Engineering for Infrastructure and Development - Proceedings of the XVI European Conference on Soil Mechanics and Geotechnical Engineering, ECSMGE 2015*. Taylor and Francis Group London, 3, pp. 1255–1260.

Byrne, B.W., McAdam, R.A., Burd, H.J., Houlsby, G.T., Martin, C.M. Beuckelaers, W.J.A.P., Zdravkovic, L., Taborda, D.M.G, Potts, D.M., Jardine, R.J., Ushev, E., Liu, T., Abadias, D., Gavin, K., Igoe, D., Doherty, P., Skov Gretlund, J., Pacheco Andrade, M., Muir Wood, A., Schroeder, F.C., Turner, S., Plummer, M.A.L. (2017) PISA: New design methods for offshore wind turbine monopiles. Offshore Site Invesitigation and Geotechnics, Societry for Underwater Technology, London, UK

Byrne, B. W., Burd, H. J., Zdravkovic, L., Abadie, C. N., Houlsby, G. T., Jardine, R. J., Martin, C. M., McAdam, R. A., Andrade, M. P., Pedro, A. M. G., Potts, D. M. and Taborda, D. M. G. (2019) ‘PISA design methods for offshore wind turbine monopiles’, *Proceedings of the Annual Offshore Technology Conference*. EDP Sciences, 2019-May(158), p. 3.

Byrne, B. W, McAdam, R., Burd, H., Beuckelaers, W., Gavin, K., Houlsby, G., Igoe, D., Jardine, R., Martin, C., Muir Wood, A. and others (2019) 'Monotonic laterally loaded pile testing in a stiff glacial clay till at Cowden', *Géotechnique*. Thomas Telford.

Byrne, B. W., Houlsby, G. T., Burd, H. J., Gavin, K. G., Igoe, D. J. P., Jardine, R. J., Martin, C M., McAdam, R. A., Potts, D. M., Taborda, D. M. G., and Zdravković, L. (2020) PISA design model for monopiles for offshore wind turbines: application to a stiff glacial clay, *Géotechnique*, https://doi.org/10.1680/jgeot.18.P.225.

Chow, F. and Jardine, R. J. (1996) 'Investigations into the behaviour of displacement piles for offshore foundations', in *Ground Engineering*, pp. 24–25.

Clukey, E. C., Aubeny, C. P. and Murff, J. D. (2004) 'Comparison of analytical and centrifuge model tests for suction caissons subjected to combined loads', in *Journal of Offshore Mechanics and Arctic Engineering*, pp. 364–367. doi: 10.1115/1.1834624.

Det Norske Vertias-Germanischer Lloyd (2016) 'DNVGL-ST-0126 : Support structures for wind turbines', *Dnv Gl As*, (April 2016).

Doyle, E. H., Dean, E. T. R., Sharma, J. S., Bolton, M. D., Valsangkar, A. J., Newlin, J. A. and others (2004) 'Centrifuge model tests on anchor piles for tension leg platforms', in *Offshore Technology Conference*.

Dunne, H. P. (2017) *Finite element limit analysis of offshore foundations on clay*. DPhil Thesis, University of Oxford, Oxford

Dunne, H.P., Martin, C.M., Muir, L., Brown, N., Wallerand, R. (2015) Undrained bearing capacity of skirted mudmats on inclined seabeds, *Frontiers in Offshore Geotechnics III - 3rd International Symposium on Frontiers in Offshore Geotechnics, ISFOG 2015*, pp. 783-788

Dunne, H. P. and Martin, C. M. (2017) 'Capacity of rectangular mudmat foundations on clay under combined loading', *Géotechnique*. Thomas Telford, 67(2), pp. 168–180. doi: 10.1680/jgeot.16.P.079.

European Wind Energy Association (2011) 'Wind in power–2010 European statistics', *Brussels: February*.

Grajales-Saavedra, F., Aubeny, C., Drew, D., Jeanjean, P. and Zakeri, A. (2017) 'Upper Bound Plastic Limit Analyses of Laterally Loaded Piles in Stratified Soils', in *Offshore Site Investigation Geotechnics 8th International Conference Proceedings*, pp. 611–619. doi: 10.3723/osig17.611.

Hamre, L., Feizi Khankandi, S., Strøm, P. J. and Athanasiu, C. (2011) 'Lateral behaviour of large diameter monopiles at Sheringham Shoal Wind Farm', *Frontiers in Offshore Geotechnics II - Proceedings of the 2nd International Symposium on Frontiers in Offshore Geotechnics*, pp. 575–580.

He, Y., Byrne, B. and Burd, H. (2017) 'Application of a Numerical-Based Design Method for Laterally Loaded Monopiles in Layered Soils', in *Offshore Site Investigation Geotechnics 8th International Conference Proceedings*, pp. 1116–1123. doi: 10.3723/osig17.1116.

Hight, D. W., Gasparre, A., Nishimura, S., Minh, N. A., Jardine, R. J. and Coop, M. R. (2007) 'Characteristics of the London Clay from the Terminal 5 site at Heathrow Airport', *Géotechnique*. Thomas Telford Ltd, 57(1), pp. 3–18.

Jeanjean, P (2009) 'Re-Assessment of P-Y Curves for Soft Clays from Centrifuge Testing and Finite Element Modeling', *2009 Offshore Technology Conference*, (Vm), pp. 1–23. doi: 10.4043/20158-MS.

Jeanjean, P., Zhang, Y., Zakeri, A., Andersen, K.H., Gilbert, R., Senanayake, A.I.M.J. (2017) A framework for monotonic p-y curves in clays, *Offshore Site Investigations and Geotechnics, Society for Underwater Technology, London, UK*

Kay, S and Palix, E. (2011) 'Caisson Capacity in Clay: VHM Resistance Envelope: Part 3—Extension to Shallow Foundations', in *ASME 2011 30th International Conference on Ocean, Offshore and Arctic Engineering*, pp. 789–798.

Klar, A. and Randolph, M. F. (2008) 'Upper-bound and load-displacement solutions for laterally loaded piles in clays based on energy minimisation', *Géotechnique*. Thomas Telford Ltd, 58(10), pp. 815–820. doi: 10.1680/geot.2007.00197.

Krabbenhøft, K., Lyamin, A. V. and Sloan, S. W. (2008) 'Three-dimensional Mohr-Coulomb limit analysis using semidefinite programming', *Communications in Numerical Methods in Engineering*. Wiley Online Library, 24(11), pp. 1107–1119. doi: 10.1002/cnm.1018.

Kraft, D. (1988) 'A software package for sequential quadratic programming', *Forschungsbericht-Deutsche Forschungs- und Versuchsanstalt fur Luft- und Raumfahrt*.

Lam, I. P. O., Martin, G. R. (1986) Seismic Design of High-way Bridge Foundations. US Department of Transportation, Report No. FHWA/RD-8/102

Li, D., Ma, S., Zhang, Y. and Chen, F. (2018) Lateral Bearing Capacity of Modified Suction Caissons Determined by Using the Limit Equilibrium Method, *China Ocean Engineering*. Springer, 32(4), pp. 461–466. doi: 10.1007/s13344-018-0048-3.

Lyamin, A. V. and Sloan, S. W. (2002a) Lower bound limit analysis using non-linear programming, *International Journal for Numerical Methods in Engineering*. Wiley Online Library, 55(5), pp. 573–611. doi: 10.1002/nme.511.

Lyamin, A. V. and Sloan, S. W. (2002b) Upper bound limit analysis using linear finite elements and non-linear programming, *International Journal for Numerical and Analytical Methods in Geomechanics*. Wiley Online Library, 26(2), pp. 181–216. doi: 10.1002/nag.198.

Lyamin, A. V., Sloan, S. W., Krabbenhøft, K. and Hjiaj, M. (2005) Lower bound limit analysis with adaptive remeshing, *International Journal for Numerical Methods in Engineering*. Wiley Online Library, 63(14), pp. 1961–1974. doi: 10.1002/nme.1352.

Makrodimopoulos, A and Martin, C. (2005) Limit analysis using large-scale SOCP optimization, *Proc. 13th Nat. Conf. of UK Association for Computational Mechanics in Engineering*, pp. 21–24.

Makrodimopoulos, A., Martin, C. M. (2005) A novel formulation of upper bound limit analysis as a second-order cone programming problem, *Computational Plasticity: Fundamentals and Applications - Proceedings of the 8th International Conference on Computational Plasticity, COMPLAS VIII*, pp. 1083–1086.

Makrodimopoulos, A., Martin, C. M. (2006) 'Lower bound limit analysis of cohesive-frictional materials using second-order cone programming', *International Journal for Numerical Methods in Engineering*. Wiley Online Library, 66(4), pp. 604–634. doi: 10.1002/nme.1567.

Makrodimopoulos, A., Martin, C. M. (2007) 'Upper bound limit analysis using simplex strain elements and second-order cone programming', *International Journal for Numerical and Analytical Methods in Geomechanics*. Wiley Online Library, 31(6), pp. 835–865. doi: 10.1002/nag.567.

Makrodimopoulos, A. and Martin, C. M. (2008) 'Upper bound limit analysis using discontinuous quadratic displacement fields', *Communications in Numerical Methods in Engineering*. Wiley Online Library, 24(11), pp. 911–927. doi: 10.1002/cnm.998.

Martin, C. M. and Randolph, M. F. (2006) 'Upper-bound analysis of lateral pile capacity in cohesive soil', *Géotechnique*, pp. 141–145. doi: 10.1680/geot.2006.56.2.141.

Martin, C. M. and Makrodimopoulos, A. (2008) 'Finite-element limit analysis of Mohr-Coulomb materials in 3D using semidefinite programming', *Journal of Engineering Mechanics*. American Society of Civil Engineers, 134(4), pp. 339–347. doi: 10.1061/(ASCE)0733-9399(2008)134:4(339).

Martin, C. M. (2011) 'The use of adaptive finite-element limit analysis to reveal slip-line fields', *Géotechnique Letters*. Thomas Telford Ltd, 1(2), pp. 23–29. doi: 10.1680/geolett.11.00018.

Martin, C. M., Dunne, H. P., Wallerand, R. and Brown, N. (2015) 'Three-dimensional limit analysis of rectangular mudmat foundations', *Frontiers in Offshore Geotechnics III - 3rd International Symposium on Frontiers in Offshore Geotechnics, ISFOG 2015*, pp. 789–794.

Martin, C. M. and White, D. J. (2012) 'Limit analysis of the undrained bearing capacity of offshore pipelines', *Géotechnique*. ICE Publishing, 62(9), pp. 847–863. doi: 10.1680/geot.12.OG.016.

Matlock, H. (1970) 'Correlations for Design of Laterally Loaded Piles in Soft clay', *Offshore Technology Conference, Houston, Texas*

McAdam, R., Byrne, B. W., Houlsby, G., Beuckelaers, W., Burd, H., Gavin, K., Igoe, D., Jardine, R., Martin, C., Muir Wood, A. and others (2019) 'Monotonic laterally loaded pile testing in a dense marine sand at Dunkirk', *Géotechnique*. Thomas Telford.

Mosek, A. P. S. (2010) 'The MOSEK optimization software', *Online at http://www. mosek. com*, 54(2–1), p. 5.

Murff, J. D. and Hamilton, J. M. (1993b) 'P-ultimate for undrained analysis of laterally loaded piles', *Journal of Geotechnical Engineering*. American Society of Civil Engineers, 119(1), pp. 91–107. doi: 10.1061/(ASCE)0733-9410(1993)119:1(91).

Murff, J. D., Wagner, D. A. and Randolph, M. F. (1989) 'Pipe penetration in cohesive soil', *Géotechnique*. Thomas Telford Ltd, 39(2), pp. 213–229.

Page, A. M., Grimstad, G., Eiksund, G. R. and Jostad, H. P. (2019) A macro-element model for multidirectional cyclic lateral loading of monopiles in clay, *Computers and Geotechnics*. doi: 10.1016/j.compgeo.2018.11.007.

Potts, D. M., Zdravkovic, L. (1999): *Finite element analysis in geotechnical engineering: Volume 1 - Theory,* Thomas Telford.

Potts, D. M., Zdravković, L. (2001) *Finite Element Analysis in Geotechnical Engineering: Volume two - Application*, Thomas Telford

Randolph, M., Houlsby, G. (1984) The limiting presusre ona acircular pile loaded laterally in cohesive soil, *Géotechnique*. Thomas Telford Ltd, 34 (4), pp. 613–623.

Randolph, M. F. and House, A. R. (2002) Analysis of Suction Caisson Capacity in Clay, in *Proceedings of the Annual Offshore Technology Conference*, pp. 2145–2155.

Randolph, M., Gourvenec, S. (2011) *Offshore geotechnical engineering*. CRC Press.

Reese, L. C. (1958) 'Discussion on soil modulus for laterally loaded piles', *Trans. American Society of Civil Engineers*, 123, pp. 1071–1074.

Reese, L. C., Welch, R. C. (1975) Lateral Loading of Deep Foundations in Stiff Clay, *ASCE J Geotech Eng Div*, 101(7), pp. 633–649.

Reese, L., Cox, W. and Koop, F. (1975) Field testing and analysis of laterally loaded piles in stiff clay, *Offshore Technology Conference*, pp. 671–690.

van Rossum, G. and Drake, F. L. (2011) *The python language reference manual*. Network Theory Ltd.

Si, H. (2015) 'TetGen, a delaunay-based quality tetrahedral mesh generator', *ACM Transactions on Mathematical Software*. ACM, 41(2), p. 11. doi: 10.1145/2629697.

Skempton, A. W. (1951) 'The bearing capacity of clays', *Selected Papers on Soil Mechanics*, pp. 50–59.

Sloan, S. W. (1988) 'Lower bound limit analysis using finite elements and linear programming', *International Journal for Numerical and Analytical Methods in Geomechanics*. Wiley Online Library, 12(1), pp. 61–77.

Sloan, S. W. (2013) Geotechnical Stability Analysis, *Géotechnique, vol 63(7), pp531-571*

Stevens, J. B., Audibert, J. M. E. (1979) 'Re-examination of p-y curve formulations', in *Proceedings of the Annual Offshore Technology Conference*, pp. 397–404.

Storn, R., Price, K. (1997) 'Differential evolution--a simple and efficient heuristic for global optimization over continuous spaces', *Journal of global optimization*. Springer, 11(4), pp. 341–359.

Sullivan, W. R., Reese, L. C. and Fenske, C. W. (1980) 'Unified method for analysis of laterally loaded piles in clay', in *Numerical methods in offshore piling*. Thomas Telford Publishing, pp. 135–146.

Taborda, D. M. G., Zdravković, L., Potts, D. M., Burd, H. J., Byrne, B. W., Gavin, K., Houlsby, G. T., Jardine, R. J., Liu, T., Martin, C. M. and McAdam, R. A. (2019) Finite element modelling of laterally loaded piles in a dense marine sand at Dunkirk, *Géotechnique*. Thomas Telford, pp. 1–47. doi: 10.1680/jgeot.18.pisa.006.

Tapper, L., Martin, C. M. and Byrne, B. W. (2014) 'Undrained bearing capacity of circular footings on Tresca soil using adaptive finite element analysis', in *Numerical Methods in Geotechnical Engineering - Proceedings of the 8th European Conference on Numerical Methods in Geotechnical Engineering, NUMGE 2014*, pp. 699–704.

Templeton, J. S. (2009) Finite element analysis of conductor/seafloor interaction, in *Offshore Technology Conference*.

Van Eekelen, H. A. M. (1980) Isotropic yield surfaces in three dimensions for use in soil mechanics, *International Journal for Numerical and Analytical Methods in Geomechanics*. Wiley Online Library, 4(1), pp. 89–101. doi: 10.1002/nag.1610040107.

Wandji, W. N., Natarajan, A., Dimitrov, N. and Buhl, T. (2015) Design of monopiles for multi-megawatt wind turbines at 50 m water depth, in *European Wind Energy Association Annual Conference and Exhibition 2015, EWEA 2015 - Scientific Proceedings*, pp. 8–12.

Wind Europe (2017) Wind in power: 2016 European statistics, *Bruksela: Wind Europe*.

Wu, D., Broms, B. B. and Choa, V. (1998) Design of laterally loaded piles in cohesive soils using p-y curves, *Soils and Foundations*. The Japanese Geotechnical Society, 38(2), pp. 17–26. doi: 10.3208/sandf.38.2_17.

Yu, J., Huang, M., Li, S. and Leung, C. F. (2017) Load-displacement and upper-bound solutions of a loaded laterally pile in clay based on a total-displacement-loading EMSD method, *Computers and Geotechnics*. Elsevier, 83, pp. 64–76. doi: 10.1016/j.compgeo.2016.10.025.

Yu, J., Huang, M. and Zhang, C. (2015) Three-dimensional upper-bound analysis for ultimate bearing capacity of laterally loaded rigid pile in undrained clay, *Canadian Geotechnical Journal*. NRC Research Press, 52(11), pp. 1775–1790. doi: 10.1139/cgj-2014-0390.

Zdravković, L., Taborda, D. M. G., Potts, D. M., Jardine, R. J., Sideri, M., Schroeder, F. C., Byrne, B. W., McAdam, R., Burd, H. J., Houlsby, G. T., Martin, C.M., Gavin, K., Doherty, P, Igoe, D., Muir Wood, A., Kallehave, D., Gretlund, J.S. (2015) 'Numerical modelling of large diameter piles under lateral loading for offshore wind applications', *Frontiers in Offshore Geotechnics III*. Taylor and Francis Group London, pp. 759–764.

Zdravković, L., Jardine, R. J., Taborda, D. M. G., Abadias, D., Burd, H. J., Byrne, B. W., Gavin, K., Houlsby, G. T., Igoe, D., Liu, T., Martin, C. M., McAdam, R. A., Muir Wood, A., Potts, D. M., Skov Gretlund, J. and Ushev, E. (2019a) Ground characterisation for PISA pile testing and analysis, *Géotechnique*. Thomas Telford, pp. 1–50. doi: 10.1680/jgeot.18.pisa.001.

Zdravković, L., Taborda, D. M. G., Potts, D. M., Abadias, D., Burd, H. J., Byrne, B. W., Gavin, K., Houlsby, G. T., Jardine, R. J., Martin, C. M., McAdam, R. A. and Ushev, E. (2019b) Finite element modelling of laterally loaded piles in a stiff glacial clay till at Cowden, *Géotechnique*. Thomas Telford, pp. 1–40. doi: 10.1680/jgeot.18.pisa.005.

Zhang, Y., Andersen, K. H. and Tedesco, G. (2016) 'Ultimate bearing capacity of laterally loaded piles in clay – Some practical considerations', *Marine Structures*. Elsevier, 50, pp. 260–275. doi: 10.1016/j.marstruc.2016.09.002.